Many-Body Phenomena in Low-Dimensional Systems:
From Simple Models to Real Materials

Dissertation

zur Erlangung des
Doktorgrades der Naturwissenschaften (Dr. rer. nat.)
der Fakultät für Physik der Universität Regensburg

vorgelegt von

Julian Siegl
aus Maxhütte-Haidhof

im Jahr 2025

Promotionsgesuch eingereicht am 25.06.2025.

Die Arbeit wurde angeleitet von Prof. Dr. John Schliemann.

Prüfungsausschuss:

Vorsitzender: PD Dr. Nicola Paradiso
Erstgutachter: Prof. Dr. John Schliemann
Zweitgutachter: Prof. Dr. Jaroslav Fabian
Weitere Prüferin: Prof. Dr. Sara Collins

Promotionskolloquium am 03.11.2025.

LIST OF PUBLICATIONS

PUBLISHED ARTICLES

- **J. Siegl**, J. Picó-Cortés, M. Grifoni, *Particle conserving approach to ac-dc driven interacting quantum dots with superconducting leads*, Physical Review B, **107**, 115405
  → covered in part 1
- **J. Siegl**, J. Schliemann, *Imperfect Many-Body Localization in Exchange-Disordered Isotropic Spin Chains*, New Journal of Physics, **25**, 123002
  → covered in part 2
- **J. Siegl**, A. Bleibaum, W. Wan, M. Kurpas, J. Schliemann, M. M. Ugeda, M. Marganska, M. Grifoni, *Friedel oscillations and chiral superconductivity in monolayer $NbSe_2$*, Nature Communications, **16**, 8228
  → covered in part 3

SUBMITTED MANUSCRIPTS

- D. Giri, **J. Siegl**, J. Schliemann, *Spin-Spin Correlation Matrix and Many-Body Localization in Disordered SU(2)-Invariant Spin Chains*, submitted to Physical Review B.
  → not covered in this thesis
- L. Gibelli, S. Höcherl, **J. Siegl**, V. Vaňo, S. C. Ganguli, M. Marganska, M. Grifoni, *A universal route to chiral Ising superconductivity in monolayer TaS_2 and $NbSe_2$*, submitted to Physical Review Letters.
  → not covered in this thesis

MANUSCRIPTS IN PREPARATION

- G. C. Duarte-Filho, **J. Siegl**, J. Schliemann, J. C. Egues, *Consecutive-gap ratio distribution for crossover ensembles*, yet to be submitted.
  → not covered in this thesis

CONTENTS

1 INTRODUCTION 1

I TRANSPORT THROUGH S-QD-S NANOJUNCTIONS

2 NAKAJIMA-ZWANZIG FORMALISM APPLIED TO TRANSPORT 7
- 2.1 Dynamics of open quantum systems 7
- 2.2 Derivation of the Nakajima-Zwanzig equation 9
- 2.3 Nakajima-Zwanzig formalism for time-periodic problems 13

3 PARTICLE CONSERVING SUPERCONDUCTIVITY 16
- 3.1 Groundstate in the particle-conserving approach 17
- 3.2 Quasiparticles and thermal density operator 20
- 3.3 Phase representation of the condensates 22

4 AC-DC-DRIVEN INTERACTING QUANTUM DOT 30
- 4.1 Evaluation of the time-propagation and current kernels 32
- 4.2 Transport in the presence of DC drive 35
- 4.3 Transport in the presence of AC-DC drive 41

II MANY-BODY LOCALIZATION IN EXCHANGE-DISORDERED HEISENBERG CHAINS

5 INTRODUCTION TO MANY-BODY LOCALIZATION 51

6 IMPERFECT MANY-BODY LOCALIZATION 59

III UNCONVENTIONAL SUPERCONDUCTIVITY IN MONOLAYER 1H-$NBSE_2$

7 SCREENING IN TWO-DIMENSIONAL METALS 75
- 7.1 Random Phase Approximation in two-dimensional metals 76
- 7.2 Screened interaction in monolayer 1H-$NbSe_2$ 88

8 CHIRAL SUPERCONDUCTIVITY IN MONOLAYER 1H-$NBSE_2$ 96
- 8.1 Overview over different descriptions of superconductivity 96
- 8.2 Kohn-Luttinger induced superconducting order in 1H-$NbSe_2$ 102
- 8.3 Comparison to scanning tunneling spectroscopy 111

9 CONCLUSION 116

IV APPENDIX

A NOTATION AND UNITS 120

B GROUP THEORY AND SYMMETRIES 121
- B.1 Translational periodicity 121
- B.2 Point groups relevant for 1H-$NbSe_2$ 123

C MODELS 126

C.1 Particle-conserving BCS theory 126
C.2 Heisenberg spin chains 137
C.3 Tight-binding model for TMD monolayers 138
D DEVELOPED CODES 148
D.1 AC-DC-driven transport code 148
D.2 Imperfect many-body localization 148
D.3 Interaction in TMD monolayers 149
D.4 Superconductivity in TMD monolayers 149

BIBLIOGRAPHY 151
ACKNOWLEDGEMENTS 185

1

INTRODUCTION

This year, the first consistent formulation of quantum mechanics by Heisenberg [1] celebrates its centenary. It provides the framework for our understanding of semiconductor physics through band theory [2], thereby enabling applications of fundamental utility to our modern way of life, such as the transistor [3] and the light-emitting diode [4]. Beyond engineering applications, the refinement of quantum mechanics by the inclusion of special relativity [5] led to the development of modern quantum field theory [6, 7], which underpins our current standard model [8, 9] of the fundamental rules governing observable physics to high energies. Remaining open questions concerning the theory's validity at extremely high energies and its connection to the theory of general relativity present a fascinating frontier of human knowledge. However, it turns out that even a well-known theory, such as the (effectively) non-relativistic quantum mechanics of the electron, results in highly complex and novel phenomena. This thesis deals with problems of the latter type, always beginning with setups where the fundamental equations are known, but where the resulting phenomena elude simple descriptions due to their intricate nature.

A clear candidate for the emergence of complex behavior from simple equations is the presence of interaction in large ensembles of "simple" constituents. To illustrate this point, consider the classical n-body problem of orbiting bodies. For two celestial bodies, the motion described by Newton's well-known law of gravitation remains integrable, and a closed-form solution exists [10]. Once three or more bodies interact, the resulting dynamics become, in general, chaotic, and no closed-form solution exists [11], despite the equations of motion being simple. The increase in complexity with interaction is much the same for quantum-mechanical systems; even for simple, non-interacting problems, the addition of interaction often results in a form of the problem that impedes an exact solution [12]. For sufficiently weak disorder, and in three dimensions, the presence of weak interactions between fermions can often be captured by invoking Landau's Fermi-liquid theory, whereby the interacting theory is adiabatically connected to the non-interacting case [13, 14]. There, one can capture the effect of interactions by an effective non-interacting theory whose parameters are accessible by calculations using quantum field theory [15, 16].

However, the dynamics of many interacting particles need not resemble the non-interacting case at all, as captured by the famous quote of Nobel laureate P.W. Anderson [17],

"More is different.".

Famous examples of such behavior include, e.g., composite fermions in the description of the fractional quantum hall effect [18, 19] and the phenomenon of superconductivity [20]. In the latter, macroscopically many bound pairs of electrons [21] establish a correlated extended phase characterized by a $U(1)$-symmetric order parameter [22]. The latter can be interpreted as a macroscopic wavefunction [23, 24] whose behavior is qualitatively different from the Bloch theory [2], which provides the non-interacting description of the electrons in crystalline metallic superconductors like, e.g., pure aluminum [25].

The effect of interactions is moreover strongly dependent on the dimensionality of the system. Examples of such dimensional dependences include the instability of the Fermi-liquid picture against even weak interactions in one dimension, where, according to Tomonaga-Luttinger liquid theory [12, 26–28] the ground state does not allow for a perturbative expansion in the interaction, as is otherwise necessary for a Fermi-liquid description. In general, reduced dimensionality tends to increase the relative importance of interactions, both due to the kinematic considerations relevant to the Luttinger liquid theory, and due to the increased spatial confinement, which in turn enhances the role of the Coulomb interaction between electrons. This thesis covers separate works on interacting systems across different dimensionalities. Part I covers a superconducting junction containing a quantum dot. The latter represents a zero-dimensional, i.e., fully localized interacting quantum-mechanical system whose physics is fundamentally affected by the charging energy due to the strong on-site Coulomb interaction [29, 30]. Part II discusses a closed one-dimensional interacting quantum system, the exchange-disordered Heisenberg spin chain. The dynamics of this system in the presence of disorder are affected by the presence or absence of many-body localization, with the global non-abelian symmetry of the model playing a crucial role in this context. Part III treats the screening of Coulomb interaction and the resulting unconventional superconducting pairing in a two-dimensional real material, the superconducting monolayer transition dichalcogenide 1H-$NbSe_2$.

Beyond this conceptual common thread, each of the works presented throughout this thesis relates to some aspect of interaction-driven physics that may be useful for future technologies. Throughout the 20th century, the employment of an effectively non-interacting quantum-mechanical description has underpinned much of the development of novel technologies. With this realm largely explored and ever-progressing miniaturization increasing the relevance of interactions, the 21st century appears poised to witness further technological advancements based on the complex, emergent phenomena of interacting quantum systems. One prominent example of such technology is the ongoing technological race

to develop practical quantum computers. The idea of manipulating quantum-mechanical systems with Hilbert spaces spanned by macroscopic states dates back to the last century [31]. It has gained traction around the turn of this century, with superconducting circuits [32–34] as the foundation for some of the currently leading architectures in quantum computing [35], and contributing to key breakthroughs in this field [36]. These superconducting circuits rely on different components, with Josephson junctions contributing a non-linear element [37] crucial to many modern qubit designs. In such Josephson junctions, the peculiarities of tunneling between superconducting leads result in the emergence of the Josephson effect [38, 39], coupling a phase difference of the order parameters of the leads with the current.

The S-QD-S junction considered in Part I represents a model for an interacting Josephson junction [40]. The work on this type of junction in this thesis further develops a microscopic description of its transport characteristics. It puts special focus on the effect of simultaneous AC and DC driving, as may be relevant when implementing such junctions in a superconducting qubit, where a readout often involves coupling to AC resonators [41]. The presence of interaction modifies the transport through such junctions [42], thereby possibly aiding the design of improved qubits, like so-called Andreev spin qubits [43–47].

The phenomenon of many-body localization, aspects of which Part II investigates, offers the prospect of stabilizing non-equilibrium states of matter. The latter is not just of conceptual interest, but may offer the option to drastically slow thermalization in certain quantum systems, potentially providing a novel building block for extremely slowly decohering memory in quantum circuitry [48–51].

A significant advantage of quantum computers based on solid-state circuitry is the prospect of planar device manufacturing, which benefits from existing industrial processes within the semiconductor industry [52]. A connection to these mature technologies is highly desirable [53]. Attempting to shrink down superconducting circuits to the appropriate sizes naturally leads to the need to consider so-called supercapacitors [54, 55], which combine superconductivity with thin layers that are ideal for compact capacitors. The logical limit of ever-thinner superconducting films is truly two-dimensional superconducting materials. Van der Waals materials, whose building blocks are atomically thin layers that are weakly bound to each other by Van der Waals forces, provide a realization of such two-dimensional materials in nature [56]. One can isolate these atomically thin two-dimensional crystals, called monolayers, either by exfoliation [57, 58] or by deposition using, e.g., chemical vapor deposition methods [59–61] or molecular beam epitaxy [62–64]. The class of transition metal dichalcogenides, whose structure for most compounds takes the form of a Van der Waals material, contains multiple members that are intrinsically superconducting and remain so even if isolated down to the monolayer limit [65, 66]. As such, they have attracted much recent interest for applications in next-generation superconducting circuitry [54, 55, 60, 67]. Part III covers an investigation into the efficacy of Kohn-Luttinger pairing [68] as a possi-

ble mechanism for unconventional superconductivity in monolayer 1H-$NbSe_2$, a two-dimensional superconducting transition metal dichalcogenide. Together with existing works on the conventional phonon-mediated pairing in this material [69], this understanding of the different prospective pairing mechanisms active in the transition metal dichalcogenides aims to lay the groundwork for a more complete description of their superconducting properties.

Part I

TRANSPORT THROUGH S-QD-S NANOJUNCTIONS

This part of the thesis covers the results published in Siegl, Picó-Cortés, and Grifoni [40], which extended previous work in a master's thesis [70] and builds on earlier results from the PhD thesis of Picó-Cortés [71]. Both the methodology and the results were extended significantly from these previous theses, warranting their inclusion here. There are three separate chapters in this part. Chapter 2 introduces the Nakajima-Zwanzig formalism for transport through open quantum systems. Chapter 3 presents an extension to the particle-conserving formulation of superconductivity [71, 72] relevant to transport through junctions with multiple superconducting leads. Finally, Chapter 4 covers the resulting charge transport characteristics for a superconductor-quantum dot-superconduct junction in the presence of simultaneous driving with DC and AC voltage bias. Since their publication in Siegl, Picó-Cortés, and Grifoni [40], the concepts developed for this work and presented here have been further extended in the follow-up publication of Picó-Cortés et al. [42] and included in a textbook [73].

2

NAKAJIMA-ZWANZIG FORMALISM APPLIED TO TRANSPORT

The interaction of a quantum mechanical system with an external environment is a complicated but important problem. Understanding the exchange of energy and charge between the system and its environment is crucial not only for research, where it serves as a commonly applied probe for the system itself, but also for everyday applications in electronics, where it enables the theoretical prediction of transport in increasingly miniaturized electronics.

Fortunately, the fundamental equations governing these dynamics are known for the energy ranges relevant to most applications. In the following, the focus is on the dynamics of electrons, as they are the most relevant carriers contributing to transport in most applications. However, the ideas are, to a large degree, general and can be applied to other quantum mechanical systems, as long as the assumptions made during the discussion below hold. The non-relativistic equations of motion for the quantum mechanics of coherent states of electrons are known [1, 74–79]. Pauli generalized this theory by introducing the concept of the density operator $\hat{\rho}_{tot}$, which allows for the inclusion of decoherence by representing a state either as a pure or a mixed state [80]. The addition of effective terms like spin-orbit interaction to a non-relativistic Hamiltonian, as in Section C.3, is usually sufficient to capture the physically important contribution of relativistic effects [6].

2.1 DYNAMICS OF OPEN QUANTUM SYSTEMS

Unfortunately, knowledge of the equations governing the exact quantum mechanical dynamics of a system and its environment is, in general, not sufficient to solve for the dynamics of open quantum systems in realistic applications. Consider a generic time-dependent open quantum system whose Hamiltonian consists of three parts: the Hamiltonian $\hat{H}_S(t)$ of the isolated central system, the

Hamiltonian $\hat{H}_\alpha(t)$ of the isolated leads α, and the coupling to each lead $\hat{H}_{T,\alpha}(t)$. The total Hamiltonian, therefore, reads

$$\hat{H}_{tot}(t) = \hat{H}_S(t) + \sum_\alpha \left(\hat{H}_\alpha(t) + \hat{H}_{T,\alpha}(t)\right) , \tag{2.1}$$

and where the Liouville-von Neumann equation,

$$i\hbar \frac{\partial \hat{\rho}_{tot}(t)}{\partial t} = \left[\hat{H}_{tot}(t), \hat{\rho}_{tot}(t)\right] = \sum_{\nu\in\{+,-\}} \nu \hat{H}^\nu_{tot}(t)\hat{\rho}_{tot}(t) , \tag{2.2}$$

governs the time evolution of the total system's density operator. Here, ν represents a Liouville index acting to the right as

$$\hat{X}^\nu \hat{Y} = \begin{cases} \hat{X}\hat{Y} : & \nu = + , \\ \hat{Y}\hat{X} : & \nu = - . \end{cases} \tag{2.3}$$

Eq. (2.1) is very general as the only condition it imposes is that distinct leads $\alpha' \neq \alpha$ may only couple via their respective interaction with the central system. This condition is part of the commonly used definition of a lead and, as such, does not overly constrain the consideration. The issue with solving Eq. (2.2) is usually not on the formal side, as the equations of motion are known. Instead, it is on the practical side, as most applications of interest will involve macroscopic leads that are not tractable either numerically or analytically. Furthermore, the knowledge of the equations of motion still requires boundary conditions to determine the state of the system at any given time t. The preparation of a known many-body eigenstate takes an exponentially long time in the number of degrees of freedom [81] and is not feasible for any macroscopic system. To describe realistic transport problems, one needs a formalism capable of treating the dynamics of an open quantum system in a tractable manner, while accounting for incomplete information about the state of the macroscopic leads.

Multiple approaches to this problem exist [82], including non-equilibrium Green's functions [83–85], the Feynman-Vernon influence functional [86–88], and (generalized) master equation approaches [89–102]. These approaches differ in their derivation, but many of them yield equivalent, formally exact equations for both the dynamics of the density operator of the system and observables as calculated from the former in the presence of the environment. For most situations, no solution of these exact equations is attainable, especially in the presence of interactions. There, one usually resorts to approximations of the formally exact equations, using, e.g., the standard tools of perturbation theory. The necessarily convergent nature of the exact expressions obtained by different approaches yields effectively identical diagrammatics [73, 87, 93] describing the perturbative expansions.

One approach commonly applied to transport through interacting tunneling junctions is the Nakajima-Zwanzig projector operator formalism [103–108]. In this formulation, projectors act on the total density operator, thereby factorizing the open quantum system's dynamics into separate parts. The original work is due to Nakajima [109], with Zwanzig [110] developing the formalism independently shortly thereafter. The introduction here follows the recent textbook by Donarini and Grifoni [73].

To introduce the projectors, one first considers the macroscopic parts of the problem as a bath for the system to interact with. The bath has the Hamiltonian

$$\hat{H}_B(t) = \sum_\alpha \hat{H}_\alpha(t)\,. \tag{2.4}$$

One then introduces an, in general, time-dependent reference density operator of the bath $\hat{\rho}_B$ obeying the condition

$$i\hbar\mathcal{L}_B(t)\hat{\rho}_B(t) := \sum_\nu \nu\hat{H}_B^\nu(t)\hat{\rho}_B(t) = 0\,, \tag{2.5}$$

where $\mathcal{L}_B(t)$ is the Liouvillian superoperator for the bath, which, according to Eq. (2.2), generates the time-evolution for the bath's density operators in the absence of any coupling to the system[1]. Eq. (2.5) states that the reference density operator of the bath is static in the absence of any coupling to the system. One introduces the Nakajima-Zwanzig projectors $\mathcal{P}(t)$ and $\mathcal{Q}(t) := \mathbb{1} - \mathcal{P}(t)$ by defining $\mathcal{P}(t)$ using a partial trace over the bath's degrees of freedom as

$$\mathcal{P}(t)\hat{\rho}_{tot}(t) := \mathrm{Tr}_B\{\hat{\rho}_{tot}(t)\} \otimes \hat{\rho}_B(t) = \hat{\rho}(t) \otimes \hat{\rho}_B(t)\,, \tag{2.6}$$

where $\hat{\rho}(t)$ is the reduced density matrix over the remaining system degrees of freedom. By construction, $\mathcal{P}(t)$ fulfills the algebra of a projector since

$$(\mathcal{P}(t))^2\hat{\rho}_{tot}(t) = \mathcal{P}(t)\hat{\rho}(t) \otimes \hat{\rho}_B(t) = \hat{\rho}(t) \otimes \hat{\rho}_B(t) = \mathcal{P}(t)\hat{\rho}_{tot}(t) \qquad \forall\hat{\rho}_{tot}(t)\,, \tag{2.7}$$

which is equivalent to $(\mathcal{P}(t))^2 = \mathcal{P}(t)$ and directly implies $(\mathcal{Q}(t))^2 = \mathcal{Q}(t)$ and $\mathcal{Q}(t)\mathcal{P}(t) = \mathcal{P}(t)\mathcal{Q}(t) = 0$. Here, $\mathcal{P}(t)\hat{\rho}_{tot}(t)$ is the part of the total density operator that is composed of an uncorrelated direct product between a reduced density operator for the system's degrees of freedom and the reference density operator of the bath. In contrast, $\mathcal{Q}(t)\hat{\rho}_{tot}(t)$ is the correlated part of the total density operator.

The benefit of introducing these projectors becomes apparent once one inserts them into Eq. (2.2). The resulting coupled set of differential equations reads

$$\mathcal{P}(t)\dot{\hat{\rho}}_{tot}(t) = \mathcal{P}(t)\mathcal{L}_{tot}(t)\mathcal{P}(t)\hat{\rho}_{tot}(t) + \mathcal{P}(t)\mathcal{L}_{tot}(t)\mathcal{Q}(t)\hat{\rho}_{tot}(t)\,, \tag{2.8}$$

$$\mathcal{Q}(t)\dot{\hat{\rho}}_{tot}(t) = \mathcal{Q}(t)\mathcal{L}_{tot}(t)\mathcal{P}(t)\hat{\rho}_{tot}(t) + \mathcal{Q}(t)\mathcal{L}_{tot}(t)\mathcal{Q}(t)\hat{\rho}_{tot}(t)\,. \tag{2.9}$$

1 The range of summation over ν is suppressed here and in the following. If not stated otherwise, sums over Liouville indices always range over $\{+,-\}$.

To solve these, one introduces a formal solution of Eq. (2.9) by introducing the full propagator

$$\mathcal{G}_{\mathcal{Q}}(t,s) = \mathcal{T}_{\leftarrow} e^{\int_s^t dt' \, \mathcal{Q}(t')\mathcal{L}_{\text{tot}}(t') + \frac{\partial \mathcal{Q}(t')}{\partial t'}} , \tag{2.10}$$

where $\mathcal{T}_{\leftarrow}$ is the time ordering operator which orders later times to the left. Using the full propagator Eq. (2.10), the formal solution for $\mathcal{Q}(t)\hat{\rho}_{\text{tot}}(t)$ takes the form [111]

$$\begin{aligned}\mathcal{Q}(t)\hat{\rho}_{\text{tot}}(t) =& \mathcal{G}_{\mathcal{Q}}(t,0)\mathcal{Q}(0)\hat{\rho}_{\text{tot}}(0) \\ &+ \int_0^t ds \, \mathcal{G}_{\mathcal{Q}}(t,s) \left(\mathcal{Q}(s)\mathcal{L}_{\text{tot}}(s) + \frac{\partial \mathcal{Q}(s)}{\partial s} \right) \mathcal{P}(s)\hat{\rho}_{\text{tot}}(s) \, . \end{aligned} \tag{2.11}$$

The proof of Eq. (2.11) providing the sought-after solution starts by noting that at $t = 0$ Eq. (2.11) describes $\mathcal{Q}(0)\hat{\rho}_{\text{tot}}(0)$. The second step of the proof verifies that the time derivative of Eq. (2.11) is consistent with Eq. (2.9) since

$$\begin{aligned}\mathcal{Q}(t)\dot{\hat{\rho}}_{\text{tot}}(t) =& \frac{\partial}{\partial t}\left(\mathcal{Q}(t)\hat{\rho}_{\text{tot}}(t) \right) - \left(\frac{\partial}{\partial t}\mathcal{Q}(t) \right) \hat{\rho}_{\text{tot}}(t) \\ =& \mathcal{Q}(t)\mathcal{L}_{\text{tot}}(t)\mathcal{P}(t)\hat{\rho}_{\text{tot}}(t) + \frac{\partial \mathcal{G}_{\mathcal{Q}}(t,0)}{\partial t}\mathcal{Q}(0)\hat{\rho}_{\text{tot}}(0) \\ &+ \int_0^t ds \, \frac{\partial \mathcal{G}_{\mathcal{Q}}(t,s)}{\partial t}\mathcal{Q}(s) \left(\mathcal{L}_{\text{tot}}(s)\mathcal{P}(s) + \frac{\partial \mathcal{Q}(s)}{\partial s} \right) \hat{\rho}_{\text{tot}}(s) \\ &- \left(\frac{\partial}{\partial t}\mathcal{Q}(t) \right) \mathcal{Q}(t)\hat{\rho}_{\text{tot}}(t) \\ =& \mathcal{Q}(t)\mathcal{L}_{\text{tot}}(t)\mathcal{P}(t)\hat{\rho}_{\text{tot}}(t) + \mathcal{Q}(t)\mathcal{L}_{\text{tot}}(t)\mathcal{Q}(t)\hat{\rho}_{\text{tot}}(t) \, . \end{aligned} \tag{2.12}$$

Inserting Eq. (2.11) into Eq. (2.8) yields the Nakajima-Zwanzig equation. It is an exact integro-differential equation for the uncorrelated part of the density operator, which, for the time-independent reference states considered in this thesis, takes the form

$$\begin{aligned}\mathcal{P}\dot{\hat{\rho}}_{\text{tot}}(t) =& \mathcal{P}\mathcal{L}_{\text{tot}}(t)\mathcal{P}\hat{\rho}_{\text{tot}}(t) + \mathcal{P}\mathcal{L}_{\text{tot}}(t)\mathcal{G}_{\mathcal{Q}}(t,0)\mathcal{Q}\hat{\rho}_{\text{tot}}(0) \\ &+ \int_0^t ds \, \mathcal{P}\mathcal{L}_{\text{tot}}(t)\mathcal{G}_{\mathcal{Q}}(t,s)\mathcal{Q}\mathcal{L}_{\text{tot}}(s)\mathcal{P}\hat{\rho}_{\text{tot}}(s) \, . \end{aligned} \tag{2.13}$$

Eq. (2.13) shows the non-local (in time) nature of the time-evolution of $\mathcal{P}\hat{\rho}_{\text{tot}}(t)$, since its time derivative at any given time t also depends on its values at previous times via the integral term.

To simplify Eq. (2.13) further, one can split the total Liouvillian superoperator into its components as

$$\mathcal{L}(t) = \mathcal{L}_S(t) + \mathcal{L}_T(t) + \mathcal{L}_B(t) \, , \qquad i\hbar\mathcal{L}_i(t) = \sum_\nu \nu \hat{H}_i(t) \, . \tag{2.14}$$

The components of the Liouvillian possess the useful properties that [73]

$$\mathcal{P}\mathcal{L}_B(t) = \mathcal{L}_B(t)\mathcal{P} = 0\,, \tag{2.15}$$
$$\mathcal{P}\mathcal{L}_S(t) = \mathcal{L}_S(t)\mathcal{P}\,, \tag{2.16}$$
$$\mathcal{P}\hat{Y}\mathcal{P} = 0 \text{ if: } \exists \hat{X} : \left[\hat{X} = \hat{X}^\dagger \wedge [\hat{X}, \hat{\rho}_B] = 0 \wedge \langle x|\,\hat{Y}\,|x\rangle = 0\ \forall\, |x\rangle \in \mathrm{Eig}(\hat{X})\right]. \tag{2.17}$$

Here, Eq. (2.15) is a direct consequence of Eq. (2.5) and allows for the elimination of $\mathcal{L}_B(t)$ in Eq. (2.13) whenever it occurs next to $\mathcal{P}$. Eq. (2.17) is written here in a more general form than in the book by Donarini and Grifoni [73]. Given a hermitian operator $\hat{X}$ that commutes with $\hat{\rho}_B$, one can diagonalize $\hat{\rho}_B$ in the eigenbasis of $\hat{X}$. If all spectral projectors of $\hat{X}$ are orthogonal to $\hat{Y}$ in the Hilbert-Schmidt inner product, i.e., if for any eigenbasis of $\hat{X}$, the operator $\hat{Y}$ is fully off-diagonal, the sequence $\mathcal{P}\hat{Y}\mathcal{P}$ vanishes. The intuitive understanding of this condition is that $\hat{X}$ represents a conserved quantity of $\hat{\rho}_B$, which $\hat{Y}$ does not conserve. A sequential projection on $\hat{\rho}_B$ with an application of $\hat{Y}$ in between, therefore, is incompatible with the conserved nature of $\hat{X}$. The most common application of this property is the one shown by Donarini and Grifoni [73], which uses this property for the case of a tunneling Hamiltonian $\hat{H}_T(t)$ changing the particle number of the bath. The latter is a conserved quantity under the free evolution of the bath if $[\hat{\rho}_B, \hat{N}_B] = 0$, where $\hat{N}_B$ is the number operator of the bath. As odd powers of $\hat{H}_T(t)$ change the particle content of the bath by an odd, and therefore non-zero, number, one finds $\mathcal{P}(\mathcal{L}_T(t))^{2n+1}\mathcal{P} = 0$. Using the above yields [73]

$$\mathcal{P}\mathcal{L}_{tot}(t)\mathcal{P} = \mathcal{L}_S(t)\mathcal{P}\,, \tag{2.18}$$
$$\mathcal{P}\mathcal{L}_{tot}(t)\mathcal{Q} = \mathcal{P}\mathcal{L}_T(t)\mathcal{Q}\,, \tag{2.19}$$
$$\mathcal{Q}\mathcal{L}_{tot}(t)\mathcal{P} = \mathcal{L}_T(t)\mathcal{P}\,, \tag{2.20}$$
$$\mathcal{Q}\mathcal{L}_{tot}(t)\mathcal{Q} = \mathcal{Q}(\mathcal{L}_S(t) + \mathcal{L}_B(t) + \mathcal{Q}\mathcal{L}_T(t)\mathcal{Q})\,, \tag{2.21}$$

which results in

$$\mathcal{P}\mathcal{L}_{tot}(t)\mathcal{G}_\mathcal{Q}(t,s)\mathcal{L}_{tot}(s)\mathcal{P} = \mathcal{P}\mathcal{L}_T(t)\bar{\mathcal{G}}_\mathcal{Q}(t,s)\mathcal{L}_T(s)\mathcal{P}\,, \tag{2.22}$$
$$\bar{\mathcal{G}}_\mathcal{Q}(t,s) = \mathcal{T}_{\leftarrow} e^{\int_s^t dt'\, \mathcal{L}_S(t') + \mathcal{L}_B(t') + \mathcal{Q}\mathcal{L}_T(t')\mathcal{Q}}\,. \tag{2.23}$$

The term $\mathcal{Q}\hat{\rho}_{tot}(0)$ in Eq. (2.13) represents an explicit dependence on the initial condition and is inconvenient for further analytical treatment of the problem. Fortunately, the dynamics at long times do not depend on initial conditions, except if they fix a conserved quantity that does not evolve with time. As such, for applications that concern the steady-state reached at long time, it is convenient to start with a factorized initial condition for which $\mathcal{Q}\hat{\rho}_{tot}(0) = 0$. The remainder of this thesis uses this condition and deals with the conserved quantities mentioned above by treating them as a parametric dependence of the resulting steady-state properties.

By inserting these simplifications into Eq. (2.13) and tracing over the bath's degrees of freedom, one finds that the Nakaima-Zwanzig equation for the reduced density operator (with factorized initial condition) reads

$$\dot{\hat{\rho}}(t) = \mathcal{L}_S(t)\hat{\rho}(t) + \int_0^t ds\, \mathcal{K}(t,s)\hat{\rho}(s)\,. \tag{2.24}$$

Here, the time-propagation kernel $\mathcal{K}(t,s)$ acts to the right as

$$\mathcal{K}(t,s)\hat{\rho}(s) = \mathrm{Tr}_B\{\mathcal{P}\mathcal{L}_T(t)\bar{\mathcal{G}}_Q(t,s)\mathcal{L}_T(s)(\hat{\rho}(s)\otimes\hat{\rho}_B)\}\,, \tag{2.25}$$

and is non-local in time. By inserting the definition of the exponential in Eq. (2.23), and using the conservation of charge in the bath, one arrives at a perturbative expansion of Eq. (2.25) in powers of $\mathcal{L}_T(t)$ which takes the form of

$$\begin{aligned}\mathcal{K}(t,s)\hat{\rho}(s) =& \mathrm{Tr}_B\Bigg\{\mathcal{L}_T(t)\sum_{n=0}^{\infty}\int_s^t dt_0\cdots\int_s^t dt_{2n+1}\,\delta_{t_{2n+1},t}\delta_{t_0,s}\\ &\times\mathcal{T}_{\leftarrow}\left(\prod_{i=0}^{2n}\Theta(t_{i+1}-t_i)\mathcal{G}_0(t_{i+1},t_i)Q\mathcal{L}_T(t_i)Q\right)(\hat{\rho}(s)\otimes\hat{\rho}_B)\Bigg\}\,,\end{aligned} \tag{2.26}$$

where $t_{2n+1} = t$, $t_0 = s$ and $\mathcal{G}_0(t,s)$ is the free propagator which has the definition

$$\mathcal{G}_0(t,s) = \mathcal{T}_{\leftarrow}e^{\int_s^t dt'\,\mathcal{L}_S(t')+\mathcal{L}_B(t')}\,. \tag{2.27}$$

In addition to the reduced density operator's time-propagation, the evaluation of expectation values for a generic operator $\hat{O}(t)$ is also non-local in time. Similarly to the derivation of the Nakajima-Zwanzig equation itself, one starts by splitting the evaluation of the expectation value into correlated and uncorrelated contributions by writing

$$\begin{aligned}\langle\hat{O}(t)\rangle =& \mathrm{Tr}\{\hat{O}(t)\mathcal{P}\hat{\rho}_{tot}(t) + \hat{O}Q\hat{\rho}_{tot}(t)\}\\ =& \mathrm{Tr}\{\hat{O}(t)\rho(t)\otimes\hat{\rho}_B\} + \mathrm{Tr}\{\mathcal{P}\hat{O}(t)\mathcal{G}_Q(t,s)Q\hat{\rho}_{tot}(0)\}\\ &+\mathrm{Tr}\left\{\int_0^t ds\,\mathcal{P}\hat{O}(t)Q\bar{\mathcal{G}}_Q(t,s)\mathcal{L}_T(s)\mathcal{P}\hat{\rho}_{tot}(s)\right\}\\ =& \mathrm{Tr}\{\hat{O}(t)\rho(t)\otimes\hat{\rho}_B\} + \mathrm{Tr}\{\mathcal{P}\hat{O}(t)\mathcal{G}_Q(t,s)Q\hat{\rho}_{tot}(0)\}\\ &+\int_0^t ds\,\mathcal{K}_O(t-s)\hat{\rho}(s)\,,\end{aligned} \tag{2.28}$$

where one introduces the kernel

$$\mathcal{K}_O(t-s)\hat{\rho}(s) = \mathrm{Tr}\left\{\mathcal{P}\hat{O}(t)Q\bar{\mathcal{G}}_Q(t,s)\mathcal{L}_T(s)(\hat{\rho}(s)\otimes\hat{\rho}_B)\right\}\,, \tag{2.29}$$

which captures the time-non-local contribution to the expectation value of $\hat{O}(t)$ due to the coupling of the system with the bath. In contrast, the first term on the right-hand side of Eq. (2.28) describes the contribution to the expectation value

that arises from the uncorrelated (factorized) part of the density operator, while the second term captures again a dependence on the initial state. This dependence is relevant only for the transient regime, before the system reaches its steady state. Analogously to the treatment of the equivalent term in the Nakajima-Zwanzig equation, one can eliminate this term by an appropriate choice of the initial state, provided it does not fix any conserved quantity that survives to long times[2].

2.3 NAKAJIMA-ZWANZIG FORMALISM FOR TIME-PERIODIC PROBLEMS

In the above, the Nakajima-Zwanzig formalism operated in the time domain. While very useful for solving transient or explicitly time-dependent problems [107], this formulation is inefficient when trying to extract steady-state behavior. Steady-state in this thesis denotes the state at long times, after which the transient behavior dominated by the initial conditions has ceased. For time-independent Hamiltonians, this steady state will usually, but not always, be time-independent. A sufficiently general starting point for the scope of this thesis is the situation where one allows for periodic driving by the environment, but with a time-independent reference state $\hat{\rho}_B = \hat{\rho}_B(0)$. This condition allows for the development of the theory in close analogy to the Floquet formalism. To this end, consider that the system's Hamiltonian is static, but that both the tunneling and bath Hamiltonians, and therefore also their Liouvillians, can be expanded as

$$\hat{H}_T(t) = \sum_m \hat{h}_{T,m} e^{im\cdot\omega t}, \qquad \hat{H}_B(t) = \sum_m \hat{h}_{B,m} e^{im\cdot\omega t}, \tag{2.30}$$

$$\mathcal{L}_T(t) = \sum_m l_{T,m} e^{im\cdot\omega t}, \qquad \mathcal{L}_B(t) = \sum_m l_{B,m} e^{im\cdot\omega t}. \tag{2.31}$$

Here ω is a vector of frequencies and m is an integer-valued vector. When trying to do the same for the free propagator $\mathcal{G}_0(t,s)$, one faces the subtle issue that after integrating over the time dependencies in the exponent in Eq. (2.27), one is still left with an exponential of trigonometric functions with, in general, incommensurate frequencies. For some problems[3], it turns out that by decomposing the superoperator into its components connecting in- and out-going Liouville-states, i.e., density matrix elements, one can individually decompose them using the Jacobi-Anger expansion [40, 70]. This procedure allows for the expansion of the free propagator as

$$\mathcal{G}_0(t-s) = \sum_m g_{0,m}(t-s) e^{im\cdot\omega s}. \tag{2.32}$$

2 A clear candidate for such a persistent property is the phase of the current in the AC Josephson effect. Consider the following thought experiment: Let $\hat{\rho}_{tot}(0)$ be the steady-state density operator for a Josephson junction whose dynamics are periodic with period T and whose current across the junction is sinusoidal with a node at $t = 0$. If one instead starts the time evolution starting from $\hat{\rho}'_{tot}(0) = \hat{\rho}_{tot}(T/4)$, the only change is a shift $t \to t + T/4$ as the current reaches a crest at $t = 0$. This shift persists indefinitely and, consequently, affects the time-dependent expectation value.

3 Examples of this type include the free propagator for the problem in Chapter 4.

Inserting this expansion, one can show that at all orders of the perturbative expansion in $\mathcal{L}_T$, one can also expand the propagation kernel as

$$\mathcal{K}(t-s) = \sum_{\mathbf{m}} \kappa_{\mathbf{m}}(t-s) e^{i\mathbf{m}\cdot\boldsymbol{\omega}s} \,. \tag{2.33}$$

Of primary interest here is the case in which the steady-state density operator $\rho(t)$ allows for a similar expansion

$$\hat{\rho}(t) = \sum_{\mathbf{m}} \hat{\rho}_{\mathbf{m}} e^{i\mathbf{m}\cdot\boldsymbol{\omega}t} \,. \tag{2.34}$$

In this case, which includes the most common scenario of a stationary steady state, $\hat{\rho}(t) = \hat{\rho}_\infty$, one can transform the Nakajima-Zwanzig equation from its integro-differential formulation in the time domain into an algebraic form in Laplace space. To this end, one first introduces the Laplace transformation,

$$\hat{\tilde{\rho}}(\lambda) = \int_0^\infty ds\, e^{-\lambda t} \hat{\rho}(t) \,, \tag{2.35}$$

which for the periodic form of $\hat{\rho}(t)$ in Eq. (2.34) has poles along the imaginary axis. The residues at these poles are the expansion coefficients in Eq. (2.34). One can extract them by taking the limit

$$\lim_{\lambda \to i\mathbf{m}\cdot\boldsymbol{\omega}+0^+} (\lambda - i\mathbf{m}\cdot\boldsymbol{\omega})\hat{\tilde{\rho}}(\lambda) = \hat{\rho}_{\mathbf{m}} \,. \tag{2.36}$$

At long times, formally $t \to \infty$, the Markovian approximation, which replaces the upper limit of the integral in the Nakajima-Zwanzig equation Eq. (2.24) with infinity, becomes exact [73]. There, the integral turns into a convolution, enabling a factorization in Laplace space as

$$0 = (\mathcal{L}_S - \lambda)\hat{\tilde{\rho}}(\lambda) + \sum_{\mathbf{m}'} \tilde{\kappa}_{\mathbf{m}'}(\lambda)\hat{\tilde{\rho}}(\lambda - i\mathbf{m}'\cdot\omega) \,. \tag{2.37}$$

Extracting the poles in the same way as done above and using that $\tilde{\kappa}(\lambda)$ is continuous, one finds

$$0 = (\mathcal{L}_S - i\mathbf{m}\cdot\boldsymbol{\omega})\hat{\rho}_{\mathbf{m}} + \sum_{\mathbf{m}'} \tilde{\kappa}_{\mathbf{m}'}(i\mathbf{m}\cdot\boldsymbol{\omega})\hat{\rho}(i(\mathbf{m}-\mathbf{m}')\cdot\omega) \,. \tag{2.38}$$

Eq. (2.38) represents a homogeneous algebraic coupled set of equations that allows for the determination of the steady-state expansion components $\hat{\rho}_{\mathbf{m}}$ via the calculation of the kernel of a superoperator. The form of Eq. (2.38) is a close analogue to Floquet theory, where a time-independent Hamiltonian in an extended space allows for the calculation of Floquet modes. The derivation here is conceptually related to Floquet theory, as it yields a description of a periodically driven open quantum system.

Given a set of steady-state $\hat{\rho}_m$, one still needs an equation relating these expansion components to the observables one is interested in. Consider a time-dependent operator that has an expansion in terms of the frequencies governing the system's driving, given by

$$\hat{O}(t) = \sum_m \hat{o}_m e^{im\cdot\omega t}\,. \tag{2.39}$$

An immediate consequence of Eq. (2.39) is that the operator kernel $\mathcal{K}_O$ itself has an expansion of the form

$$\mathcal{K}_O(t-s) = \sum_m \kappa_{O,m}(t-s)e^{im\cdot\omega s}\,, \tag{2.40}$$

provided Eq. (2.33) holds. The time-local part of the expectation value has a time-dependence governed by the product of the time-dependence of the operator itself and the time-dependence of the reduced density operator. Due to Eq. (2.40), the time-non-local part has an equivalent dependence on a product of the same periodicities. Since the product of periodic functions is itself a periodic function, one can expand for long times

$$\langle\hat{O}\rangle(t) = \sum_m o_m e^{im\cdot\omega t}\,, \tag{2.41}$$

where in general $o_m \neq \langle\hat{o}_m\rangle$. Instead, applying the Laplace transform to Eq. (2.28) in the limit of long times t, one can again extract the residues at the poles $im\cdot\omega$. The resulting equation for the expansion coefficients of the expectation values reads

$$o_m = \sum_{m'} \mathrm{Tr}\{\hat{o}_{m'}\hat{\rho}_{m-m'}\otimes\hat{\rho}_B\} + \sum_{m'} \mathcal{K}_{O,m'}(im\cdot\omega)\hat{\rho}_{m-m'}\,. \tag{2.42}$$

Eqs. (2.38) and (2.42) provide the basis for the work on periodically driven superconductor-quantum-dot-superconductor junctions in the following chapters. The works by Grifoni and Hänggi [112] and by Platero and Aguado [113] provide more in-depth reviews on driven quantum transport.

3

PARTICLE CONSERVING SUPERCONDUCTIVITY

The topic of this part of the thesis is transport through interacting nanojunctions with superconducting leads. For the application of the Nakajima-Zwanzig formalism introduced in the last chapter, it is of paramount importance to make the proper selection of what parts of an open quantum system one considers as the bath and which part constitutes the system. When discussing superconducting junctions, this question is rather intricate, since the naive first guess of treating the superconducting leads individually as baths runs into multiple distinct problems: First, the diagonalization of a superconducting lead into a condensate and excited Boguliubov quasiparticles results in the separation of the lead into a thermalizing dissipative part comprised of the quasiparticles, and a non-dissipative part comprised of the superconducting condensate. An inclusion of the latter into the bath raises issues due to their non-dissipative nature. This lack of dissipation results in extended bath correlation times, invalidating the perturbative expansion often employed for tunneling junctions. Second, it is a well-known effect in weakly linked junctions containing multiple superconducting leads that such junctions display a non-dissipative supercurrent, including the Josephson current [38] governed by a gauge-invariant "phase difference" between leads. The exact nature of this phase difference and its interpretation as an actual difference of individual phases for each lead raises conceptual questions that should be answered satisfactorily [114]. Third, the standard treatment of the superconductor as non-particle conserving can result in violation of the conservation of currents across the junction for non-symmetric applications [115]. Such violations of the conservation of charge are artifacts of an incomplete theory that can be avoided consitently by working with a particle-conserving formulation of the problem.

To address these problems, this chapter introduces a particle-conserving formulation of superconductivity that allows for a concise formulation of the problem in the presence of finite chemical potentials. Importantly, there exists already a large body of work on this problem that this presentation relies on [22, 38, 39, 116, 117]. In order to avoid duplication, this chapter refers the reader to these earlier works where applicable for a more detailed introduction. The starting point for this introduction is the discussion found in the textbook by Leggett [117]. Therein, Leggett outlines the similarities between the superconducting theory by Bardeen,

Cooper, and Schrieffer [22] and Bose-Einstein condensation [118], finding that due to the conserved number of charge carriers, one should be able to describe a superconducting state in a closed system by a number-representation that tracks the occupation of the condensate [119]. In this approach, the remaining free charge carriers enter the theory as the Bogoliubov quasiparticles [120, 121]. An inclusion of this description into the Nakajima-Zwanzig formalism is possible [105, 106], and was developed in the PhD thesis of Picó-Cortés [71], on which the following introduction is based.

3.1 GROUNDSTATE IN THE PARTICLE-CONSERVING APPROACH

The ground state in the microscopic BCS theory of superconductivity [22] consists of time-reversal symmetric electron pairs, dubbed Cooper pairs [21]. Trying do do the same for a non-interacting isotropic electron gas, one can create the Fermi sea in momentum space by adding Kramers pairs $\hat{B}^\dagger_k = \hat{c}^\dagger_{\mathbf{k},\uparrow}\hat{c}^\dagger_{\bar{\mathbf{k}},\downarrow}$ [1] of electrons $\hat{c}^\dagger_{\mathbf{k},\sigma}$ with well-defined momenta $\mathbf{k}$ and spin quantum number σ to the empty state for all $|\mathbf{k}| \leqslant k_F$, where the Fermi momentum k_F fixes the particle content[2]. The resulting ground state reads

$$|FS\rangle = \prod_{\mathbf{k}} \left(\hat{B}^\dagger_{\mathbf{k}}\right)^{\Theta(k_F-|\mathbf{k}|)} |0\rangle = \prod_{\mathbf{k}} \left(\Theta\left(k_F - |\mathbf{k}|\right) \hat{B}^\dagger_{\mathbf{k}} + \Theta\left(|\mathbf{k}| - k_F\right)\right) |0\rangle \ . \tag{3.1}$$

Within Fermi liquid theory, one postulates a ground state of the interacting isotropic electron gas similar to the Fermi sea, but with the occupancy governed by a general distribution function $\alpha_{\mathbf{k}}$ instead of the sharp cutoff at the Fermi momentum in Eq. (3.1)[3]. However, due to conservation of charge during the adiabatic switching on of the interactions, it is clear that the definition Eq. (3.1) is not a good ansatz for the resulting ground state since a straightforward replacement of $\Theta(k_F - |\mathbf{k}|)$ with $\alpha_{\mathbf{k}}$ would result in an mixture of different particle numbers. In the presence of time-reversal symmetry, the ground state can again be build up from Kramers pairs. The Kramers pair creation operators are nilpotent and commute as $[\hat{B}_{\mathbf{k}}, \hat{B}_{\mathbf{k}'}] = [\hat{B}^\dagger_{\mathbf{k}}, \hat{B}^\dagger_{\mathbf{k}'}] = 0$, while $[\hat{B}_{\mathbf{k}}, \hat{B}^\dagger_{\mathbf{k}'}] = \delta_{\mathbf{k},\mathbf{k}'}\left(1 - \hat{n}_{\mathbf{k},\uparrow} - \hat{n}_{\bar{\mathbf{k}},\downarrow}\right)$. Using the nilpotence of the pair creation operators, one rewrites Eq. (3.1) as

$$|FS\rangle = \frac{1}{M!}\left(\sum_{\mathbf{k}} \Theta\left(k_F - |\mathbf{k}|\right) \hat{B}^\dagger_{\mathbf{k}}\right)^M |0\rangle \ , \tag{3.2}$$

1 Here and in the following, the notation $\bar{x} = -x$ is used to suppress the length of subscripts and superscripts.

2 This procedure does not yield the general case, since it only allows for fixed steps in the particle content that miss, e.g., all odd particle numbers. However, one can easily connect the cases with particle numbers in between the allowed steps of the procedure above to those allowed cases by adding the respective missing charges as quasiparticles and symmetrizing.

3 The generalization to a crystal is straightforward by restricting the momenta $\mathbf{k}$ to the first Brillouin zone and by replacing $\mathbf{k}$ with a generic index containing also any additional quantum numbers.

where this construction fixed the particle number to $N = 2M$. Note that k_F Eqs. (3.1) and (3.2) fixes N, such that the particle content agrees in both formulations. Due to the nilpotence of the $\hat{B}_{\mathbf{k}}$, any $\mathbf{k}$ in the sum may only occur once in the product. The individual terms with distinct $\mathbf{k}$ commute trivially, enabling the application of the multinomial theorem as

$$\left(\sum_{\mathbf{k}} \Theta\left(k_F - |\mathbf{k}|\right) \hat{B}_{\mathbf{k}}^{\dagger}\right)^{M} = \sum_{\beta} \binom{M}{\beta} \prod_{\mathbf{k}} \left(\Theta\left(k_F - |\mathbf{k}|\right) \hat{B}_{\mathbf{k}}^{\dagger}\right)^{\beta_{\mathbf{k}}} . \tag{3.3}$$

Here, the sum over β runs over all K-entry multiindices such that $\sum_{\mathbf{k}} 1 = K$ and $|\beta| := \sum_{\mathbf{k}} \beta_{\mathbf{k}} = M$. The nilpotence of $\hat{B}_{\mathbf{k}}^{\dagger}$ forces all non-vanishing summands on the right-hand side of Eq. (3.3) to have multiindices in the range $\{0, 1\}$. Thus, the multinomial coefficients of all non-vanishing terms are $M!$. The Heaviside function ensures that only the summand with $\beta_{\mathbf{k}} = \Theta\left(k_F - |\mathbf{k}|\right)$ contributes.

From Eq. (3.2), a general ansatz for the ground state of the interacting electron gas containing $N = 2M$ electrons in the presence of time-reversal symmetry follows as

$$|M\rangle = \mathcal{N}_M \left(\sum_{\mathbf{k}} \alpha_{\mathbf{k}} \hat{B}_{\mathbf{k}}^{\dagger}\right)^{M} |0\rangle \ , \tag{3.4}$$

with $\mathcal{N}_M$ the appropriate normalization factor. One may assume a normalized distribution function that obeys $\sum_{\mathbf{k}} |\alpha_{\mathbf{k}}|^2 = 1$. The normalization of the state itself is included only in the $\mathcal{N}_M$, while the $\alpha_{\mathbf{k}}$ are independent of M[4].

Section C.1 contains a proof that for arbitrary $n << M$ and disjunct momenta $\{\mathbf{k}\} = \{\mathbf{k}_0, \cdots, \mathbf{k}_n\}$ one can separate[5]

$$\begin{aligned} |M, \{\mathbf{k}\}\rangle \approx & \frac{1}{\sqrt{1 + |\tilde{\alpha}_{\mathbf{k}_n}|^2}} \left(|M, \{\mathbf{k}\}\rangle + \tilde{\alpha}_{\mathbf{k}_n} \hat{B}_{\mathbf{k}_n}^{\dagger} |M-1, \{\mathbf{k}\}\rangle\right) \\ & =: u_{\mathbf{k}_n} |M, \{\mathbf{k}\}\rangle + v_{\mathbf{k}_n} \hat{B}_{\mathbf{k}_n}^{\dagger} |M-1, \{\mathbf{k}\}\rangle \ , \end{aligned} \tag{3.5}$$

where

$$|M, \{\mathbf{k}\}\rangle = \mathcal{N}_{M,\{\mathbf{k}\}} \left(\sum_{\mathbf{k}' \neq \{\mathbf{k}\}} \alpha_{\mathbf{k}'} \hat{B}_{\mathbf{k}'}^{\dagger}\right)^{M} |0\rangle \ , \tag{3.6}$$

is a normalized state with the same distribution function for all $\mathbf{k}' \neq \{\mathbf{k}\}$ and identical particle content, but excluding all momenta in $\{\mathbf{k}\}$. Eq. (3.5) further introduced a renormalized distribution function

$$\tilde{\alpha}_{\mathbf{k}} = \frac{M \mathcal{N}_{M-1,\mathbf{k}}}{N_{M,\mathbf{k}}} \alpha_{\mathbf{k}} \, , \tag{3.7}$$

4 This lack of a dependence of $\alpha_{\mathbf{k}}$ on M is approximate. See the discussion in Section C.1.

5 The proof of this separation to first order $n = 0$ is due to Picó-Cortés [71].

accounting for the change in normalization when splitting the ground state[6]. This renormalized distribution function is equivalent to the well-known Bogoliubov-Valatin transformation parameters [120, 122] $u_{k,\sigma}$ and $v_{k,\sigma}$ governing the particle/hole nature of a quasiparticle of specific $\mathbf{k}$ and σ, where one can identify[7]

$$u_{k\sigma} = \frac{1}{\sqrt{1+|\tilde{\alpha}_{k\sigma}|^2}}, \qquad v_{k\sigma} = \frac{\tilde{\alpha}_{k\sigma}}{\sqrt{1+|\tilde{\alpha}_{k\sigma}|^2}}. \tag{3.8}$$

One can obtain these coefficients by variation of the free energy. Section C.1 demonstrates this procedure for $T = 0$, where one finds the usual zero temperature gap equation for the order parameter Δ

$$\Delta_k = -\frac{1}{\mathcal{V}} \sum_{q\neq 0} V_q \frac{\Delta_{k+q}}{2E_{k+q}}, \qquad \Delta_k = -\frac{1}{\mathcal{V}} \sum_{k'\neq k} V_{k'-k} \frac{\tilde{\alpha}^*_{k'}}{1+|\tilde{\alpha}_{k'}|^2}. \tag{3.9}$$

In defining the particle-conserving groundstate and its properties, one often encounters the approximation of dropping some dependence on the number of Kramers pairs M. This approximation is crucial to the concept of the Josephson $\hat{S}^\dagger$ operator as an operator that raises the number of Cooper pairs in the condensate without affecting the properties of the quasiparticles in the superconductor. This nominal separation between a condensate and a system of quasiparticles can only ever be approximate. For a macroscopic M, the dependence of the order parameter on a change to $M \pm 1$ is negligible. As such, both the dynamics and the composition of each quasiparticle, which know about the gap via the Bogoliubov parameters u and v, will be almost unaffected. However, since

$$\sum_k |v_k|^2 = M, \tag{3.10}$$

the sum of all the individual small changes for $M \pm 1$ remains finite. It is in this sense that, in the following, some operators will "almost" commute, since the remainder terms scale as $1/N$ individually but cannot be neglected if they occur under sums over macroscopically many contributions. With this complication in mind, the formal definition of the Josephson operator reads

$$\hat{S} = \sum_{M=M_{min}}^{M_{max}} |M\rangle\langle M+1|, \tag{3.11}$$

where M_{max} and M_{min} represent the largest and smallest M considered in the summation over M, respectively. The most convenient choice mathematically, but not conceptually, is the choice $M_{min} = 0$ and $M_{max} = \infty$. Conceptually, a choice of $M_{min} \sim M_{max}$ is more convenient. A restriction of M to the range

6 This change of normalization for $\mathbf{k}_n$ is for $n << M$ again approximated as independent of $\mathbf{k}_0, \cdots, \mathbf{k}_{n-1}$.

7 The product $\mathbf{k}\sigma$ represents $\mathbf{k}$ for spin up and $\bar{\mathbf{k}}$ for spin down.

$M \in [\bar{M} - \delta M, \bar{M} + \delta M]$ with $\delta M << \bar{M}$ and macroscopically large $\bar{M}$ satisfies the above requirement of a negligible dependence of the order parameter on the exact M. In the following, the latter form is assumed for macroscopic $\bar{M}$, such that δM can still be large when compared to the usual number of charges in the central system. An important property of the Josephson operator is that

$$\hat{S}\hat{S}^\dagger = \sum_{M=M_{min}}^{M_{max}} |M\rangle\langle M| \,, \qquad \hat{S}^\dagger\hat{S} = \sum_{M=M_{min}}^{M_{max}} |M+1\rangle\langle M+1| \,, \tag{3.12}$$

which allows for the approximation $\hat{S}\hat{S}^\dagger \approx \hat{S}^\dagger\hat{S} \approx \mathbb{1}$ as long as the range δM is sufficiently large, ensuring the probability of encountering an M outside this range to be negligible for the calculation at hand.

3.2 QUASIPARTICLES AND THERMAL DENSITY OPERATOR

Starting from the superconducting ground state with fixed particle content $|M\rangle$ introduced above, one can introduce a definition of a quasiparticle with well-defined (crystal-)momentum $\mathbf{k}$, band index n and a (nearly) fermionic creation operator $\hat{\gamma}^\dagger_{\mathbf{k},n}$. Here, and in the following, n indicates only the spin σ, but a generalization is straightforward. The starting point of the construction of the quasiparticles is the observation that the operator

$$\hat{\gamma}_{\mathbf{k},\sigma} = u_{\mathbf{k}\sigma}\hat{c}_{\mathbf{k},\sigma} - \sigma v_{\mathbf{k}\sigma}\hat{c}^\dagger_{-\mathbf{k},-\sigma}\hat{S} \,, \tag{3.13}$$

with $\sigma \in \{\uparrow = +, \downarrow = -\}$ is (nearly) fermionic as

$$\{\hat{\gamma}_{\mathbf{k},\sigma}, \hat{\gamma}_{\mathbf{k}',\sigma'}\} \approx 0 \,, \qquad \{\hat{\gamma}_{\mathbf{k},\sigma}, \hat{\gamma}^\dagger_{\mathbf{k}',\sigma'}\} \approx \delta_{\mathbf{k},\mathbf{k}'}\delta_{\sigma,\sigma'} \,, \tag{3.14}$$

if one drops the dependence of u and v on M and uses the above approximate properties of $\hat{S}$. Furthermore, under the same approximations, this operator annihilates the ground state $|M\rangle$ as [71]

$$\hat{\gamma}_{\mathbf{k},\sigma}|M\rangle = \sigma u_{\mathbf{k}\sigma}v_{\mathbf{k}\sigma}\hat{c}^\dagger_{-\mathbf{k},-\sigma}|M-1,\mathbf{k}\rangle - \sigma u_{\mathbf{k}\sigma}v_{\mathbf{k}\sigma}\hat{c}^\dagger_{-\mathbf{k},-\sigma}|M-1,\mathbf{k}\rangle = 0 \,. \tag{3.15}$$

This property enables the interpretation of the ground state $|M\rangle$ as the vacuum state with respect to the addition of quasiparticles. The addition energy of the quasiparticle created by $\hat{\gamma}^\dagger_{\mathbf{k},\sigma}$ is $E_{\mathbf{k},\sigma} + \mu$ with $E_{\mathbf{k},\sigma}$ the typical BCS excitation energy and μ the chemical potential. The PhD thesis of Picó-Cortés [71] already covered the construction of the remaining spectrum of possible states containing the simultaneous presence of a condensate and additional excited quasiparticles.

Most relevant to the application here, the Hamiltonian of a superconductor α within this particle-conserving formalism splits into two separate parts as

$$\hat{H}_\alpha(t) = \hat{H}_{QP}(t) + \hat{H}_{CP}(t) \,, \tag{3.16}$$

$$\hat{H}_{QP}(t) = \sum_{\mathbf{k},\sigma}(E_{\mathbf{k},\sigma} + \mu_\alpha(t))\hat{\gamma}^\dagger_{\alpha,\mathbf{k},\sigma}\hat{\gamma}_{\alpha,\mathbf{k},\sigma} \,, \tag{3.17}$$

$$\hat{H}_{CP}(t) = 2\mu_\alpha(t)\hat{N}_M \,, \tag{3.18}$$

where the Cooper pair Hamiltonian $\hat{H}_{CP}$ is just the chemical potential $\mu_\alpha(t)$ times twice the number of Cooper pairs measured by $\hat{N}_M$. As such, the grand canonical Hamiltonian of the superconductor α, $\hat{K} = \hat{H}_\alpha(t) - \mu_\alpha(t)\hat{N}_\alpha$, fulfills

$$\hat{K}_\alpha(t) = \hat{K}_{QP} = \sum_{k,\sigma} E_{k,\sigma}\hat{\gamma}^\dagger_{\alpha,k,\sigma}\hat{\gamma}_{\alpha,k,\sigma}\,, \tag{3.19}$$

and is time-independent. Therefore, and despite the time-dependence of the chemical potential $\mu(t)$, the thermal grand canonical density operator

$$\hat{\rho}_{GC,\alpha} = \frac{1}{Z_{GC,\alpha}} e^{-\beta_\alpha \hat{K}_\alpha} = \frac{1}{Z_{GC,\alpha}} e^{-\beta_\alpha \hat{K}_{QP,\alpha}}\,, \tag{3.20}$$

is static. An issue arises with the interpretation of Eq. (3.20) when calculating the form of the density operator for the composite Hilbert space $\{\{k,\sigma\},M\}$ of the quasiparticles and the Cooper pairs. The density operator for the quasiparticles is well-defined as

$$\hat{\rho}_{QP,GC,\alpha} = \mathrm{Tr}_{CP}\{\hat{\rho}_{GC,\alpha}\} = \frac{1}{Z_{QP,GC,\alpha}} e^{-\beta_\alpha \hat{K}_{QP,\alpha}}\,, \tag{3.21}$$

but the density operator for the Cooper pairs is ill-defined as

$$\hat{\rho}_{CP,GC,\alpha} = \mathrm{Tr}_{QP}\{\hat{\rho}_{GC,\alpha}\} = \frac{1}{Z_{CP,GC,\alpha}}\mathbb{1}\,. \tag{3.22}$$

Here, Eq. (3.22) is, at first glance, nonsensical, since a partition function for a constant matrix cannot be finite for an infinite Hilbert space $M \in \mathbb{N}_0$. However, one can endow the formalism with meaning by restricting M to a large but finite range, as done above. Mathematically, the necessity of imposing this restriction originates with the lack of a dependence of the grand canonical Hamiltonian on the electronic density. In real superconductors, terms like the charging energy, which are absent from the model Hamiltonian investigated here, solve this issue. The contribution of such weak, but conceptually important, contributions to the Hamiltonian for macroscopic superconductors yields a finite range of realistic M that contribute to Eq. (3.22). As such, one should interpret the above density operator for the Cooper pairs as the limit

$$\hat{\rho}_{CP,GC,\alpha} = \lim_{C\to 0^+} \frac{1}{Z_{QP,GC,\alpha}(C)} e^{-\beta_\alpha C(\hat{N}_M - \bar{M})^2}\,. \tag{3.23}$$

The lack of a finite grand canonical Hamiltonian for the Cooper pairs indicates their non-dissipative nature, which complicates their inclusion into the bath of an open quantum system. Instead, the quasiparticles act as a thermal bath that remains uncoupled to the Cooper pairs within the model for an isolated supercondcutor discussed here. The Cooper pair part of the density operator of the leads couples only indirectly to this thermal bath via its interaction with the central system and as such should be conceptually treated as part of the

latter. In addition to this conceptual reason for this particular choice, early works on transport through junctions with superconducting leads that employed the particle-conserving theory found that the Josephson effect fundamentally relies on the correlation between the condensates in multiple leads [105, 106]. Considering the Cooper pairs as part of the bath amounts to a secular approximation, neglecting these types of coherences, thereby rendering this description incomplete. that are not permitted provided the condensates are considered as parts of independent leads In contrast, approaches that considered the condensates as part of the system and thus allowed for the inclusion of correlations between the condensates in distinct leads were able to recover a Josephson effect at the appropriate order in the perturbative expansion in the tunneling coupling [42, 123]. The remainder of this thesis will assume the treatment of the superconducting condensates in all leads as part of the central system in the Nakajima-Zwanzig formulation. The quasiparticles in the leads comprise the thermal bath with its reference state provided by their grand canonical thermal density operator in Eq. (3.21).

3.3 PHASE REPRESENTATION OF THE CONDENSATES

When studying an open quantum system with superconducting leads treated in the particle-conserving approach, the inclusion of the superconducting condensate in the respective leads into the central system poses an issue with the desired tractability of the problem. More concisely, one wishes to reduce the dimensionality of the reduced density operator to a degree that the resulting equations allow for either an analytical or a numerical solution to the desired degree of accuracy. Since the leads are macroscopic by nature, the range that the number of Cooper pairs M in the condensate may take for each superconducting lead is also large. Numerically, reduced density operators with a dimensionality in Liouville space of multiple hundreds to a few thousand dimensions, equivalent to $\leqslant 100$ states in the underlying Hilbert space, still allow for an exact calculation of the kernel of the operator in Eq. (2.38).

Since the composite Hilbert space of the actual central system and the condensate even of just one superconducting lead is given by a direct product of the two spaces, the dimensionality of the resulting problem already grows untractable even for a single superconducting lead with δM restricted to an unphysically narrow range of $\delta M \sim 100$. As such, this formalism is not realistically applicable without the following simplifications that drastically reduce the dimensionality of the resulting problem.

Consider first the dynamics of the Cooper pair condensate under the action of the Liouvillian associated with the Hamiltonian in Eq. (3.18). For the element $|\mathbf{M}+\mathbf{m}\rangle\langle\mathbf{M}|$ of the Cooper pair density operator, the Liouvillian acts as

$$\begin{aligned}\mathcal{L}_{CP}(t)\,|\mathbf{M}+\mathbf{m}\rangle\langle\mathbf{M}| &= \sum_{\nu} \frac{-i\nu}{\hbar}\hat{H}_{CP,l}(t)^{\nu}\,|\mathbf{M}+\mathbf{m}\rangle\langle\mathbf{M}| \\ &= \frac{-i2\boldsymbol{\mu}(t)\cdot((\mathbf{M}+\mathbf{m})-\mathbf{M})}{\hbar}\,|\mathbf{M}+\mathbf{m}\rangle\langle\mathbf{M}| \\ &= \frac{-i2\boldsymbol{\mu}(t)\cdot\mathbf{m}}{\hbar}\,|M+\mathbf{m}\rangle\langle M|\,, \end{aligned} \tag{3.24}$$

which depends only on the difference $\mathbf{m}$ measuring the off-diagonality of a element of the density operator. The lack of dependence on $\mathbf{M}$ suggests that such degrees of freedom, which are irrelevant to the density operator's dynamics, can be eliminated through generalized off-diagonal partial traces of the form

$$\hat{\rho}_{\mathbf{m}}(t) = \sum_{\mathbf{M}} \langle\mathbf{M}+\mathbf{m}|\,\hat{\rho}(t)\,|\mathbf{M}\rangle\,. \tag{3.25}$$

Siegl, Picó-Cortés, and Grifoni [40] demonstrate that this procedure enables rewriting the equations for both the density operator of the central system coupled to the superconducting leads and the current in the Nakajima-Zwanzig formalism as functions of these reduced quasi-density operators[8]. Consider the following decomposition of the kernel $\mathcal{K}_O$:

$$\mathcal{K}_O(t,s)\hat{\rho}(s) = \sum_{\mathbf{N}^+,\mathbf{N}^-} \kappa_O(t,s,\mathbf{N}^+,\mathbf{N}^-)\mathrm{Tr}_{CP}\{\hat{S}^{\mathbf{N}^+,\nu=+}\hat{S}^{\mathbf{N}^-,\nu=-}\hat{\rho}(s)\otimes\hat{\rho}_B\}\,, \tag{3.26}$$

$$\hat{S}^{\mathbf{N}} := \prod_{\alpha}\left(\hat{S}_{\alpha}^{p=\mathrm{sgn}(N_\alpha)}\right)^{|N_\alpha|}\,, \tag{3.27}$$

which allows for the definition of

$$\kappa_{O,\mathbf{m}}(t,s) = \sum_{\mathbf{N}} \kappa_O(t,s,\mathbf{N},-\mathbf{N}-\mathbf{m})\,. \tag{3.28}$$

If the individual $\kappa_O(t,s,\mathbf{N}^+,\mathbf{N}^-)$ do not contain any dependence on $\mathbf{M}$, one can rewrite the last term in Eq. (2.28) as

$$\int_0^t ds\,\mathcal{K}_O(t,s)\hat{\rho}(s) = \int_0^t ds\,\sum_{\mathbf{m}} \kappa_{O,-\mathbf{m}}(t,s)\hat{\rho}_{\mathbf{m}}(s)\,, \tag{3.29}$$

while an insertion of the equivalent expansion for the time-propagation kernel results in

$$\dot{\hat{\rho}}_{\mathbf{m}}(t) = \mathcal{L}_S\hat{\rho}_{\mathbf{m}}(t) + \int_0^t ds\,\sum_{\mathbf{m}'} \kappa_{\mathbf{m}-\mathbf{m}'}(t,s)\hat{\rho}_{\mathbf{m}}(s)\,. \tag{3.30}$$

8 Only the element $\mathbf{m}=\mathbf{0}$ is an actual reduced density operator.

As such, the Nakajima-Zwanzig equation for the reduced density operator turns into a coupled set of equations between the reduced quasi-density operators.

As is suggested by the identical use of notation, for a static chemical potential $\boldsymbol{\mu}(t) = \boldsymbol{\mu}$, the identification of the quasi-density operators with the expansion coefficients in the Fourier expansion for periodically driven systems is possible via the unitary transformation

$$U(t, t_0) = \mathcal{T}_{\leftarrow} e^{\int_{t_0}^{t} dt' - \mathcal{L}_{CP}(t')}, \tag{3.31}$$

which if applied to $\hat{\rho}_{tot}(t)$ results in the elimination of the Cooper pair Liouvillian from the system Liouvillian at the price of making the Josephson $\hat{S}^\dagger$ operator time dependent. As this operator enters the tunneling Liovillian $\mathcal{L}_T$, the resulting problem after the unitary transformation has no energetic dependence on the Cooper pair degrees of freedom. Instead, the problem takes the form of a time-periodically driven tunneling problem. Provided a difference in the chemical potentials of two superconducting leads α and α', the resulting difference frequency of these drivings is exactly the Josephson frequency $2(\mu_\alpha - \mu_{\alpha'})/\hbar$ expected from the AC Josephson effect [39]. The above suggests that one can treat the AC Josephson effect using the theory for periodically driven open quantum systems introduced above.

Beyond the elimination of $\mathbf{M}$, the application of selection rules based on conserved quantities puts a further constraint on the range of $\mathbf{m}$. Since the grand canonical quasiparticle Hamiltonian is an effective single-particle Hamiltonian with well-defined charge for each occupied state, the reference bath density operator is block-diagonal in the particle number. Furthermore, the conservation of charge by both the tunneling and system Hamiltonians ensures that the reduced density operator remains block-diagonal in the particle number, provided it starts as such at initial times[9]. For the composite Hilbert space of the central system and the Cooper pairs $|\chi, \mathbf{M}\rangle = |\chi\rangle \otimes |\mathbf{M}\rangle$, this ensures that the element $|\chi, \mathbf{M} + \mathbf{m}\rangle\langle\chi', \mathbf{M}|$ vanishes if

$$\sum_\alpha 2m_\alpha + N_\chi - N_{\chi'} \neq 0\,. \tag{3.32}$$

Consider the simplest case of two superconducting leads (left/right); The imbalances $m_L = -m_R$ are always allowed due to the possibility $\chi = \chi'$ fulfilling Eq. (3.32) in this case. Fig. 3.1 shows the allowed $\mathbf{m}$ for a finite range around $\mathbf{m} = 0$, with the case discussed above shown in green along the diagonal. As the central system can host more charges, the range of $\mathbf{m}$ fulfilling Eq. (3.32) for some χ, χ' increases. The conservation of charge does not limit the range of m_L itself. For finite allowed charge differences $2n$ in the central system, the range

9 Any other choice sees the off-block-diagonal coherences vanish for the steady state. An exception is the pathological case of a coherence at initial time that cannot decay due to a missing coupling to the environment.

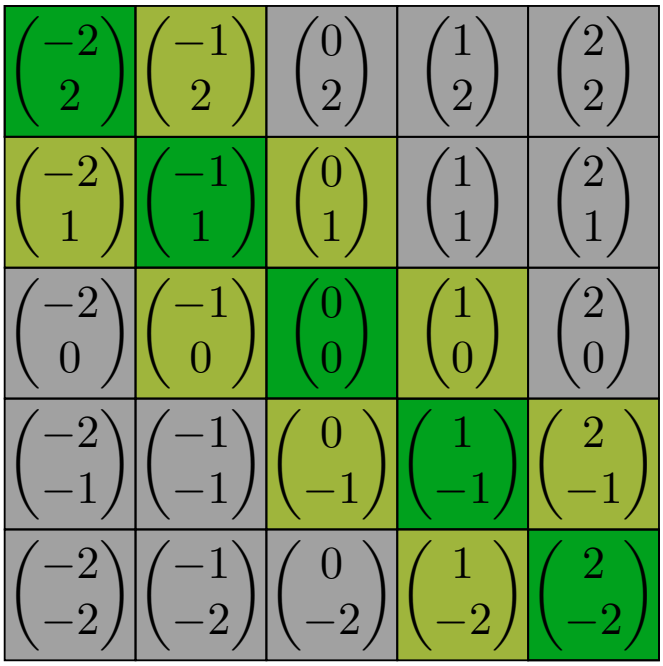

Figure 3.1: **Allowed $\mathfrak{m}$ for a single-impurity connected to two superconducting leads.** The strong green color on the diagonal shows the range for which no constraint based on particle conservation exists. This range broadens to include more possibilities as the central system's ability to hold charge increases. For the single-impurity model, the only allowed possibilities are the main diagonal and the first supra- and sub-diagonal.

of $\mathfrak{m}$ with non-vanishing $\hat{\rho}_{\mathfrak{m}}$ takes the form of the first n super/sub-diagonals of the diagonal $m_L = -m_R$, thereby rendering the numerical problem of solving the Nakajima-Zwanzig equation of the steady state equivalent into the known form of determining the kernel of a band-diagonal matrix. For chemical potential $\mu = 0$, the Cooper pair Liouvillian vanishes, and the problem becomes invariant under any shift $\mathfrak{m} \to \mathfrak{m} + j(1,-1)$ with $j \in \mathbb{Z}$. The Töplitz-form of the resulting problem allows for an elegant solution by switching to a conjugate variable to the (nearly)[10] infinitely ranged discrete variable m_L. This conjugate variable is a well-defined phase variable that enters the dynamics of the model, in line with the expectation for the presence of a Josephson effect [38], but crucially, without the requirement of assuming a broken $U(1)$ symmetry at the level of the superconductors themselves [114]. In general, the space of allowed $\mathfrak{m}$ for d-superconducting leads is $d-1$-dimensional with a finite extent along the remaining dimension provided by the maximum allowed charge difference between eigenstates of the central system.

10 The actual range of m_L is finite, but very large for macroscopic leads. The situation is similiar to a one-dimensional periodic lattice, where the bulk spectrum is well-approximated as independent of the actual applied boundary conditions. The impact of extraordinarily far off-diagonal blocks of the density operator encountering the limits imposed by the choice of δM is negligible.

Transforming the kernel and the density operator to the phase-representation [40] yields

$$\hat{\rho}_{\boldsymbol{\phi}}(s) = \sum_{\mathbf{m}} e^{i\mathbf{m}\cdot\boldsymbol{\phi}} \hat{\rho}_{\mathbf{m}}(s)\,, \qquad \kappa_{O,\boldsymbol{\phi}}(t,s) = \sum_{\mathbf{m}} e^{i\mathbf{m}\cdot\boldsymbol{\phi}} \kappa_{O,\mathbf{m}}(t,s)\,, \tag{3.33}$$

which makes use of the fact that[11]

$$\hat{S}^{p}_{\alpha} \approx e^{-ip\hat{\phi}_{\alpha}}\,. \tag{3.34}$$

Notably, the transformation to phase space allows a formal decoupling of the set of equations in Eq. (3.30) even at finite bias, as

$$\dot{\hat{\rho}}_{\boldsymbol{\phi}}(t) = \mathcal{L}_S \hat{\rho}_{\boldsymbol{\phi}}(t) + \int_0^t ds\, \kappa_{\boldsymbol{\phi}}(t,s)\hat{\rho}_{\boldsymbol{\phi}}(s)\,. \tag{3.35}$$

However, the off-diagonals $\mathbf{m} \neq \mathbf{0}$ correspond directly to the components of the density operator that oscillate with the frequencies associated to the AC Josephson effect. The Fourier expansion of the kernels reads

$$\kappa_{O,\boldsymbol{\phi}}(t,s) = \sum_{n,\mathbf{m}} \kappa_{O,n,\mathbf{m}}(t-s) e^{i[\mathbf{m}\cdot(\boldsymbol{\omega}_{DC}s+\boldsymbol{\phi})+n\omega_{AC}s]}\,, \tag{3.36}$$

where n is the separate Fourier index associated to the external driving, while the index $\mathbf{m}$ resurfaces as the integer-valued vector of Fourier components of the quasi-reduced density operators. At zero bias, where one can set $\boldsymbol{\mu} = \mathbf{0}$ by a global shift of all energies, the expansion with respect to $\mathbf{m}$ in Eq. (3.36) is still well-defined as an expansion of the kernel in terms of its dependence on the phase. The fact that $\hat{S}_{\alpha}$ is diagonal in phase space renders the systems' dynamics trivial in this variable as Eq. (3.35) only couples components of $\hat{\rho}_{\boldsymbol{\phi}}$ with the same phase $\boldsymbol{\phi}$. This lack of mixing between different $\hat{\rho}_{\boldsymbol{\phi}}$ is an artifact of the model employed here, where, as previously noted, the Cooper pairs have no associated energy scale in the grand canonical Hamiltonian. Eq. (3.36) states that the dynamics associated with the phase corresponds to the "trivial" time evolution expected from the 2nd Josephson equation $i\hbar\dot{\phi}_{\alpha}(t) = 2\mu_{\alpha}(t)$, which in this thesis has been moved onto the tunneling Liouvillian by merit of the unitary transformation in Eq. (3.31).

This lack of a non-trivial dynamic of the phase $\boldsymbol{\phi}$ raises some conceptual issues about the applicability of the theory for transport calculation. Consider the following extreme case: The system at the initial time is such that all condensates in the leads are uncorrelated. The corresponding density operator fulfills $\hat{\rho}_{\mathbf{m}}(t_0) = 0$ for all $\mathbf{m} \neq \mathbf{0}$. In phase space, the density operator at the initial time is independent of $\boldsymbol{\phi}$, since $\hat{\rho}_{\boldsymbol{\phi}}(t_0) = \hat{\rho}_0(t_0)$. The lack of a dependence on the state of

11 The approximate sign indicates that this does not hold at the boundaries of the considered range of m. One can safely use this approximation in the following, provided the range of m is large enough.

the condensate, except via the action of the $\hat{S}$ operators, results in the dynamics of $\hat{\rho}_{\boldsymbol{\phi}}(t)$ being independent of $\boldsymbol{\phi}$ apart from the initial condition $\hat{\rho}_{\boldsymbol{\phi}}(0)$ and a fixed relative phase between components. The latter cancels during the evaluation of observables inside a trace.[12]. This case corresponds to a system where the phase is maximally ill-defined, in the sense that the system is always in a complete superposition of all possible phases.

The distribution in phase has observable consequences as, e.g., the time-dependent current in Eq. (3.29) is calculated by summing over $\mathfrak{m}$, which in phase space turns into an integral over the phase $\boldsymbol{\phi}$ as

$$I(t) = \int_0^t ds \int_{\square} d\boldsymbol{\phi}\, \mathrm{Tr}_S\{\kappa_{I,\boldsymbol{\phi}}(t,s)\hat{\rho}_{\boldsymbol{\phi}}(s)\}, \tag{3.37}$$

where $\int_{\square} = (2\pi)^{-\#\alpha}\prod_\alpha \int_0^{2\pi} d\phi_\alpha$ the integration over all phases and $\#\alpha$ is the number of superconducting leads. The conventional non-particle conserving BCS theory fixes all components of the phase with

$$\hat{\rho}_{\boldsymbol{\phi},\mathrm{BCS}}(s) = (2\pi)^{\#\alpha}\delta(\boldsymbol{\phi}-\boldsymbol{\phi}_{\mathrm{BCS}})\hat{\rho}_{\boldsymbol{\phi}_{\mathrm{BCS}}}(s)\,, \tag{3.38}$$

which, however, is incompatible with the constraint on particle conservation, provided the central system is finite. A well-defined phase for the particle-conserving theory only contains at most $\#\alpha - 1$ fixed phases, since the particle-conservation constraint on $\mathfrak{m}$ ensures that at least one phase is ill-defined, since the maximum allowed charge in-balance of the central system limits the respective support of $\mathfrak{m}$ along at least one axis in its configuration space. For a completely conserved total number of charge in the leads, the global phase is completely ill-defined, while a finite size of the central system allows the particle number of the leads to fluctuate. Fixing all relative phases to ϕ_0, an example of a well-defined phase in the particle-conserving theory is

$$\hat{\rho}_{\boldsymbol{\phi},\text{well-defined}}(s) = (2\pi)^{\#\alpha-1}\Big(\prod_{\alpha=2}^{\#\alpha}\delta(\phi_\alpha-\phi_0-\phi'_\alpha)\hat{\rho}_{\phi_0}(s)\,, \tag{3.39}$$

where only a single phase is left free. The resulting current has a parametric dependence on the fixed relative phases

$$I(t,\phi'_2,\cdots,\phi'_{\#\alpha}) = \int_0^t ds \int_{\square} d\boldsymbol{\phi}\,\mathrm{Tr}_S\{\kappa_{I,\boldsymbol{\phi}}(t,s)\hat{\rho}_{\boldsymbol{\phi},\text{well-defined}}(s)\}. \tag{3.40}$$

12 The proof of this relies on the fact that the phase enters as a relative phase between elements connected by the action of $\hat{S}$. All elements of the time-propagation kernel connecting two entries of $\hat{\rho}_{\boldsymbol{\phi}}$ have opposing relative phases depending on the in/outgoing state, thereby cancelling any dependence on $\boldsymbol{\phi}$ in the time-propagation kernel's action on $\hat{\rho}_{\boldsymbol{\phi}}(t)$.

Conversely, the case of an ill-defined phase corresponds to the integral over all possible relative phases, thereby averaging out all possible dependencies on $\phi'_2, \cdots, \phi'_{\#\alpha}$ as

$$I_{\text{ill-defined phase}}(t) = \frac{1}{(2\pi)^{\#\alpha-1}} \left(\prod_{\alpha=2}^{\#\alpha} \int_0^{2\pi} d\phi'_\alpha \right) I(t, \phi'_2, \cdots, \phi'_{\#\alpha}) \,. \tag{3.41}$$

Eq. (3.41) can contain neither a DC nor an AC Josephson current, since both rely on the presence of a relative phase, with the average over all possible relative phases vanishing. As such, starting from an uncorrelated initial condition, the lack of non-trivial dynamics in the phase variable ensures that the dynamics remain uncorrelated at all times, thereby never developing a Josephson effect. One can introduce a function governing the distribution $F(\boldsymbol{\phi})$ of the junctions density operator in phase space. This distribution depends on the initial conditions and shows up when solving the phase-dependent equations of motion with the ansatz [40]

$$\hat{\rho}_{\boldsymbol{\phi},n,m} = e^{im\cdot\Phi} F(\boldsymbol{\phi}) \hat{\rho}'_{n,m} \,, \tag{3.42}$$

where $F(\boldsymbol{\phi}) = 1$ for the case of uncorrelated initial conditions and $F(\boldsymbol{\phi}) = (2\pi)^{\#\alpha-1} \prod_{\alpha=2}^{\#\alpha} \delta(\phi_\alpha - \phi_0 - \phi'_\alpha)$ for the maximally well-defined phase introduced above. The trace property of the reduced density operator ensures

$$\int_\square d\boldsymbol{\phi}\, F(\boldsymbol{\phi}) = 1 \,. \tag{3.43}$$

This description is not directly suitable for real Josephson junctions, since those do develop a Josephson effect independent of the initial conditions. The missing ingredient in the theory here is the small, but finite, impact of additional terms in the Cooper pair Hamiltonian, like the charging energy of the leads. Nonlinear terms in the Cooper pair number operator break the Töplitz structure of the equations of motion, and thereby result in off-diagonal contributions to the propagation kernels connecting different phases. As such, the equations of motion no longer uncouple in phase space, and the phase recovers non-trivial dynamics.

Like with any other small perturbation to the Hamiltonian, the associated dynamics of the open quantum system are slow. However, for most small contributions to the Hamiltonian, these dynamics compete as a perturbation against the dynamics induced by the dominant terms in the Hamiltonian, thereby justifying their omission. The ability to neglect small, irrelevant terms in a system's Hamiltonian is a central concept of physical modelling, and as such often implicitly invoked. The breakdown of this approach here is due to the associated induced dynamics concerning a conserved quantity of the remaining Hamiltonian. As such, one can interpret the model introduced here as a model for the "fast" dynamics of a junction with fixed phase. The latter follows the "slow" dynamics induced by the

small contributions to the Hamiltonian not captured within the model discussed here. These fast dynamics only resolve the phase via a parametric dependence, which is justified if the transient regime of the fast dynamics is short compared to the time scale of the dynamics of the phase.

The realistic modelling of a junction then proceeds as follows: Consider an arbitrary initial condition at $t = 0$. The phase reaches its steady state $\boldsymbol{\phi} = \boldsymbol{\phi}(t_0)$ by letting the junction relax under the applied external biases until a time t_0 much larger than the time scale of the dynamics of the phase τ_{phase}, such that $\tau_{\text{phase}} \ll t_0$. One then applies the Nakajima-Zwanzig formalism starting from t_0 with an initial guess $\hat{\rho}_{\boldsymbol{\phi}}(t_0)$ and keeping the phase fixed. Evolving the density operator to long times t, such that $\tau_{\text{junction}} \ll t - t_0 \ll \tau_{\text{phase}}$ holds for the transient time scale of the junction τ_{junction}, the density operator approaches the steady-state density operator within the Nakajima-Zwanzig formalism, which has, in general, a parametric dependence on $\boldsymbol{\phi}(t_0)$. Given the slow dynamics of the phase, one then has an approximate form of the junctions density operator, since $\boldsymbol{\phi}(t) \approx \boldsymbol{\phi}(t_0)$. This protocol allows the application of the theory developed here without the conceptual issues mentioned above.

For most applications, the approximation of a well-defined phase across the junction should be justified, thereby recovering the known and experimentally verified predictions of the Josephson effect [38, 39, 42, 124]. Beyond this approach, which utilizes a well-defined relative phase, one can employ phenomenological modelling to account for decoherence or attempt to solve the slow dynamics of the phase numerically. While recovering the known behavior of the particle non-conserving theory in the appropriate limit, this generalized description might yield novel insights when applied to increasingly miniaturized superconducting circuits, where the decreasing size should make a consistent inclusion of charge conservation more relevant.

4

AC-DC-DRIVEN INTERACTING QUANTUM DOT

To illustrate the formalism for transport through interacting nanojunctions with superconducting leads as introduced above, this chapter covers its application to the problem of an interacting quantum dot coupled to two superconducting leads under both AC and DC driving. This setup corresponds to a minimal model for an interacting Josephson junction, with the central system modelled by the single-impurity Anderson model [125], which is the atomic limit of the Hubbard model [126]. In the sequential tunneling approximation, one expects the appearance of thermal subgap features [105, 106, 127], finite coherences in the central system due to proximity [128–140] and photo-assisted tunneling [141, 142]. In contrast, the Josephson effect occurs at the next perturbative order [42, 104, 123, 143], while infinite order effects in strong-coupling or Kondo regimes [144–146] are best treated in other approaches, such as the slave-boson method [147–149] or renormalization group techniques [146, 150–152]. The Hamiltonian of the single-impurity Anderson model reads

$$\hat{H}_{QD} = \sum_{\sigma} (\epsilon_\sigma + a_G e V_G) \hat{d}_\sigma^\dagger \hat{d}_\sigma + U \hat{d}_\uparrow^\dagger \hat{d}_\uparrow \hat{d}_\downarrow^\dagger \hat{d}_\downarrow , \tag{4.1}$$

where V_G is a gate voltage and a_G is a lever arm introduced to vary the efficacy of an applied gate voltage in shifting the single-particle energies of the quantum dot. Earlier works showed that interactions inside a Josephson junction can result in a sign-reversal of the DC Josephson effect, resulting in so-called π-junction behavior [153]. Multiple experimental realizations of superconductor-quantum dot-superconductor junctions exist. They include approaches based on semiconductor nanowires [154], carbon nanotubes [127, 155–161], fullerenes [162], and graphene [163]. More recently, Andreev spin qubits based on quantum dots have been proposed [43, 45–47].

The tunnel coupling to the superconducting leads has the Hamiltonian

$$\begin{aligned}\hat{H}_T &= \sum_{\alpha,k,\sigma} t_\alpha \hat{c}^\dagger_{\alpha,k,\sigma}\hat{d}_\sigma + \text{h.c.}\\ &= \sum_{\alpha,k,\sigma} t_\alpha (u_{\alpha,k\sigma}\hat{\gamma}^\dagger_{\alpha,k,\sigma} + \sigma v^*_{\alpha,k\sigma}\hat{S}^\dagger_\alpha \hat{\gamma}_{\alpha,\bar{k},\bar{\sigma}})\hat{d}_\sigma + \text{h.c.}\\ &= \sum_{\alpha,k,\sigma,p} t^{\bar{p}}_\alpha p(u^{\bar{p}}_{\alpha,k\sigma}\hat{\gamma}^p_{\alpha,k,\sigma} + \sigma v^p_{\alpha,k\sigma}\hat{S}^p_\alpha \hat{\gamma}^{\bar{p}}_{\alpha,\bar{k},\bar{\sigma}})\hat{d}^{\bar{p}}_\sigma\,, \end{aligned} \tag{4.2}$$

where $p = \in \{+,-\}$ and $p = +$ indicates hermitian conjugation while $p = -$ indicates no action. Making use of the property $(\hat{X}\hat{Y})^\nu = \nu\hat{X}^\nu\hat{Y}^\nu$ for anticommuting $\hat{X}$ and $\hat{Y}$, the associated tunneling Liouvillian after the unitary transformation of Eq. (3.31) reads

$$\mathcal{L}_T(t) = \sum_{\alpha,k,\sigma,p,\nu} \frac{p t^{\bar{p}}_\alpha}{i\hbar}(u^{\bar{p}}_{\alpha,k\sigma}\hat{\gamma}^{p,\nu}_{\alpha,k,\sigma} + \sigma v^p_{\alpha,k\sigma}\hat{\gamma}^{\bar{p},\nu}_{\alpha,\bar{k},\bar{\sigma}}\hat{S}^{p,\nu}_\alpha(t))\hat{d}^{\bar{p},\nu}_\sigma\,, \tag{4.3}$$

$$\hat{S}_\alpha(t) = \hat{S}_\alpha e^{\frac{2i}{\hbar}\int_{t_0}^t dt'\,\mu_\alpha(t')}\,. \tag{4.4}$$

The chemical potential of the leads is, up to an global chemical constant μ_0, which in the wide-band limit with flat density of states can be absorbed into the gate voltage on the dot, a superposition of a DC voltage bias V_{DC} and a sinusoidal AC voltage bias V_{AC}. Setting $\mu_0 = 0\,\text{eV}$, the chemical potential in lead α thus reads

$$\mu_\alpha(t) = a_\alpha e(V_{DC} + V_{AC}\sin(\omega_{AC}t))\,, \tag{4.5}$$

where $a_L - a_R = 1$ and $0 \leqslant a_L \leqslant 1$ allows for the asymmetric application of bias voltage across the junction [164]. Employing the Jacobi-Anger expansion to the time dependence of $\hat{S}_\alpha(t)$, one can write [165]

$$e^{\frac{2i}{\hbar}\int_{t_0}^t dt'\,\mu_\alpha(t')} = e^{iu_\alpha\cdot\omega_{DC}(t-t_0)}\sum_n i^n J_n(a_\alpha\epsilon_{AC})e^{in\omega_{AC}t}\,, \tag{4.6}$$

where $\mathbf{u}_\alpha$ is the unit vector $(\mathbf{u}_\alpha)_{\alpha'} = \delta_{\alpha,\alpha'}$, $\epsilon_{AC} = \frac{2eV_{AC}}{\hbar\omega_{AC}}$ is a unitless amplitude of the AC driving that governs the importance of photo-assisted effects, J_n are the n-th order Bessel functions of the first kind, $t_0 = \pi/2\omega_{AC}$ for convenience, and the vector of Josephson frequencies

$$(\boldsymbol{\omega}_{DC})_\alpha = \frac{2eV_{DC}a_\alpha}{\hbar}\,. \tag{4.7}$$

The main observable of interest is the time-dependent current, where in the following, the current is the flow of charge from the quantum dot into the left lead, defined as[1]

$$\hat{I} = -e\dot{\hat{N}}_L = \frac{-ie}{\hbar}\left[\hat{H}_{tot}(t),\hat{N}_L\right] = \frac{-ie}{\hbar}\left[\hat{H}_T(t),\hat{N}_L\right] = \frac{ie}{\hbar}\sum_{k,\sigma,p} t^{\bar{p}}_L\hat{c}^p_{L,k,\sigma}\hat{d}^{\bar{p}}_\sigma\,. \tag{4.8}$$

1 Due to charge conservation, any displacement current vanishes in its time-average, resulting in $\langle I_L(t)\rangle_t = -\langle I_R(t)\rangle_t$.]For the AC current, the choice of a different convention may result in more significant differences. One can easily adaptat both the formalism and the code to calculate the current in conventions different from the one used here.

In sequential tunneling, which is equivalent to the second order in the perturbative expansion in terms of $\mathcal{L}_T$, the time-propagation and current kernels in the time domain read

$$\mathcal{K}(t,s)\hat{\rho}(s) = \mathrm{Tr}_B\{\mathcal{L}_T(t)\mathcal{G}_0(t,s)\mathcal{L}_T(s)\hat{\rho}(s)\otimes\hat{\rho}_B\}, \tag{4.9}$$

$$\mathcal{K}_I(t,s)\hat{\rho}(s) = \mathrm{Tr}_B\{\hat{I}(t)\mathcal{G}_0(t,s)\mathcal{L}_T(s)\hat{\rho}(s)\otimes\hat{\rho}_B\}. \tag{4.10}$$

The evaluation of these kernels simplifies by using

$$\hat{\gamma}^{p,\nu}_{\alpha,k,\sigma}\mathcal{G}_0(t,s) = \mathcal{G}_0(t,s)\exp\left(\int_s^t ds'\,\frac{ip}{\hbar}(E_{\alpha,k}+\mu_\alpha(s'))\right)\hat{\gamma}^{p,\nu}_{\alpha,k,\sigma}, \tag{4.11}$$

$$\mathrm{Tr}_B\{\mathcal{G}_0(t,s)\hat{O}\} = \mathcal{G}_{QD}(t,s)\mathrm{Tr}_B\{\hat{O}\}, \tag{4.12}$$

where Eq. (4.11) enables one to move all operators acting on the quasiparticles to the right. At the same time, Eq. (4.12) allows for the separate calculation of the partial trace over the bath where $\mathcal{G}_{QD}(t,s) = \exp(\mathcal{L}_{QD}(t-s))$ is the free propagator of the quantum dot and the resulting kernel to second order reads

$$\begin{aligned}
\mathcal{K}(t,s)\hat{\rho}(s) = &\sum_{\substack{\alpha,\alpha',k,k',\sigma,\sigma'\\ p,p',\nu,\nu'}} \frac{-\nu\nu' pp' t^{\bar{p}}_{\alpha} t^{\bar{p}'}_{\alpha'}}{(i\hbar)^2}\hat{d}^{\bar{p},\nu}_{\sigma}\mathcal{G}_{QD}(t,s)\hat{d}^{\bar{p}',\nu'}_{\sigma'}\hat{\rho}(s)\\
&\times \mathrm{Tr}_{QP}\Bigg\{\Bigg[u^{\bar{p}}_{\alpha,k\sigma}e^{\int_s^t ds'\,\frac{i\bar{p}}{\hbar}(E_{\alpha,k}+\mu_\alpha(s'))}\hat{\gamma}^{p,\nu}_{\alpha,k,\sigma}\\
&+\nu^{p}_{\alpha,k\sigma}e^{\frac{2ip}{\hbar}\int_{t_0}^t dt'\,\mu_\alpha(t')}\sigma e^{\int_s^t ds'\,\frac{i\bar{p}}{\hbar}(E_{\alpha,k\sigma}+\mu_\alpha(s'))}\hat{S}^{p,\nu}_{\alpha}\hat{\gamma}^{\bar{p},\nu}_{\alpha,\bar{k},\bar{\sigma}}\Bigg]\\
&\times\left[u^{\bar{p}'}_{\alpha',k'\sigma'}\hat{\gamma}^{p',\nu'}_{\alpha',k',\sigma'}+\sigma'\nu^{p'}_{\alpha',k'\sigma'}e^{\frac{2ip'}{\hbar}\int_{t_0}^s dt'\,\mu_{\alpha'}(t')}\hat{S}^{p',\nu'}_{\alpha'}\hat{\gamma}^{\bar{p}',\nu'}_{\alpha',\bar{k}',\bar{\sigma}'}\right]\hat{\rho}_{QP}\Bigg\}.
\end{aligned} \tag{4.13}$$

The kernel in Eq. (4.13) splits into four terms by considering the occurrence of the Josephson $\hat{S}$ operator acting on the density operator. These four separate terms correspond to the four possible sequential tunneling diagrams in the diagrammatics associated to the Nakashima-Zwanzig formalism [71, 73]. The formulation of the kernel in diagrams allows a natural extension to regimes beyond weak coupling by diagrammatic resummation techniques [91, 104]. Here, it is sufficient that the resulting diagrams allow for the identification of two distinct types of contributions to the expansion components in Eq. (3.26). The component κ_0 is the normal kernel, since it does not alter the state of the condenstate. The normal kernel includes only terms with $\hat{S}_\alpha$ operators paired up to compensate, i.e., $(\hat{S}\hat{S}^\dagger)^j$

with $j \in \mathbb{Z}$, and therefore survives also in normal-conducting limit $\Delta \to 0$. The normal sequential tunneling kernel reads

$$\begin{aligned}\kappa_0(t,s) = &\sum_{\alpha,\sigma,p,\nu,\nu'} \frac{\nu\nu'|t_\alpha|^2}{(i\hbar)^2} \hat{d}^{\bar{p},\nu}_\sigma \mathcal{G}_{QD}(t,s) \hat{d}^{p,\nu'}_\sigma \\ &\times \int_{-\infty}^{\infty} dE\, D_\alpha(E) e^{\frac{i}{\hbar}\int_s^t ds'\,(E+p\mu_\alpha(s'))} f^{\nu'}(E)\,,\end{aligned} \tag{4.14}$$

where $f^q(E) = 1/(1+e^{q\beta E})$ is the Fermi-Dirac distribution and $D_\alpha(E)$ is the normal density of states for the excitation energies $E_{\alpha,k,\sigma}$. In the wide-band limit, and with a constant s-wave gap, this normal density of states takes the usual BCS-form [22, 166] of

$$D_\alpha(E) = D^0_\alpha \mathrm{Re}\left\{\sqrt{\frac{(E-i\gamma)^2}{(E-i\gamma)^2 - |\Delta_\alpha|^2}}\right\}, \tag{4.15}$$

where D^0 is the (assumed to be) flat density of states in the vicinity of the Fermi level of the normal-conducting state. γ is a Dynes parameter [167] accounting for a finite broadening of the superconducting density of states. The broadening acts here as a phenomenological parameter, but arises naturally at higher orders in the tunneling problem as is discussed by Yeyati et al. [168] for a non-interacting resonant level.

The trace over the quasiparticles restricts the possible contributions to the kernel, with the only other possible contribution corresponding to the so-called "anomalous" kernel with a sole $\hat{S}^{p,\nu}_\alpha$ operator. The anomalous kernels are therefore of the form

$$\begin{aligned}\kappa_{pu_\alpha}(t,s) = &\sum_{\sigma,\nu,\nu'} \frac{p\nu\nu'|t_\alpha|^2}{(i\hbar)^2} \sigma e^{-ip\phi_\alpha} \hat{d}^{\bar{p},\nu}_\sigma \mathcal{G}_{QD}(t,s) \hat{d}^{\bar{p},\nu'}_{\bar{\sigma}} e^{\frac{ip}{\hbar}\int_0^s dt'\, 2\mu_\alpha(t')} \\ &\times \int_{-\infty}^{\infty} dE\, A_\alpha(E) e^{\frac{i}{\hbar}\int_s^t ds'\,(E+p\mu_\alpha(s'))} f^{\nu'}(E)\,,\end{aligned} \tag{4.16}$$

where the phase shift $\phi_\alpha = \arg(\Delta_\alpha(t^*_\alpha)^2) + \frac{2}{\hbar}\int_0^{t_0} ds\, \mu_\alpha(s)$ absorbs all static phase shifts due to a phase of the order parameter and the choice of t_0. Here, $A_\alpha(E)$ takes the role of the density of states for the "anomalous" processes modifying the condensate. It is the largest in and around the gap, and vanishes as $|\Delta_\alpha|/|E|$ outside the gap. Using the wide band limit, one can express the anomalous density of states as

$$A_\alpha(E) = D^0_\alpha \mathrm{Re}\left\{\sqrt{\frac{|\Delta_\alpha|^2}{(E-i\gamma)^2 - |\Delta_\alpha|^2}}\right\} \mathrm{sgn}(E)\,. \tag{4.17}$$

Inserting the Jacobi-Anger expansion for the specific form of the AC drive considered here, one can express the kernels as

$$\kappa_0(t,s) = \sum_{\alpha,\sigma,p,\nu,\nu',n} \frac{\nu\nu'|t_\alpha|^2 p^n}{i\hbar} \hat{d}^{\bar{p},\nu}_\sigma \Upsilon^{\nu'}_{\alpha,n}(p\mu_\alpha(0) - i\hbar\mathcal{L}_{QD}, t-s)\hat{d}^{p,\nu'}_\sigma e^{in\omega_{AC}s}\,, \tag{4.18}$$

$$\begin{aligned}\kappa_{pu_\alpha}(t,s) = &\sum_{\sigma,\nu,\nu',n} \frac{\nu\nu'|t_\alpha|^2 p^{n+1}}{i\hbar}\sigma e^{-ip\phi'_\alpha} \\ &\times \hat{d}^{\bar{p},\nu}_\sigma Z^{\nu'}_{\alpha,n}(p\mu_\alpha(0) - i\hbar\mathcal{L}_{QD}, t-s)\hat{d}^{\bar{p},\nu'}_{\bar{\sigma}} e^{in\omega_{AC}s} e^{ip\omega_{DC,\alpha}s}\,,\end{aligned} \tag{4.19}$$

with the associated integrals

$$\begin{aligned}\Upsilon^q_{\alpha,n}(\xi,\tau) =& \frac{(-1)^n}{i\hbar} J_n\left[a_\alpha \epsilon_{AC}\sin\left(\frac{\omega_{AC}}{2}\tau\right)\right] \\ &\times \int_{-\infty}^{\infty} dE\, D_\alpha(E) f^q(E) e^{i\frac{E+\xi+(n\hbar\omega_{AC}/2)}{\hbar}\tau}\,,\end{aligned} \tag{4.20}$$

$$\begin{aligned}Z^q_{\alpha,n}(\xi,\tau) =& \frac{(i)^n}{i\hbar} J_n\left[a_\alpha \epsilon_{AC}\cos\left(\frac{\omega_{AC}}{2}\tau\right)\right] \\ &\times \int_{-\infty}^{\infty} dE\, A_\alpha(E) f^q(E) e^{i\frac{E+\xi+(n\hbar\omega_{AC}/2)}{\hbar}\tau}\,.\end{aligned} \tag{4.21}$$

In Laplace space, one can eliminate ξ, combining the energies λ and ξ as

$$\int_0^\infty d\tau\, e^{-\lambda\tau}\Upsilon^q_{\alpha,n}(\xi,\tau) = \tilde{\Upsilon}^q_{\alpha,n}(\lambda - i\xi/\hbar)\,, \tag{4.22}$$

$$\tilde{\Upsilon}^q_{l,n}(\lambda) := \int_0^\infty d\tau\, e^{-\lambda\tau}\Upsilon^q_{\alpha,n}(0,\tau)\,, \tag{4.23}$$

with analogous definitions for $\widetilde{Z}$. In the absence of AC driving, one can evaluate the resulting normal and anomalous sequential tunneling integrals using complex analysis, thereby obtaining exact analytic formulas for them [40, 70, 71]. The integrals for simultaneous AC and DC driving can be related to these analytic results via expansions of the Bessel functions for finite ϵ_{AC} [40]. With this, one can write [40, 71][2]

$$\widetilde{k}_{n,0}(\lambda) = \sum_{\alpha,\sigma,p,\nu,\nu'} \frac{p^n}{i\hbar}|t_\alpha|^2\nu\nu'\hat{d}^{\bar{p},\nu}_\sigma \widetilde{\Upsilon}^{\nu'}_{\alpha,n}(\lambda - \mathcal{L}_{QD} - ip\mu_\alpha(0)/\hbar)\hat{d}^{p,\nu'}_\sigma\,, \tag{4.24}$$

and

$$\begin{aligned}\widetilde{k}_{n,pu_\alpha}(\lambda) = &\sum_{\sigma,\nu,\nu'} \frac{p^{n+1}}{i\hbar}|t_\alpha|^2\sigma\nu\nu' e^{-ip(\phi_\alpha + a_\alpha\frac{\epsilon_{AC}}{2})} \\ &\hat{d}^{\bar{p},\nu}_\sigma \widetilde{Z}^{\nu'}_{\alpha,n}(\lambda - \mathcal{L}_{QD} + ip\mu_\alpha(0)/2)\hat{d}^{\bar{p},\nu'}_{\bar{\sigma}}\,.\end{aligned} \tag{4.25}$$

2 There is a difference in notation between the results here and as published in Siegl, Picó-Cortés, and Grifoni [40], wherein the sequential tunneling integrals are written here as functions of λ instead of $i\hbar\lambda$.

The current kernel can be obtained from the tunneling kernel by adding a factor $ep\delta_{\nu,+}\delta_{\alpha,L}$ under the sum.

Perturbation theory in the tunneling coupling requires the introduction of a (small) expansion parameter[3], which is here provided by the rate of tunneling of normal electrons in and out of lead α

$$\Gamma_\alpha = \frac{2\pi}{\hbar}|t_\alpha|^2 D_\alpha^0 \,. \tag{4.26}$$

An issue with the perturbative expansion in Γ_α[4] arises for superconducting leads, since near the coherence peaks the density of states increases by a factor $|\Delta_\alpha|/2\gamma$, thereby potentially invalidating the requirement of a small perturbative parameter. The weak coupling limit is justified provided that $\hbar\Gamma_\alpha|\Delta_\alpha|/2\gamma$ remains the smallest energy scale in the system for all α. As will become clear in the following, the issue with perturbative expansions to any particular order in Γ_α around energetic resonances persists throughout the problem. See, e.g., the thesis by Picó-Cortés [71] or the reference [42] for a further discussion.

4.2 TRANSPORT IN THE PRESENCE OF DC DRIVE

One should first discuss briefly the expected signatures in the simpler DC-driven case, as they will to a significant degree persist into the regime of simultaneous AC and DC driving. The single-impurity Hubbard model is often used to model quantum dots for which the charging energy, here modelled by a Hubbard U, is non-negligible and potentially reaches tens of meV [169]. As such, the realistic scenario considered here is that for tunneling through small quantum dots or molecules, the charging energy U exceeds the modulus $|\Delta|$ of the s-wave gaps in the leads, which are typically not larger than a few meV, by at least an order of magnitude. The limit of very large $|\Delta|$ has been studied before [123, 143, 170–172]. Further works covered the opposite limit of very large interactions U, such that all double occupancy of the dot can be neglected, thereby enabling a treatment of Andreev bound states in the junction by infinite-order resummation techniques [134, 173, 174]. Such Andreev bound states contribute subgap features [175–177] and are of theoretical interest both due to the information they carry about the junction's current characteristics [178] and due to their potential applicability for the engineering of an Andreev-spin qubit [179, 180]. Strong interaction also modifies the supercurrent through interacting Josephson junctions by inducing a 0-π transition [181–183]

While the assumption of weak coupling $\hbar\Gamma_\alpha \ll \Delta, k_B T, U, \cdots$ allows for the perturbative expansion of the kernel in this parameter, some effects like the supercurrent

3 Strictly speaking, this expansion parameter should be dimensionless. The rate Γ_α is dimensionful and one should rather understand the expansion here in terms of Γ_α/Ω with $\hbar\Omega = \min(\beta, U, \dots)$ the smallest energy scale of the problem other than $\hbar\Gamma_\alpha$.

4 If multiple leads are involved, $\mathcal{O}(\Gamma)$ is to be understood as the expansion in $\max_\alpha \Gamma_\alpha$.

arise only at the non-leading order in this perturbative expansion [184]. The next-to-leading order calculation within the framework presented here can be found in the work by Picó-Cortés et al. [42]. Other effects arising at stronger coupling strengths include quasiparticle poisoning [185, 186] and branch imbalance effects [187, 188], both of which assume the injection or removal of quasiparticles into or out of a lead, respectively, to have a noticeable effect on the local equilibrium configuration of the lead's interface with the junction. Such effects are incompatible with the assumption of macroscopic leads which are large enough not to be affected by exactly these types of effects. Furthermore, the impact of excess charges is proportional to the rate of injection of out-of-equilibrium charge carriers. As such, one can safely neglect them in the weak-coupling limit.

To the lowest order in the tunneling rate Γ_α, correlations involving Cooper pairs from both leads simultaneousyly can be neglected[5]. Their shaped density of states allows for an enhanced energetic resolution in transport spectroscopy with superconducting leads [155, 156, 189], subgap features due to thermally excited quasiparticles [105, 106, 127, 190], and results in a gap in the current characteristics of this quasiparticle current, if all available levels of the dot align with the gap in the density of states of either the source or the drain. This non-monotonic current characteristic due to the non-monotonic density of states in superconductors allows for a sign reversal in the conductance [191].

The first step in the Nakajima-Zwanzig formalism is the determination of the reduced density operator. By formally inverting Eq. (2.38), one can express the steady-state form of $\hat{\rho}_{0,\mathbf{m}}$ as

$$\hat{\rho}_{0,\mathbf{m}} = \frac{1}{i\mathbf{m}\cdot\boldsymbol{\omega}_{\mathrm{DC}} - \mathcal{L}_{\mathrm{QD}} - \widetilde{\kappa}_{0,0}(i\mathbf{m}\cdot\boldsymbol{\omega}_{\mathrm{DC}})} \sum_{p,\alpha} \widetilde{\kappa}_{0,\bar{p}u_\alpha}(i\mathbf{m}\cdot\boldsymbol{\omega}_{\mathrm{DC}})\hat{\rho}_{0,\mathbf{m}+pu_\alpha}\,. \tag{4.27}$$

Here, each component $\hat{\rho}_{0,\mathbf{m}}$ of the steady-state density operator is expressed as a pumping term (the sum over different $\hat{\rho}_{0,\mathbf{m}'}$), followed by the action of precession (imaginary part of the denominator) and damping (real part of the denominator). Of note is the fact that the precession, which is linked with differences in energy between levels, is not just due to the action of the Liouvillian, but also contains the Josephson frequencies $i\mathbf{m}\cdot\boldsymbol{\omega}_{\mathrm{DC}}$ and a "Lamb-shift" due to $\mathfrak{Im}\{\widetilde{\kappa}_{0,0}(i\mathbf{m}\cdot\boldsymbol{\omega}_{\mathrm{DC}})\}$ accounting for shifts in energy levels due to coupling to the environment.

The "resonances" mentioned above correspond to the vanishing of the precession term up to order Γ_α, i.e., the condition $|\mathbf{m}\cdot\boldsymbol{\omega}_{\mathrm{DC}} - \omega_{\chi,\chi'}| \leqslant \Gamma_\alpha$ where $\omega_{\chi,\chi'}$ is the frequency associated with the action of the Liouvillian on a Liouville state (element of the density operator) as $\mathcal{L}_{\mathrm{QD}}|\chi\rangle\langle\chi'| = -i\omega_{\chi,\chi'}|\chi\rangle\langle\chi'|$. It is clear that populations ($\chi = \chi'$ and $\mathbf{m} = 0$) always correspond to "trivial" resonances in this sense, such that in the followinag, populations are excluded whenever resonances are mentioned. A second type of resonance is provided by the enhancement of

5 Along certain resonances, the Cooper pairs can contribute already to the lowest order.

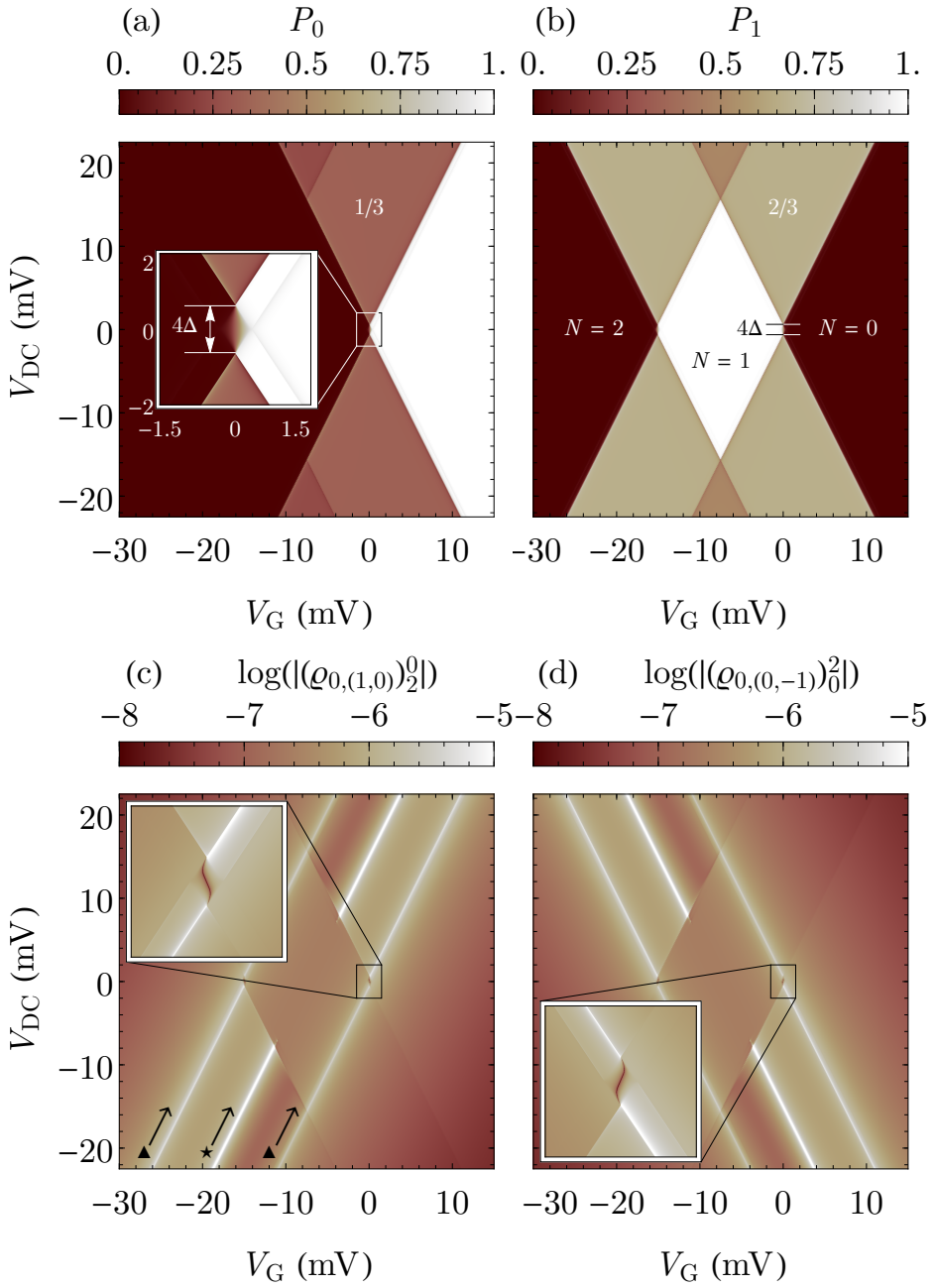

Figure 4.1: **Population of the unoccupied (a), singly occupied states (b), and modulus of the proximitized superconducting coherences on the dot for different leads (c and d) as a function of applied DC bias voltage and gate voltage.** The calculations were performed using $a_L = -a_R = 0.5$, $U = 15\,\text{meV}$, $\beta_\alpha = \beta = (k_B 1.2\,\text{K})^{-1}$, $|\Delta| = 0.32\,\text{meV}$, $\gamma = 100\,\text{neV}$ and $\hbar\Gamma_\alpha = 93\,\text{neV}$. Adapted from Siegl, Picó-Cortés, and Grifoni [40].

the pumping term due to the peaks in the density of states. Starting with the secular case where no resonances are present [192], the form of Eq. (4.27) allows for a perturbative expansion of the density operators in terms of Γ_α. The highest level in this hierarchy contains the populations, which are of order $\mathcal{O}(\Gamma^0)$ and can thus remain finite even at vanishing tunneling coupling.

Fig. 4.1 shows the populations of the unoccupied P_0 and singly occupied P_1 state for a symmetric and spin-degenerate single-impurity Anderson model in a stability diagram as a function of the DC voltage bias and the gate voltage with lever arm $\alpha_G = 1$. The population of the double occupied state P_2 follows due to particle-hole symmetry by inverting the axis of V_G around $V_G = -U/2$ for the panel of P_0. As expected for the case of strong interactions U, the stability diagram shows clear signatures of Coulomb blockade [12, 193], wherein the charge on the dot is fixed by the energetic cost of a change in occupancy, thereby inhibiting transport through sequential tunneling. The region of Coulomb blockade is dubbed the Coulomb diamond and is shown in Fig. 4.1 b as the central region in white. The exponential suppression of transport with U/k_BT inside the Coulomb blockade region results in the dominant contribution to transport originating from higher-order processes in the tunneling coupling, which include virtual changes of the dots population that evade the exponential suppression [73]. The behavior inside the Coulomb blockade region becomes even more subtle below the so-called Kondo temperature, where a non-perturbative rearrangement of the state of the leads on either side of the junction results in the reemmergence of zero-bias conductivity via the formation of a correlated singlet state across the junction [12]. However, already in the simpler case investigated here, there are some non-standard features visible which are shown in the inset of Fig. 4.1 a. There, the presence of a small gap results in a broadening of the transition between populations at the charge-degeneracy point $V_G = V_{DC} = 0\,\mathrm{mV}$. Furthermore, thermally activated populations of the singly occupied state are faintly visible as darker stripes running parallel to the edge between the plateaus labelled 1/3 and the continuous region of population $P_0 \approx 1$ at gate voltages $V_G > |V_{DC}|/2$.

The next lowest level contains the coherences associated with $\mathbf{m} = p\mathbf{u}_\alpha$, which, due to the particle number constraint in Eq. (3.32), are always of the form $|0\rangle\langle 2|$ for $p = +$ and $|2\rangle\langle 0|$ for $p = -$, respectively. Previous works interpreted these coherences as superconducting correlations on the dot due to the proximity effect and investigated them; however, so far only along high-symmetry lines or in either the infinite U or infinite $|\Delta|$ limit [128, 129, 133, 137, 139, 140, 183]. The general nature of the formalism employed here enables the calculation of these coherences for arbitrary finite and even asymmetric values of these parameters. Complex conjugation relates the coherences that only differ in p; however, no such relation between the coherences with different α exists. Therefore, the results obtained here generalize previous results that combined these two, in principle distinct, coherences into a single object [137, 139] which is only valid for symmetric coupling and at $V_{DC} = 0\,\mathrm{mV}$. Fig. 4.1 c and d show the logarithms of the moduli of the two independent coherences. The coherences differ at finite bias voltage but are, in the symmetric coupling case considered here, related by the symmetry $V_{DC} \to -V_{DC}$ that effectively exchanges the leads. In line with expectations, the coherences are suppressed exponentially inside the Coulomb diamond. The precession resonance condition, which is non-trivial for these coherences, is clearly visible as the central diagonal feature outside of the

Coulomb diamond, indicated by a star in panel c. The two additional features indicated by the triangles in panel c correspond to the resonant pumping due to the coherence peaks in the density of states of the leads.

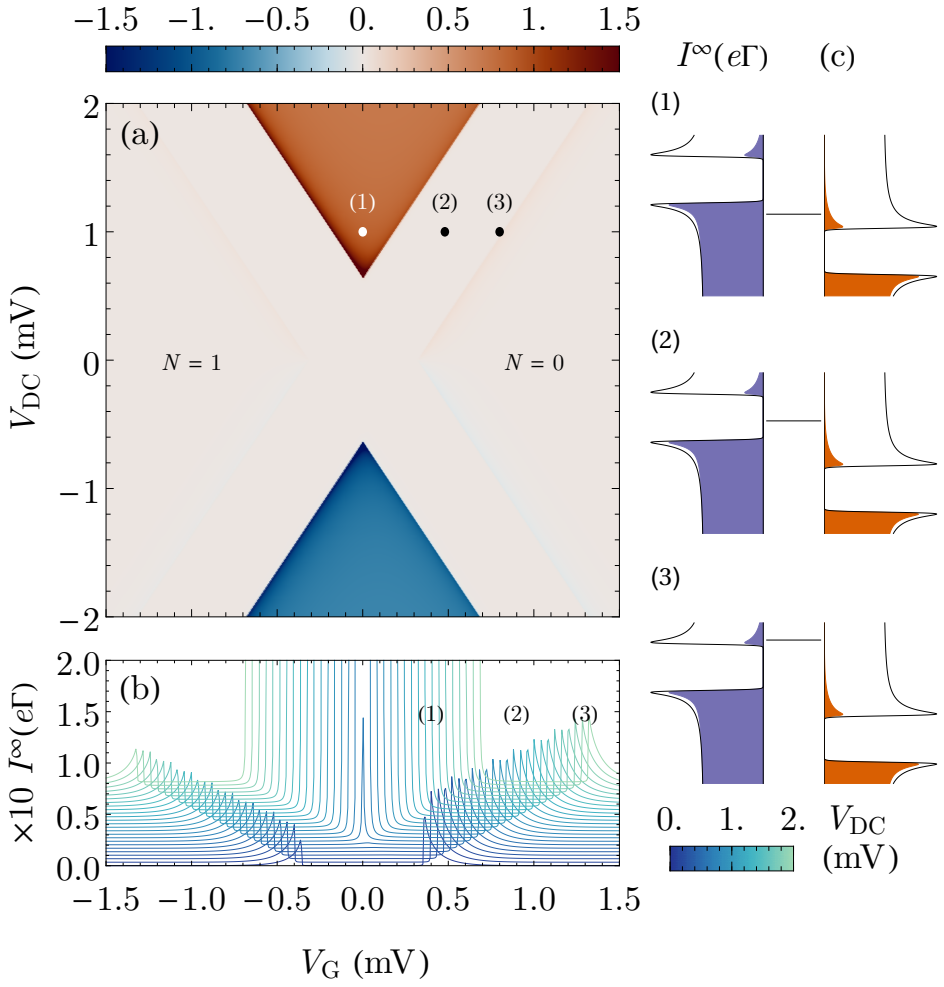

Figure 4.2: **DC current $I_{0,0}$ in the vicinity of the charge degeneracy point between singly occupied (N=1) and unoccupied (N=0) states of the dot.** The axes cover the DC bias voltage V_{DC} and the gate voltage V_G. The superconducting gap in the leads results in the absence of transport at low bias voltages, apart from faint thermally excited subgap features. Adapted from Siegl, Picó-Cortés, and Grifoni [40].

Turning to the current, Fig. 4.2 a shows the DC current in the vicinity of the charge-degeneracy point between the unoccupied and singly occupied state. As expected from the semiconductor picture of superconductors [166], the stability diagram exhibits a low-bias gap in the current even at formal degeneracy between adjacent charge levels of the dot. The thermally excited subgap features are visible faintly in panel a, but are more clearly visible in the cascade plot of panel b. Panel c shows the alignment between the relevant dot level and the two leads for different positions in the stability diagram labelled as (1), (2), and (3). For position (1), the peaked densities of states in both leads align with the level, thereby yielding enhanced current as compared to the plateau region at higher

biases. In contrast, the alignment of at least one lead's gap with the level (2) results in a region of suppressed current bordering the plateau. Finally, the position (3) corresponds to a thermally activated feature, whereby the finite thermally excited population of quasiparticles above one lead's gap aligns with the level, thereby yielding a finite thermally activated current that is exponentially suppressed in $\beta_\alpha|\Delta_\alpha|$. The current to sequential tunneling order is a function of the populations P_χ on the dot and the rates $\Gamma_\alpha^{\chi,\chi'}$ of population change due to the presence of lead α connecting different populations as

$$I = -e\left\{ \sum_\sigma \left[\Gamma_L^{\sigma,0} P_0 + (\Gamma_L^{2,\sigma} - \Gamma_L^{0,\sigma}) P_\sigma - \Gamma_L^{\sigma,2} P_2 \right] + 2\Gamma_L^{2,0} P_0 - 2\Gamma_L^{0,2} P_2 \right\}. \quad (4.28)$$

The impact of the coherences, to lowest non-trivial order in the tunneling coupling, is captured by truncating Eq. (4.27) as

$$(\hat{\rho}_{0,(1,0)})_2^0 = -\frac{1}{(\kappa_{0,0}(i\omega_{DC,L})_{2,2}^{0,0}} \sum_\chi (\kappa_{0,u_L}(i\omega_{DC,L}))_{2,\chi}^{0,\chi} P_\chi \,, \quad (4.29)$$

with the elements of the respective kernels defined as

$$(\kappa)_{a',b'}^{a,b} = \langle a| \left(\kappa \left|a'\right\rangle\!\left\langle b'\right|\right) |b\rangle \,. \quad (4.30)$$

The effective rates $\Gamma_\alpha^{\chi,\chi'}$ accounting for these steady-state coherences read

$$\begin{aligned} \Gamma_\alpha^{\chi,\chi'} =& (\kappa_{0,0}(0)|_{\text{only }\alpha})_{\chi,\chi'}^{\chi,\chi'} \\ & -2\mathrm{Re}\left[\frac{i\hbar(\widetilde{\kappa}_{0,u_\alpha}(0))_{\chi,0}^{\chi,2} (\widetilde{\kappa}_{0,-u_\alpha}(-i\omega_\alpha))_{0,\chi'}^{2,\chi'}}{2eV_G + U - \hbar\omega_\alpha + i\hbar(\widetilde{\kappa}_{0,0}(-i\omega_\alpha))_{0,0}^{2,2}} \right] . \end{aligned} \quad (4.31)$$

The second term on the right-hand side of Eq. (4.31) accounts for the impact of superconducting correlations on both the steady-state current and the populations of the dot by a renormalization of the rates [133]. As such, the proximity-induced superconducting correlations might be weak in this case, but they contribute to measurable observables. Of note here is the fact that due to the suppression of the steady-state coherences in the secular case by at least an order of Γ_α, the change in the current induced by them is already of order Γ_α^2 despite the treatment of both the propagation and the current kernel to lowest order in Γ_α. This mixing of different orders in the perturbative expansion is a persistent feature of the Nakajima-Zwanzig formalism. It inevitably follows from the step-wise solution involving two consecutive perturbative expansions of first the propagation kernel and then the kernel for the observable of interest. To get a consistent picture, including all contributions of order Γ_α^2, one can therefore extend the treatment here by going to the cotunneling (next-to-leading) order treatment of the DC-driven problem [42].

The simultaneous presence of both AC and DC driving results, via the AC Josephson effect, in bichromatic dynamics of a superconducting junction. When these intrinsic frequencies of the problem become commensurate, the current voltage characteristics of the junction become modulated with replicas of the DC Josephson effect, i.e., finite ranges of different imposed DC currents result in the same measured DC bias. These features, called Shapiro steps [124, 194, 195], carry information on the underlying current-phase relationship of the junction, like, e.g., the vanishing of odd-steps for $4-\pi$ periodicity in junctions containing Majorana bound states [196–201] or subharmonic Shapiro steps indicating the presence of multiple-Andreev reflections [202, 203]. The semiclassical description of these dynamics relies on the motion of a quantum mechanical phase-variable following classical equations of motions[199, 204–206] in order to describe, e.g., topological superconductivity in a Josephson junctions is yet available [207–209] However, for increasingly minituarized systems the charging energy stops being negligible, motivating the study of interacting driven Josephson junctions.

The theory presented here serves as a first step in a microscopic treatment of this problem. It should, if combined with the derivation of the supercurrent within the same formalism [42], enable the treatment of more complicated junctions and strong interactions. Since the Nakajima-Zwanzig formalism allows for a simple inclusion of thermal transport, the quasiparticle transport discussed here also promises to be useful for the study of thermal heating during manipulation of Andreev-spin qubits using AC fields [210]. Further applications include AC-driven superconductor-to-superconductor scanning tunneling spectroscopy [211–213] and the potential for Floquet engineering of Josephson junctions [214, 215]. The benchmark of the results obtained here is the phenomenological Tien-Gordon theory for photo(n)-assisted-tunneling [112, 113, 216–218], which has been applied to quasiparticle transport in the AC-DC-driven S-QD-S junctions [141]. However, a significant drawback of this phenomenological theory is its breakdown for bichromatic driving [219, 220]. In the sequential tunneling regime, where the bichromatic nature of the junction's dynamics only affects the coherences, the dynamics should, to a large degree, follow the existing phenomenological theory. Already, this theory predicts rich behavior like current inversion [217, 218, 221].

A natural starting point for the discussion of the transport is the question of how the presence of the AC driving modifies the results obtained in Section 4.2. The condition for the secular approximation is modified in the presence of AC driving as

$$|\mathfrak{m}\cdot\boldsymbol{\omega}_{\mathrm{DC}}+n\omega_{\mathrm{AC}}+\omega_{\chi\chi'}|\gtrsim\Gamma_{\alpha}\,. \tag{4.32}$$

According to the result of Section 4.2, the effect of including finite $\mathfrak{m}\neq 0$ in the solution of the density matrix reduces for weak coupling to a small renormalization of the rates. The following discussion omits this minor correction

when discussing the results, although the underlying numerics include it. Writing the formal solution for the remaining Fourier expansion elements of the density operator yields

$$\hat{\rho}_{n,0} = \frac{1}{in\omega_{AC} - \widetilde{\kappa}_{T,0,0}(in\omega_{AC})} \sum_{n'} \widetilde{\kappa}_{n',0}(in\omega_{AC}) \hat{\rho}_{n-n',m} \,. \tag{4.33}$$

Compared to Eq. (4.27), the hierarchy of Eq. (4.33) in terms of the powers of Γ_α is flat. More precisely, the sequential tunneling kernel $\widetilde{\kappa}_{n,0}$ contains all $n \in \mathbb{Z}$ due to the Jacobi-Anger expansion in Eq. (4.18). The decay with large n of the Bessel functions of the first kind $J_n(x)$ for fixed x enables a truncation, thereby again endowing the numerical problem with the structure of a banded matrix with finite width. However, the width of this structure, and therefore the numerical difficulty of solving the resulting problem by truncating to a finite region around $n = 0$, depends on the strength of the driving and the driving frequency ω_{AC}. The weak coupling alone is not sufficient to limit the dimensionality of the resulting problem.

Faced with such a general dependence on multiple parameters, it is helpful to investigate first some limiting cases. The trivial case for the AC drive is the adiabatic limit. There, the frequency of the drive is slow compared to the duration of the transient behavior of the system under a change in the parameters used for the DC calculation above. As such, one can neglect transient behavior, approximate the system to be in its steady state for the equivalent DC case with constant parameters, and accordingly approximate the time-dependent current as

$$I(t)|_{\text{adiabatic}} = I_{DC}(V_{DC,\text{eff}}(t)) \,, \tag{4.34}$$

$$V_{DC,\text{eff}}(t) = V_{DC} + V_{AC} \sin(\omega_{AC} t) \,. \tag{4.35}$$

The opposite limit of high-frequency driving is equivalent to the boson-assisted transport through the model [222]. There, one recovers the Tien-Gordon theory of photo-assisted tunneling [216], where the densities of occupied[6] states $D^*_\alpha(E)$, and therefore also the rates between populations [141], are replaced as

$$D(E)_{\alpha,\text{Tien-Gordon}} = \sum_{n=-\infty}^{\infty} J_n^2 \left(\frac{a_\alpha \epsilon_{AC}}{2} \right) D_\alpha(E + n\hbar\omega_{AC}) \,. \tag{4.36}$$

Fig. 4.3 a depicts the photo-assisted DC current in the same region of the stability diagram as Fig. 4.2 for finite AC driving with $\hbar\omega_{AC} = 0.5\,\text{meV}$. One can interpret the resulting more elaborate stability diagram as a consequence of the Tien-Gordon-like replacement of the tunneling rates according to Eq. (4.36). Fig. 4.3 b illustrates the level alignment between the leads and the dot levels for select points in the stability diagram. The full line illustrates the relevant dot level in

6 The product of the density of states with the relevant distribution of occupied states.

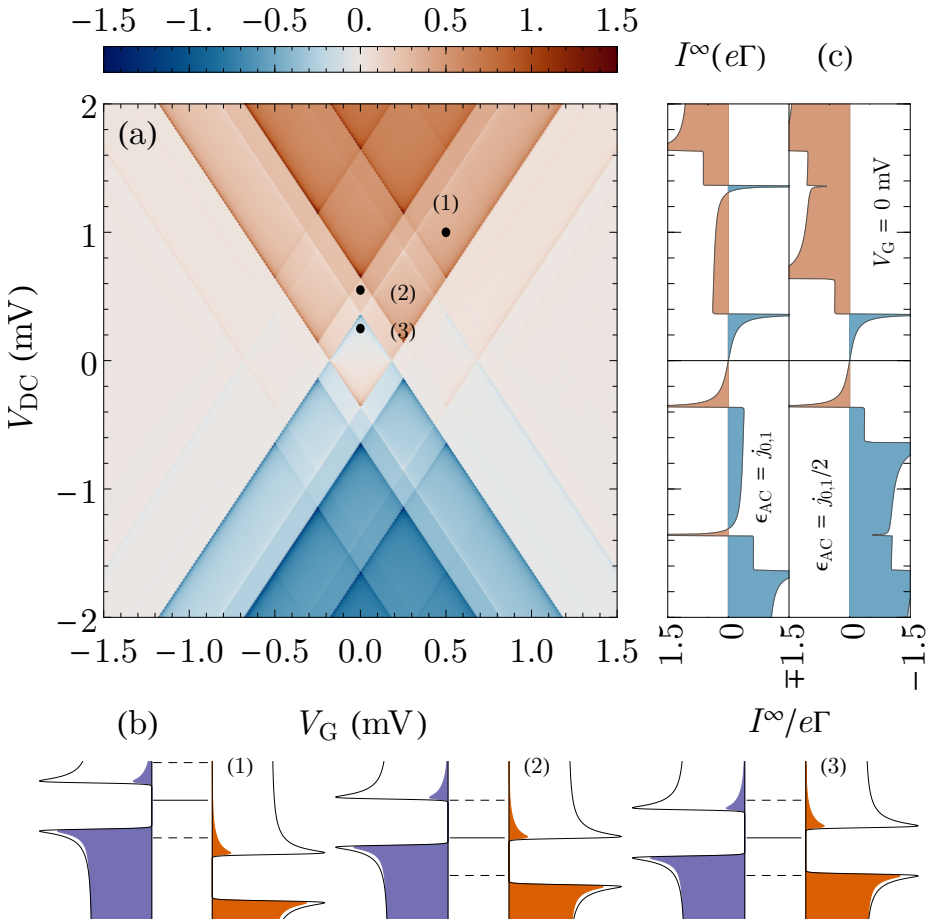

Figure 4.3: **DC current near the 1-0 charge degeneracy point (a) in the presence of AC driving, level alignment between the dot and the leads (b), and cuts along the bias direction at $V_G = 0$ mV for different ϵ_{AC} (c).** The driving frequency is $\omega_{AC} = 0.5\,\mathrm{mV}/\hbar$, $n \in [-30 : 30]$, $\mathbf{m} \in 0, \pm\mathbf{u}_\alpha$ and the driving strength is $\epsilon_{AC} = 2j_{0,1}$, where $j_{m,n}$ is the $n-$th zero of the m-th Bessel function of the first kind. All remaining parameters are the same as in Fig. 4.2. Adapted from Siegl, Picó-Cortés, and Grifoni [40].

the absence of AC driving, while the dashed lines are the replicas of the dot level due to absorption/emission of one photon of energy $\hbar\omega_{AC}$. The transport at (1) and (2) is dominated by transport through such a replica level, while the situation at (3) is more subtle. There, no charge can leave or enter the dot without the photo-assisted processes, due to the alignment of the dot level with the gaps in either lead. However, the replica levels align with both leads. It aligns with the peaked density of states in the drain for the process of pumping charge into the dot, while the process of emptying the dot aligns with the source. While charge flows into and out of the dot from both leads, this resonant alignment of the replica levels favors the flow of charge from the nominal drain into the dot and from there into the source, yielding current inversion [223]. This phenomenon is, of course, only possible in the presence of an additional source of energy, here provided by the photo-assisted pumping of charge against the direction of the

applied DC bias. Fig. 4.3 c shows a cut along the bias direction for gate voltage $V_G = 0\,\mathrm{mV}$. One can identify replicas of the coherence peaks at the boundaries of the plateau regions. These replicas are the most visible regions of inversion of the DC current.

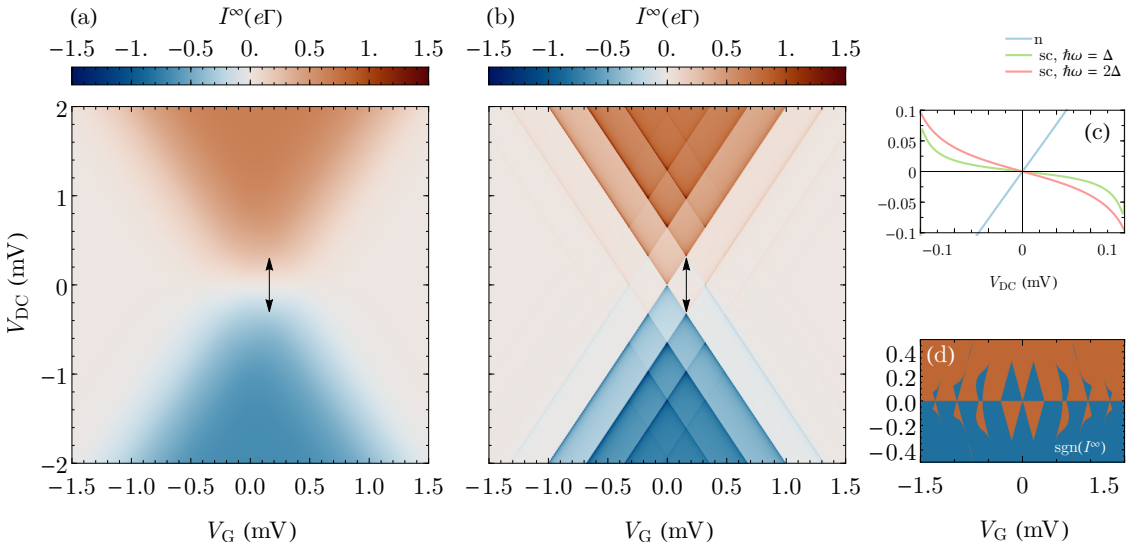

Figure 4.4: **Photo-assisted steady-state DC current** I^∞. Shown is the vicinity of the 1-0 charge dengeneracy point for the normal conducting case (a), the resonant driving case $\hbar\omega_{AC} = |\Delta|$ (b), traces along V_{DC} at $V_G = 0.15\,\mathrm{mV}$, as illustrated by the arrows in panels (a) and (b) for different cases (c), and the sign of the DC current in panel (b) at low bias voltages (d). Adapted from Siegl, Picó-Cortés, and Grifoni [40].

The occurrence of current inversion relies only on the non-monotonic nature of the density of states of the superconducting leads. Fig. 4.4 a shows the same PAT stability diagram for normal conducting leads, where no current inversion is present. Fig. 4.4 b depicts the case of resonant driving $\hbar\omega_{AC} = |\Delta|$, where the resulting stability diagram simplifies considerably. However, even without the current inversion due to the replicas of the coherence peaks as in Fig. 4.3, there still occurs current inversion for low bias, as is illustrated in Fig. 4.4 c and d.

Fig. 4.5 a shows the conductivity as a function of the applied AC and DC voltages. One can observe a fan-like pattern caused by the Bessel functions emanating from the edges of the gap, in line with previous experimental observations in AC-driven superconductor-to-superconductor STS [212]. Fig. 4.5 b shows cuts along V_{DC} for different strengths of the AC driving. Panel c of the same figure illustrates the agreement of the conductivity with the Bessel functions of the first kind, thereby confirming the good applicability of the Tien-Gordon theory for this problem [216].

The results presented here are mostly well described by the Tien-Gordon theory [216] applied to the tunneling through a quantum dot [141]. However, despite similarities one expects between the sequential tunneling regime order and the

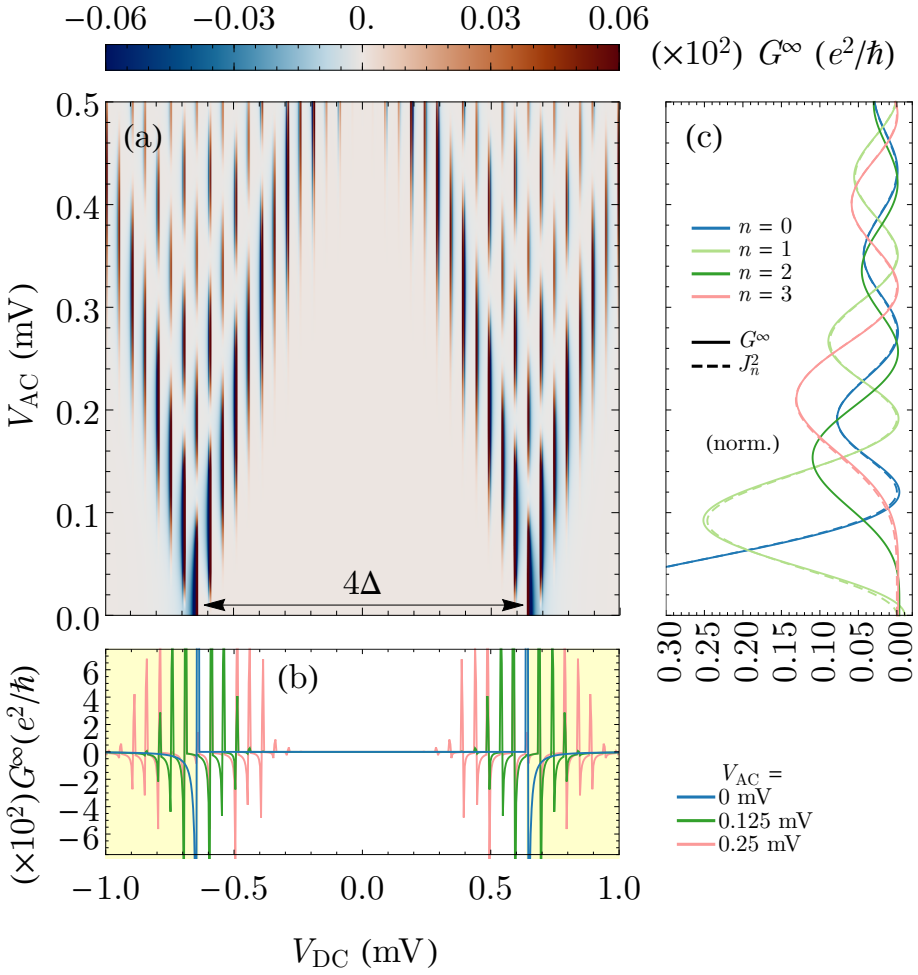

Figure 4.5: **Conductivity as a function of both the applied DC (V_{DC}) and AC (V_{AC}) voltage biases.** The conductance displays sharp features at the boundary of the gap due to the coherence peaks in the density of states. These peaks in the conductance fan out for stronger driving by the creation of replicas. Adapted from Siegl, Picó-Cortés, and Grifoni [40]

.

phenomenological approach, some subtle differences remain even in the respective limits covered in the phenomenological approach. For example, the creation of replicas in the density of states as described by the Tien-Gordon theory occurs for the microscopic theory in the sequential tunneling integrals themselves. While the imaginary part of these integrals corresponds, via contour integration, to a Fermi-Dirac distribution multiplying the respective normal or anomalous density of states, their real part acts as a Lamb shift of the dot's levels due to the coupling to the leads [108]. Since both these terms occur in Eq. (4.33), a simple replacement of the former as in the phenomenological Tien-Gordon theory fails to account for the modification of the latter. Beyond these subtle differences between the microscopic derivation and the existing phenomenological theory, the knowledge of the equations for the general case at intermediate frequencies or in transient

regimes promises, by numerical solution of the respective equations of motion, a description of experiments outside of such known limiting cases.

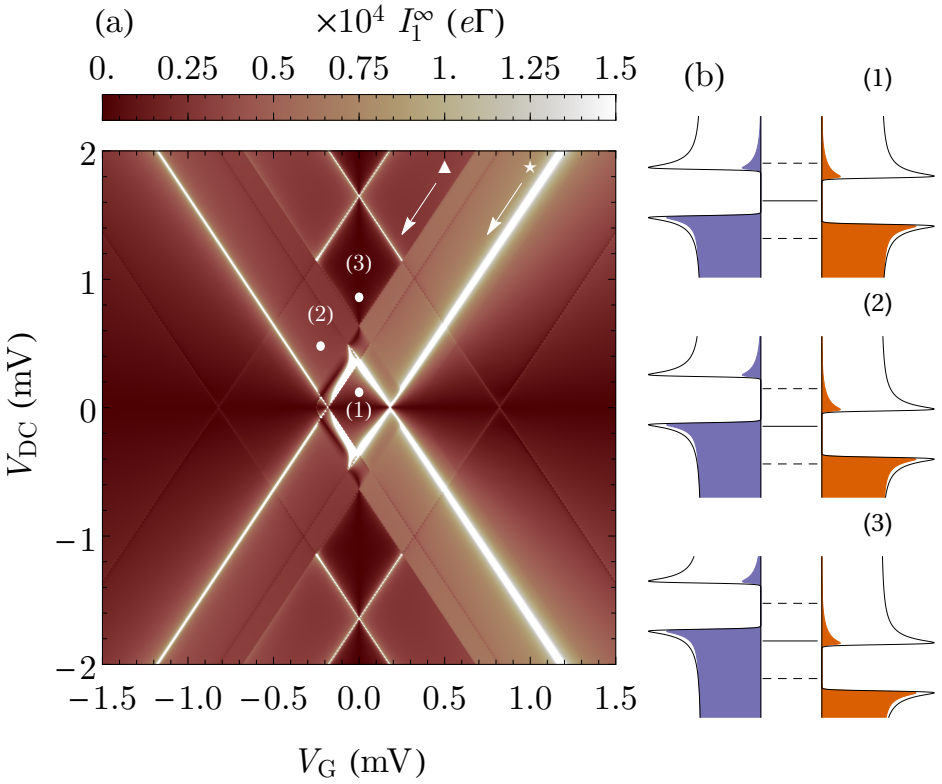

Figure 4.6: **First harmonic of the steady-state current in the driving frequency ω_{AC} (a) and level alignment for selected points in the stability diagram (b).** The weak-driving limit was used by setting $\epsilon_{AC} = 0.1$ with the remaining parameters the same as in Fig. 4.3. Adapted from Siegl, Picó-Cortés, and Grifoni [40].

In principle, the formalism used here also covers other observables like the dynamic response of the current at the frequency of the AC drive, described by the first harmonic of the steady-state current I_1^∞. This harmonic relates to the nonlinear dynamic susceptibility $\chi(\omega_{AC}, \epsilon_{AC})$ of the junction via the condition $I_1^\infty = \epsilon_{AC}\chi(\omega_{AC}, \epsilon_{AC})$. To eliminate displacement currents from the result, one can employ the symmetrized form of the current operator $\hat{I} = \frac{1}{2}(\hat{I}_L - \hat{I}_R)$ as is used for the remainder of this chapter. Since the higher Fourier components of the density operator $\hat{\rho}_{n\neq 0,m}$ are all at least of order Γ_α^2, the lowest order contribution to the first harmonic is

$$I_1^\infty = \frac{1}{2}(\tilde{\kappa}_{I_L,1,0}(i\omega_{AC}) - \tilde{\kappa}_{I_R,1,0}(i\omega_{AC}))\hat{\rho}_{0,0}\,. \tag{4.37}$$

Fig. 4.6 a depicts the modulus of the first harmonic of the symmetrized current. The resulting stability diagram displays sharp features stemming from replicas of the DC Coulomb resonance (▲) at

$$\pm V_{DC} = 2|V_G| - 2V_0\,, \tag{4.38}$$

with $V_0 = \hbar\omega - \Delta$ (★), and

$$\pm V_{DC} = 2|V_G| + 4\hbar\omega_{AC} - 2V_0 \,. \tag{4.39}$$

Fig. 4.6 b again illustrates the level alignment for select points in the stability diagram. One can interpret these level alignments via an expansion of the respective sequential tunneling integral in orders of ϵ_{AC} as

$$\widetilde{\gamma}^{q}_{\alpha,1}(\xi) \propto a_\alpha \epsilon_{AC} \left(\widetilde{\gamma}^{q}_{\alpha,DC}(\xi + \hbar\omega_{AC}) - \widetilde{\gamma}^{q}_{\alpha,DC}(\xi) \right) + \mathcal{O}(\epsilon^2_{AC}) \,. \tag{4.40}$$

As a consequence of this expansion, the AC response to the lowest order in Γ_α and ϵ_{AC} is driven by the difference in the DC tunneling rates connecting a lead to either the dot's relevant energy level or its replicas offset by $\pm\hbar\omega_{AC}$.

The results shown in this chapter illustrate the versatility of the theoretical approach for transport through interacting junctions with superconducting leads developed here. Experiments in the realm of quantum transport have recently outpaced the existing theory [42] and are increasingly pushing the boundaries of the validity of existing phenomenological models [224]. As such, the need for a viable microscopic approach for the more exact modelling of such experiments is clear. The presentation of the Nakajima-Zwanzig formalism for AC-DC-driven transport through interacting superconducting junctions in this thesis made multiple simplifying assumptions along the way. They offer obvious avenues for the further refinement of the theory, like the inclusion of higher orders in the tunneling coupling [42], the calculation of transient behavior [225, 226], the inclusion of non-trivial dynamics in the phase of the junction, and the extension to topological superconductors [196].

Part II

MANY-BODY LOCALIZATION IN EXCHANGE-DISORDERED HEISENBERG CHAINS

This part of the thesis covers an investigation into the fate of many-body localization in exchange-disordered Heisenberg chains, as published in the New Journal of Physics [227]. There are two chapters in this part. Chapter 5 provides a brief introduction to the phenomenon of many-body localization which has recently gathered much attention not only due to its theoretical implications for the assumptions regarding the applicability of equilibrium statistical mechanics [81], but also its experimental realization [228–238] which promises potential future functionality by stabilizing non-equilibrium quantum phases [81] thereby potentially finding application, e.g., in quantum computation [239]. Chapter 6 presents novel results on the possibility of an incomplete transition to a many-body localized phase in the presence of a global non-abelian symmetry. Evidence for the possible existence of a distinct, non-many-body-localized phase, as has been predicted in earlier works [81, 240–245], is presented for the exchange-disordered Heisenberg spin chain. After discussing the different results presented in Siegl and Schliemann [227], conclusions are drawn by accounting for more recent progress in the field. Finally, a brief outlook discusses approaches to remaining open questions.

5

INTRODUCTION TO MANY-BODY LOCALIZATION

This chapter follows the review of many-body localization by Abanin et al. [81]. Parts of this chapter further build on an earlier review by the same first author [246], a more recent review by Sierant et al. [247] and personal discussions with D. Abanin. This chapter covers no novel results as it serves as an introduction to the field and prepares the reader for the content of Chapter 6 by providing a comparison to the phenomenology discussed there while simultaneously introducing the methodology.

The starting point for this introduction is a brief account of localization and its relation to thermodynamics and insulating behavior. Here, a (nearly) ideal insulator is understood to be a system with sufficiently low conductivity both of charge and energy that, at the time-scales relevant to any experimental observation, an initial non-equilibrium configuration fails to thermalize. While an ideal insulator along these lines fails to reach equilibrium even in the asymptotic behavior for infinite system size and infinite evolution time, this definition is more flexible as it concerns experimentally observable behavior and allows for the consideration of a nearly ideal insulator, which will become relevant later. This distinction is equivalent to the differentiation by Sierant et al. between a many-body localized regime, which shows the hallmarks of a localized phase, as will be introduced below, on experimental time scales and an actual many-body localized phase, which realizes an ideal insulator in the above sense [247]. The nomenclature of this distinction remains in flux as, e.g., a distinction between "pre-MBL" and "proper MBL" is also used in the literature [248].

To understand how a system can fail to equilibrate, one should first consider the options by electrons can transport charge and energy throughout a system. To this end, it is helpful to classify the eigenstates of a quantum mechanical system as either localized or extended. Extended states connect different regions within the system and, in general, allow for the efficient transport of charge and energy, provided an imbalance exists across the system. The archetypical example of this type of conductivity is the free electron gas within the jellium model of simple metals [12]. However, localized electronic states can also allow for transport by hopping between sites, either by adjacent states interacting or by additional parts of the system, such as phonons, providing thermal activation [81]. For perfectly

periodic bulk systems, the non-interacting theory predicts extended eigenstates which take the form of Bloch waves [2, 249]. At finite temperatures, partially occupied bands exist either intrinsically in metals or by thermal activation for semiconductors. These allow for finite conductivities of both charge and energy transport in such fully periodic systems at finite temperatures.

In the simple Drude picture [12], disorder results in scattering, thereby slowing ballistic transport and yielding diffusive behavior. A violation of this predicted diffusive behavior in experiments motivated the pivotal work by Anderson, which demonstrated the possibility of localized wave functions of non-interacting electrons in disordered systems [250]. In dimensions lower than $d = 3$, all non-topological eigenstates of the non-interacting theory with uncorrelated [251] disorder are localized. In contrast, in three dimensions, the system can undergo a metal-insulator transition depending on the strength of the disorder. In the latter case, a mobility edge separates localized states at low energy from extended states at high energy [81, 252]. The exponential spatial decay away from their pinning center hinders the diffusive transport of charge between such localized wave functions, thereby yielding insulating behavior by localization. This phenomenon, where disorder induces insulating behavior in non-interacting electronic systems due to destructive interference of scattered wave functions, is known as Anderson localization [253–257].

If all states are localized, the Anderson insulator becomes an ideal insulator, and as such, it evades thermalization, as noted in the original work by Anderson [81, 250]. Many theoretical descriptions of physical systems start from the idealized assumption of an equilibrium configuration that was reached through thermalization in the distant past, enabling the application of the powerful toolbox of thermodynamics to describe the macroscopic behavior of complex systems. As such, the possible existence of an ideal insulator that violates core assumptions of statistical mechaniscs, like ergodicity, is of immediate interest to fundamental research. Beyond this interest, the possibility to evade thermalization for long time scales promises to have great utility for the pursuit of stabilizing non-equilibrium quantum phases [81].

As noted above, a system may fail to realize a nearly ideal insulator even if all its eigenstates are localized in the absence of interaction if the inclusion of interaction opens new transport channels either by enabling hopping transport between adjacent sites or by delocalizing some states in the spectrum [81]. The many-body localized phase is equivalent to an interacting system remaining an (nearly) ideal insulator even at finite temperatures [81]. Early works in this context demonstrated that even weak interactions lead to the delocalization of parts of the spectrum [258–262]. Follow-up works showed the possibility of a temperature-dependent delocalization via a "many-body mobility edge" [81, 263–266]. Finally, Oganesyan and Huse claimed that certain low-dimensional disordered quantum systems can remain fully localized even at infinite temperatures, thus lacking

any mobility edge and realizing a true temperature-independent many-body localized phase [267].

For their numerical investigations, Oganesyan and Huse relied on a one-dimensional chain of interacting spinless fermions in a closed quantum system. The benefit of investigating closed quantum systems is the conceptual ease with which one can access the many-body eigenstates. However, to connect such numerical investigations to the previous discussion about thermalization, it is important to define thermalization for closed quantum systems properly. In the literature, thermalization for closed quantum systems is commonly regarded as equivalent to the validity of the eigenstate thermalization hypothesis [268–272]. A more in-depth introduction to the eigenstate thermalization hypothesis and the ongoing research on its validity in various systems would be out of place here. A good introduction can be found in the reviews by Abanin et al. [81] and Sierant et al. [247]. More importantly, the eigenstate thermalization hypothesis, and thus in the above sense thermal behavior, implies that local perturbations of the Hamiltonian result in global changes of eigenstates [81, 273]. The middle of the resulting spectrum follows Random Matrix Theory, which predicts, depending on the symmetry class of the Hamiltonian, the presence of level-repulsion between adjacent eigenvalues. In Random Matrix Theory, universal probability distributions, which depend only on the symmetry class of the Hamiltonian, govern the statistics of the ratio between consecutive gaps in the spectrum. More precisely, the consecutive gap ratio r is defined [267, 274] as

$$r_n = \frac{\min\{s_n, s_{n-1}\}}{\max\{s_n, s_{n-1}\}}, \tag{5.1}$$

where $s_n = e_{n+1} - e_n$ is the gap between adjacent eigenenergies e_n in ascending order. For large system sizes and in sufficiently dense regions of the spectrum, which typically excludes extremal values of the spectrum, the consecutive gap ratio r can be considered a random variable in the interval $[0, 1]$ following a probability distribution $p(r)$. The different equivalency classes of random matrix theory are the Gaussian Orthogonal Ensemble (GOE), the Gaussian Unitary Ensemble (GUE), and the Gaussian Symplectic Ensemble (GSE). For the Heisenberg spin chains introduced in Section C.2, the Hamiltonian is a symmetric real-valued matrix and is equivalent to the GOE. The probability distribution for the GOE [274] is

$$p(r)|_{\mathrm{GOE}} = \frac{27}{4} \frac{r + r^2}{(1 + r + r^2)^{\frac{5}{2}}}, \tag{5.2}$$

which has average value $\langle r \rangle|_{\mathrm{GOE}} = 4 - 2\sqrt{3} \approx 0.5359$ and displays level repulsion as $p(0) = 0$.

Whereas thermalization is related to the classical notions of chaotic behavior and ergodicity, the fact that an ideal insulator fails to thermalize corresponds to the classical counterpart of integrable behavior [246, 275]. The concept of

(quasi-)local integrals of motion provides one interpretation of localization in many-body localized phases [81, 246, 276–280]. In this interpretation of many-body localization, the Hamiltonian is diagonalizable by a sequence of (quasi-)local unitary transformations. A unitary transformation $\hat{U}$, consisting of a sequence of transformations $\hat{U} = \prod_n \hat{U}_n$, is quasi-local if its parts $\hat{U}_n$ are of ever-increasing range and fulfill the condition that they exponentially approach the identity with increasing range n. The mathematical condition for a quasi-local transformation reads $\|\mathbb{1} - \hat{U}_n\|_F \propto \exp(-n/\xi)$, where $\|\cdot\|_F$ is the operator norm and ξ provides a length scale of the transformation [81]. As such, all eigenstates relate to a set of quantum numbers (the integrals of motion) of the diagonalized Hamiltonian by a series of quasi-local transformations. This structure implies less than extensive growth of entanglement as for an arbitrary subdivision of such a system into connected subregions A, A^c, the number of degrees of freedom in region A that contribute to the entanglement between these subregions grows proportional to the surface $\mathrm{vol}(\partial A)$ instead of the volume $\mathrm{vol}(A)$ [276]. This area-law entanglement has direct consequences on the growth of entanglement during time propagation, where it slows the spread of entanglement to be logarithmic in the evolution time [81, 277, 281–283]. The latter represents the connection to what was dubbed a nearly ideal insulator above. Despite finite growth in the entanglement with time, the logarithmic speed of this growth and less than extensive scaling of the characteristic time scale implies for sufficiently large systems that the time until entanglement has spread across the entire sample sufficently to represent some degree of thermalization will exceed the relevant time-scales of observation in the experiment [230]. For the remainder of this part of the thesis, the labels 'ergodic', 'non-integrable', and 'thermalizing' will be used interchangeably to refer to the non-many-body localized phase. In contrast, the labels 'non-ergodic', 'integrable', and 'localized' will be used for the many-body localized phase [284].

The fact that entanglement at long ranges is weak for a many-body localized phase implies that local changes to the Hamiltonian should only result in local modifications of the eigenstates [81]. This interpretation of localization suggests that different eigenstates are effectively independent of each other [81, 246]. The spectrum for such randomly drawn independent variables does not display level repulsion and follows the Poisson distribution [81]. The associated probability distribution reads

$$p(r)|_{\mathrm{Poisson}} = \frac{2}{(1+r)^2}\,, \tag{5.3}$$

and has average value $\langle r\rangle|_{\mathrm{Poisson}} = 2\ln(2) - 1 \approx 0.3863$ [246]. Level clustering is present as the distribution reaches its highest value at $r = 0$.

According to the above discussion, one can determine the ergodic or integrable nature of a closed quantum system in the presence of interaction by studying its spectral properties. A logical next step is to determine the numerical approach for such an investigation. This thesis follows Schliemann et al. [285], which

introduces the methodology employed in Chapter 6. The probability distribution $p(r)$ of the consecutive gap ratio provides a key indicator of the ergodicity of a closed quantum system [286].

For models with random disorder in their Hamiltonians, one can numerically extract the probability distribution of spectral properties by performing a disorder average. To this end, let Q be the number of randomly drawn disorder realizations labeled by α. For each realization α, one can obtain the spectrum either completely using exact diagonalization [267] or partially using approximate methods like Krylov space methods or by constructing approximate eigenstates, e.g., by matrix product states [287] or by tensor network approaches [242]. Such numerical investigations of interacting systems require, in general, a finite size of the investigated Hilbert space, which implies that the distribution $p_\alpha(r)$ will only be non-vanishing for a discrete set of support points for any given disorder realization due to the discrete nature of the spectrum. As such, even for large Q, the distribution $p(r)$ cannot be obtained by direct averaging of $p_\alpha(r)$. However, by introducing a finite broadening kernel $K(r, r', \sigma)$, which fulfills $\lim_{\sigma\to 0^+} K(r, r', \sigma) = \delta(r - r')$, one can write

$$\begin{aligned} p(r) &= \lim_{\sigma\to 0^+} \lim_{Q\to\infty} \frac{1}{Q} \sum_{\alpha=1}^{Q} \int_{-\infty}^{\infty} dr'\, K(r, r', \sigma) p_\alpha(r) \\ &\approx \frac{1}{Q} \sum_{\alpha=1}^{Q} \int_{-\infty}^{\infty} dr'\, K(r, r', \sigma(Q)) p_\alpha(r)\,, \qquad Q \gg 1\,, \end{aligned} \tag{5.4}$$

where the second line indicates that one approximates the formal disorder average with a sufficiently large number of disorder realizations Q and chooses a Q-dependent broadening $\sigma(Q)$ to smooth out the discrete nature of the individual $p_\alpha(r)$. For expectation values like $\langle r \rangle$, no broadening is required, and one can directly evaluate the disorder average as

$$\langle r \rangle = \lim_{Q\to\infty} \frac{1}{Q} \sum_{\alpha=1}^{Q} \langle r \rangle_\alpha \approx \frac{1}{Q} \sum_{\alpha=1}^{Q} \langle r \rangle_\alpha =: \bar{r}\,, \qquad Q \gg 1\,. \tag{5.5}$$

Since many-body localization emerges for increasing disorder due to an equally increasing number of local integrals of motion, the transition in $\langle r \rangle$ between the values associated with an ergodic and a non-ergodic phase will be smooth for a finite system size.

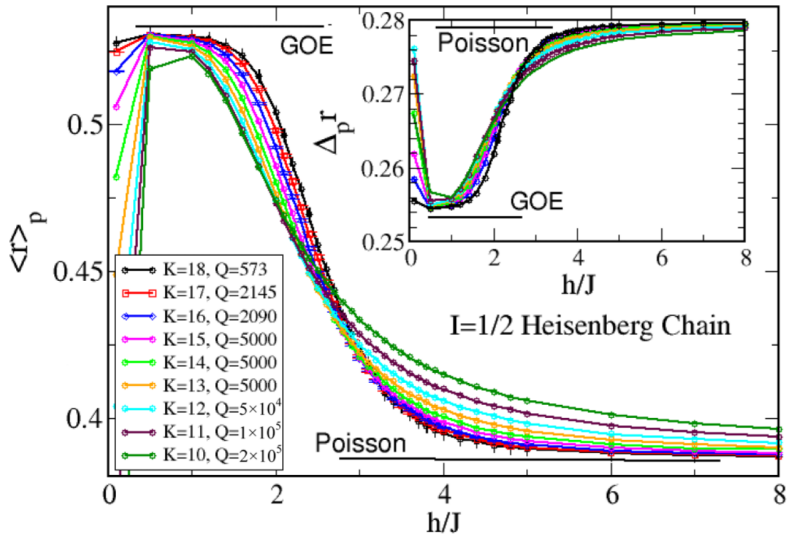

Figure 5.1: **Average consecutive gap ratio $\langle r \rangle$ in a local-field disordered Heisenberg chain for varying strength of the disorder h/J and different system sizes N.** The average consecutive gap ratio displays a transition from its predicted value in an ergodic (GOE) phase to the value predicted for an integrable (Poisson) phase as a function of the ratio between the disorder strength h and the exchange coupling between adjacent spins J. The inset shows a similar transition for the total standard deviation $\Delta_p r$, but it is not relevant to the discussion here. Reproduced with permission of the authors from Schliemann et al. [285].

Fig. 5.1, reproduced from Schliemann et al. [285], illustrates this transition in $\langle r \rangle$ between an ergodic (GOE) and a many-body localized phase (Poisson) in the local-field-disordered Heisenberg chain (see Section C.2 for an introduction to the model). The deviation from the GOE value for vanishing disorder $h/J \approx 0$ is due to the residual approximate translational symmetry for weak disorder. For an actual quantum phase transition, the position of the transition should collapse to a critical value of the disorder strength as the system size increases [247]. However, the estimates of the critical disorder strength obtained by different approaches drift with increasing system size for the currently numerically tractable system sizes, thereby indicating potential finite-size effects [247, 285]. It is thus still an open question whether a critical disorder strength actually exists for infinite system sizes and, consequently, whether a many-body localized phase exists in the thermodynamic limit [247, 248, 288].

Beyond the average consecutive gap ratio $\langle r \rangle$, Schliemann et al. also proposed investigating the disorder-dependent emergence of integrability in many-body localized systems by studying other statistical measures of the spectrum. The average consecutive gap ratio within a specific disorder realization α represents

itself a random variable $x = \langle r \rangle_\alpha$ governed by a probability distribution $s(x)$ which by construction obeys the relation

$$\int_0^1 dx\, x s(x) = \int_0^1 dr\, r p(r) = \langle r \rangle \,, \tag{5.6}$$

even though $p(r)$ and $s(x)$ do in general not coincide[1] [285]. Here, a subscript indicates the probability distribution used in the calculation of an average or variance. As such, Eq. (5.6) states that $\langle r \rangle_s = \langle r \rangle_p = \langle r \rangle$. While the average values agree, the variances do not. The sample-so-sample variance $(\Delta_s r)^2$ reads

$$(\Delta_s r)^2 = \int_0^1 dx\, (x - \langle r \rangle)^2 s(x) \,. \tag{5.7}$$

In contrast, one can relate the total variance with respect to the distribution p to the sample-to-sample variance by

$$(\Delta_p r)^2 = (\Delta_s r)^2 + \lim_{Q\to\infty} \frac{1}{Q} \sum_{\alpha=1}^{Q} (\Delta_\alpha r)^2 \,, \tag{5.8}$$

where $(\Delta_\alpha r)^2$ is the variance within a specific disorder realization α. Note that since both x and $\langle r \rangle$ are restricted to lie inside the interval $[0, 1]$ by construction, one has $|x - \langle r \rangle| \leqslant 1$, which implies that $(\Delta_s r)^2 \leqslant \|s\|_1 = 1$. Since the second term on the right-hand side of Eq. (5.8) is strictly non-negative, it further follows that $(\Delta_p r)^2 \geqslant (\Delta_s r)^2$.

Numerically, one is limited to finite Q and thus cannot access either $p(r)$ or $\langle r \rangle$ exactly. In turn, is it helpful to investigate the speed of convergence between the finite average $\bar{r}$ and the exact result $\langle r \rangle$ with increasing number of disorder realizations Q. Given a number Q of indepently drawn random disorder configurations, the probability distribution $s(x)$ allows us to interpret $\bar{r}$ as a sum over uncorrelated random variables with a joint distribution

$$\pi(x_1, \cdots, x_Q) = \prod_{\alpha=1}^{Q} s(x_\alpha) \,, \tag{5.9}$$

with an expectation value $\langle \bar{r} \rangle_\pi = \langle r \rangle$. Notably, the variance of $\bar{r}$ away from its expectation value $\langle r \rangle$ follows from the additivity of variances, since

$$\langle (\bar{r} - \langle r \rangle)^2 \rangle_\pi = \frac{1}{Q} (\Delta_s r)^2 \leqslant \frac{1}{Q} \,, \tag{5.10}$$

and, as such, vanishes at least as Q^{-1}. Using this convergence enables one to replace the unknown $\langle r \rangle$ in Eq. (5.7) with the finite average $\bar{r}$ as

$$(\Delta_s r)^2 \approx \frac{1}{Q} \sum_{\alpha=1}^{Q} (\langle r \rangle_\alpha - \bar{r})^2 \,. \tag{5.11}$$

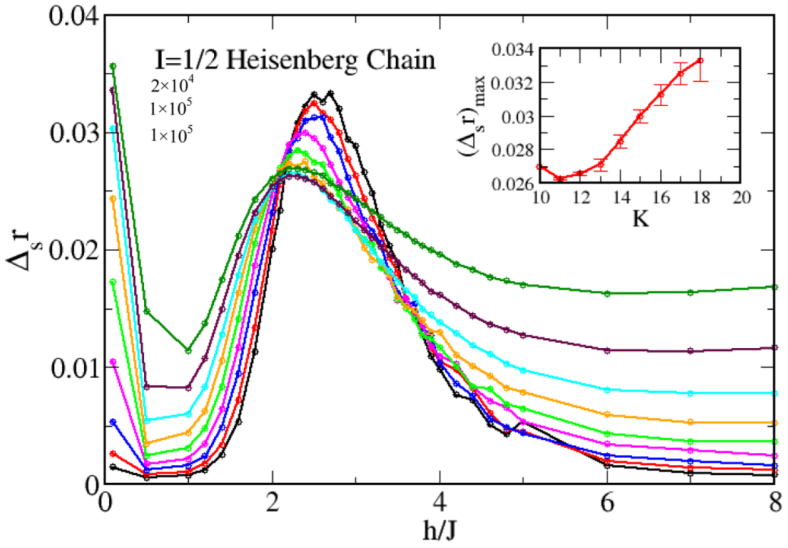

Figure 5.2: **Sample-to-sample standard deviation $\Delta_s r$ of the consecutive gap ratio in a local-field disordered Heisenberg chain as a function of the strength of the disorder h/J and for different system sizes** N. With increasing chain length N, the sample-to-sample standard deviation reduces to a peak around $h/J \approx 2.6$ while diminishing elsewhere. Reproduced with permission of the authors from Schliemann et al. [285].

A signature of a quantum phase transition is a peak in the sample-to-sample variance and thus also the sample-to-sample standard deviation $\Delta_s r$ close to the critical value of the transition [285]. Fig. 5.2, reproduced from Schliemann et al. [285], shows a peak close to $h/J \approx 2.6$, in line with the presence of a phase transition from an ergodic phase at low disorder strength to a many-body localized phase at high disorder strength. While the peak narrows for increasing N in line with the existence of a critical disorder strength, its position, which agrees roughly with the inflection point of $\langle r \rangle$ in Fig. 5.1, displays a slow drift to larger values for increasing chain lengths. In line with the current debate about the stability of many-body localization in the thermodynamic limit [247], this drift complicates a meaningful extrapolation to $N \to \infty$ and thus leaves open a possible explanation of the observed behavior as a finite-size effect [247, 285, 289, 290].

1 Consider, e.g., the case of each realization α having the same average $\langle r \rangle_\alpha$, in which case $\Delta_s r = 0$. A vanishing variance of r in each realization and thus a vanishing $\Delta_p r$ is a stronger statement.

6

IMPERFECT MANY-BODY LOCALIZATION

This chapter covers the material published in Siegl and Schliemann [227] and follows the presentation therein closely. The primary focus of this work is a numerical investigation of a prediction by Potter and Vasseur [241] regarding the incompatibility of many-body localization with global non-abelian symmetries. To this end, a version of the Heisenberg spin chain model introduced in Section C.2, which implements such a non-abelian symmetry, is numerically investigated. A schematic of this model, the exchange-disordered Heisenberg chain, is shown in Fig. 6.1.

Before covering the numerical results obtained by the code discussed in Section D.2, it is instructive to start the discussion with a brief recalling of the argument of Potter and Vasseur [240, 241] about the incompatibility of many-body localization with the presence of a global non-abelian symmetry. As mentioned in Chapter 5, the emergent integrability of the many-body localized phase is due to the emergence of an increasing number of local integrals of motion with increasing disorder. The emergence of such local integrals of motion impacts the dynamics first by slowing down and eventually completely stalling the growth of entanglement throughout the sample, where the latter regime is equivalent to the presence of an exhaustive set of local integrals of motion, indicating that integrability has been reached. Within this interpretation of the emergence of integrability, the impact of a global non-abelian symmetry is clear intuitively, as the symmetry of the full model enforces a non-trivial lower bound on the non-locality of any eigenstate of the Hamiltonian. In other words, a local change of the Hamiltonian cannot result in a (quasi-)local modulation of the eigenstates, since any such change requires non-local changes of the eigenstates in order to conform to the non-abelian symmetry of the model. It is this fundamental requirement of non-locality that any non-abelian symmetry imposes on the system, that Potter and Vasseur argue limits the number of local integrals of motion that can emerge in such systems to be less than exhaustive, even at arbitrarily strong disorder. As such, the presence of non-abelian symmetries should hinder the emergence of a fully integrable phase. The impact of non-abelian symmetries has also been discussed in the literature regarding the eigenstate-thermalization

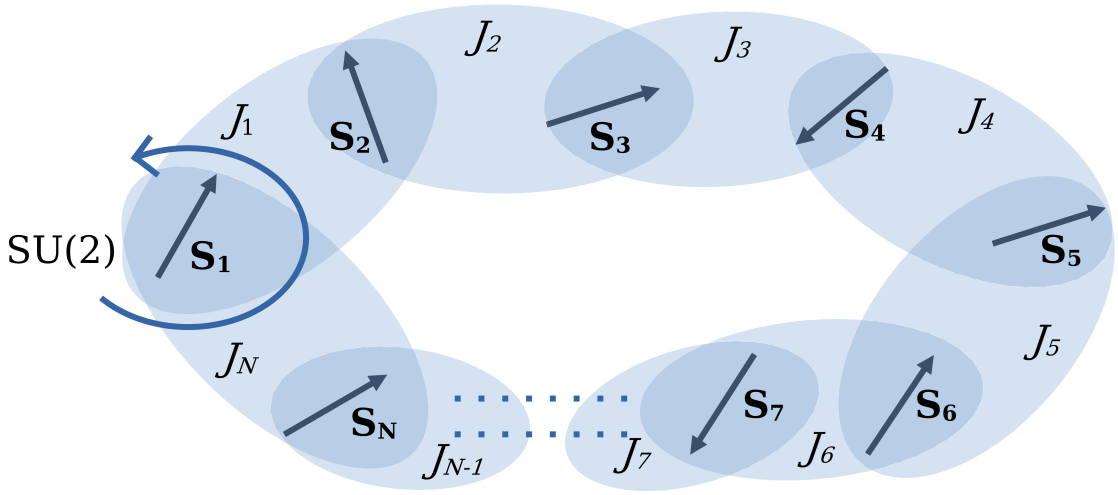

Figure 6.1: **Schematic representation of an exchange-disordered Heisenberg spin chain.** The model consists of a finite number of localized spins $\hat{S}_i$, which interact via exchange couplings J_i, that vary between sites due to a random modulation. The exchange coupling between the spins is invariant under a simultaneous (global) rotation of all spins, which is equivalent to the free $SU(2)$ rotation of a single spin.

hypothesis [291] and the spread of entanglement entropy [292], yielding similar conclusions.

Turning to results, Fig. 6.2 shows the numerically obtained probability distribution $p(r)$ according to Eq. (5.4) for different ratios between the fixed exchange coupling J and the range b of the random modulation. Since the Hamiltonian of the exchange-disordered Heisenberg chain has $SU(2)$ symmetry, all eigenstates have well-defined S_{tot}, S^z_{tot}, and lie in multiplets whose degeneracy depends on S_{tot}. The study of consecutive gap ratios is thus performed by accounting for this degeneracy and identifying different eigenstates in the same multiplets when investigating the level spacings. Since, for sufficiently long chain lengths, the extremal states of the spectrum have negligible weight in the statistics, one can include all multiplets in the spectrum, eliminating the need for a restriction to the middle of the spectrum. An additional benefit of this approach is the direct relation to the discussion of an insulator at infinite temperature, where all states in the spectrum are equally occupied. The red line represents the expected probability distribution for the integrable case, as given in Eq. (5.3). In contrast, the green line shows the expected probability distribution for the ergodic case, which, for the symmetry class of the model's Hamiltonian, is equivalent to the Gaussian Orthogonal Ensemble (GOE).

The mapping to the GOE is only valid within each block of the Hamiltonian after one has block diagonalized it with respect to any remaining symmetry. This requirement complicates the comparison, since at nearly vanishing disorder, the periodic boundary conditions result in an approximate additional translational symmetry, which such a block diagonalization cannot eliminate. Since already

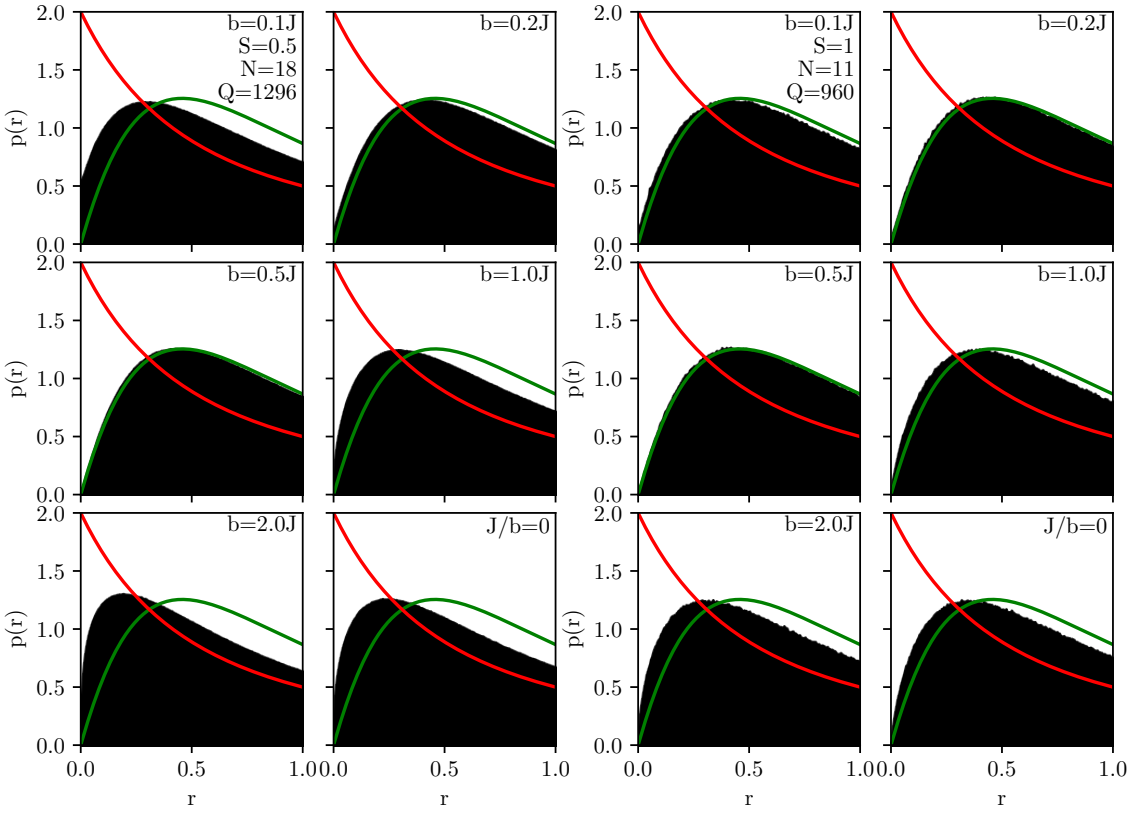

Figure 6.2: **Numerically determined probability distribution** $p(r)$ **of the consecutive gap ratio in an exchange-disordered Heisenberg chain for varying disorder strength** b **and spin length** $S = 0.5, 1$. Shown is $p(r)$ as numerically determined according to Eq. (5.4). The predictions for the ergodic (GOE) and the integrable (Poisson) phases are shown in green and red, respectively. Reproduced from Siegl and Schliemann [227].

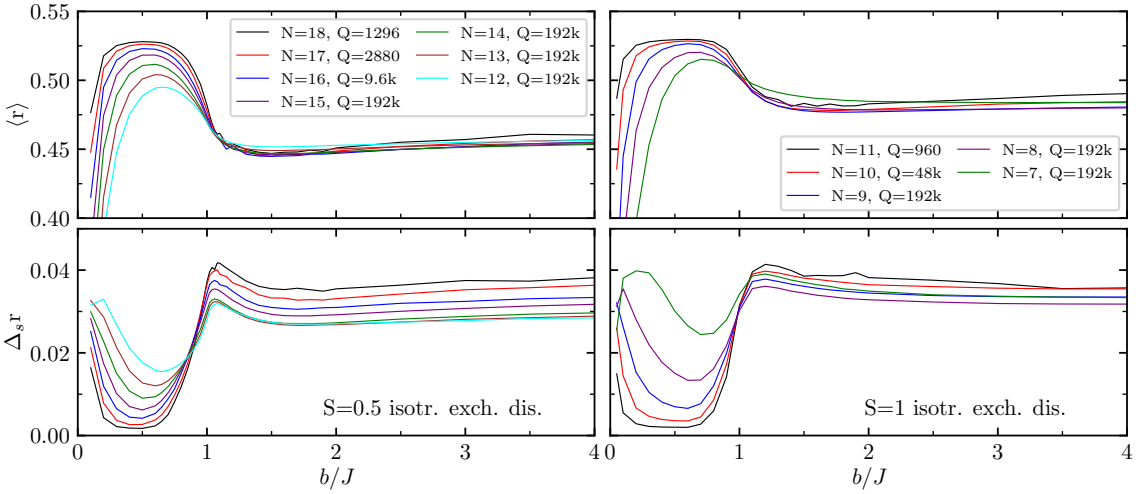

Figure 6.3: **Average consecutive gap ratios (upper panels) and sample-to-sample standard deviation (lower panels) for spin lengths $S = 0.5$ (left side) and $S = 1$ (right side) of the exchange-disordered Heisenberg chain**. All quantities are shown for different system sizes N and as functions of the ratio b/J, which describes the strength of the disorder on the exchange couplings. Both quantities show for both considered spin lengths signatures of a critical disorder strength, $b_c \gtrapprox 1.0J$, at which a transition from an ergodic phase to another phase, whose signatures do not agree with either the fully ergodic (GOE) or the fully integrable phase. Reproduced from Siegl and Schliemann [227].

arbitrarily weak disorder breaks the exact symmetry, one can only perform the necessary block diagonalization at truly vanishing disorder. As the probability distribution for the investigated finite sizes evolves smoothly with increasing disorder, $p(r)$ for (nearly) vanishing disorder remains distinct from the GOE prediction. Increasing disorder breaks the residual approximate translational symmetry, and $p(r)$ recovers the form predicted by GOE, as is shown in Fig. 6.2 for both spin lengths $S = 0.5$ and $S = 1$ at $b/J = 0.5$ for spin length $S = 0.5$ and $b/J = 0.2$ for spin length $S = 1$. As the disorder strength increases further, the probability distribution starts to drift away from the GOE prediction towards the prediction of the integrable phase. However, it never reaches the integrable phase, as is evident from the fact that level repulsion survives even in the infinite disorder limit $J/b = 0$. This result agrees with earlier works [242, 245], which observed the failure of the exchange-disordered Heisenberg chain to reach integrability even at arbitrarily strong disorder.

Beyond a study of $p(r)$, one can obtain further insight into the impact of global non-abelian symmetries on the regime of strong disorder by investigating the transition between different regimes using the established methodology of both the average consecutive gap ratio [293] and sample-to-sample standard deviation [266, 285]. To this end, Fig. 6.3 shows both of these quantities as a function of disorder strength for varying system sizes N and total spin lengths $S = 0.5$ and $S = 1$. The average consecutive gap ratios for either spin length start, at (nearly) vanishing disorder, well below the value $\langle r \rangle|_{GOE} \approx 0.5359$ expected for an

ergodic phase due to the approximate translational symmetry mentioned above. At $b = 0.5J$ (earlier for $S = 1$), they reach $\langle r \rangle|_{GOE}$, and the sample-to-sample standard deviation reaches a minimum as expected for the ergodic phase. Both spin lengths then display a rapid decline in $\langle r \rangle$ at $b/J \gtrapprox 1.0$ from a value close to $\langle r \rangle|_{GOE}$ to a value still above the prediction of $\langle r \rangle \approx 0.3863$ for the many-body localized phases in agreement with the behavior of $p(r)$ discussed above. This transition becomes sharper with increasing system size N, in line with the possible existence of a critical disorder strength $b_c \gtrapprox 1.0J$ for a potential phase transition from an ergodic phase at low disorder to a yet-to-be described phase at high disorder. The slow increase of $\langle r \rangle$ with increasing b above b_c is finite and results in $\langle r \rangle_{Poisson} < \langle r \rangle_{J/b=0} < \langle r \rangle_{GOE}$, not shown in Fig. 6.3. The sample-to-sample standard deviation also displays a peak in the vicinity of a hypothetical b_c in the above panels, thereby strengthening the case for the existence of an actual phase transition. However, unlike the behavior observed in Fig. 5.2, the sample-to-sample standard deviation does not decrease with increasing system size on both sides of the region containing the potential b_c. Instead, $\Delta_s r$ remains finite and increasing with system size at large disorder. Additionaly, the sample-to-sample standard deviation exhibits a slow trend of growth or decline to a finite asymptotic value (not shown in Fig. 6.3) above b_c for spin lengths of $S = 0.5$ and $S = 1$, respectively. While the presence of a transition in $\langle r \rangle$ of increasing sharpness with increasing system size N and an inflection point around the same b/J as a peak in $\Delta_s r$ hints at a possible phase transition at a critical disorder strength b_c, the behavior at large disorder fails to show the signatures associated with an integrable many-body localized phase in line with both the earlier observations on $p(r)$ and the prediction by Potter and Vasseur [241].

The original argument about the incompatibility of global non-abelian symmetries with many-body localization provides an interpretation of the observed phase at strong disorder as a phase characterized by an incomplete set of local integrals of motion even at arbitrarily high disorder. This phase, if thermodynamically stable, should therefore exhibit a slowed-down thermalization and entanglement growth when compared to the ergodic behavior at low disorder, but distinct from the nearly ideal insulating behavior within the many-body localized phase, in a direct analogy to the transition regime between ergodic and fully integrable phases for finite system sizes. As such, Siegl and Schliemann dubbed this potential phase an *imperfect many-body localized phase* [227]. However, the finite sizes available to numerics and the slow growth of $\langle r \rangle$ above b_c with increasing system size complicate a meaningful extrapolation to the thermodynamic limit, which is in line with similar behavior observed in works on related models [245, 294]. Therefore, one should best understand the result in Siegl and Schliemann as a numerical observation with an associated hypothesis about the possible existence of a phase distinct from the ergodic and the many-body localized phases independently of finite-size effects [227]. More recently, Saraidaris et al. have identified what they dubbed a "subthermal regime" in disordered $SU(N)$

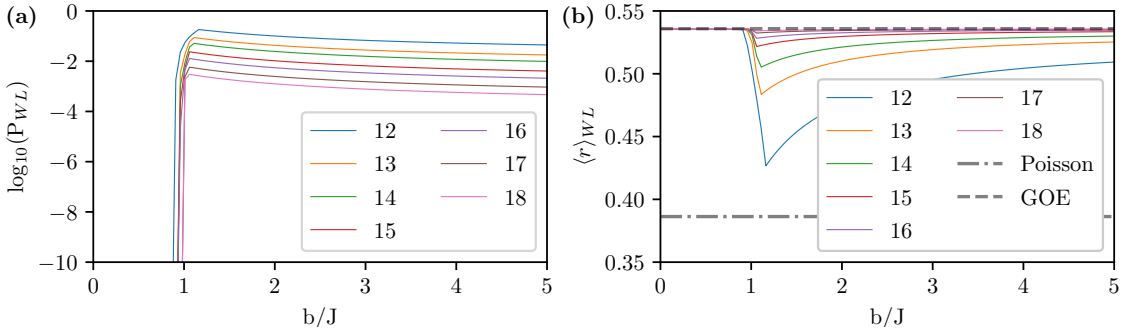

Figure 6.4: **Probability of the occurrence of at least two weak links (a) and the maximum false positive signal they can contribute in $\langle r \rangle$ (b).** While the probability becomes finite for all system sizes above $b/J = 1$, it decreases exponentially with increasing system size N, as evident from the nearly constant spacing between the lines in the log-plot and as verified in the analytics below. While the occurrence of weak links can contribute a false positive signal for a transition of $\langle r \rangle$ from $\langle r \rangle|_{GOE}$ to $\langle r \rangle|_{Poisson}$ around $b/J \approx 1.0$, this false positive signal is decreasing with increasing N and returning to $\langle r \rangle|_{GOE}$ in contradiction to the behavior observed in the numerics. Reproduced from Siegl and Schliemann [227].

symmetric Heisenberg chains with slowed-down thermalization predicted to be experimentally accessible in such systems.

When discussing the possibility of a distinct, imperfect many-body localized phase in the exchange-disordered Heisenberg chains considered here, it is essential to consider alternative explanations for the observable phenomenology in the large disorder regime. As pointed out by Gao and Römer in private discussion before the publication of the material covered in this chapter [227] and during the review process for said publication, a possible alternative explanation for the rapid change in $\langle r \rangle$ above $b_c \gtrapprox 1.0$ is the finite possibility within any realization α to have a finite number of exchange couplings whose modulus $|J_i| \lll J, b$. Such so-called *weak links* impact the connectivity of the model as they effectively split the chain into separate sections [242, 245]. As the probability of a random exchange coupling of magnitude $|J_i| \leqslant \delta$ with $0 \leqslant \delta < |J|, |b|$ is strictly zero for $|b| < |J| - \delta$, it is evident that one expects a finite probability of arbitrarily weak links only for $b/J \approx 1.0$ or above. It is therefore essential to check whether the occurrence of such weak links is responsible for the signatures observed in $p(r)$ and thus in the statistics of $\langle r \rangle$. To start this discussion, one needs to fix the δ below which one considers an exchange coupling to represent a weak link. Since the both the total spin and the z-component of the total spin $\hat{S}^z_{tot} = \sum_j \hat{S}^z_j$ commute with the Hamiltonian, all eigenvectors lie in multiplets of the type $|S_{tot}, S^z_{tot}\rangle$. Focussing on a subspace i of fixed S^z_{tot} and dimensionality N_i, the average level spacing δ_i provides a meaningful threshold criterion for weak links for which

$$\delta_i \leqslant S^2(J + b)N/N_i \,. \tag{6.1}$$

Given a specific threshold δ, the probability q for an exchange coupling to have a modulus less than δ is given by

$$q = \begin{cases} \Theta(b-J)\frac{\delta}{b} : & \delta \leqslant |J-b|\,, \\ (\delta+b-J)/2b : & |J-b| < \delta \leqslant J+b\,, \\ 1 : & \delta > J+b\,. \end{cases} \tag{6.2}$$

The probability of at least two weak links occurring and thereby impacting the chain's connectivity reads

$$P_{WL} = 1-(1-q)^N - Nq(1-q)^{N-1}\,, \tag{6.3}$$

as it is equivalent to the complimentary case to either zero or a single weak link occurring. For large N, one can rewrite

$$\lim_{N\to\infty} P_{WL} = 1-(1+c)e^{-c}\,, \qquad c := \lim_{N\to\infty} Nq\,. \tag{6.4}$$

Eq. (6.3) implies that a vanishing c and thereby a decrease of q faster than N^{-1} is sufficient to guarantee a vanishing impact of weak links for large system sizes N. To proof that this is indeed the case, one proceeds by investigating the scaling of N_i which for the case of $S = 0.5$ (the case $S = 1$ proceeds analagosly) is given by

$$N_i = \binom{N}{i} - \binom{N}{i} = \frac{2i+1-N}{N+1}\binom{N+1}{i}\,, \tag{6.5}$$

which shows that the largest subspaces are the ones of low S^z_{tot} which grow exponentially in the system size N. Since the average level spacing δ_i scales as N/N_i and even the slowest scaling non-trivial[1] subspace $S^z_{tot} = S-2$ scales as $N_i \propto N^2$, one can assume that δ approaches zero at least as N^{-1} for large N. This rapid decrease in δ for increasing N leaves only two cases as either $b = J$ such that $\delta \geqslant |J-b| = 0$ even for large N and $q = \frac{\delta}{2b}$, or $|J-b| \neq 0$ in which case for large N one always is in the first case of Eq. (6.2). For $J \neq b$ and large N this implies $q \leqslant \frac{\delta}{\max\{J,b\}}$. Irrespective of the value of b, q has the same scaling with N as δ, immediately yielding the result that weak links do not impact the connectivity of any subspace that scales faster with N than N^2. The only subspace potentially impacted by weak links is the subspace of $S^z_{tot} = S-2$, which, according to Eq. (6.4), will be affected with a finite probability. However, the numerics average over all subspaces and since the only affected subspace is the one with the slowest scaling in N, the impact of weak links on any average quantity like $\langle r\rangle$ vanishes exponentially with increasing N. The exponential decrease of the probability of encountering at least two weak links is supported by Fig. 6.4 (a), which shows the decimal logarithm of the probability Eq. (6.3) for

1 Subspaces of $S^z_{tot} = S, S-1$ are trivial in the sense that the possible eigenstates are known and independent of the disorder configuration.

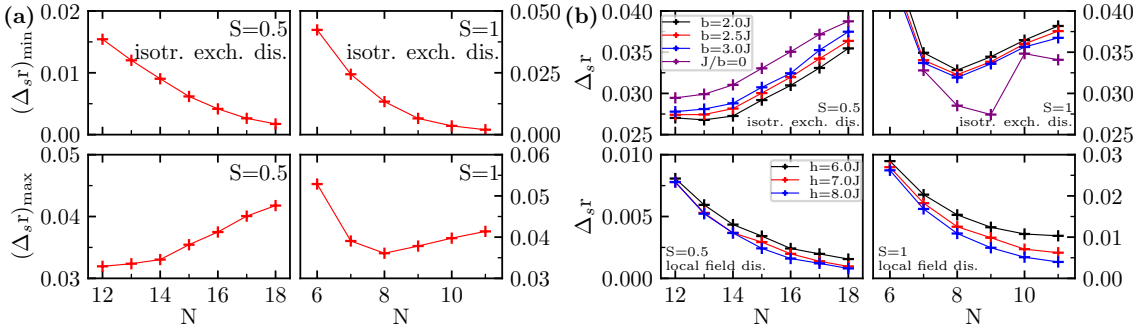

Figure 6.5: **Extremal values of the sample-to-sample standard deviation (a) and the average sample-to-sample standard deviation for different models(b) for varying system sizes** N**.** For larger N, the extremal values of the sample-to-sample standard deviation show a decrease, respectively growth for the minima and maxima respectively. The scaling of the sample-to-sample standard deviation in the large disorder regime is qualitatively different between the exchange-disorderd Heisenberg chain (upper panels in b) and the local-field-disordered Heisenbrg chain (lower panels in b). Taken from Siegl and Schliemann [227].

the system sizes considered in this chapter. The nearly constant spacing between the curves for consecutive chain lengths is compatible with the exponential suppression predicted by the considerations above. However, the fact that weak links do not contribute significantly for large N does not directly address the underlying question of whether they are relevant for the observations at finite N. To rule out this possibility, one can upper-bound the false positive signal weak links can provide for a possible transition in $\langle r \rangle$. To this end, one assumes that all disorder realizations not affected by weak links remain fully in the ergodic phase. In contrast, one overestimates the impact of weak links by considering all realizations affected by weak links to obey $\langle r \rangle|_{WL} = \langle r \rangle|_{Poisson}$. The resulting overestimate of a potential false signal is shown in Fig. 6.4 (b), and does not agree qualitatively with the observed transition in Fig. 6.3. This is evident both from the fact that the false signal strongly decreases with N for the considered chain lengths and from the fact that the false signal is sizeable only close to $b/J \approx 1.0$ but quickly returns to $\langle r \rangle|_{GOE}$ as b/J increases further. Given these observations, one can conclude that weak links are not relevant for the observed transition in Fig. 6.3 and are also not expected to become more relevant with increasing chain lengths.

A more detailed analysis of the sample-to-sample standard deviation provides further evidence of the identification of the regime above $b \geqslant b_c \gtrapprox 1.0$ with a distinct phase. To this end, Fig. 6.5 shows the scaling of the extremal values of the sample-to-sample standard deviation with increasing system size N in subplot (a) for both of the considered spin lengths and the scaling of the sample-to-sample standard deviation itself for both the exchange-disordered Heisenberg chain (isotrop. exch. dis. in the figure) and the local-field-disordered analogue as investigated by Schliemann et al. [285] in subplot (b). The trend for larger

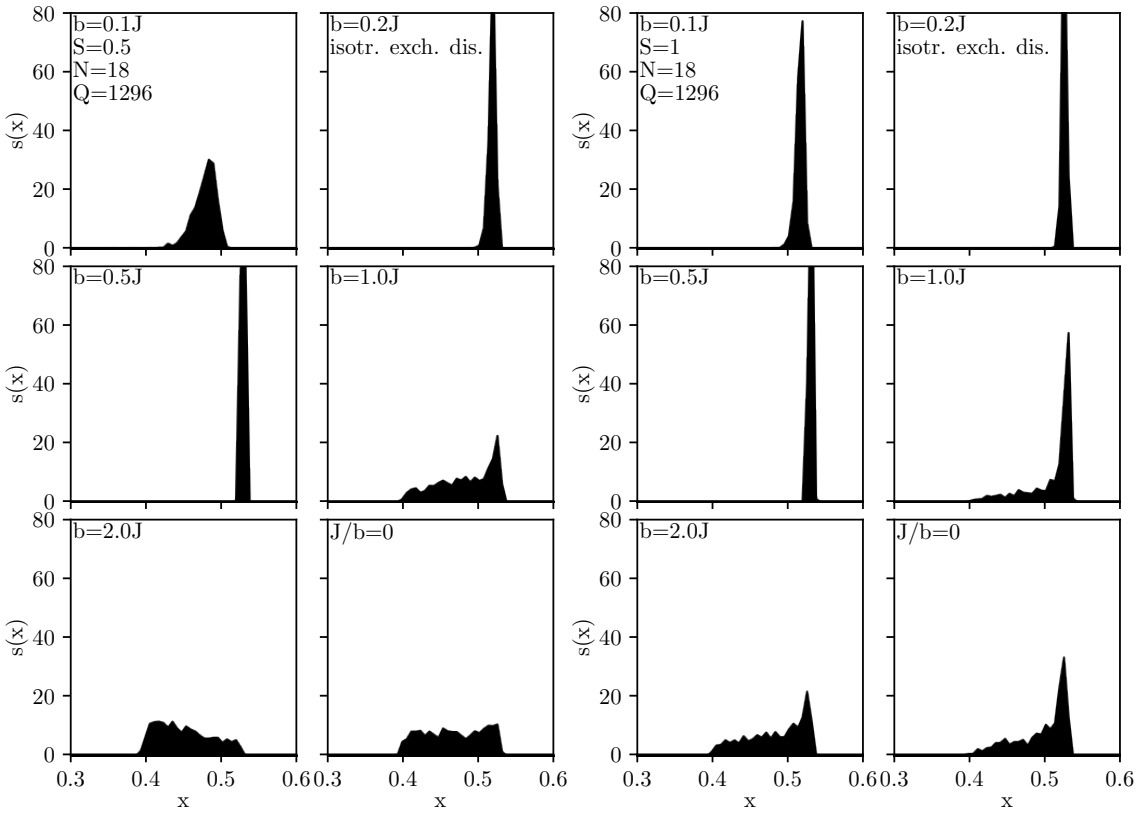

Figure 6.6: **Probability distribution** $s(x)$ **of** $\langle r \rangle$ **for varying disorder strengths and spin lengths.** The peak around $\langle r \rangle|_{GOE}$ broadens around b_c without a revival even for arbitrarily strong disorder. Reproduced from Siegl and Schliemann [227].

system sizes in subplot (a) indicates a decrease of $(\Delta_s r)_{min}$ compatible with the limiting behavior $(\Delta_s r)_{min} \to 0$ for $N \to \infty$. $(\Delta_s r)_{max}$ instead follows a monotonically increasing trend for sufficiently large N. Both of these trends are typical signatures of a phase transition wherein $\langle r \rangle$ takes on the role of an order parameter distinguishing the phases on either side of the transition [227, 285]. Subplot (b) shows the sample-to-sample standard deviation for large disorder. It displays a distinct behavior for the exchange-disordered Heisenberg chain (upper panels of subplot (b)) wherein $\Delta_s r$ grows with N in contrast to the local-field disordered Heisenberg chain, where it monotonically decreases with N [285] (lower panels of subplot (b)). The growth with N is monotonically increasing for $N \geqslant 14$ for $S = 0.5$, but curiously not for $S = 1$ in the considered range of N and for infinite disorder. A possible candidate for an explanation of this behavior is the presence of finite-size even-odd effects[2].

Signatures of a potential phase transition should also be present in the probability distribution $s(x)$ introduced in Chapter 5. Fig. 6.6 shows the respective probability

2 Such even-odd effects are known to occur in the numerics of Heisenberg chains. Unfortunately, they are primarily subject to personal discussion, e.g., with J. Richter, J. Schliemann, P. Wenk, and D. Abanin but are not covered in the literature, with multiple works instead simply stating their restriction to even chain lengths [227, 285, 296–298].

distribution $s(x)$ and displays a narrow peak at $x = \langle r \rangle|_{\mathrm{GOE}}$ at intermediate disorder $b/J \approx 0.5$, in line with the expected behavior of the ergodic phase, where $\Delta_s r$ should be small and decrease with increasing system size. Around the critical value of the disorder, the distribution broadens significantly with a remaining small peak of the distribution around the GOE prediction of $\langle r \rangle$. For the local-field disordered Heisenberg chain, the distribution $s(x)$ again narrows into a peak around the expectation value of the integrable phase [285]. However, here, no such revival of a narrow distribution with increasing disorder strength occurs. Instead, the distribution is effectively featureless for spin length $S = 0.5$, while curiously, a smaller broadened peak at the GOE value of $\langle r \rangle$ survives for $S = 1$ on top of a similarly broadened background. A possible interpretation of the latter peak for $S = 1$ is a finite probability that, given a fixed disorder strength, a specific disorder realization has sufficiently few emergent local integrals of motion that the Hamiltonian for this specific realization behaves effectively ergodic as in the regime of low disorder. No such feature is visible for $S = 0.5$ in Fig. 6.6. The origin of this difference between spin length is not yet known. There is no equivalent difference for the local-field disordered Heisenberg chain [285]. However, there exist fundamental differences between the spectra of integer and half-integer Heisenberg spin chains [299–303]. More recently, Gao and Römer [295] further investigated the same model for spin length $S = 0.5$ and concluded that above $b/J \approx 1.0$ parts of the spectrum remain ergodic. However, they did not provide a definitive explanation for the origin of the localization in parts of the spectrum. Similar to the local-field disordered Heisenberg chain, Gao and Römer claim the observation of a drift of the estimate for a critical disorder strength with increasing system size [295].

Along the same lines as the current discussion on the stability of the many-body localized phase [247], the possible existence of a phase transition towards an imperfect many-body localized phase for systems with global non-abelian symmetry thus remains to be disentangled from the impact of finite-size effects. Towards this end, further approaches related to the work in this thesis and subject to follow up publications which are currently in preparation include the analytical modeling of the distribution $p(r)$ of the exchange-disordered Heisenberg chain in the strong disorder limit and an investigation of the incomplete many-body localized phase using generalized inverse participation ratios [295, 304, 305] calculated for the one-particle density matrix [306]. The random-spin phases [307] present in the exchange-disordered model are the most likely candidates [305] for the imperfect many-body localized phase observed here.

The problem of investigating many-body localization is numerically hard on classical computers [247, 290] and may require first further developments in the field of quantum computation [308]. It has thus motivated a plethora of different approaches that are actively pursued in the community, including approaches based on machine-learning [309–311], renormalization group [242, 245, 294, 312–316], and matrix product states [287]. Whether either of them

allows the community to settle the debate regarding the highly complicated and remarkable phenomenon of many-body localization on today's hardware in less than exponential time is itself an open question.

Part III

UNCONVENTIONAL SUPERCONDUCTIVITY IN MONOLAYER 1H-$NbSe_2$

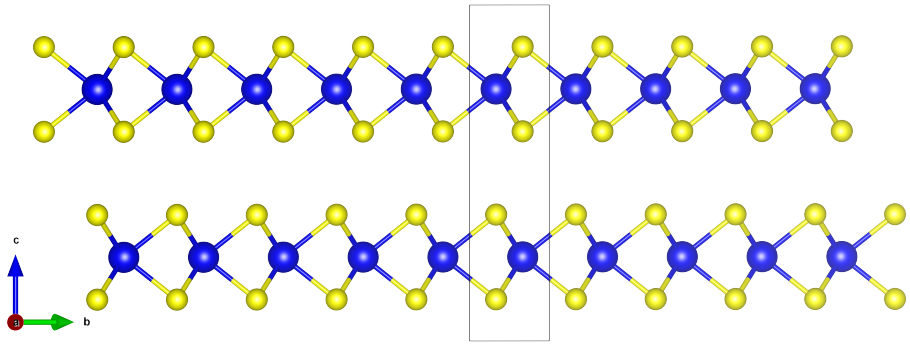

Figure 6.7: **View along the a-axis of the crystal structure of bulk 2H-$NbSe_2$ in a ball and stick model.** The box indicates the unit cell of the crystal with space group $P6_3/mmc$, and the arrows indicate the crystal axes. Niobium atoms are shown in blue, while the selenium atoms are shown in yellow. The 2H polytype consists of two 1H-monolayers per out-of-plane period arranged in an AB-stacking [317]. This visualization used VESTA3 [318].

This part of the thesis covers work on screening in 1H-$NbSe_2$ and the possibility of superconductivity mediated by the Kohn-Luttinger mechanism in this material. $NbSe_2$ is a transition metal dichalcogenide (TMD), whose bulk in the 2H-polytype [317] is a Van der Waals material with the space group $P6_3/mmc$ that consists of a staggered sequence of two 1H-monolayers, as depicted in Fig. 6.7. These monolayers can be isolated [319] and consist of a trigonal Bravais lattice with a prismatic basis, resulting in a crystal structure with space group P3m1, depicted in Fig. 6.8, in the hexagonal crystal system. As two-dimensional hexagonal crystals, TMD monolayers have a similar structure to graphene, with which they share the valley degree of freedom that may enable valley-based functionalities [320–326]. While ungated graphene is semimetallic and offers an effective relativistic dispersion at low energies [57, 58, 327, 328], the TMD monolayers' low-energy band structure varies between compounds [329] and tends to have much more pronounced spin-orbit interaction [330]. The latter is enhanced due to the broken inversion symmetry in the 1H-polytype [317] and due to the heavier transition metal nucleus, which increases the importance of relativistic effects like spin-orbit interaction [329]. The presence of the in-plane mirror symmetry for the 1H-polytype results in an effective magnetic field acting on the spins along the out-of-plane direction [65], yielding the so-called Ising spin-orbit interaction. This type of spin-orbit interaction splits the spin-degeneracy of the bands throughout most of the Brillouin zone[3], and locks the spins to an orientation along the c-axis. This orientation locking has a profound impact on the behavior under external in-plane magnetic fields, with the superconductivity in monolayer TMDs strongly violating the Pauli limit for the in-plane critical magnetic field [331].

3 The effect of spin-orbit interaction vanishes along the $\Gamma - M$-direction for symmetry reasons.

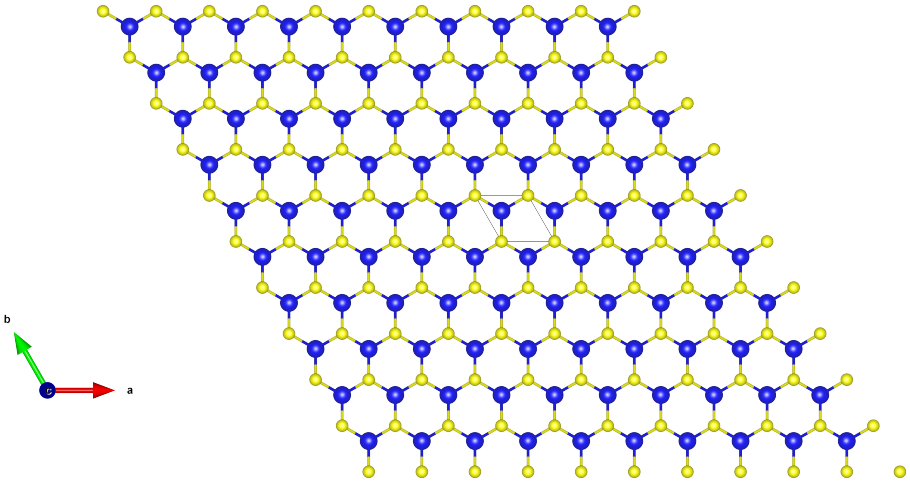

Figure 6.8: **View along *c*-axis of monolayer 1H-$NbSe_2$ in a ball and stick model.** The box indicates the unit cell of the crystal with space group P3m1, and the arrows indicate the crystal axes. Niobium atoms are shown in blue, while the selenium atoms are shown in yellow. The 1H polytype consists of two hexagonal selenium sublattices sandwiching a central hexagonal niobium sublattice, forming a trigonal prismatic unit cell.

The spin-orbit field flips its orientation between valleys [332], realizing a coupling between the valley and spin degrees of freedom, both of which promise novel electronic functionalities [321, 323, 324, 332, 333]. The resulting band structure allows optical valley-selective manipulation [322, 334–339], thereby rendering these materials highly interesting for potential opto-electronic applications like, e.g., optical spin injection [340]. The emergence of charge order is common in (quasi-)two-dimensional layered TMDs [341], with a non-commensurate charge-density wave phase present in bulk 2H-$NbSe_2$ and in monolayer 1H-$NbSe_2$ [342]. This charge order has a higher onset temperature than the superconducting phase, with both faces concurring at low temperatures [343–352]. The different scenarios for the interplay between these phases range from competition [353–356] to mutual enhancement [357] and even to the charge order enabling the superconductivity in the first place [348].

Of primary interest to the work here is the fact that some TMDs, like $NbSe_2$ and TaS_2, are intrinsic superconductors and remain so to the monolayer limit [66, 358]. The latter is noteworthy, since the efficacy of screening decreases in two dimensions, resulting in stronger Coulomb interactions [359]. Yet other TMD monolayers, like MoS_2, develop a superconducting phase under sufficiently strong gating [360–363], e.g., by field-effect gating [364], utilizing ionic liquids [365–369], chemical doping [370, 371], or inclusion into a misfit layer compound [372].

All together, the realizations of superconductivity in systems with strong spin-orbit interaction [373–376], as well as the variety of different compounds, make TMDs an interesting platform for device manufacturing [377–381] and fundamen-

tal research [377, 378, 382]. For 1H-$NbSe_2$, the possibility of nodal topological superconducting states with Majorana flat bands has been proposed [383, 384], possibly enabling its use in future topological quantum computing platforms [384]. Furthermore, the requirements of a supercapacitor [54, 55] motivate the further search for suitable two-dimensional superconductors [385]. Beyond all these, few-layer 2H-$NbSe_2$, which shares many of the characteristics with the monolayer discussed here, displays the superconducting diode effect [386].

Driven by the conceptual similarity to the two-dimensional oxide layers in the cuprates, some authors proposed the possibility of superconductivity in the TMD monolayers originating from an unconventional Coulomb-interaction-driven mechanism. At the same time, bulk 2H-$NbSe_2$, which is a metal at high temperatures, is believed to be a conventional multigap superconductor with $T_c \approx 7\,K$ [387–394]. The conventional phonon-mediated pairing dominating in the bulk should thus still contribute to the pairing in the monolayer case [21, 22, 69, 395–399]. As such, the exact origin of the superconductivity in TMD monolayers is subject to an ongoing debate, as the relative strength of these contributions to the pairing from phonon-mediated attractive interactions and the Kohn-Luttinger mechanism remains unknown [64, 69, 400–404].

The work here is motivated by a desire to understand whether the Kohn-Luttinger mechanism is sufficiently strong in these materials to make a scenario of dominant non-phonon mediated pairing feasible, and, if so, to calculate the resulting pairing symmetry. To this end, Chapter 7 covers the discussion of screening for two-dimensional crystals. This chapter starts with the derivation of an effective two-dimensional description of the screening in the metallic 1H-TMDs, before discussing the results obtained within the random-phase approximation (RPA). Chapter 8 deals with the superconducting order induced by the screened interaction via the Kohn-Luttinger mechanism. The resulting pairing symmetries at T_c serve as an initial guess for the self-consistent calculation of the order parameter at lower temperatures, before comparing this prediction of the superconducting order to scanning tunneling spectroscopy data. The symmetry of the superconducting order has important consequences, as it affects, e.g., the possibility of driving a topological phase transition by the application of external magnetic fields [383, 400].

7

SCREENING IN TWO-DIMENSIONAL METALS

In order to properly describe interaction-induced phase transition towards superconductivity in two-dimensional metals, it is important to account for the collective nature of the electronic interactions in metals [405–414]. A convenient starting point for this task is to start from Landau's Fermi liquid theory for the metallic phase at higher temperatures. The Fermi liquid theory deals with the presence of the interaction by invoking an adiabatic connection to a known reference state of the non-interacting theory. To this end, a formerly time-independent interaction in the Hamiltonian is made time-dependent in the past ($t < 0$) using an adiabatic "turning on" as $\hat{V} \to \hat{V}e^{\epsilon t}$ with $\epsilon > 0$. Assuming the absence of any phase-transition during this turning on of the interaction, one can systematically evaluate the behavior (expectation values, response functions, etc) of the system at times $t \geqslant 0$ using the tools of quantum field theory [13, 15].

One can demonstrate the importance of considering the emergent collective behavior of many-body systems by considering the failure of simple perturbation theory to evaluate the ground state of an electron gas in the presence of a compensating homogeneous background charge ("jellium") [12, 409]. There, the collective nature of the response of the electron gas to any additional probing charge takes the form of a self-consistency problem [415]. Let $\rho(\mathbf{r})$ be the equilibrium electronic density and modify it by adding an arbitrary local charge $\delta\rho(0)$. The new charge distribution $\rho' = \rho + \delta\rho$ will, in general, not be in equilibrium since the excess charge at 0 modifies via the Coulomb interaction the electronic potential also at all $\mathbf{r} \neq 0$. Any induced charge in response to the original probing charge will, in turn, further modify the potential for all other positions. The new equilibrium distribution, including the probing charge, is thus given by a self-consistency problem whereby the sum of the original equilibrium charge, the probing charge, and the induced charges is such that it reaches a new equilibrium. It is exactly this collective nature of the response of the electron gas to additional charges, which colloquially has been dubbed *screening* of the Coulomb interaction, that has important implications for the unconventional superconductivity investigated later in this thesis.

The study of electronic systems in reduced dimensions predates the modern ability to manufacture truly atomically-thin devices [57, 58] with early exam-

ples of systems showcasing the phenomenology of electronic interactions in lower dimensions including surface states of liquid helium [416], layered compounds [417] and interfacial layers in semiconductor devices [418, 419] all of which display quasi-two-dimensional electromagnetic properties [417, 420, 421]. For thin films of dielectrics and semimetals, the reduced thickness results in weaker screening and thus conversely in stronger Coulomb interaction [422]. The reduced finite out-of-plane extent of the interacting charge distributions results in two-dimensional materials in a qualitative change between very short range, where the interaction remains finite due to the smearing of the interacting charges and long range interactions where the screening in absence of any additional dielectric environment is dominated by the induced charges in the two-dimensional material itself [423, 424]. The same phenomenology exists in metals, where the Coulomb interaction in two-dimensional materials is of much longer range than in the three-dimensional case [423], indicating the reduced efficacy of screening [425–428]. The polarizability of a two-dimensional electron gas [419, 429] represents the limiting case of a negligible impact of the lattice on the polarizability. The lattice periodic case requires the introduction of a polarizability tensor [430, 431] whose indices range over the, in principle, infinitely many vectors in the reciprocal lattice. This structure corresponds to local-field corrections of the macroscopic polarizability [432, 433]. Usually, these corrections need to be determined by a numerical calculation of sufficiently many elements of the polarizability tensor to justify a truncation. For some limit cases, there exist analytical microscopic models simplifying the calculation of such corrections due to the lattice structure [434, 435].

In two dimensions, the stability of metallic behavior at low temperatures is dependent on the density, resulting in a so-called metal-insulator transition [252, 328, 436–441]. The scaling theory of localization predicts that for non-interaction charge carriers at zero temperature no metallic phase can exist [252, 437, 442–444]. The prevailing view was long that thus at zero temperature two-dimensional metals must undergo a phase transition either via the aforementioned metal-insulator transition, or some other type of correlated phase like a superconductor [439, 440]. More recently, the observation of anomalous two-dimensional metals at low temperatures has overturned this view [382, 445, 446], with the field still actively developing.

7.1 Random phase approximation in two-dimensional metals

The divergence in the perturbative treatment of the Coulomb interaction is due to a particular class of diagrams that contains only the repeated action of the non-interacting polarizability [12]. As such, the easiest approximation that remedies this divergence is the infinite order resummation of these diagrams in the so-called random-phase approximation (RPA) [409]. Physically, this repeated action of the non-interacting polarizability corresponds to the interaction of the

induced charge with itself. Therefore, the RPA is equivalent to the self-consistent determination of the charge distribution in the presence of a source term, with the self-consistency effectively treating the interaction between any charges induced by the non-interacting polarizability [415]. Equivalently, this self-consistency implies the collective motion of the charge carriers [405, 407, 412–414], which also immediately provides an interpretation of the resulting collective excitations, the plasmons [12]. This treatment of the screening in metallic systems is by its very nature incomplete. However, it remains widely employed for two key reasons: It captures the most drastic failure of the perturbative approach, while remaining easy both conceptually and computationally. The selection of the diagrams corresponds to the corrections which have the fastest growth in r_s^{-1}, where r_s is the Wigner-Seitz radius r_s [447] in two dimensions [440], which serves as a measure of the ratio between kinetic and potential energy in an electron gas. The unitless value of r_s is indicative of the validity of different descriptions for interacting electron systems with large r_s implying a Mott-insulator phase [440, 447] and low r_s corresponding to the high-density Fermi liquid picture. The RPA becomes more accurate for small r_s, i.e., dense electron gases, providing a clear intuition for its range of validity. However, the RPA is also widely employed for real materials, where it can still yield reasonable descriptions for screening of the Coulomb interaction, provided the starting single-particle basis is chosen appropriately for the non-interacting problem [448], and r_s is not too large, typically taken to mean $r_s \leqslant 5$. To check whether this is indeed the case for the 1H-TMD monolayers of interest in the following, one can calculate r_s according to [440]

$$r_s = \frac{1}{\sqrt{\pi n a_B^2}}, \tag{7.1}$$

where n is the areal density of electrons and a_B is the effective Bohr radius. Monolayer 1H-$NbSe_2$, which is metallic at high temperatures [449, 450], is a monovalent compound resulting in $n = \Omega^{-1} = 1/(10.28\text{Å}^2)$, with Ω the area of the unit cell. The usual expression for the effective Bohr radius in two dimensions [440] is not valid for metals as it includes the constant part of the dielectric function, which is divergent in metals. The radial extent of the niobium d-shell orbitals, here taken to mean the radial position of the maximum modulus of its wavefunction at 0.789 Å [451], acts as a substitute as it governs the spatial confinement of the electron and, in turn, its kinetic energy. Taking this radius as the effective Bohr radius for the d-shell orbitals, the Wigner-Seitz radius for 1H-$NbSe_2$ turns out to be $r_s \approx 2.29$.Even with the relative uncertainty of the above approximation and r_s in general, this relatively low r_s suggests for 1H-$NbSe_2$ and similar metallic monolayer TMDs a degree of validity of the RPA.

Despite its relative ease of numerical calculation, the RPA is commonly simplified further by invoking the constant-matrix-element (CME) approximation [452–454],

which drastically reduces the numerical complexity of evaluating the polarizability tensor entering the RPA.

7.1.1 *Diagrammatic derivation of the RPA in two dimensions*

As mentioned above, there are multiple equivalent ways to derive the RPA. One of the most powerful options is to start with the diagrammatic formulation of the perturbative expansion of the two-particle Matsubara Green's functions [12, 15, 16, 455]. There, the RPA corresponds to an approximation of a fundamental two-body response function, the irreducible polarizability diagram, with the non-interacting polarizability [455]. To show this, one can start with a generic Hamiltonian of interacting fermionic (quasi-)particles

$$\hat{H} = \hat{H}_0 + \hat{V}\,, \tag{7.2}$$

where $\hat{H}_0$ is a single particle Hamiltonian whose eigenbasis is known, such that one can write

$$\hat{H}_0 = \sum_{\nu} \xi_\nu \hat{c}^\dagger_\nu \hat{c}_\nu\,, \tag{7.3}$$

where the creation (annihilation) operators $\hat{c}^{(\dagger)}_\nu$ of the quasiparticle ν follow fermionic anticommutation properties $\{\hat{c}_\nu, \hat{c}'^\dagger_\nu\} = \delta_{\nu,\nu'}$. For simplicity, one can assume here a time-independent interaction in normal order

$$\hat{V} = \frac{1}{2} \sum_{\nu_1,\nu_2,\nu_3,\nu_4} V_{\nu_1,\nu_2,\nu_3,\nu_4} \hat{c}^\dagger_{\nu_1} \hat{c}^\dagger_{\nu_2} \hat{c}_{\nu_3} \hat{c}_{\nu_4}\,, \tag{7.4}$$

with the symmetries

$$V_{\nu_1,\nu_2,\nu_3,\nu_4} = -V_{\nu_2,\nu_1,\nu_3,\nu_4} = V_{\nu_2,\nu_1,\nu_4,\nu_3} = -V_{\nu_1,\nu_2,\nu_4,\nu_3}\,, \tag{7.5}$$

$$V_{\nu_1,\nu_2,\nu_3,\nu_4} = V^*_{\nu_4,\nu_3,\nu_2,\nu_1}\,. \tag{7.6}$$

The following makes use of the notation and conventions defined in Chapter A and Section B.1. The non-interacting case of interest to the screening in two-dimensional crystals is the Bloch problem [2] of electrons in a static ionic lattice. In the following, the combination of the crystal momentum $\mathbf{k}$ inside the first Brillouin zone, the imaginary frequency $\mathrm{i}k$, and the band index ν replace the generic index ν. The free quasiparticle Matsubara Green's function (="propagator" = "fermion line") in momentum space is

$$\underset{\longrightarrow}{\mathbf{k},\mathrm{i}k,\nu} = G_0(\mathbf{k},\mathrm{i}k,\nu) = \frac{1}{\mathrm{i}k - \xi_{\mathbf{k},\nu}}\,. \tag{7.7}$$

The interaction $V_{\nu_1,\mathbf{k}_1,\nu_2,\mathbf{k}_2,\nu_3,\mathbf{k}_3,\nu_4,\mathbf{k}_4}$ simplifies due to the conservation of crystal momentum, which ensures that $\mathbf{k} = \mathbf{k}_4, \mathbf{k}' = \mathbf{k}_3$ and the momentum exchange

$\mathbf{q}$ is such that $\mathbf{k}_1 = \mathcal{Q}(\mathbf{k}+\mathbf{q}), \mathbf{k}_2 = \mathcal{Q}(\mathbf{k}'-\mathbf{q})$, where $\mathcal{Q}$ represents the projection onto the equivalent crystal momentum according to Section B.1. Introducing the shorthand $\{\nu\}$ for the set of all involved band indices, one can write the matrix element of the unscreened Coulomb interaction

$$\begin{aligned} &V(\mathbf{k},\mathbf{k}',\mathbf{q},\{\nu\}) = \langle \mathcal{Q}(\mathbf{k}+\mathbf{q}),\nu_1,\mathcal{Q}(\mathbf{k}'-\mathbf{q}),\nu_2|\,\hat{V}\,|\mathbf{k},\nu_4,\mathbf{k}',\nu_3\rangle \\ =&\frac{1}{N^2}\iint_{\mathcal{V}} d\mathbf{r}d\mathbf{r}'\,\mathbf{u}^{\dagger}_{\nu_1,\mathbf{k}+\mathbf{q}}(\mathbf{r})\mathbf{u}_{\nu_4,\mathbf{k}}(\mathbf{r})e^{-i\mathbf{q}\cdot\mathbf{r}}\mathbf{u}^{\dagger}_{\nu_2,\mathbf{k}'-\mathbf{q}}(\mathbf{r}')\mathbf{u}_{\nu_3,\mathbf{k}'}(\mathbf{r}')e^{i\mathbf{q}\cdot\mathbf{r}'}V(\mathbf{r},\mathbf{r}')\,, \end{aligned} \tag{7.8}$$

where N is the number of unit cells, and $\mathcal{V}$ denotes the volume as introduced in Section B.1. A key building block of the diagrammatics is the interaction line connecting two vertices. This interaction follows from the matrix element between the in- and outgoing states, which one can determine by inserting into Eq. (7.8) the Fourier transformation of the three-dimensional unscreened Coulomb interaction [430]

$$V(\mathbf{r},\mathbf{r}') = \frac{1}{\mathcal{V}}\sum_{\mathbf{G},\mathbf{G}',\mathbf{q}} e^{i(\mathbf{q}+\mathbf{G})\cdot\mathbf{r}}V_{\mathbf{G},\mathbf{G}'}(\mathbf{q})e^{-i(\mathbf{q}+\mathbf{G}')\cdot\mathbf{r}'}\,. \tag{7.9}$$

This specific form of the Fourier transformation is in between the general case, where one takes the Fourier transform of the coordinates $\mathbf{r}$ and $\mathbf{r}'$ independently, and the translationally invariant case $V(\mathbf{r},\mathbf{r}') = V(\mathbf{r}-\mathbf{r}')$. The screened interaction $\hat{W}$ is in between these two cases, as one needs to account for the positions $\mathbf{r}$ and $\mathbf{r}'$ within the lattice but retains translational invariance under a shift by lattice vectors, due to the periodic nature of the considered Bloch states. The following calculations use a right-handed cartesian coordinate system whose z-axis points along the crystal $\mathbf{c}$-axis, while its x-axis points along the crystal $\mathbf{a}$-axis. For a translational invariant interaction, as is the case for the unscreened Coulomb interaction, the tensor

$$V_{\mathbf{G},\mathbf{G}'}(\mathbf{q}) = \delta_{\mathbf{G},\mathbf{G}'}V_{\mathbf{q}+\mathbf{G}'} := \delta_{\mathbf{G},\mathbf{G}'}V^{3D}(\mathbf{q}+\mathbf{G}) = \delta_{\mathbf{G},\mathbf{G}'}\frac{e^2}{4\pi\epsilon_0}\frac{1}{\|\mathbf{q}+\mathbf{G}\|_2^2}\,, \tag{7.10}$$

is diagonal, which results in

$$\begin{aligned} &V(\mathbf{k},\mathbf{k}',\mathbf{q},\{\nu\}) \\ =&\frac{1}{\mathcal{V}}\sum_{\mathbf{G}}\sum_{\mathbf{q}_z} V^{3D}(\mathbf{q}+\mathbf{q}_z+\mathbf{G})F^{\nu_1,\nu_4}_{\mathbf{k}+\mathbf{q},\mathbf{k}}(-\mathbf{q}_z-\mathbf{G})F^{\nu_3,\nu_2}_{\mathbf{k}'-\mathbf{q},\mathbf{k}'}(\mathbf{q}_z+\mathbf{G})\,. \end{aligned} \tag{7.11}$$

In Eq. (7.11), the F is a shorthand for the integral

$$F^{\nu,\nu'}_{\mathbf{k},\mathbf{k}'}(\mathbf{G}) = \int_{\mathcal{V}^p} d\mathbf{r}\,\mathbf{u}^{\dagger}_{\nu,\mathbf{k}}(\mathbf{r})\cdot\mathbf{u}_{\nu',\mathbf{k}'}(\mathbf{r})e^{-i\mathbf{G}\cdot\mathbf{r}}\,. \tag{7.12}$$

These integrals of the Bloch spinors over the primitive unit cell of the lattice $\mathcal{V}^p$ occur frequently when discussing screened interactions on a lattice, and are referred

to largely interchangeably in the literature as overlaps, matrix elements [427, 452], or oscillator strengths [415, 456].

Neither of these names is truly fitting, since they are only overlaps for $\mathbf{G} = 0$, are by far not the only matrix elements occurring in the theory of screening, and are completely unrelated to any oscillator except for some simple models in which they occur [456]. Throughout this thesis, these integrals will be referred to as "overlaps", despite the above-mentioned conceptual confusion associated with this name.

More relevant to the physics of the screened interaction, the impact of the lattice depends sensitively on the shape and $\mathbf{G}$-dependence of the overlaps. Consider the "isotropic" case, inspired by a simple "s"-wave metal, where the orbitals overlap strongly between adjacent lattice sites, electron wavefunctions are itinerant and the Bloch-wave functions u in Eq. (7.12) reduce to a near constant factor, yielding the condition $F^{\nu,\nu'}_{k,k'}(\mathbf{G}) = \delta_{\mathbf{G},0} F^{\nu,\nu'}_{k,k'}(0)$, illustrating that in this case no umklapp scattering can occur. In the opposite "atomistic" limit, the Bloch functions have support only in a narrow region around the lattice sites. In this approximation, the dependence on $\mathbf{G}$ drops completely, and all $\mathbf{G}$ enter equivalently, which would imply umklapp scattering with arbitrarily high momentum exchange between the Bloch states and the lattice, which is not realistic. Indeed, one finds a divergence of the interaction strength from summing up these high-momentum umklapp processes. One can regularize this divergence by assuming a small, but finite, extent of the Bloch wavefunctions around the lattice sites, which causes a drop off of the overlaps for large $\mathbf{G}$. Real materials sit somewhere in between these two extreme cases, with the lattice yielding a finite correction via finite $\mathbf{G}$ umklapp scattering.

Returning to the problem at hand, a remaining issue with Eq. (7.11) is the three-dimensional formulation of the problem. The two-dimensional extended nature of TMD monolayers makes a treatment of the problem as effectively two-dimensional desirable. At the same time, one cannot entirely neglect the small extent of the orbitals along the out-of-plane z-axis, since the "internal" degree of freedom mediated by the multi-orbital nature of the relevant d-shell-derived metallic band of the TMDs requires the presence of this spatial dimension. There exist multiple approaches for the treatment of finite, but limited, extent of thin films in the discussion of screening in two-dimensional systems [423]. In the monolayer limit, the choice of assuming all charges to be tightly bound to the layer, such that one can neglect the q_z dependence in the overlaps F, is justified. The resulting overestimation of the interaction at extremely short distances, where the finite extent out-of-plane is noticeable [424], reduces to a minor correction in

this limit [423]. Using this approximation enables the definition of an effective two-dimensional formulation in the limit of large out-of-plane periodicities L, as

$$\lim_{L\to\infty} \frac{1}{L} \sum_{q_z} V^{3D}(\mathbf{q}+\mathbf{q}_z) = V^{2D}(\mathbf{q}) = \frac{e^2}{2\epsilon_0 \|\mathbf{q}\|_2}, \tag{7.13}$$

$$V^{2D}(\mathbf{k},\mathbf{k}',\mathbf{q},\{\nu\}) = \frac{1}{N\Omega} \sum_{\mathbf{G}} V^{2D}(\mathbf{q}+\mathbf{G}) F^{\nu_4,\nu_1}_{\mathbf{k}+\mathbf{q},\mathbf{k}}(-\mathbf{G}) F^{\nu_3,\nu_2}_{\mathbf{k}'-\mathbf{q},\mathbf{k}'}(\mathbf{G}), \tag{7.14}$$

where the impact of the z-direction reduces to the overlap integrals, which remain three-dimensional.

One can then diagrammatically represent the unscreened interaction between two Bloch states as

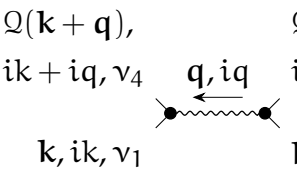

$$= -N\Omega V^{2D}(\mathbf{k},\mathbf{k}',\mathbf{q},\{\nu\}). \tag{7.15}$$

In Eq. (7.15), the interaction line itself is not defined as an isolated object, but instead retains information about the scattered states. Such a dependence on the scattered states forces the calculation of the screened interaction for each possible combination of interacting states separately, which is computationally expensive. Instead, the following will make use of the ability to split this dependence off into vertices, which, in turn, multiply the screened interaction, thereby allowing for the isolated calculation of the former without any dependence on the scattered states. To do so, one introduces the vertex for incoming momentum $\mathbf{q}$

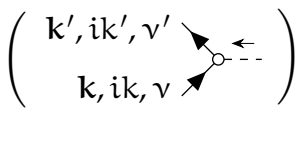

$$\begin{aligned} &= \delta_{\mathbf{G},\mathbf{G}'} \int_{\mathcal{V}_P} d\mathbf{r}\, \mathbf{u}^{\dagger}_{\mathbf{k}',\nu'}(\mathbf{r}) \cdot \mathbf{u}_{\mathbf{k},\nu}(\mathbf{r}) e^{i\mathbf{G}\cdot\mathbf{r}} \\ &= \delta_{\mathbf{G},\mathbf{G}'} F^{\nu',\nu}_{\mathbf{k}',\mathbf{k}}(-\mathbf{G}), \end{aligned} \tag{7.16}$$

and for outgoing momentum $\mathbf{q}$

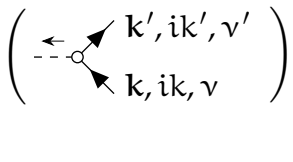

$$\begin{aligned} &= \delta_{\mathbf{G},\mathbf{G}'} \int_{\mathcal{V}_P} d\mathbf{r}\, \mathbf{u}^{\dagger}_{\mathbf{k}',\nu'}(\mathbf{r}) \cdot \mathbf{u}_{\mathbf{k},\nu}(\mathbf{r}) e^{-i\mathbf{G}\cdot\mathbf{r}} \\ &= \delta_{\mathbf{G},\mathbf{G}'} F^{\nu',\nu}_{\mathbf{k}',\mathbf{k}}(\mathbf{G}). \end{aligned} \tag{7.17}$$

The labels $\mathbf{G},\mathbf{G}'$ represent the fact that these vertices are matrix valued, with the indices ranging over the reciprocal lattice vectors and where outgoing reciprocal lattice momenta $-\mathbf{G}$ are equivalent to incoming momenta $\mathbf{G}$. The unscreened

interaction connecting them is independent of the frequency iq and takes the form

$$\left(\begin{array}{c} \mathbf{q}, iq \\ \longleftarrow \\ \text{- - - - - -} \end{array} \right)_{\mathbf{G},\mathbf{G}'} = -V^{2D}(\mathbf{q}+\mathbf{G}')\,, \tag{7.18}$$

such that one can identify the free interaction with

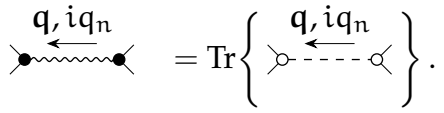

(7.19)

The vertices with flipped particle-hole legs are

$$\left(\begin{array}{c} \mathbf{k}', ik', \nu' \\ \mathbf{k}, ik, \nu \end{array} \right)_{\mathbf{G},\mathbf{G}'} = \delta_{\mathbf{G},\mathbf{G}'} F^{\nu,\nu'}_{\mathbf{k},\mathbf{k}'}(-\mathbf{G})\,, \tag{7.20}$$

$$\left(\begin{array}{c} \mathbf{k}', ik', \nu' \\ \mathbf{k}, ik, \nu \end{array} \right)_{\mathbf{G},\mathbf{G}'} = \delta_{\mathbf{G},\mathbf{G}'} F^{\nu,\nu'}_{\mathbf{k},\mathbf{k}'}(\mathbf{G})\,. \tag{7.21}$$

The diagrammatic rules for interacting fermions are [12]

- Conserve both the crystal momentum and the frequency at each vertex between a free propagator and an interaction line.
- At order n, draw all topologically distinct connected diagrams containing n interaction lines, $2n$ internal fermion lines, two external fermion lines, such that each vertex connects to one interaction line and two fermion lines.
- Add a prefactor of -1 for each closed loop of fermions.
- For each internal set of quantum numbers $\nu, \mathbf{p}, ip$ perform the sum $\frac{1}{\beta N \Omega} \sum_{\nu,\mathbf{p},p}$ with p the fermionic Matsubara frequencies.

The definition of a screened interaction in the context of these diagrammatics is the definition of a "dressed" interaction line that accounts for all allowed connected diagrams connecting to the scattered in- and out-going states by a single vertex each. As such, this definition is conceptually related but distinct from the pair-scattering vertex, which also contains an arbitrary number of successive interactions, i.e., also contains ladder diagrams, like

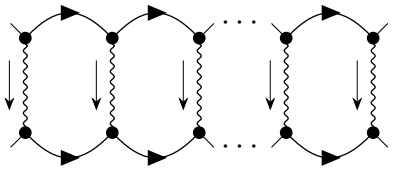

, (7.22)

which, crucially, do not enter the screened interaction. This distinction can result in conceptual confusion, especially when discussing the meaning of what one considers for the RPA, as well as which of these objects one should consider when investigating superconductivity. The discussion on the latter issue is part of Chapter 8, where it fits better thematically.

Focussing on the screened interaction, one finds that the resulting object obeys a Dyson equation of the form [12, 455]

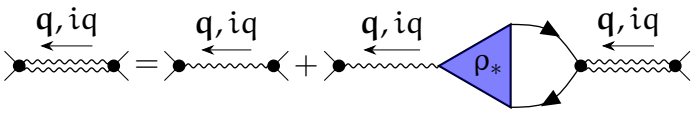

, (7.23)

where ρ_* is the proper density vertex [455]. This Dyson equation thus contains in the second term of the right-hand side the irreducible polarizabiltiy[1] P^* with its associated diagrammatic expansion.

The RPA consists of approximating the irreducible polarizability with the non-interacting polarizability, which is equivalent to considering only the leading term in the Dyson equation for the proper density vertex [455]

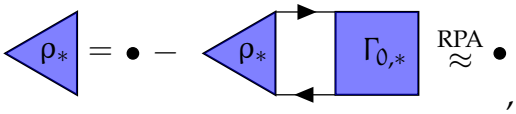

, (7.24)

where $\Gamma_{0,*}$ is the irreducible pair scattering vertex. Applying the RPA to the Dyson equation for the screened interaction yields

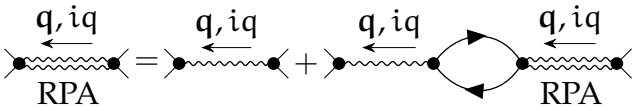

. (7.25)

This Dyson equation is solvable via a geometric series, by bringing the second term on the right-hand side of Eq. (7.25) to the left and separating the screened interaction. However, the above-mentioned dependence on the scattered states complicates this approach. To separate this dependence, one uses the fact that for all orders of the insertion of the polarizability in the Dyson equation Eq. (7.25), one can convert the unscreened interaction into a trace as

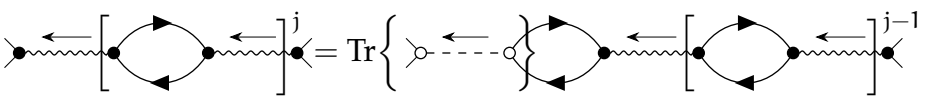

. (7.26)

1 In the textbook by Fabrizio [455], this object is referred to as the irreducible susceptibility. Textbooks disagree on this naming, and in some works [12] the distinction between polarizability and susceptibility comes down to a relative minus sign. This thesis considers the names interchangable, with no extra minus sign, and thus uses exclusively the name polarizability.

Due to the matrix structure of the vertices, one can combine two neighboring traces into a trace over a matrix product

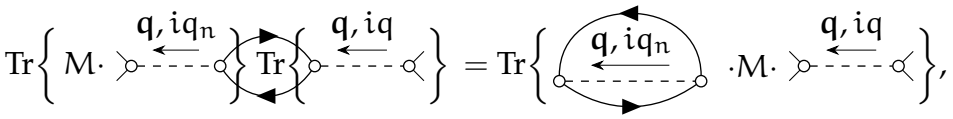

(7.27)

where M is a generic matrix in the same space. Using Eq. (7.27) recursively allows the conversion of each order in the insertion of the polarizability into a power of the same matrix, thereby recasting the Dyson equation Eq. (7.25) explicitly into the shape of a geometric series, which inside its convergence radius yields

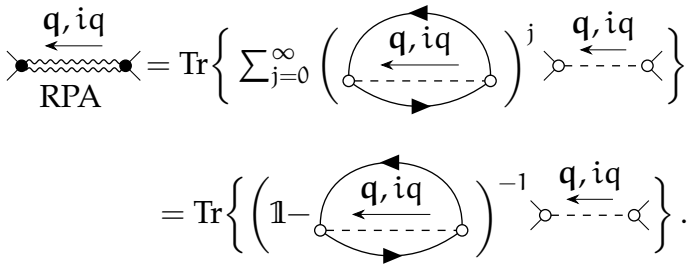

(7.28)

The Matsubara sum in Eq. (7.28) is of a standard form found in the literature [457]

$$\frac{1}{\beta}\sum_{p}\frac{1}{i(p+q)-\xi_{\mathbf{p}+\mathbf{q},\nu'}}\frac{1}{ip-\xi_{\mathbf{p},\nu}}=\frac{f(\xi_{\mathbf{p},\nu})-f(\xi_{\mathbf{p}+\mathbf{q},\nu'})}{\xi_{\mathbf{p},\nu}-\xi_{\mathbf{p}+\mathbf{q},\nu'}+iq}, \tag{7.29}$$

which yields

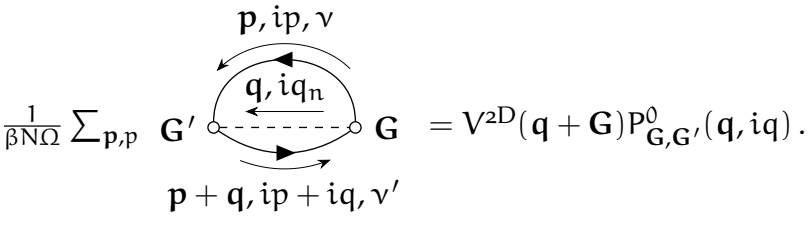

(7.30)

Here, the polarizability tensor for complex frequency iq reads

$$P^{0}_{\mathbf{G},\mathbf{G}'}(\mathbf{q},iq)=\frac{1}{N\Omega}\sum_{\mathbf{p},\nu,\nu'}\frac{f(\xi_{\mathbf{p},\nu})-f(\xi_{\mathbf{p}+\mathbf{q},\nu'})}{\xi_{\mathbf{p},\nu}-\xi_{\mathbf{p}+\mathbf{q},\nu'}+iq}F^{\nu,\nu'}_{\mathbf{p},\mathbf{p}+\mathbf{q}}(\mathbf{G})F^{\nu',\nu}_{\mathbf{p}+\mathbf{q},\mathbf{p}}(-\mathbf{G}'). \tag{7.31}$$

The linear response polarizability follows upon using the analytic continuation $iq \to \omega + i0^{+}$. The polarizability tensor as introduced in Eq. (7.31) is the two-dimensional analogue of the known result for three dimensions [430, 431].

Introducing the dielectric tensor

$$\epsilon^{0}_{\mathbf{G},\mathbf{G}'}(\mathbf{q},\omega)=\delta_{\mathbf{G},\mathbf{G}'}-V^{2D}(\mathbf{q}+\mathbf{G})P^{0}_{\mathbf{G},\mathbf{G}'}(\mathbf{q},\omega), \tag{7.32}$$

and identifying the screened interaction in analogy to Eq. (7.15) with

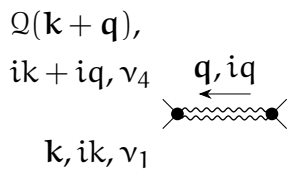

$$= -N\Omega W^{2D,RPA}(\mathbf{k},\mathbf{k}',\mathbf{q},\omega,\{\nu\})\,, \tag{7.33}$$

one can read off the two-dimensional screened interaction from Eq. (7.28) as

$$W^{2D,RPA}(\mathbf{k},\mathbf{k}',\mathbf{q},\omega,\{\nu\}) = \frac{1}{N\Omega}\sum_{\mathbf{G},\mathbf{G}'} W^{2D,RPA}_{\mathbf{G},\mathbf{G}'}(\mathbf{q},\omega) F^{\nu_4,\nu_1}_{\mathbf{k}+\mathbf{q},\mathbf{k}}(-\mathbf{G}) F^{\nu_3,\nu_2}_{\mathbf{k}'-\mathbf{q}.\mathbf{k}'}(\mathbf{G}') \tag{7.34}$$

$$W^{2D,RPA}_{\mathbf{G},\mathbf{G}'}(\mathbf{q},\omega) = \left(\left(\epsilon^0\right)^{-1}\right)_{\mathbf{G},\mathbf{G}'}(\mathbf{q},\omega) V^{2D}(\mathbf{q}+\mathbf{G}')\,. \tag{7.35}$$

Note that the calculation of the inverse precedes the selection of the tensor element in Eq. (7.35), as is indicated by the order of the brackets. Eq. (7.35) is the two-dimensional version of the known result for three dimensions [430].

A strength of this diagrammatic derivation is the relative ease with which one can extend this approach beyond the RPA and incorporate, e.g., screening due to phonon-mediated interactions with background charges [458, 459]. Furthermore, the (approximate) calculation of the pair scattering vertex in the same formalism [404] allows for the detection of phase transitions by checking for divergences in the pair scattering [404, 460–462]. It further enables a connection to the Eliashberg formalism for superconductivity [463, 464].

7.1.2 *Real space derivation*

An alternative derivation of the RPA uses a formulation in the real space [415, 465]. The Dyson equation for the screened interaction W in real space reads [430]

$$W(1,2) = V(1,2) + \int d(3,4)\, V(1,3) P(3,4) W(4,2)\,, \tag{7.36}$$

with the notation $1^{(+)} \equiv (r,\sigma,t(+0^+))$, and where V is the unscreened interaction and P the polarizability. The RPA amounts to replacing the full polarizability P with the non-interacting polarizability P^0 by dropping higher order corrections in the interaction vertex[2] ρ_* [430, 455]

$$\begin{aligned}\rho_*(1,2;3) =& \delta(1,2)\delta(1,3) + \int d(4567)\, \frac{\delta\Sigma(1,2)}{\delta G(4,5)} G(4,6) G(7,5) \rho(6,7;3) \\ \overset{RPA}{\approx}& \delta(1,2)\delta(1,3)\,,\end{aligned} \tag{7.37}$$

2 The interaction vertex is also referred to as Γ in the literature [430, 457]. This thesis follows the notation of Fabrizio for this object in order to avoid confusion with the earlier use of Γ for the pair scattering vertex.

which enters the polarizability as

$$\begin{aligned} &P(1,2) \\ &= -i \int d(34)\, G(1,3)G(4,1^+)\rho_*(3,4;2) \overset{RPA}{\approx} -iG(1,2^+)G(2,1) = P^0(1,2), \end{aligned} \tag{7.38}$$

with G the single-particle Green's function and Σ the self-energy. Note that the functional derivative of the self-energy Σ with respect to the Green's function in Eq. (7.37) is the definition of the proper irreducible two-particle vertex $\Gamma_{0,*}$ in Eq. (7.24), indicating the convergent nature of these derivations. Inserting Eq. (7.38) into Eq. (7.36) yields the Dyson equation for the screened interaction in random phase approximation

$$W^{RPA}(1,2) = V(1,2) + \int d(3,4)\, V(1,3)P^0(3,4)W^{RPA}(4,2)\,. \tag{7.39}$$

Physically, Eq. (7.39) has the same interpretation as the self-consistent field by Ehrenreich and Cohen [415], namely that the actual field experienced by charge 1 due to the presence of charge 2 should self-consistently take into account not just the bare interaction $V(1,2)$, but also the interaction of 1 with the induced charge 3 due to the, potentially non-local, effect of the presence of charge 2. The self-consistency of this condition is equivalent to accounting to all orders for the effect of inducing additional charges, highlighting the conceptual relation to the diagrammatic treatment.

The unscreened interaction V is independent of the spin, which implies $V(1,2) = V(\mathbf{r}_1, \mathbf{r}_2, t_1, t_2)$. It follows that at all orders of the Dyson equation, the screened interaction in RPA also has no dependence on spin. One can absorb the contraint $\sigma_3 = \sigma_4$ and the summation over this free spin index in the integration over $(3,4)$ into the definition of the polarizability, completly eliminating the spin dependence of the quantities occurring in Eq. (7.39). Using the properties of Fourier transforms of triple convolutions, it follows that, as long as $P^0(\mathbf{r}_3, \mathbf{r}_4, t_3, t_4) = P^0(\mathbf{r}_3, \mathbf{r}_4, t_3 - t_4)$, one can factorize the frequency dependence in real space

$$\begin{aligned} W^{RPA}(\mathbf{r}_1, \mathbf{r}_2, \omega) =& V(\mathbf{r}_1, \mathbf{r}_2, \omega) \\ &+ \int d\mathbf{r}_3\, d\mathbf{r}_4\, V(\mathbf{r}_1, \mathbf{r}_3, \omega)P^0(\mathbf{r}_3, \mathbf{r}_4, \omega)W^{RPA}(\mathbf{r}_4, \mathbf{r}_2, \omega)\,, \end{aligned} \tag{7.40}$$

where, for most applications relevant to condensed-matter theory, one can neglect retardation effects of the unscreened interaction such that $V(\mathbf{r}_1, \mathbf{r}_2, t_1, t_2) = V(\mathbf{r}_1, \mathbf{r}_2)\delta(t_1 - t_2)$ and the frequency drops for V. The screened interaction in real space is related to its momentum-space representation via [430, 431]

$$W^{RPA}(\mathbf{r}, \mathbf{r}', \omega) = \frac{1}{\mathcal{V}} \sum_{\mathbf{G},\mathbf{G}',\mathbf{q}} e^{i(\mathbf{q}+\mathbf{G})\cdot\mathbf{r}} W^{RPA}_{\mathbf{G},\mathbf{G}'}(\mathbf{q}, \omega) e^{-i(\mathbf{q}+\mathbf{G}')\cdot\mathbf{r}'}, \tag{7.41}$$

$$W^{RPA}_{\mathbf{G},\mathbf{G}'}(\mathbf{q}, \omega) = \iint d\mathbf{r}\, d\mathbf{r}'\, e^{-i(\mathbf{q}+\mathbf{G})\cdot\mathbf{r}} W^{RPA}(\mathbf{r}, \mathbf{r}', \omega) e^{i(\mathbf{q}+\mathbf{G}')\cdot\mathbf{r}'}\,. \tag{7.42}$$

The matrix element of the screened interaction with $\mathbf{k}, \mathbf{k}', \mathbf{q}$ in-plane can again be approximated with a two-dimensional object due to the strong localization of the Bloch states in the plane as

$$\begin{aligned}
&W^{\mathrm{RPA}}(\mathbf{k}, \mathbf{k}', \mathbf{q}, \{\nu\}) \\
&\quad = \langle \mathcal{Q}(\mathbf{k}+\mathbf{q}), \nu_1, \mathcal{Q}(\mathbf{k}'-\mathbf{q}), \nu_2 | \hat{W} | \mathbf{k}, \nu_4, \mathbf{k}', \nu_3 \rangle \\
&\quad = \frac{1}{N^2} \iint_{\mathcal{V}} d\mathbf{r} d\mathbf{r}' \, \mathbf{u}^{\dagger}_{\nu_1, \mathbf{k}+\mathbf{q}}(\mathbf{r}) \mathbf{u}_{\nu_4, \mathbf{k}}(\mathbf{r}) e^{-i\mathbf{q}\cdot\mathbf{r}} \mathbf{u}^{\dagger}_{\nu_2, \mathbf{k}'-\mathbf{q}}(\mathbf{r}') \mathbf{u}_{\nu_3, \mathbf{k}'}(\mathbf{r}') e^{i\mathbf{q}\cdot\mathbf{r}'} \\
&\quad \times W^{\mathrm{RPA}}(\mathbf{r}, \mathbf{r}') \\
&\quad = \frac{1}{N\Omega} \sum_{\mathbf{G}, \mathbf{G}'} \frac{1}{L} \sum_{q_z} W^{\mathrm{RPA}}_{\mathbf{G}, \mathbf{G}'}(\mathbf{q} + q_z \hat{z}) F^{\nu_1, \nu_4}_{\mathbf{k}+\mathbf{q}, \mathbf{k}}(-q_z \hat{z} - \mathbf{G}) F^{\nu_3, \nu_2}_{\mathbf{k}'-\mathbf{q}, \mathbf{k}'}(q_z \hat{z} + \mathbf{G}) \\
&\quad \approx \frac{1}{N\Omega} \sum_{\mathbf{G}, \mathbf{G}'} W^{\mathrm{2D,RPA}}_{\mathbf{G}, \mathbf{G}'}(\mathbf{q}) F^{\nu_1, \nu_4}_{\mathbf{k}+\mathbf{q}, \mathbf{k}}(-\mathbf{G}) F^{\nu_3, \nu_2}_{\mathbf{k}'-\mathbf{q}, \mathbf{k}'}(\mathbf{G}) \, . \qquad (7.43)
\end{aligned}$$

In the matrix element between Bloch states $W^{\mathrm{RPA}}_{\mathbf{G}, \mathbf{G}'}(\mathbf{q})$ does not enter directly; instead, it enters only via $W^{\mathrm{2D,RPA}}_{\mathbf{G}, \mathbf{G}'}(\mathbf{q}) = L^{-1} \sum_{q_z} W^{\mathrm{RPA}}_{\mathbf{G}, \mathbf{G}'}(\mathbf{q} + q_z \hat{z})$. Inserting this definition into Eq. (7.41), one finds for the screened interaction in-plane the form

$$W^{\mathrm{RPA}}(\mathbf{r}_{\parallel}, \mathbf{r}'_{\parallel}, \omega) = \frac{1}{N\Omega} \sum_{\mathbf{G}, \mathbf{G}', \mathbf{q}_{\parallel}} e^{i(\mathbf{q}_{\parallel} + \mathbf{G})\cdot\mathbf{r}_{\parallel}} W^{\mathrm{2D,RPA}}_{\mathbf{G}, \mathbf{G}'}(\mathbf{q}_{\parallel}, \omega) e^{-i(\mathbf{q}_{\parallel} + \mathbf{G}')\cdot\mathbf{r}'_{\parallel}} \, , \quad (7.44)$$

with $\mathbf{r}_{\parallel}, \mathbf{q}_{\parallel}$ the in-plane position and momentum, respectively. The sum over out-of-plane momenta q_z constitutes a delta function with regard to the out-of-plane component of the position, resulting in

$$W^{\mathrm{2D,RPA}}_{\mathbf{G}, \mathbf{G}'}(\mathbf{q}_{\parallel}, \omega) = \iint d\mathbf{r}_{\parallel} \, d\mathbf{r}'_{\parallel} \, e^{-i(\mathbf{q}_{\parallel} + \mathbf{G})\cdot\mathbf{r}_{\parallel}} W^{\mathrm{RPA}}(\mathbf{r}_{\parallel}, \mathbf{r}'_{\parallel}, \omega) e^{i(\mathbf{q}_{\parallel} + \mathbf{G}')\cdot\mathbf{r}'_{\parallel}} \, . \quad (7.45)$$

Inserting Eq. (7.40) into Eq. (7.45) and using the fact that $P^0(\mathbf{r}, \mathbf{r}')$ is only finite for $r_z, r'_z \approx 0$ yields

$$\begin{aligned}
W^{\mathrm{2D,RPA}}_{\mathbf{G}, \mathbf{G}'}(\mathbf{q}_{\parallel}, \omega) = &\iint d\mathbf{r}_{\parallel,1} \, d\mathbf{r}_{\parallel,2} e^{-i(\mathbf{q}_{\parallel} + \mathbf{G})\cdot\mathbf{r}_{\parallel,1}} e^{i(\mathbf{q}_{\parallel} + \mathbf{G}')\cdot\mathbf{r}_{\parallel,2}} V(\mathbf{r}_{\parallel,1}, \mathbf{r}_{\parallel,2}) \\
&+ \iiiint d\mathbf{r}_{\parallel,1} \, d\mathbf{r}_{\parallel,2} \, d\mathbf{r}_{\parallel,3} \, d\mathbf{r}_{\parallel,4} \, e^{-i(\mathbf{q}_{\parallel} + \mathbf{G})\cdot\mathbf{r}_{\parallel,1}} e^{i(\mathbf{q}_{\parallel} + \mathbf{G}')\cdot\mathbf{r}_{\parallel,2}} \\
&\times V(\mathbf{r}_{\parallel,1}, \mathbf{r}_{\parallel,3}) P^0(\mathbf{r}_{\parallel,3}, \mathbf{r}_{\parallel,4}, \omega) W^{\mathrm{RPA}}(\mathbf{r}_{\parallel,4}, \mathbf{r}_{\parallel,2}, \omega) \, . \qquad (7.46)
\end{aligned}$$

Upon inserting the reverse Fourier transformation, Eq. (7.46) becomes a Dyson equation for the screened two-dimensional intearction tensor of the form

$$\begin{aligned}
W^{\mathrm{2D,RPA}}_{\mathbf{G}, \mathbf{G}'}(\mathbf{q}_{\parallel}, \omega) = &\delta_{\mathbf{G}, \mathbf{G}'} V^{\mathrm{2D}}_0(\mathbf{q}_{\parallel} + \mathbf{G}) \\
&+ \sum_{\mathbf{G}''} V^{\mathrm{2D}}_0(\mathbf{q}_{\parallel} + \mathbf{G}) P_{\mathbf{G}, \mathbf{G}''}(\mathbf{q}_{\parallel}, \omega) W^{\mathrm{2D,RPA}}_{\mathbf{G}'', \mathbf{G}'}(\mathbf{q}_{\parallel}, \omega) \, , \qquad (7.47)
\end{aligned}$$

where $P_{G,G'}(q_\parallel, \omega)$ is the two-dimensional non-interacting polarizability defined in the same way as the interaction in Eq. (7.45), which yields the same two-dimensional polarizability tensor as obtained in Eq. (7.31). Rewriting Eq. (7.47) as a matrix equation, one recovers

$$W^{2D,RPA}_{G,G'}(q_\parallel, \omega) = (\epsilon(q_\parallel, \omega))^{-1}_{G,G'} V^{2D}(q_\parallel + G'), \tag{7.48}$$

$$\epsilon_{G,G'}(q_\parallel, \omega) = \delta_{G,G'} - V^{2D}(q_\parallel + G) P_{G,G'}(q_\parallel, \omega), \tag{7.49}$$

which is the same result as obtained in the diagrammatic derivation.

7.2 SCREENED INTERACTION IN MONOLAYER 1H-$NbSe_2$

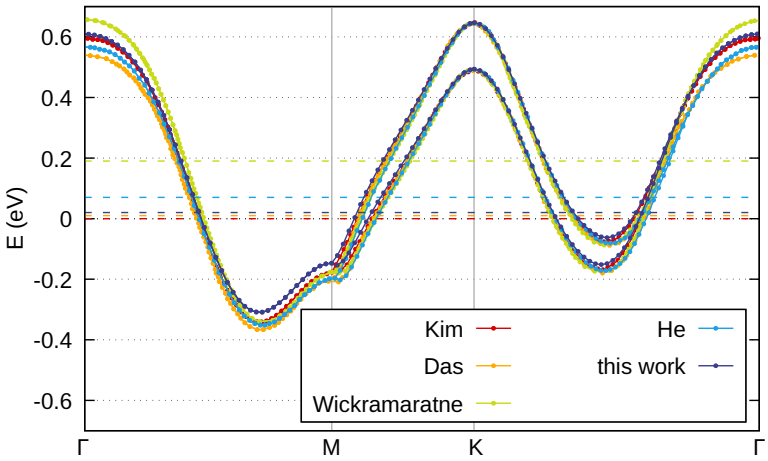

Figure 7.1: **Structure of the metallic band of 1H-$NbSe_2$ reported in the literature as obtained by different *ab initio* based approaches.** The band structures are taken from Siegl et al. [64] ("this work"), from which the figure was adopted, Kim and Son [466], S. Das et al. [69], Wickramaratne et al. [467], and He et al. [383]. The band structures agree qualitatively, but disagree on the relative height of the peaks at Γ and K (the latter being fixed here for comparison) and the position of the Fermi level (here indicated by the colored dashed lines).

Having derived the RPA form of the screened interaction in an effectively two-dimensional real material, one can turn to discussing the resulting form of the screened interaction in metallic 1H-TMD monolayers, like 1H-$NbSe_2$.Multiple works calculated the band structure of the relevant metallic band crossing the Fermi level for 1H-$NbSe_2$ within ab initio methods. Fig. 7.1 depicts the different band structures reported in the literature, with their value at the K-point aligned. The dashed lines indicate the Fermi level as obtained in the different approaches. The band structures agree qualitatively, with minor differences in the relative height of the K-points when compared to the Γ-point. The by far most-significant difference concerns the Fermi level, which has profound consequences as it changes the Fermi surfaces, and accordingly also the density of states at the Fermi level. The latter, in turn, affects the screened interaction, yielding a significant uncertainty in the efficacy of Kohn-Luttinger-like pairing in Chapter 8.

In principle, one can carry out most of the following calculations within density-functional theory, since many codes of this type include features to directly calculate optical properties like the dielectric function [431, 468]. However, in the discussion of the superconducting pairing in Chapter 8 one requires not just the polarizabiltiy but also the Bloch states entering the overlaps in Eq. (7.34), which are not commonly provided.

Faced with this issue, two approaches to approach the problem naturally present themselves: One can adopt an analytic, usually tight-binding, model for the band structure that fits the input from ab initio calculations and provides an approximate form of the eigenstates, enabling a straightforward implementation of the calculation of the screened interaction and the resulting pairing. Alternatively, one can try incorporating the Kohn-Luttinger like pairing directly into an ab initio code.

Both of these approaches have their merits, with this thesis pursuing the former. This choice is due to the relative ease of development and the ability to implement approximations like a truncation in the space of considered orbitals, which simplifies the numerical problem at the cost of sacrificing some of the accuracy of the results. Conversely, the latter approach, while slower to implement, offers a presumably more accurate description and the ability to treat the superconductivity either on the level of the Bogoliubov-de Gennes formalism [469] or even frequency-dependent within the Eliashberg formalism [463, 470–472].

Currently, there exist some codes that allow for the inclusion of the screened Coulomb interaction beyond the local μ^* corrections [473] usually employed in Eliashberg theory [69, 464] and including the spin-fluctuation mechanism [463, 474–477]. However, the existing approximate exchange-correlation functional for this description remains untested for the problem at hand and has already encountered problems when applied to simpler systems [476]. Due to the large uncertainty present in the band structures obtained within different ab initio approaches (see Fig. 7.1), one can expect the results of an ab-initio-based approach itself to remain, for now, still non-quantitative despite the much longer development time and larger computation cost when compared to the tight-binding approach. This inherent uncertainty in currently available methods thus justifies the use of approximate non-ab initio approaches, whose relatively minor additional error is compensated for by their ease of use. Such approaches can serve as first steps to gain some insight into the efficacy of different pairing mechanisms for the metallic monolayer TMDs before more quantitative approaches to the problem mature.

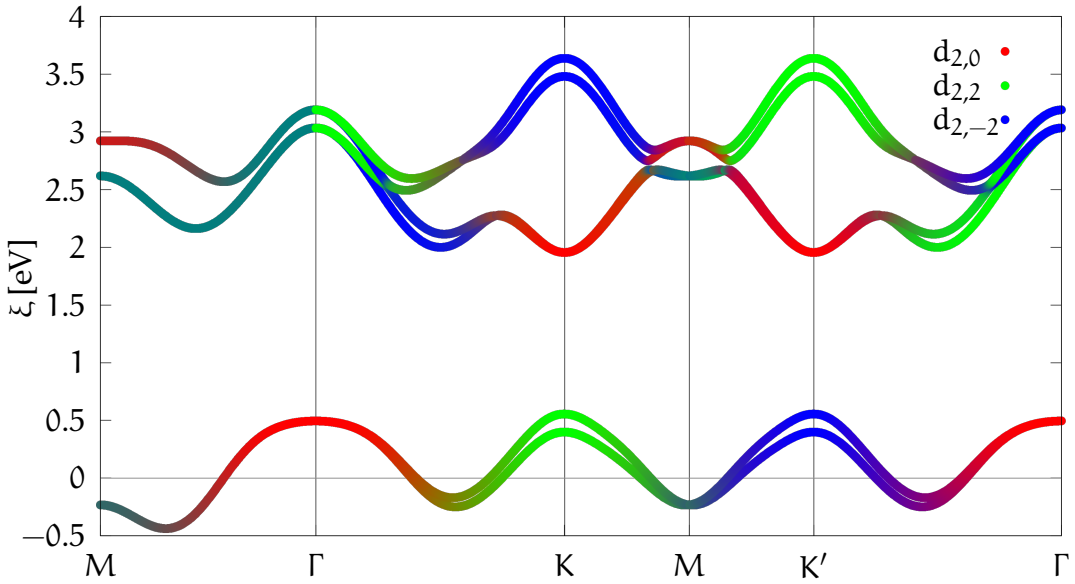

Figure 7.2: **Tight-binding band structure along high symmetry lines of monolayer 1H-$NbSe_2$ in the model of G.-B. Liu et al. [329] using the parametrization of He et al. [383].** The orbital composition in terms of the three considered niobium 4d shell orbitals is encoded as the respective RGB color values. The RGB color values encode the orbital composition in terms of the three considered niobium 4d-shell orbitals.

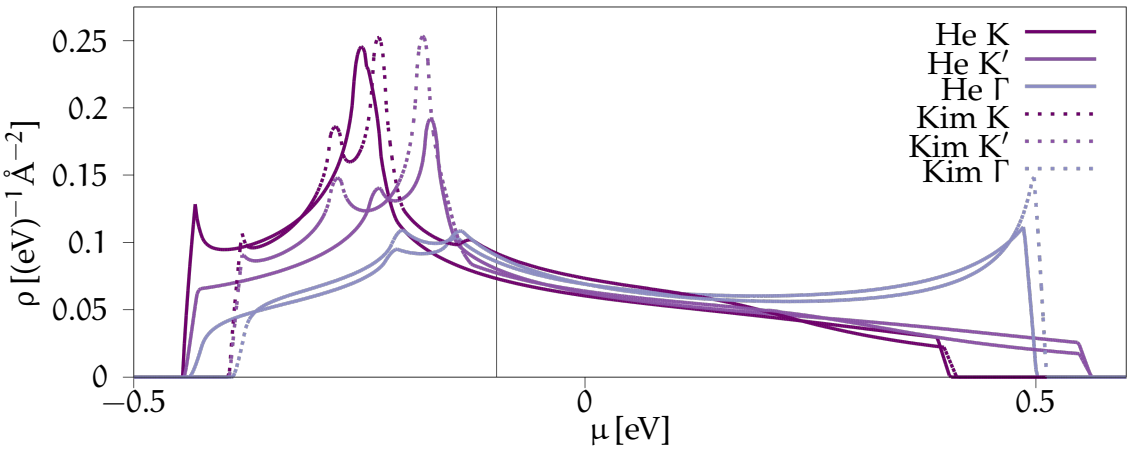

Figure 7.3: **Valley-resolved density of states for the metallic band of monolayer 1H-$NbSe_2$.** The curves correspond to the tight-binding parametrizations [329] of Kim and Son using GGA [466] and He et al. [383]. The chemical potential of the curves for Kim and Son has been shifted to align the band maximum with that of He et al., with the vertical line indicating the position of zero chemical potential before the shift.

Section C.3 introduces the three-band tight-binding model for the 1H-TMDs, which underpins the numerical calculation throughout the remainder of this part of the thesis. Fig. 7.2 depicts the composition of the included bands in terms of the three considered transition metal d-shell orbitals for monolayer 1H-$NbSe_2$, while Fig. 7.3 shows the resulting density of states for two commonly applied sets of DFT-derived parameters for this model. The densities of states are qualitatively similar between the models. In line with Fig. 7.1, their Fermi levels differ, yielding a large uncertainty in the density of states at the Fermi level and the associated Thomas-Fermi momenta.

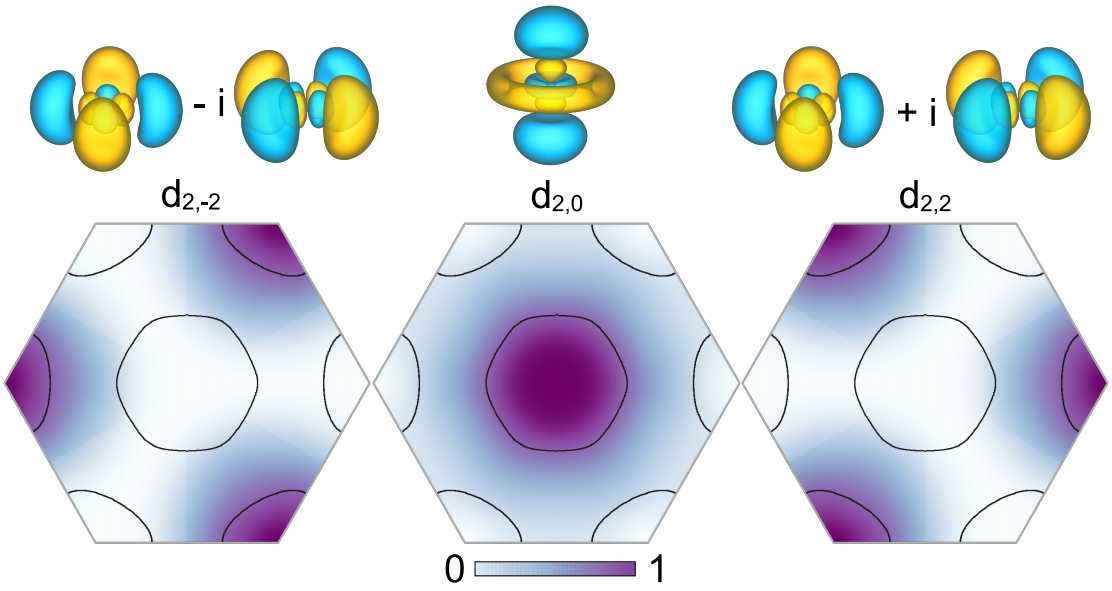

Figure 7.4: **Distribution of the three d-orbitals contributing to the metallic band of 1H-$NbSe_2$ throughout the Brillouin zone.** The calculations used the model by G.-B. Liu et al. [329] with the parametrization of He et al. [383]. The figure was adopted from Siegl et al. [64].

Fig. 7.4 shows the distribution of the three relevant d-shell orbitals for the spin up metallic band of 1H-$NbSe_2$ throughout the first Brillouin zone. The Bloch states in each Fermi pocket are strongly orbitally selective, with the states along the Γ-pocket mostly comprised of the niobium valence $d_{2,0}$ orbital. The SOI polarizes the Bloch states in the K/K′-pockets as $d_{2,2}$ and $d_{2,-2}$, respectively.

In momentum space, one expects the screened interaction in RPA no longer to follow the $1/q$-like divergence present in the unscreened interaction. Rather, this limit corresponds to the Thomas-Fermi screening, where the divergent $1/q$ dependence at low momentum exchanges gives way to a well-behaved form $1/(q + q_{\text{Thomas-Fermi}})$. The two-dimensional Thomas-Fermi screening vector is

$$q_{\text{Thomas-Fermi}} = \frac{e^2 \rho(E_F)}{2\epsilon_0}, \tag{7.50}$$

with $\rho(E)$ the density of states[3], and ϵ_0 the vacuum permittivity.

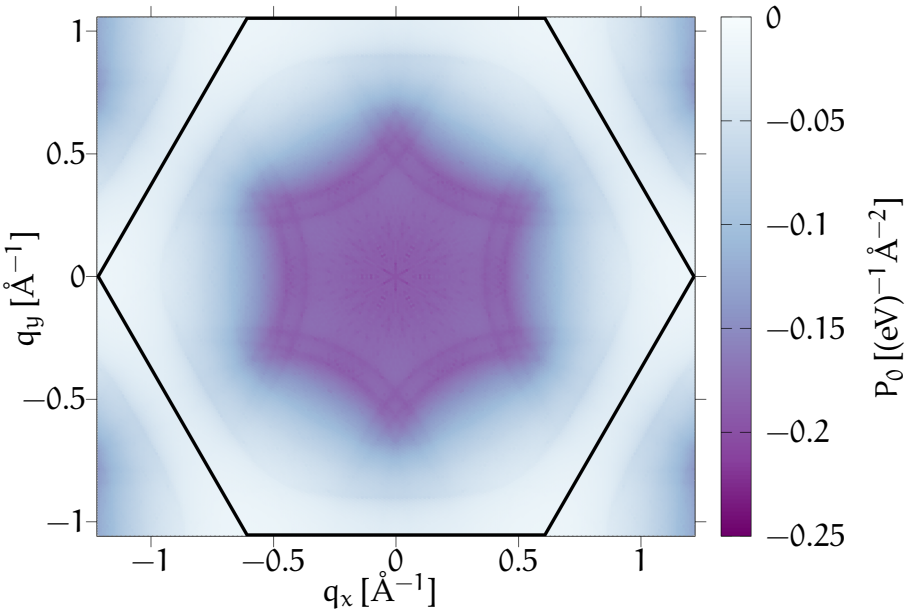

Figure 7.5: **Macroscopic polarizability $P^0_{0,0}(q)$ of monolayer 1H-$NbSe_2$.** The calculation uses the tight-binding model discussed in Section C.3 with the parameters of He et al. [383] at $\beta = 10\,\mu eV$. The black line marks the extent of the first Brillouin zone.

Fig. 7.5 depicts the macroscopic non-interacting static polarizability for 1H-$NbSe_2$.For the two-dimensional electron gas, the polarizability is constant in a circular plateau centered around the Γ point, before dropping off for larger momenta with a discontinuity of the derivative at the border of the plateau [429]. The polarizability of the metallic 1H-TMDs retains many of these features, albeit with significant modifications. First and foremost, the central "plateau" region remains visible, but the polarizability is no longer completely constant within it. Furthermore, the polarizability is no longer isotropic, but obeys the D_6 symmetry expected for non-spin-dependent quantities within the model of G.-B. Liu et al. [329].

To get an intuition for how the different tensor elements enter, Fig. 7.6 depicts the intraorbital overlap in the d_z^2 orbital for the first few reciprocal lattice vectors surrounding the origin. The calculation uses the lattice spacing of the model by He et al. [383] as introduced in the appendix Section C.3 together with a hydrogen-like wavefunction for the d-shell with effective atomic charge $Z_{\text{eff}} = 3.0796$ [478] to account for atomic screening effects of lower-lying orbitals [479]. A rapid decay for larger $|\mathbf{G}|$ is visible, justifying a treatment of the reciprocal lattice with a

3 Unfortunately, ρ also commonly denotes the density vertex in the literature. Since these objects occur in distinct contexts, there should be no confusion with keeping this duplicative notation.

simple truncation to the shown region surrounding the origin. The numerical results presented in the following use this truncation.

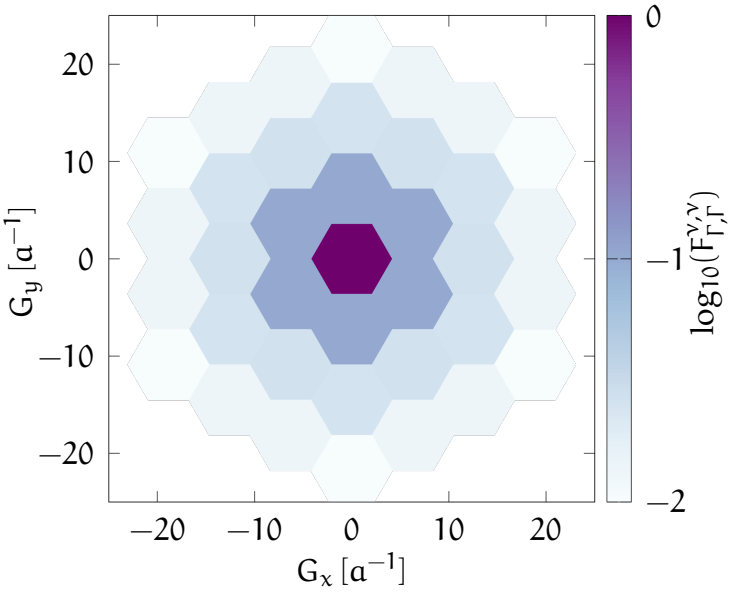

Figure 7.6: **Diagonal part of the overlap integrals for the model by He et al. [383] shown as a function of the position inside the reciprocal lattice.** Each hexagon represents the value of the overlap integral for the reciprocal lattice vector at its center in the metallic band at the Γ point, where it is independent of the spin, and where the only orbital contributing to this band is the niobium d_{z^2} orbital.

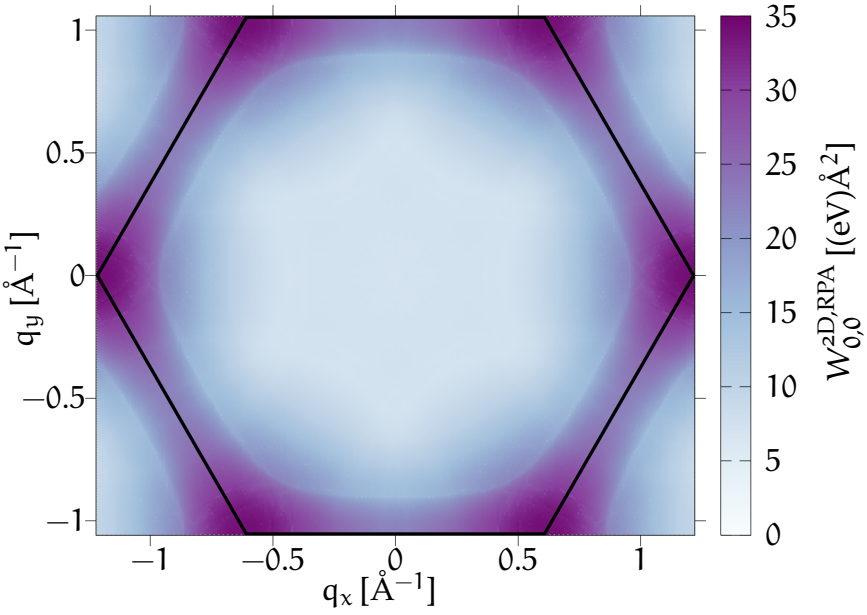

Figure 7.7: **Macroscopic two-dimensional screened interaction $W^{2D,RPA}_{0,0}(q)$ for 1H-$NbSe_2$.** The calculation uses the tight-binding model discussed in Section C.3 with the parameters of He et al. [383] at $\beta = 10\,\mu eV$. The black line marks the extent of the first Brillouin zone.

Fig. 7.7 depicts the macroscopic $(0,0)$ element of the two-dimensional screened interaction tensor, which, according to Fig. 7.6, is also the dominant contribution to the overall interaction strength. As expected from the Thomas-Fermi picture combined with the polarizability in Fig. 7.5, the interaction is weaker for small momentum exchanges $\mathbf{q}$ as compared to larger momentum exchanges. This increase of the interaction strength for larger momentum exchanges is crucial for the possibility of unconventional superconductivity in Chapter 8.

Previous works discussed the screening in real space for a two-dimensional Fermi liquid [480, 481], where, according to the Lighthill theorem [482], the discontinuity in the derivative of the polarizability at the Fermi momentum results in long-range oscillations in the screened interaction potential. These oscillations in the potential result in Friedel oscillations of the electronic density around impurities [483]. In real materials, spin-orbit interactions of the Bychkov-Rashba or Dresselhaus type can modify these oscillations by imposing beatings [484]. Making a connection to the polarizability above, the presence of more discontinuities in the derivative of the polarizability and the lack of isotropy should reflect in a modulation of the Friedel oscillations [485]. For the results presented here, the computation of the interaction strength proceeds numerically in momentum space before calculating the real-space representation of the screened interaction via a back-Fourier transform according to Eq. (7.41).

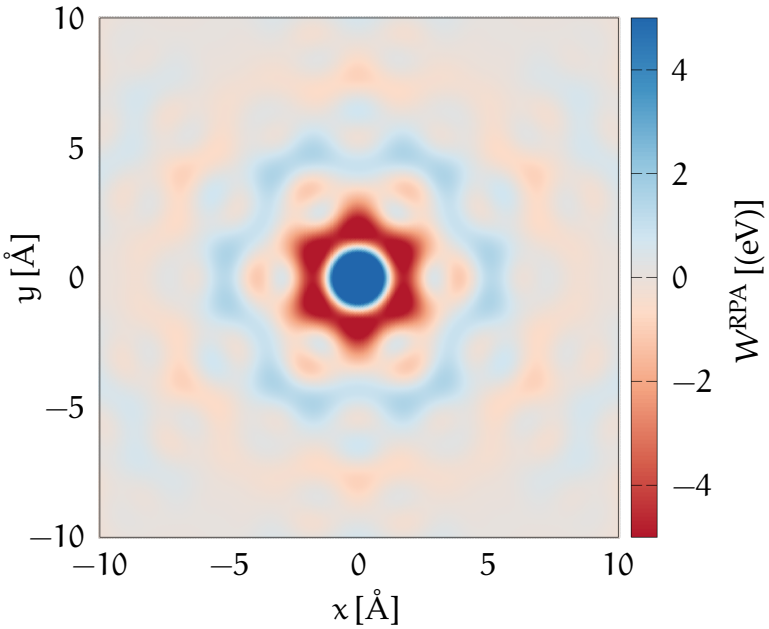

Figure 7.8: **Short-range screened interaction $W^{\mathrm{RPA}}(\mathbf{r})$ for 1H-$NbSe_2$.** The short-ranged part of the interaction displays strong oscillations on the length-scale of the underlying lattice with a pronounced on-site rpulsion (here truncated in the color scheme to highlight the oscillations). The latter suggests the possibility of treating the short-range part of the screened interaction with an effective Hubbard-Kanamori type model.

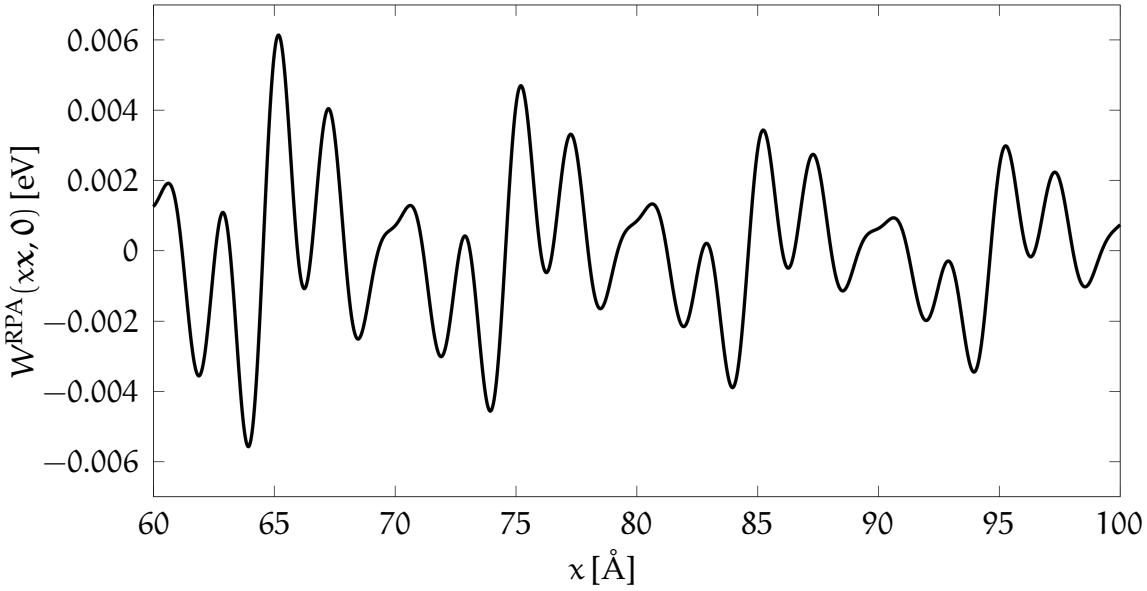

Figure 7.9: **Long-range screened interaction $W^{\mathrm{RPA}}(x\mathbf{x}, \mathbf{0})$ for 1H-$NbSe_2$.** The long-ranged part of the interaction consists of an asymptotic power-law decay with a superimposed oscillation governed by the position of the discontinuities of the derivative in the polarizability [482, 484].

Fig. 7.8 depicts the short-range part of the screened interaction as a function of the distance relative to a lattice site, i.e., $\mathbf{r}' = \mathbf{0}$. The interaction potential displays oscillations on the length scale of the underlying lattice, as opposed to the Fermi wavelength governing the oscillations in the isotropic case [481]. A Hubbard-Kanamori model can capture the pronounced on-site interaction and the interaction at the first few nearest-neighbor sites, motivating its widespread use in the literature [383, 404, 460, 486–494].

In contrast, the long-range part of the interaction, which is not captured by such a local real-space model, retains the oscillatory behavior expected from the Lighthill theorem applied to the peaked features in Fig. 7.5. Fig. 7.9 depicts these long-range oscillations along the $\mathbf{x}$-direction at large distances. The exact power law of the asymptotic decay at large distances depends on the nature of the singularities in the second derivative of the polarizability [484]. Due to the complex nature of the polarizability for the TMD monolayers, the determination of the analytical expressions for the observed long-range oscillations is subject to a follow-up effort [495] to the work published in Siegl et al. [64].

8

CHIRAL SUPERCONDUCTIVITY IN MONOLAYER 1H-$NbSe_2$

This chapter covers the superconductivity mediated by the screened Coulomb interaction discussed in Chapter 7. Section 8.1 covers different possibilities of investigating this pairing, discussing briefly their strengths and drawbacks, before introducing the approach employed for the remainder of this chapter. Section 8.2 discusses the superconductivity arising from Kohn-Luttinger-like pairing in 1H-$NbSe_2$, before Section 8.3 covers a comparison of the predicted form of the gap with scanning tunneling spectroscopy measurements performed on monolayer 1H-$NbSe_2$ in the group of M. Ugeda at the Donostia International Physics Center [64].

8.1 OVERVIEW OVER DIFFERENT DESCRIPTIONS OF SUPERCONDUCTIVITY

There exist multiple approaches for the description of superconductivity. Phenomenological modifications of the electromagnetic equations for superconductors via the London equations [496] capture some aspects of the superconducting order in isotropic superconductors, like the vanishing of resistance [20] and the expulsion of external magnetic fields [497]. The phenomenological Ginzburg-Landau theory [24] introduces a coarse-grained $U(1)$-symmetric superconducting order parameter. It allows for the treatment of spatial inhomogeneities, such as the formation of vertices in type II superconductors [498]. Phenomenological theories enable the description of a large part of the experimentally observable behavior of superconductors with comparatively low computational cost, allowing for the treatment of complex experimental setups [188, 499]. As such, they remain a vital tool even in the presence of microscopic theories.

Microscopic theories need to account for the emergence of the superconducting order from interaction, which, differently from the phenomenological approaches above, implies that the pairing via this interaction will be sensitive to the emergence of the superconducting order itself, requiring a self-consistent solution. The first truly successful theory of this type is the microscopic theory of Bardeen,

Cooper, and Schrieffer (BCS) [22]. Within this theory, the order parameter arises as an anomalous[1] expectation value,

$$\langle \hat{c}_{\bar{k},\bar{\sigma}} \hat{c}_{k,\sigma} \rangle = \Delta_{k,\sigma} \Pi(E_{k,\sigma}) \,, \qquad \Pi(E_{k,\sigma}) = \frac{\tanh(\beta E_{k,\sigma}/2)}{2E_{k,\sigma}} \,, \tag{8.1}$$

in the mean-field treatment of the interaction between pairs of electrons. In the simplest case of an isotropic, constant, attractive interaction, the anomalous expectation value then gives rise to bound-state formation of the Kramers pairs, so-called Cooper pairs, against which the zero-temperature Fermi surface is unstable [21], yielding a new superconducting ground state [395]. In the resulting theory, the isotropic (s-wave) order parameter directly reflects as a gap in the excitation spectrum of the ground state [22, 188], thereby giving rise to the common moniker "gap" for the order parameter. This theory explained key universal properties in conventional superconductors, including a fixed ratio between the critical temperature T_c and the magnitude of the superconducting order parameter at vanishing temperature of $|\Delta(T = 0\,K)| = k_B T_c \pi e^{-\gamma_{\text{Euler}}}$ [22, 166] or the jump in the specific heat at the critical temperature [500]. While the original work of BCS derived the gap equation governing the order parameter in momentum space, the Bogoliubov-de-Gennes (BdG) equations provide a real-space formulation [501]. The latter implies the Ginzburg-Landau theory [23] as a limiting case for a fixed phenomenological order parameter and close to the critical temperature T_c of the superconducting order. Intermediate approaches that combine the BdG formulation with a phenomenological order parameter enable the treatment of complex real-space geometries below T_c and the inclusion of spin-physics via spin-orbit interaction [499, 502, 503].

The constant attractive interaction assumed by BCS corresponds to the static limit of a retarded effective interaction mediated by virtual phonon-exchange [12, 396, 455]. As such, this model omits equivalent contributions from pairing mediated by the virtual exchange of other bosonic excitations [470, 504], like, e.g., plasmons [505, 506], excitons [507], and magnons [508]. Kohn and Luttinger [68] proposed an alternative mechanism for the emergence of superconductivity based on the effective pairing emerging from a repulsive interaction for higher angular momentum order parameters on a single Fermi surface. The Kohn-Luttinger mechanism induces a superconducting phase at low temperatures even for a repulsive two-dimensional electron gas in the absence of any lattice mediating a retarded attractive interaction [481, 509]. In momentum space, this pairing comes at the hand of the fermionic anticommutivity during the exchange of the constituents of a Cooper pair in a nominally repulsive scattering process. In contrast, in real space, the pairing originates from the aforementioned oscillations in the interaction potential, yielding effectively attractive regions that pairing in higher-angular momentum channels can exploit. The exchange of the (crystal-)momenta of the constituents of a Kramers pair is equivalent to the spin-fluctuation mechanism [510], which, if there is an equivalent bosonic excitation

1 Anomalous here means the fact that it vanishes in the absence of superconducting order.

of the superconductor whose virtual exchange during a scattering mediates the same action, is also equivalent to the magnon-exchange mentioned above. As such, in the following, the Kohn-Luttinger mechanism is taken as the broadest conceptual class of superconducting pairings arising from repulsive interactions, and the realization discussed here is more specifically equivalent to the spin-flip mechanism [404, 460]. This mechanism is a candidate for the pairing in a wide range of unconventional superconductors, including the cuprates [511], the iron-based superconductors [460, 488, 512–518], heavy-fermion superconductors [519], Sr_2RuO_4 [520, 521], and few-layer materials with flat bands [522, 523], although the possibility of phonon-mediated superconductivity dominating in at least some of these materials remains [524, 525]. The marginal nature of the Fermi liquid, which is often close to a transition to magnetic phases, in known unconventional superconductors like the cuprates [511], hints at these mechanisms underpinning their unconventional pairing [526]. Relevant to the discussion here, 1H-$NbSe_2$ is itself close to a magnetic instability [69, 467, 527, 528], possibly hinting at a significant contribution due to unconventional pairing [529]. As such, recent works actively discuss an unconventional origin of superconductivity in monolayer 1H-$NbSe_2$ [400–404], although the phonon-mediated conventional pairing, which dominates the bulk case [530, 531], remains viable here as well [69, 532–534]. Fig. 8.1 shows the fragmented topology of the Fermi surfaces in 1H-$NbSe_2$, which strengthens the case for unconventional pairing by enabling large differences between intravalley and intervalley scattering processes, which aids in the establishment of anisotropic gaps as required in the unconventional superconductors [403, 535].

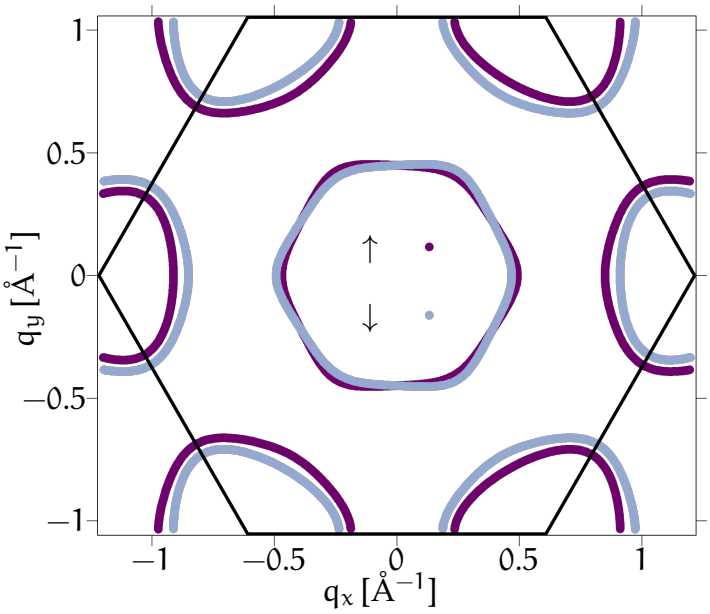

Figure 8.1: **Fermi surfaces of 1H-$NbSe_2$ for the tight-binding parameter set of He et al. [383].** The Fermi surface splits into three distinct valleys around the K, K′, and Γ points, which lend their name to the respective pockets.

To investigate the efficacy of the Kohn-Luttinger mechanism, an important starting point is the discussion of the magnitude of the resulting unconventional pairing, which is orders of magnitude below the T_c of conventional superconductors for three-dimensional simple metals [68], where, according to Migdal's theorem [504], the corrections to the phonon-mediated pairing due to Kohn-Luttinger like contributions can be neglected. However, this conventional picture, in which the Kohn-Luttinger pairing represents a minor correction to the phonon-mediated pairing, has some clear limitations. Firstly, it fails to account for the presence of unconventional superconductors, such as the cuprates, where the pairing likely originates from electronic interactions in the effectively two-dimensional oxide layers [526, 536, 537]. Secondly, the weaker screening of the Coulomb interaction in two dimensions [423, 481] violates the assumptions made in the original work on the effective phonon-mediated interaction [396].

To determine the critical temperature T_c of pairing via the Kohn-Luttinger mechanism, one must first select an appropriate description of the problem. In general, superconducting pairing can occur at finite momenta [538, 539], all combinations of spins in the constituents of the Cooper pair, i.e., spin-singlet and x, y, and z-triplets [540], and even between multiple bands [402]. In addition to these options, the treatment of the interplay between charge-density-wave formation and superconductivity further complicates matters. Accounting for all of these possibilities renders the problem much more complex than is required for 1H-$NbSe_2$ for multiple reasons; Both the finite-momentum FFLO-phase and the same-spin x and y-triplet pairings arise for 1H-$NbSe_2$ only in the presence of strong Rashba-type spin-orbit interaction [400] or strong in-plane magnetic fields [400, 490, 541, 542] via singlet-to-triplet conversion [541, 543–545]. However, the z-triplet arises from opposite-spin pairing in the same way as the spin-singlet, allowing for singlet-triplet mixing in the realized order parameters due to the violation of the inversion symmetry [489]. One can omit the inclusion of multiple bands in the discussion, since there is only a single metallic band crossing the Fermi level. However, the fact that this band crosses the Fermi level multiple times, yielding topologically distinct Fermi surfaces, results in multivalley superconductivity [546], which is similar to multiband superconductivity [547, 548] both conceptually[2] and physically. The restriction to the metallic band still yields multi-orbital unconventional superconductivity as in some iron-based superconductors [460, 486]. Regarding the charge-density wave, this thesis proceeds under the simplifying assumption that this type of charge-order represents a concurrent type of order that only weakly interacts with the superconducting pairing, as argued by Hsu et al. [489].

At this point, one faces a choice between multiple possible approaches to determine the critical temperature and other properties of the superconducting

2 Both amount to an arbitrary separation in the summation over all quantum numbers of the system in the gap equation.

phase. The following comprises a short, and necessarily incomplete, list of such approaches to the problem, including their benefits and drawbacks.

- The order parameter within the Ginzburg-Landau theory follows from the minimization of the corresponding free energy [401]. The process itself is computationally very cheap and provides a form of the gap in the vicinity of T_c, where the Ginzburg-Landau theory is valid [23]. However, the above requires knowledge of the form of the free energy, which is often not available except through phenomenological modeling. Furthermore, the resulting form of the order parameter is not valid at temperatures below T_c, which are relevant to many experiments.
- One can solve the BCS self-consistency equation, which remains valid at low temperatures. Many works consider model interactions [22, 383, 400, 401, 403], but one can also insert the screened interaction [472] itself. The computational cost remains limited near T_c, where the gap equation can be linearized, allowing for the inclusion of the full momentum dependence of the interaction. However, the inclusion of all momenta is costly when combined with the required energetic resolution inside the gap. Beyond these issues, the underlying assumptions of weak coupling cause this theory to fail for stronger coupling, where a BCS-Bose-Einstein-condensate crossover occurs [549, 550].
- In principle, the minimization of the free energy within the BCS ansatz yields the gap equation as the condition for an extremum. As such, one can equivalently determine the gap by numerically minimizing the free energy. However, the exact form of the free energy is often unknown and, as such, only phenomenologically modelled [383]. Furthermore, not all extrema correspond to physically stable solutions, requiring the careful imposition of additional constraints on the minimization [402].
- Renormalization group techniques [400, 489] allow for a potentially more accurate determination of T_c, provided the model captures the underlying physics. However, the high computational cost of more elaborate models of the interaction results in the common use of simpler approximate models, such as piece-wise constant interactions [400] or Hubbard models [489].
- Evaluating the pair scattering vertex [404, 455, 460, 488] offers the option to go beyond RPA and is a commonly used tool in the investigation of other correlated phases [461, 462]. As pointed out in Chapter 7, the pair scattering vertex goes beyond the screened interaction by including, via its Dyson equation [455], also higher orders in the interaction. The latter often necessitates the limitation to simple models for the interaction, like the Hubbard-Kanamori model [404]. The hallmark of a phase transition, including the onset of superconducting order, is the divergence of the pair scattering vertex at the critical value of the varied parameter [12, 404]. The latter is usually the temperature, enabling a straightforward

determination of the critical temperature. However, this same property results in this approach not yielding any information on the behavior of the gap at lower temperatures. Despite some works utilizing the pair-scattering vertex in determining the effective interaction entering the BCS gap equation [460, 488], it is worth noting that this procedure is only valid above T_c, where the vertex has not yet diverged. Entering the static pair scattering vertex itself into a non-frequency-dependent gap equation at or below T_c is mathematically nonsensical, as only the frequency dependence of the pair scattering vertex and the order parameter combined yields finite results in the fully frequency-dependent DMFT/Eliashberg/SCDFT approaches.

- Finally, ab-initio-based calculations that include an approximate functional for the spin-fluctuation-mediated contribution to the pairing [471, 472, 551, 552] offer a potentially quantitative, if numerically very costly, approach to the problem. As pointed out in Chapter 7, the recent advances in this field are promising. However, there currently does not exist a reliable method to control the uncertainty in the results, even for simpler geometries of the Fermi surfaces and fewer orbitals [474, 476], rendering the results still largely qualitative in nature. This remaining uncertainty, combined with the high computational cost, therefore limits the applicability of this approach for now.

All of the methods above have their strengths and their drawbacks, rendering the choice of the most suitable approach dependent on the problem at hand. In this thesis, the aim is to extend existing works on the feasibility of Kohn-Luttinger-like pairing [400–404] by utilizing a realistic interaction beyond the strongly parameter-dependent models employed so far. The resulting superconducting order is then compared with scanning tunneling spectroscopy measurements carried out well below T_c to determine the feasibility of the predicted gap symmetry. These requirements rule out any approach limited to the pure determination of T_c. The relative computational and conceptual ease of working with the BCS gap equation makes it the logical choice for the remainder of the thesis. However, once the SCDFT/DMFT approaches mature further, they should be employed to complement the results obtained here. Specifically, they should offer the possibility to settle some issues that arise in the following partially phenomenological modelling, such as the interplay between the Kohn-Luttinger-like pairing discussed here and the, undoubtedly still present, contribution from conventional phonon-mediated pairing.

Before continuing with the BCS gap equation, it is helpful to briefly argue why one should consider the static screened interaction when applying it to the Kohn-Luttinger-like pairing. In the quantum field theoretical approach [15, 553], the order parameter corresponds to an anomalous Green's function [504, 554, 555] whose frequency dependence has physical consequences, e.g., in the optical properties of a superconductor. Importantly, the screened interaction enters the

frequency-dependent pairing inside an integral over the imaginary part of the pair scattering vertex, which, according to the Kramers-Kronig relation, reduces to an effective pairing interaction given by its static real part [460, 486]. Selecting from this pairing only the contribution that does not contain ladder diagrams, thus ensuring it does not diverge at the onset of superconductivity, yields a gap equation where the pairing interaction is limited to the static screened interaction. The resulting gap equation, containing the screened interaction, reads

$$\Delta_{\mathbf{k},\sigma} = -\sum_{\mathbf{k}'} W_{\mathbf{k},\mathbf{k}',\sigma} \Pi(E_{\mathbf{k}',\sigma}) \Delta_{\mathbf{k}',\sigma}\,, \tag{8.2}$$

where $W_{\mathbf{k},\mathbf{k}',\sigma} := \langle \mathbf{k}', \sigma; \bar{\mathbf{k}}', \bar{\sigma} | \hat{W} | \mathbf{k}, \sigma; \bar{\mathbf{k}}, \bar{\sigma} \rangle$ is the matrix element of the screened interaction between Kramers pairs of Bloch states in the metallic band. By definition, the order parameter in Eq. (8.2) is not independent for different spin species. Instead, the condition $\Delta_{\mathbf{k},\sigma} = -\Delta_{\bar{\mathbf{k}},\bar{\sigma}}$ indicates that it is sufficient to determine the gap for one spin orientation before using this property to obtain the gap for the remaining spin orientation. The same gap equation follows from the SCDFT treatment if one retains only the Kohn-Luttinger-like contribution to pairing, as seen, e.g., in Eqs. 73 and 75 in chapter 16, page 18 of Pavarini et al. [472] in the limit $g \sim 0$. This form of the odd-spin pairing and time-reversal symmetric BCS gap equation with the screened Coulomb interaction underpins the remaining results about Kohn-Luttinger-like superconductivity in 1H-$NbSe_2$.

8.2 Kohn-Luttinger induced superconducting order in 1H-$NbSe_2$

In principle, the sum over momenta in the gap equation Eq. (8.2) runs over all momenta. However, states close to the Fermi level contribute more to the pairing due to the energetic suppression of contributions with $|\Delta_{\mathbf{k}',\sigma}|/|E_{\mathbf{k}',\sigma}|$. To limit the computational complexity of the problem, one can either employ kernel-polynomial methods [556, 557], or restrict the calculation to the vicinity of the Fermi surfaces, where most of the relevant pairing occurs [401]. This thesis employs the latter approach, which has the benefit of evading the large number of expansion components necessary to reach the required sub-gap energetic resolution [490].

To restrict the gap equation to the vicinity of the Fermi surfaces, one can introduce an energy range Λ, and truncate the sum over $\mathbf{k}'$ in the gap equation to include

only momenta with $|\xi_{k',\sigma}| \leqslant \Lambda$. Splitting the remaining sum as $k' = k'_F + k'_\perp$, the gap equation for momenta on the Fermi surface reads

$$\begin{aligned}
\Delta_{k_F,\sigma} &= -\sum_{k'_F}\sum_{k'_\perp} W_{k,k',\sigma}\Pi(E_{k',\sigma})\Delta_{k',\sigma} \\
&\approx -\sum_{k'_F}\sum_{k'_\perp} W_{k,k'_F,\sigma}\Pi(E(\xi_{k',\sigma},\Delta_{k'_F,\sigma}))\Delta_{k'_F,\sigma} \\
&= -\sum_{k'_F} W_{k,k'_F,\sigma}\Delta_{k'_F,\sigma}\int_{-\Lambda}^{\Lambda} d\xi\, \rho_{k'_F,\sigma}(\xi)\Pi(E(\xi,\Delta_{k'_F,\sigma})) \\
&\approx -\sum_{k'_F} W_{k,k'_F,\sigma}\Delta_{k'_F,\sigma}\rho_{k'_F,\sigma}\alpha(\Delta_{k'_F,\sigma},\beta,\Lambda)\,, \qquad (8.3)
\end{aligned}$$

$$\alpha(\Delta,\beta,\Lambda) = \int_{-\Lambda}^{\Lambda} d\xi\,\Pi(E(\xi,\Delta)) = \int_0^{\lambda} d\xi\,\frac{\tanh(\beta E(\xi,\Delta)/2)}{\xi}\,, \qquad (8.4)$$

where $\rho_{k,\sigma}(\xi)$ is a local density of states in the momentum space perpendicular to the Fermi surface[3], and where one uses two approximations based on the smallness of the energy window Λ. In the first step, the approximation $k' \approx k'_F$ eliminates $k'_\perp$ from the gap and the matrix element of the interaction. In the second step, one can approximate the integral over the quasiparticle energy, and thus the momentum direction perpendicular to the Fermi surface, by considering a constant local density of states $\rho_{k',\sigma}$ within the narrow energy range around the Fermi surface. Figs. 7.1 and 7.3 illustrate that this approximation holds for 1H-$NbSe_2$ for the different Fermi levels predicted in the literature.

While simpler than the full gap equation Eq. (8.2), Eq. (8.3) is still a self-consistent equation due to the occurrence of $\Delta_{k'_F,\sigma}$ on its right-hand side. For the study of the critical temperature, one can linearize the gap equations using the fact that, close to T_c, all $\Delta_{k,\sigma} \approx 0$ [4]. Defining a vector $\boldsymbol{\Delta_\sigma}$ of the gaps along the Fermi surfaces, with the momenta acting as its indices, this vector fulfills close to T_c the condition

$$(\mathbb{1} + \alpha(0,\beta,\Lambda)\mathbb{U}_\sigma)\cdot\boldsymbol{\Delta}_\sigma = 0\,, \qquad (\mathbb{U}_\sigma)_{k,k'} = W_{k,k',\sigma}\rho_{k',\sigma}\,. \qquad (8.5)$$

The possible solutions to the gap equation, together with their respective critical temperatures, obey the condition that at their respective critical temperatures,

3 There are multiple possible definitions, which differ in their normalization of the density of states. Here, the local density of states is cumulative in a summation over k and thus includes the integral over the line element dk_F along the Fermi surface between two neighboring momenta. As such, the density of states at the Fermi surface is $D_\sigma = \sum_{k\in FS}\rho_{k,\sigma}$.

4 Since all momenta in the following discussion are on the Fermi surfaces, one can discard the subscript F in the following.

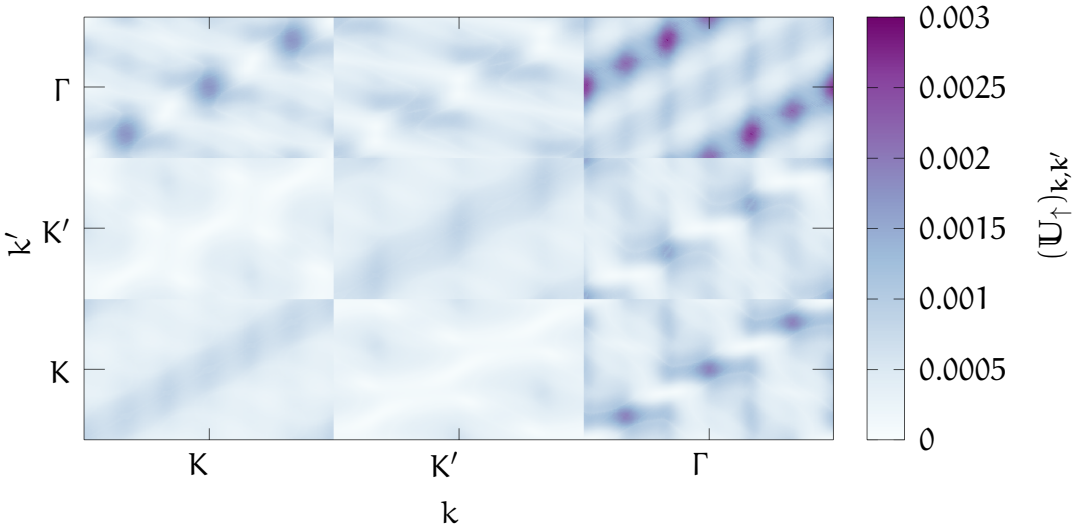

Figure 8.2: **The pairing kernel $\mathbb{U}_\uparrow$ between the three distinct Fermi surfaces.** The strongest pairing occurs between states on the opposite sites of the Γ-pocket, favoring p-like gap symmetries. The Fermi surfaces are sampled along each Fermi surfaces with 240 equidistant angles relative to the center point K, K', Γ of the respetive surface.

they are eigenvectors of the pairing kernel [400, 404, 460, 488] $\mathbb{U}_\sigma$ with the real eigenvalue[5]

$$\lambda_i = \frac{-1}{\alpha(0, T_{c,i}, \Lambda)} \,. \tag{8.6}$$

Fig. 8.2 depicts the pairing kernel for the interaction calculated in Section 7.2, where the dominant pairing occurs between states in opposing sides of the Γ-pocket. Contrary to previous models [400, 403, 467], the Γ-pocket is not just a spectator in this calculation, instead favoring the emergence of p-like pairing.

For fixed cutoff Λ, $\alpha(0, T, \Lambda)$ is a monotonically decreasing function of T, thereby identifying the highest T_c with the lowest negative eigenvalue of $\mathbb{U}_\sigma$. Since $\mathbb{U}_\sigma$ is, by construction, a square matrix, one can calculate the eigensystem using standard solvers, such as the Numpy function linalg.eig() [558]. For a repulsive interaction, each element of $\mathbb{U}_\sigma$ is positive and real. Hence, any gap satisfying Eq. (8.2) for a repulsive interaction necessarily is anisotropic [519]. The pairing kernel inherits the symmetry of the crystal, resulting in solutions that fall within the irreducible representations of the crystal's symmetry group. Since the in-plane momentum dependence of the gap necessarily is symmetric under σ_h, one can restrict the following considerations to the smaller group D_3, which is equivalent

5 The cumulative form of $\rho_{k,\sigma}$ in the summation over momenta ensures that the eigenvalues of $\mathbb{U}_\sigma$ become, for sufficiently high resolution, independent of the number of sampled momenta along the Fermi surface.

to the three irreducible representations A_1', A_2', and E' of D_{3h} as discussed in Section B.2.

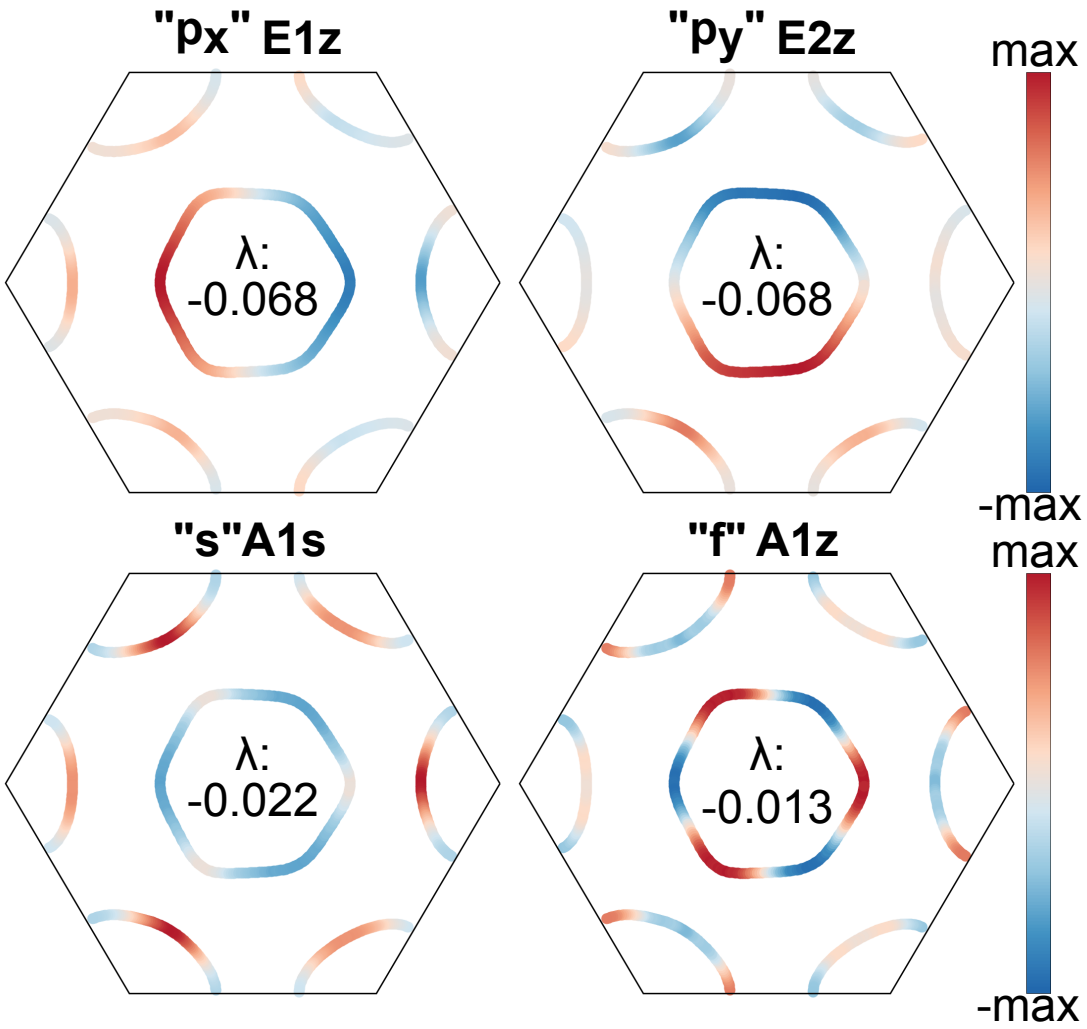

Figure 8.3: **Solutions with the highest T_c in the linearized gap equations.** The leading solutions are two degenerate solutions within the E' irreducible representation of the crystal. The figure was adopted from Siegl et al. [64].

Fig. 8.3 depicts the four solutions leading in their respective T_c as mediated by the Kohn-Luttinger mechanism. It further lists their respective eigenvalue as obtained from the interaction calculated in Section 7.2. The leading solutions are two degenerate solutions within the E irreducible representation, which, in the presence of inversion symmetry, would roughly correspond to the p-wave gaps. This finding is in agreement with the model calculation by Roy et al. [404]. The next two solutions are the A_1 s-like and f-like solutions, which other works considered as candidates for the ground state symmetry [400–403]. Note, though, that the classification in terms of s/p/d/f/...-wave gaps breaks down in the absence of inversion symmetry since different such solutions within the same irreducible representation of the crystal's symmetry group can mix [489]. This

mixing is clearly evident in the s-like and f-like solutions, both of which are nodal on either Fermi surface, despite the former having a larger component of the A_1 singlet than the A_1 z-triplet. In the absence of SOI, the singlet corresponds to the pure s-wave solution, while the z-triplet corresponds to the pure f-wave solution.

The value λ required to match the experimental T_c depends on the cutoff Λ. The choice of Λ is somewhat arbitrary, since contributions at energies $|\xi| \gg |\Delta|$ only enter the gap equation strongly suppressed. Instead, the main effect of Λ is to act as a reference scale across which the considered pairing acts. Similar to the Debye frequency [559] in the standard BCS treatment [22, 166], this energy scale enters the T_c linearly. In contrast, the product of the interaction and the density of states, and thus the eigenvalue λ, enters the expression for the critical temperature inside an exponential, rendering any uncertainty in these quantities much more relevant. Taking $\Lambda = 100\,\mathrm{meV}$, the λ required for $T_c = 2\,\mathrm{K}$ is $\lambda = -0.154$ which is lower than any any of the eigenvalues in Fig. 8.3. Therefore, the pairing strength $|\lambda|$ from the Kohn-Luttinger mechanism as obtained here is too small to explain the experimental $T_c \approx 2\,\mathrm{K}$, observed in both epitaxially grown [63] and mechanically exfoliated samples [560].

At the same time, the contribution by the Kohn-Luttinger mechanism is not a small correction either, as previously assumed in some works [69, 561]. Importantly, considering an additional small[6], constant, and attractive component of the interaction, perhaps counterintuitively, enhances the pairing strength. Such a synergetic interplay between conventional and unconventional pairing [562] raises the possibility of a scenario where the Kohn-Luttinger mechanism alone is not sufficient to explain the observed pairing strength, but where it remains the dominant contribution, with the phonon-mediated interaction amplifying it to explain the larger experimentally observed T_c. Unfortunately, the considerable uncertainty in determining the screened interaction complicates definitive statements. Both a scenario where the phonon-mediated interaction dominates outright and one where the isolated Kohn-Luttinger pairing yields the observed T_c are possible within the errors inherent to this calculation. The feasibility of two such diametrically opposed scenarios yet again demonstrates the current lack of certainty, until the aforementioned ab-initio-based approaches to the problem become sufficiently quantitative to settle the open questions regarding the ratio between the unconventional and conventional pairing in 1H-$NbSe_2$.

For now, one can proceed by determining whether the superconducting ground state predicted by dominant Kohn-Luttinger-mediated pairing is compatible with experimental evidence. To this end, and explicitly phenomenologically, one can rescale the pairing kernel $\mathbb{U}_\sigma$ with a parameter γ to fit the T_c of the theory to the experimental critical temperature. This procedure amounts to the fitting of the interaction strength that is commonly applied in the field [400, 403, 404], while

6 Such that $|V_{\mathrm{BCS}}| < \min_{\mathbf{k},\mathbf{k}',\sigma} W_{\mathbf{k},\mathbf{k}',\sigma}$.

keeping the relative strength of the contributions in the interaction fixed, thereby ensuring that no transition in the leading solutions [404] occurs.

To do so, one needs to determine the solution to the BCS gap equation below T_c from the solutions to the linearized gap equation. The starting point for such a calculation is Eq. (8.3), which, however, still represents a potentially high-dimensional self-consistency problem. One can simplify this problem by neglecting some of the momentum dependence, e.g., through a piece-wise constant interaction [400, 401, 403] or by projecting onto a limited set of basis functions [400, 401].

Following the latter approach, one expands the gap for one spin orientation in terms of a limited set of basis functions as

$$\forall_{\mathbf{k}\in\pi}: \quad \Delta_{\mathbf{k},\uparrow} = \sum_{\mu} f^{\pi}_{\mu}(\mathbf{k})\Delta^{\pi}_{\mu}\,, \tag{8.7}$$

where μ labels basis functions and $\pi \in \{\Gamma, K\}$ labels the Fermi surfaces, where K and K' are combined. Accounting for the number N_π of momenta sampled on each Fermi surface π, one can define an inner product on each Fermi surface

$$\langle f^{\pi}_{\mu}, f^{\pi}_{\mu'}\rangle_{\pi} := \frac{1}{N_\pi}\sum_{\mathbf{k}\in\pi} f^{\pi}_{\mu'}(\mathbf{k}) f^{\pi}_{\mu}(\mathbf{k})\,. \tag{8.8}$$

By choosing the basis functions orthonormal on each Fermi surface, i.e., enforcing $\langle f^{\pi}_{\mu}, f^{\pi}_{\mu'}\rangle = \delta_{\mu,\mu'}$, one can project out the expansion coefficients according to

$$\Delta^{\pi}_{\mu} = \sum_{\mathbf{k}\in\pi} f^{\pi}_{\mu}(\mathbf{k})\Delta_{\mathbf{k},\uparrow}\,. \tag{8.9}$$

Inserting Eqs. (8.7) and (8.9) into Eq. (8.3) yields

$$\Delta^{\pi}_{\mu} = -\frac{1}{N_\pi}\sum_{\pi',\mu'}\sum_{\substack{\mathbf{k}\in\pi\\ \mathbf{k}'\in\pi'}} f^{\pi}_{\mu}(\mathbf{k})(\mathbb{U}_{\uparrow})_{\mathbf{k},\mathbf{k}'}\alpha(\Delta_{\mathbf{k}',\uparrow},\beta,\Lambda) f^{\pi'}_{\mu'}(\mathbf{k}')\Delta^{\pi'}_{\mu'}\,. \tag{8.10}$$

At T_c, this equation simplifies, and the orthogonality Eq. (8.8) yields a linearized gap equation for the expansion coefficients

$$\Delta^{\pi}_{\mu} = -\alpha(0,\beta,\Lambda)\sum_{\pi',\mu'} U^{\pi,\pi'}_{\mu,\mu'}\Delta^{\pi'}_{\mu}\,, \tag{8.11}$$

where the pairing matrix $\mathbb{U}$ in this representation is given by

$$U^{\pi,\pi'}_{\mu,\mu'} = \frac{1}{N_\pi}\sum_{\mathbf{k}\in\pi,\mathbf{k}'\in\pi'} f^{\pi}_{\mu}(\mathbf{k})(\mathbb{U}_{\uparrow})_{\mathbf{k},\mathbf{k}'} f^{\pi'}_{\mu'}(\mathbf{k}')\,. \tag{8.12}$$

Below T_c, no such simple equation coupling the expansion coefficients exists due to the momentum dependence of α. However, one can also expand the

product $\alpha(\Delta_{k',\sigma}, \beta, \Lambda) f_\mu^{\pi'}(k')$ itself in terms of the basis functions. Introducing the expansion coefficients

$$\Upsilon^{\pi}_{\mu,\mu'}(\boldsymbol{\Delta}_\uparrow) = \frac{1}{N_\pi} \sum_{k \in \pi} f^{\pi}_{\mu}(k) \alpha(\Delta_{k,\uparrow}, \beta, \Lambda) f^{\pi}_{\mu'}(k)\,, \tag{8.13}$$

one finds the self-consistent gap equation for the expansion coefficients

$$\Delta^{\pi}_{\mu} = -\sum_{\pi',\mu',\mu''} U^{\pi,\pi'}_{\mu,\mu'} \Upsilon^{\pi'}_{\mu',\mu''}(\boldsymbol{\Delta}_\uparrow) \Delta^{\pi'}_{\mu''}\,. \tag{8.14}$$

For an incomplete basis, the above is equivalent to an approximate insertion of unity, which remains valid provided the product αf is well-described by an expansion in terms of the available basis functions. Since for small values of the gap $\alpha(\Delta_{k,\sigma}, \beta, \Lambda) \approx \alpha(0, \beta, \Lambda)$, which transforms according to A_1, it is clear that the above holds close to T_c. Below T_c, this approximation needs to be tested by considering a larger basis, including the A_1 and A_2 irreducible representations. Eq. (8.14) is the basis of the numerical calculations below T_c as implemented in the code discussed in Section D.4.

One can generate a set of basis functions by starting from a function, in this case $\exp(i\mathbf{R}_1 \cdot k)$, which by construction is periodic upon shifts along the reciprocal lattice. For each irreducible representation Γ of the crystal's point group, one can define a projector onto the component transforming according to said irreducible representation as

$$\mathcal{P}_\Gamma = \frac{\dim(\Gamma)}{|G|} \sum_{g \in G} \chi_\Gamma(g) g\,, \tag{8.15}$$

where $\chi_\Gamma(g)$ is the character of the conjugacy class of g for the irreducible representation Γ and the right-most g in Eq. (8.15) indicates the application of the group action of g on the function one wishes to project. Due to the different transformation behaviour under D_3, the basis functions of each irreducible representation only need to be orthonormalized with respect to functions in the same irreducible representation. The leading solutions to the linearized gap equations transform according to the two-dimensional E irreducible representation. Since one needs basis functions for both the spin singlets and triplets, a minimum basis set capturing the physics of singlet-triplet mixing needs at least four basis functions. Applying this projector for the E irreducible representation yields a complex function whose real and imaginary parts yield two independent basis functions due to their different symmetries under C_2'. However, they remain of a mixed singlet and triplet nature. Applying the same projector approach for the larger group D_6, which represents the case without SOI and no spin-triplet mix-

ing, isolates their respective spin-singlet and spin-triplet content. The resulting basis functions for the singlets are

$$f^{\pi}_{E1s} = \frac{1}{\mathcal{N}^{\pi}_{E1s}} \left(\cos(k_x a) - \cos(k_x a/2) \cos\left(k_y a\sqrt{3}/2 \right) \right) , \tag{8.16}$$

$$f^{\pi}_{E2s} = \frac{1}{\mathcal{N}^{\pi}_{E2s}} \left(\sin(k_x a/2) \sin\left(k_y a\sqrt{3}/2 \right) \right) , \tag{8.17}$$

where

$$\mathcal{N}^{\pi}_{\mu} = \sqrt{\langle f^{\pi}_{\mu}, f^{\pi}_{\mu} \rangle_{\pi}} . \tag{8.18}$$

The z-triplet basis functions obtained by the above method are

$$f_{E1z} = \sin(k_x a) + \sin(k_x a/2) \cos\left(k_y a\sqrt{3}/2 \right) , \tag{8.19}$$

$$f_{E2z} = \cos(k_x a/2) \sin\left(k_y a\sqrt{3}/2 \right) . \tag{8.20}$$

To restore orthonormality, one can use the Gram-Schmidt procedure by subtracting the inner product between the singlet and z-triplet components as

$$f^{\pi}_{E1z} = \frac{1}{\mathcal{N}^{\pi}_{E1z}} \left(f_{E1z} - \frac{\langle f_{E1z}, f^{\pi}_{E1s} \rangle_{\pi}}{\langle f^{\pi}_{E1s}, f^{\pi}_{E1s} \rangle_{\pi}} f^{\pi}_{E1s} \right) , \tag{8.21}$$

$$f^{\pi}_{E2z} = \frac{1}{\mathcal{N}^{\pi}_{E2z}} \left(f_{E2z} - \frac{\langle f_{E2z}, f^{\pi}_{E2s} \rangle_{\pi}}{\langle f^{\pi}_{E2s}, f^{\pi}_{E2s} \rangle_{\pi}} f^{\pi}_{E2s} \right) , \tag{8.22}$$

before normalizing in the same way as above. Performing the aforementioned test concerning the need to include further basis functions yields no significant change in the results [64]. This lack of a significant contribution from further basis functions is in line with the good agreement between the constructed basis functions and the shape of the solution to the linearized equations in Fig. 8.3. As a larger expansion slows down the numerics, one can restrict the calculation in the following to the aforementioned basis functions within the E irreducible representation.

Since the leading linearized solutions fall within a two-dimensional irreducible representation, they are necessarily degenerate and can contribute simultaneously to the gap below T_c. They can thus pair up with a non-trivial phase winding number, representing a spontaneous symmetry breaking to a chiral superconducting ground state [563, 564]. To what degree the individual nematic gaps, as obtained in the linearized calculation, or such a chiral gap, represent the ground state follows from a calculation of the free energy.

Fig. 8.4 depicts the temperature dependence of the expansion coefficients for three possible superconducting solutions to the self-consistent gap equation Eq. (8.14). For each of these calculations, the self-consistent gap equation is started slightly below T_c with an initial guess based on either of the two leading nematic solutions to the linearized gap equation, or their chiral superposition $(1/\sqrt{2})(p_x + ip_y)$. The nematic solutions are mostly z-triplets with a minor admixture of the respective singlet. The chiral solution remains stable until $T = 0\,K$ and close to T_c.

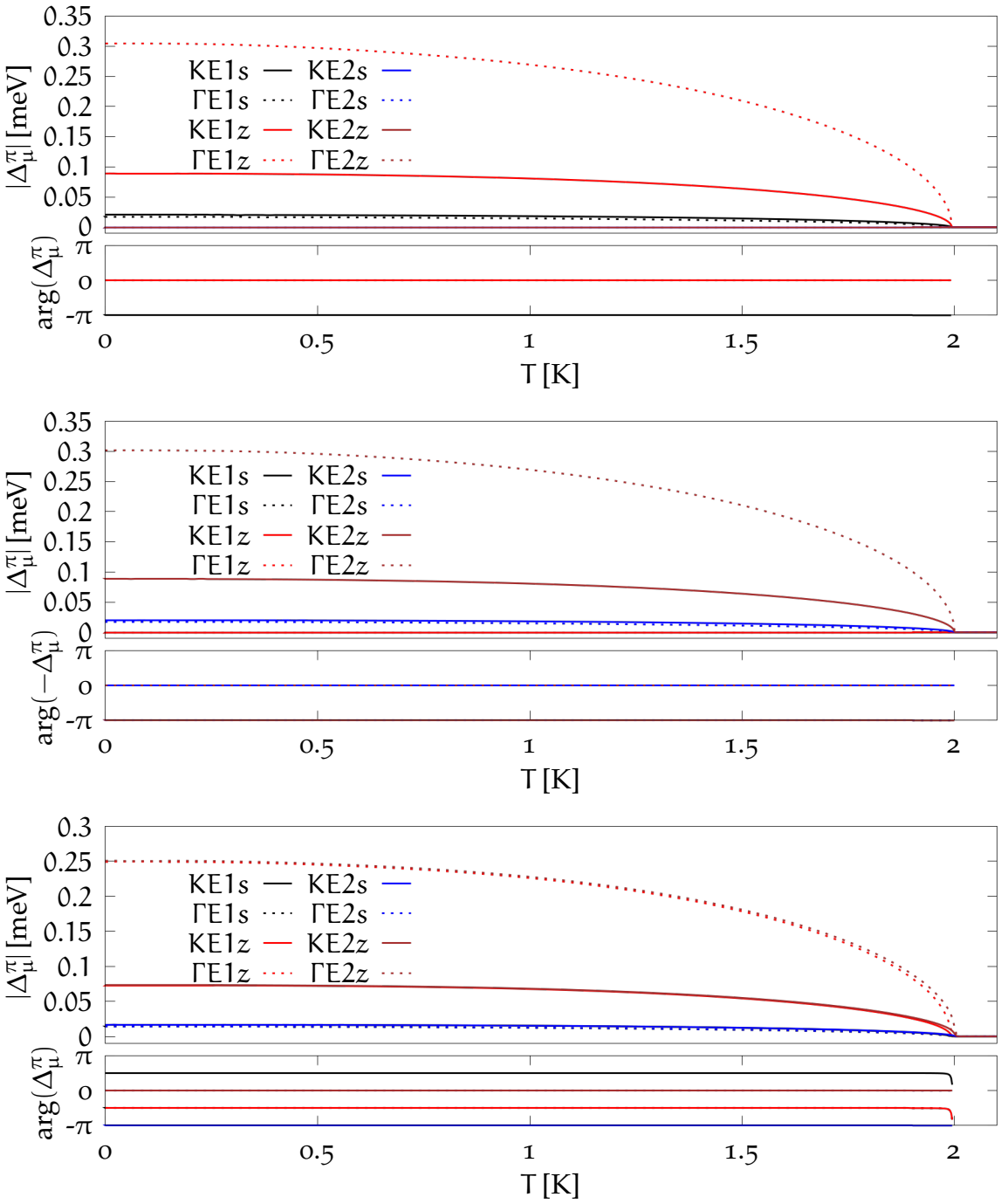

Figure 8.4: **Temperature evolution of the expansion coefficients.** The top panel shows the nematic p_x-like solution, the center panel the p_y-like solution, while the bottom panel depicts the same for the chiral $p_x + ip_y$-like solution. Adapted from Siegl et al. [64].

However, just below T_c, there is a breakdown of the chiral solution with the gap reverting to a nematic p_y-like solution. Here, this chiral-to-nematic transition is due to a minor splitting between the critical temperatures of its two, in theory, degenerate nematic components. This splitting originates in the approximate nature of the projection, and as such, is an artifact. For real systems, a small symmetry breaking, e.g., due to strain [565] or disorder, lifts this degeneracy,

providing an alternative explanation for the emergence of nematicity near the breakdown of superconductivity [490]. Few-layer 2H-$NbSe_2$ and monolayer 1H-$NbSe_2$ display such nematic features under in-plane magnetic fields [566, 567].

Fig. 8.5 a shows the root-mean-square amplitude of the gap over the Fermi surfaces, clearly indicating that the chiral solution, although lower in its maximum amplitude, provides an overall larger expected decrease in free energy from forming a condensate with this symmetry, as opposed to the nematic solutions. This property of the chiral solution is due to its non-nodal structure on the Γ-pocket, which Fig. 8.5 b depicts. The free energy of a superconductor obeying the gap equation in Eq. (8.2) is

$$F = \frac{1}{2}\sum_{k,\sigma}(\xi_{k,\sigma} - E_{k,\sigma} + \Pi(E_{k,\sigma})|\Delta_{k,\sigma}|^2) - k_B T \sum_{k,\sigma} \ln\left(1 + e^{-E_{k,\sigma}/k_B T}\right). \tag{8.23}$$

Since the different solutions to the gap equation and even the normal conducting state do not differ significantly much above or below the Fermi level, one can limit the summation in Eq. (8.23) to a narrow band around the Fermi level, conditional on the width of this range being sufficiently large compared to the gap. One can then approximate the neglected parts of the sum as independent of Δ, meaning that this contribution does not enter the discussion about which solution minimizes the free energy. Fig. 8.5 c shows the free energy calculated in this way for the different solutions to the gap equation compared to that of the normal conducting state. The chiral solution has the lowest free energy and remains the stable solution throughout the considered temperature range. The panels d, e, and f of the same figure belong to the discussion of the comparison with the experiment in the next section.

8.3 Comparison to scanning tunneling spectroscopy

Section 8.2 demonstrated that the Kohn-Luttinger mechanism can, within the uncertainty of the considered approach, mediate unconventional superconductivity in monolayer 1H-$NbSe_2$, roughly in line with the experimentally observed critical temperature. Utilizing the approach pursued therein, the result is a falsifiable prediction of the expected pairing symmetry should the Kohn-Luttinger mechanism really represent the dominant pairing for this material.

One option to rule out the above possibility is to compare the predicted spectral function with spectroscopic measurements of the superconducting gap. Nodal superconducting states, like the nematic solutions obtained from the linearized gap equations, reflect in the presence of low-energy excitations inside the gap, yielding a soft "v-shaped" gap in its excitation spectrum [404], while a nearly constant gap throghout the observable part of the Brillouin zone reflects in a "u-shaped" gap as expected from the conventional s-wave BCS theory [22] in the presence of some broadening [167]. More precisely, the spectral function in

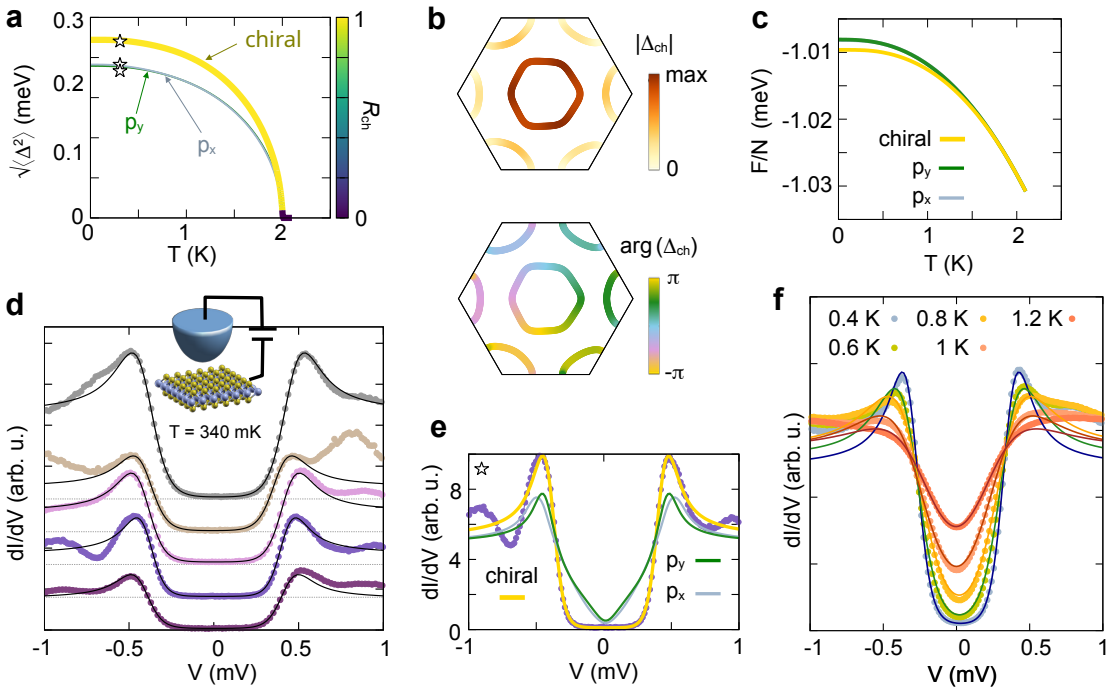

Figure 8.5: **Theoretical results for the ground state symmetry (a-c) and comparison with the experiment (d-f).** Shown is the temperature dependence of the root mean square modulus of the leading E' symmetry solutions (a), the magnitude and phase of the thermodynamically stable chiral solution (b), the free energies of the E' superconducting phases as compared to the normal conducting phase (c), fits of the chiral phase to multiple low-temperature scanning tunneling spectrocopy traces on 1H-$NbSe_2$ (d), fits of the different E' gaps to one of the STS traces (e) and fits of the chiral phase to an STS trace for different measurement temperatures (f). The figure was adopted from Siegl et al. [64].

the tunneling regime satisfies [12] $A_s(\mathbf{k}, \sigma, E) = 2\pi D_{\mathbf{k},\sigma}(E)$, where the local BCS density of states takes the form

$$D_{\mathbf{k},\sigma}(E) = \rho_{\mathbf{k},\sigma} \mathrm{Re} \sqrt{\frac{E^2}{E^2 - |\Delta_{\mathbf{k},\sigma}|^2}}, \tag{8.24}$$

which is valid as long as the normal conducting local density of states is constant within the considered energy range of a few multiples of the gap. As such, the spectral function serves as a measure of the modulus of the gap along the Fermi surfaces.

A commonly used way to measure the spectral function is scanning tunneling spectroscopy [63, 116, 568–571]. According to the Kubo formula for conductance [12, 116, 568–570]

$$G(V) = \sum_{\mathbf{k},\sigma} C_{\mathbf{k}\sigma} \int_{-\infty}^{\infty} dE \, \frac{1}{2\pi} A_s(\mathbf{k}, \sigma; E) \left(-\frac{\partial f(E + eV)}{\partial E} \right), \tag{8.25}$$

the conductivity at low temperatures represents a direct measure of the sample's spectral function A_s. In Eq. (8.25), $C_{k,\sigma}$ are momentum- and spin-dependent coupling constants between a metallic tip with a sufficiently flat density of states and the substrate. The weighting of the individual contributions by the coefficients C and the fact that Eq. (8.25) sums up contributions from all momenta hinders a direct extraction of the gap's modulus along the Fermi surfaces.

For measurements at low bias, the coefficients C contain the matrix element between states in the tip and the Bloch states along the Fermi surfaces. The latter differ between the different Fermi surfaces both due to the different orbitals contributing to the metallic band and due to their different in-plane momenta [569, 570]. Approximating this coupling as constant between the tip and each Fermi surface, i.e., $C_{k,\sigma} \approx C_\pi$, one can calculate the conductivity as

$$G(V) \approx \sum_\pi C_\pi G_\pi(V)\,, \tag{8.26}$$

$$G_\pi(V) = \int_{-\infty}^{\infty} dE\, D_\pi(E) \left(-\frac{\partial f(E+eV)}{\partial E}\right)\,, \tag{8.27}$$

where the density of states is

$$D_{\pi,\sigma}(E) = \sum_{k\in\pi} D_{k,\sigma}(E)\,. \tag{8.28}$$

Eq. (8.26) represents a simple model for the experimentally measured conductivity and does not include additional sources of broadening due to radiation or voltage noise [64, 572]. Instead, a fit parameter providing an effective temperature in excess of the measured experimental temperature acts as a simple model of these unaccounted-for sources of broadening [63]. Beyond the coupling coefficients C_π and the effective temperature T_{eff}, two further fit coefficients, A and V_B, account for a mismatch between the predicted amplitude of the gap and the observed gap and a small asymmetry in the bias due to an imperfect calibration of the lock-in amplifier [64]. The shown experimental curves were measured in the group of M. Ugeda at the Donostia International Physics Center [64]. The experiments used 1H-NbSe2 monolayers grown by molecular beam epitaxy on bilayer graphene on a (0001) 6H-SiC substrate. The experimentalist protected the samples with a capping layer during transfer to avoid oxidation [573]. They performed all measurements at the base temperature of their scanning tunneling microscope at 340 mK, except where noted otherwise. The spectroscopy measurements used Pt/Ir and utilized the lock-in technique with AC modulations of $20-40\,\mu V$ at 833 Hz. The methods section in Siegl et al. [64] provides further details regarding the sample preparation. The fits between Eq. (8.26) and the experimental curves use the trust region reflective algorithm implemented by SciPy's "curve_fit" function [574].

Fig. 8.5 d depicts the resulting fits between multiple experimentally measured conductivity traces obtained at different positions on the sample and the chiral

solution obtained within the self-consistent gap equation for the same temperature. The agreement inside the gap and up to the coherence peaks is excellent, with a small correction to the required amplitude of $A = 1.17$ and a broadening of $T_{eff}/T_{exp} = 1.31$. The additional sidepeaks are not contained in the simple model of Eq. (8.26) and are due to collective excitations [63] that can arise in multiband superconductors with multiple condensates [63, 72, 117]. Fig. 8.5 e depicts the fit to one of the conductivity traces for the chiral and the two nematic leading solutions. The chiral solution exhibits a u-shaped gap, in agreement with the experiment, whereas the nodal nematic solutions have a v-shaped gap that does not fit the observed gap. The origin of this difference lies in the nodal nature of the nematic solutions. While the chiral solution has a lower modulus on the K/K′-pockets than on the Γ-pocket, the latter is much more visible in the resulting conductivity since $C_K \ll C_\Gamma$ [64]. As the chiral solution has a near-constant modulus on the Γ-pocket, the resulting density of states is u-shaped. Fig. 8.5 f shows the agreement between the conductivity predicted for the chiral gap, as determined by the self-consistent gap equation, and the experimental conductivity at varying temperatures. The self-consistent solution remains in good agreement with minimal modification of the required fit parameters.

Perhaps surprisingly, the hard u-shaped gap in the spectroscopy of 1H-$NbSe_2$, which, so far, has been attributed to conventional *s*-wave superconductivity [63], is compatible also with chiral $p + ip$-like superconductivity, due to the aforementioned stronger contribution from the Γ-pocket. However, this observation is not conclusive, as a conventional phonon-mediated pairing remains a viable option. Other experimental measurements, such as quasiparticle interference measurements [575–578] or dynamic scanning tunneling spectroscopy measurements [579], which are more sensitive to the gap on the K-pockets, may shed further light on this possibility. The noticeable deviation from the BCS ratio [63] in monolayer 1H-$NbSe_2$ provides yet another indicator for a possible unconventional nature of its superconductivity. For the reported $T_c \approx 2\,K$ [63, 573], the BCS-ratio between the critical temperature and the modulus of an isotropic gap predicts a gap of roughly 0.3 meV. This prediction contrasts with the roughly 0.4 meV observed in the spectroscopy [63, 64], indicating an anisotropic gap. Such deviations are known to occur for unconventional superconductors [512, 580]. However, such signatures also arise in conventional multiband superconductors with anisotropic gaps, possibly including bulk 2H-$NbSe_2$ [392, 394, 581–586]. Furthermore, the impact of the substrate [587, 588] remains to be explored, with some works indicating a strong sensitivity of the superconducting properties of the 1H-TMDs with respect to the chosen substrate [589, 590]. Regardless, the possibility of 1H-$NbSe_2$ realizing chiral superconductivity with potential topological properties [591, 592] remains an exciting prospect.

Beyond settling the open question surrounding the origin of the superconductivity of monolayer 1H-$NbSe_2$, future works may apply the same methodology used here to the study of different material classes of two-dimensional super-

conductors [593] and other TMD monolayers like 1H-TaS_2 [495], where a nodal superconducting phase may be present [66]. An extension of such studies to more complex geometries, including Van der Waals heterostructures[56, 594] and twisted multi-layer systems [595], is possible using phenomenological real-space formulations [596]. To strengthen the connection between such theoretical investigations and experiments beyond spectroscopy, one can investigate the superfluid stiffness [597] and kinetic inductance [386] predicted by the different possible pairing mechanisms. Finally, one can further extend the theory by including the phonon-mediated pairing phenomenologically into the BCS equation on the same footing as the screened Coulomb interaction [459, 598], or by working on the refinement of ab initio approaches including unconventional pairing [464, 471, 472, 474, 476, 551, 552, 599].

9

CONCLUSION

This thesis covered three separate works, each of which culminated in a publication. Despite their thematic separation, a common thread connecting them is the complicated behavior induced by interaction.

Part I dealt with a description of transport through an interacting superconducting tunneling junction. There, one of the novelties was the further refinement of the particle-conserving description and its interpretation for the experiment, including the protocol by which the phase-space representation can be employed for transport through realistic junctions. Since the publication of the associated work [40], some of the coauthors continued the research on this topic, publishing a follow-up study [42] and including it in a textbook [73]. Future efforts may include the combination of the cotunneling code with the conceptual framework and code written to incorporate additional AC driving, thereby yielding an analytical and numerical tool set for investigating Shapiro steps in interacting Josephson junctions. The possibility of implementing complex junction geometries, like, e.g., double quantum dot junctions [108, 600], promises the possibility to aid in the design of future qubits. Simultaneously, the ongoing implementation of heat transport in these codes aims to enhance the future applicability of these tools to the study of complex quantum circuits.

Part II covered an investigation into the compatibility of global non-abelian symmetries with the phenomenon of many-body localization. There, the key result is the identification of a possible imperfect many-body localized phase, whose full localization is hindered by the inherent symmetries of the model. These findings, while primarily of conceptual interest, demonstrate the presence of non-abelian symmetries as a disqualifying feature when striving to possibly utilize many-body localization for quantum technological applications, in line with earlier predictions [240, 241]. Follow-up efforts, both by the authors [305] and the community [295], further investigated this complex interplay between strong random-strength interactions and global symmetries, finding multifractal behavior in the imperfect many-body localized regime [305]. Beyond a further investigation of this phase, future endeavors might focus on the spin-length dependence for even larger spins and, crucially, try to reduce the uncertainty due to finite-size effects in these findings. Such finite-size effects affect most

current numerical approaches to many-body localization, and it remains to be seen whether the community finds a way to resolve this problem systematically.

Part III investigated the superconducting order induced by the Kohn-Luttinger mechanism for monolayer transition metal dichalcogenides. It included a discussion of screening in two-dimensional metals, the resulting interaction for monolayer 1H-$NbSe_2$, and the superconducting pairing induced by the Kohn-Luttinger mechanism in this material. The resulting chiral p-like order parameter fits the available experimental data surprisingly well, opening up the possibility of this mechanism actually contributing the dominant pairing. However, these findings are inconclusive on their own, and further experimental evidence, as well as the inclusion of the phonon-mediated pairing on the same conceptual footing, are required to make progress. Still, these results shine light on which signatures one might expect in the experiment, provided a dominant Kohn-Luttinger pairing is indeed realized, thereby providing the community with a falsifiable prediction to test against. Combined with earlier results for the opposite limit of a dominant phonon-mediated pairing, this promises a better understanding of the origin of the superconducting order in these atomically thin superconductors. Such an improved grasp on the underlying microscopic physics will assist the community in their active pursuit of harnessing the fascinating interaction-driven physics of low-dimensional materials for novel technological applications.

Together, these separate projects all illustrate the highly complex nature of interaction-driven physics in low-dimensional systems. From the non-trivial microscopic origin of the phase variable in Part I, to the open questions about the possibility of novel phases in disordered quantum systems in Part II, and the remaining uncertainty of the origin of superconductivity in two-dimensional monolayer TMDs, this field of physics harbors a plethora of novel and exciting phenomena waiting to be discovered. Continued investigation of them and the yet unforeseen functionalities they enable may pave the way for sustained technological progress throughout the current century.

Part IV

APPENDIX

A

NOTATION AND UNITS

This thesis adopts the notation of Bruus et al. [12] where possible, and uses the following conventions:

- Energy is measured in electron Volts [eV].
- Charge is measured in elementary charges [e], where $e > 0$.
- Time is measured in seconds [s].
- Length is measured in Ångstroms [Å].
- Voltage is measured in Volts [V].

This thesis adopts the notation of Cornwell for group operations, Schönflies notation for point groups, and Hermann-Mauguin notation for space groups. $\|\cdot\|_p$ denotes the p-norm, while $\|\cdot\|_F$ is the Frobenius operator norm. Integrals with vectorial infinitesimals like $\int d\mathbf{r}$ denote scalar integrals over the range of $\mathbf{r}$, with any scalar product with the unit vector along $\mathbf{r}$ written explicitly. The arguments of Matsubara Green's functions are written as $\mathbf{k}, ik$, where ik is an imaginary frequency.

B

GROUP THEORY AND SYMMETRIES

B.1 TRANSLATIONAL PERIODICITY

When working with lattice periodic systems in d-dimensions:

- $N = \prod_{j=1}^{d} N_j$ is the number of unit cells, where N_j is the periodicity along direction j.
- $\mathbf{a}_j$ denotes primitive lattice vectors with $a_j = \|a_j\|_2$.
- $\mathbf{b}_j$ denotes the primitive vectors of the reciprocal lattice with $b_j = \|b_j\|_2$.
- Momenta are quantized along j in units of $\Delta k_j = \frac{2\pi}{a_j N_j}$.
- $\mathcal{V}$ is the volume of the considered periodic system which fulfills $\mathcal{V} = N\mathcal{V}^p$, where $\mathcal{V}^p = \mathrm{Vol}(\{\mathbf{a}_j\})$ is the volume of the primitive unit cell of the lattice.
- The continuum limit corresonds to $\frac{1}{\mathcal{V}} \sum_{\mathbf{k}} \to \int_{-\infty}^{\infty} \frac{d\mathbf{k}}{(2\pi)^d}$.
- The Bloch basis [2] is $\psi_{n,\mathbf{k}}(\mathbf{r}) = \frac{1}{\sqrt{N}} e^{i\mathbf{k}\cdot\mathbf{r}} \mathbf{u}_{n,\mathbf{k}}(\mathbf{r})$, where $\mathbf{u}$ is the Bloch spinor containing all internal degrees of freedom, and n is the band index. $\mathbf{u}$ in this convention has units $[\mathrm{length}^{\frac{-d}{2}}]$ and has the norm

$$\forall_{n,\mathbf{k}} : \int_{\mathcal{V}^p} d\mathbf{r}\, \mathbf{u}^{\dagger}_{n,\mathbf{k}}(\mathbf{r}) \cdot \mathbf{u}_{n,\mathbf{k}}(\mathbf{r}) = 1 \,. \tag{B.1}$$

- The Bloch spinors fulfill $\mathbf{u}_{n,\mathbf{k}}(\mathbf{r} + \mathbf{R}) = \mathbf{u}_{n,\mathbf{k}}(\mathbf{r})$ for all lattice vectors $\mathbf{R}$ and $\mathbf{u}_{n,\mathbf{k}+\mathbf{G}}(\mathbf{r}) = e^{i\mathbf{G}\cdot\mathbf{r}} \mathbf{u}_{n,\mathbf{k}}(\mathbf{r})$ for all reciprocal lattice vectors $\mathbf{G}$. Only the crystal momenta in the first Brillouin zone generate unique states and summations over $\mathbf{k}$ are thus restricted to the first Brilloin zone.
- Discrete Fourier transforms in a periodic region with N discrete sites correspond to

$$f(\mathbf{R}_j) = \frac{1}{\sqrt{N}} \sum_{\mathbf{k}} f_{\mathbf{k}} e^{i\mathbf{k}\cdot\mathbf{R}_j} \,, \qquad f_{\mathbf{k}} = \frac{1}{\sqrt{N}} \sum_{j} f(\mathbf{R}_j) e^{-i\mathbf{k}\cdot\mathbf{R}_j} \,. \tag{B.2}$$

  In this convention, the units remain unaffected by the discrete Fourier transform as $[f_{\mathbf{k}}] = [f(\mathbf{r})]$.

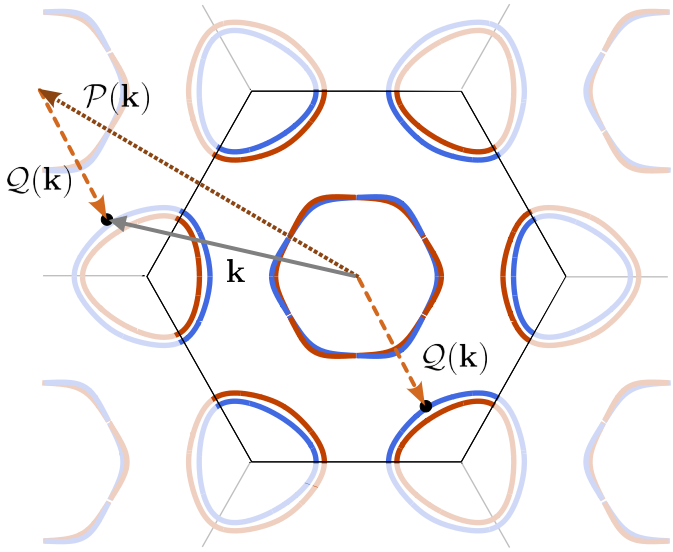

Figure B.1: **Projectors on the reciprocal lattice ($\mathcal{P}$) and the crystal momentum ($\mathcal{Q}$), respectively.** Taken from Siegl et al. [64].

- To distinguish between actual and crystal momenta, one can introduce a projector $\mathcal{P} : \mathbf{k} \to \mathbf{G}$, such that $\mathbf{k} = \mathbf{k}_{\text{crystal}} + \mathcal{P}(\mathbf{k}) = \mathbf{k}_{\text{crystal}} + \mathbf{G}$ with $\mathbf{k}_{\text{crystal}}$ an associated crystal momentum and $\mathbf{G}$ a reciprocal lattice vector. $\mathcal{P}$ defines a projecttion as it is an idempotent endomorphism, i.e., $\mathcal{P}$ is linear and obeys $\mathcal{P}^2 = \mathcal{P}$. A projection on the compliment of its image in the codomain, in this case the crystal momenta, is given by $\mathcal{Q} = 1 - \mathcal{P}$. It is again idempotent since $\mathcal{Q}^2 = \mathcal{Q}$.
- Continous Fourier transforms in a periodic region correspond to

$$f(\mathbf{r}) = \frac{1}{\mathcal{V}} \sum_{\mathbf{k}} f_{\mathbf{k}} e^{i\mathbf{k}\cdot\mathbf{r}}, \qquad f_{\mathbf{k}} = \int_{\mathcal{V}} d\mathbf{r}\, f(\mathbf{r}) e^{-i\mathbf{k}\cdot\mathbf{r}}. \tag{B.3}$$

  In this convention, the units change upon taking the Fourier transform as $[f_{\mathbf{k}}] = [f(\mathbf{r})][\text{length}^d]$.
- Continous Fourier transforms in an infinite region correspond to

$$f(\mathbf{r}) = \int \frac{d\mathbf{k}}{(2\pi)^d} f_{\mathbf{k}} e^{i\mathbf{k}\cdot\mathbf{r}}, \qquad f_{\mathbf{k}} = \int d\mathbf{r}\, f(\mathbf{r}) e^{-i\mathbf{k}\cdot\mathbf{r}}. \tag{B.4}$$

- In the energy domain, the Fourier transform corresponds to

$$f_\omega = \int dt\, f(t) e^{-i\omega t} \qquad f(t) = \int \frac{d\omega}{2\pi} f_\omega e^{i\omega t}, \tag{B.5}$$

  where by convention the sign differs when compared to the Fourier transform between real space and momentum.

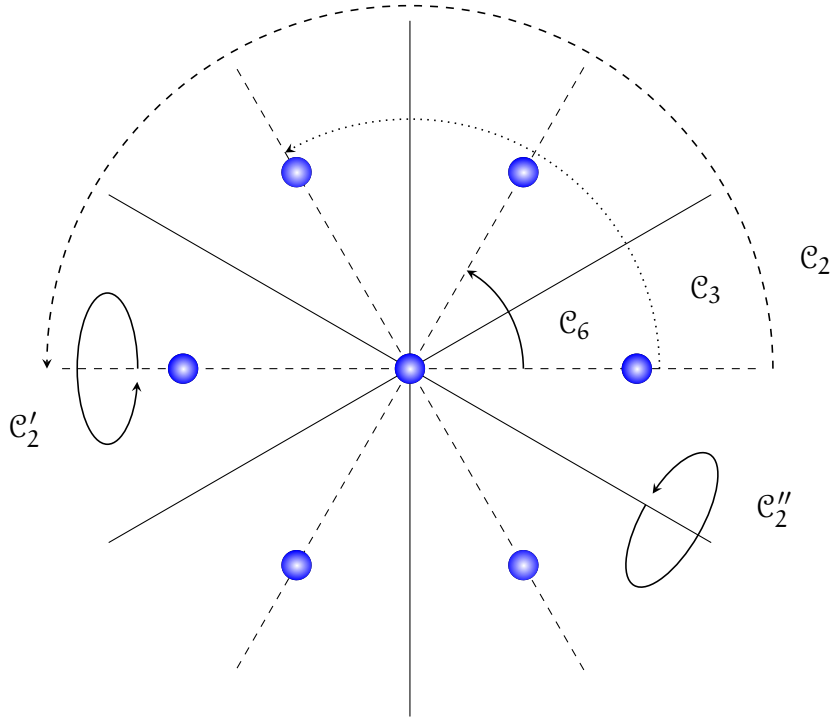

Figure B.2: **Group actions of D_6 on the lattice.** The group contains two sets of three equivalent two-fold in-plane axes $\mathcal{C}_2'$, $\mathcal{C}_2''$, as well as a six-fold rotational axes along the out-of-plane z-direction, which implies also the presence of a three-fold and two-fold axis along the same direction.

B.2 POINT GROUPS RELEVANT FOR 1H-$NBSE_2$

For the discussion of monolayer 1H-$NbSe_2$ in Part III, it is convenient to briefly collect here the properties of the most relevant point groups occurring in the study of this material. In this thesis, the $\mathbf{c}$-axis of the crystal points along the positive z-axis and the $\mathbf{a}$-axis points along the positive x-axis of the coordinate system. Not only are these symmetry groups helpful during the construction of the tight-binding model in Section C.3, they also enter the symmetry classification of possible superconducting solutions in Chapter 8. The two-dimensional point group describing the hexagonal lattice of the 1H-TMDs is D_6, which differs from the point group of the full crystal discussed below. D_6 has six conjugacy classes of group elements, given by the identity E, six fold rotation around the z-axis $\mathcal{C}_6$, three-fold rotation around the z-axis $\mathcal{C}_3$, two-fold rotations either around the z-axis $\mathcal{C}_2$, an axis along the a primitive lattice vector C_2', or a dihedral axis C_2''. Table B.1 shows the character table of D_6.

The three-dimensional point group of the M sublattice is $D_{6h} = D_6 \bigoplus C_i$, which is direct product of D_6 and the group $C_i = \{E, i\} \equiv C_2$ with i the inversion. Concatenating inversion with D_6 yields the new conjugacy classes i, S_3, S_6, σ_h,σ_d and σ_v. The character table of D_{6h} in Table B.2 follows from Table B.1. The basis of the 1H-polytype lacks inversion symmetry and reduces the symmetry

D_6	E	$2\mathcal{C}_6$	$2\mathcal{C}_3$	$\mathcal{C}_2$	$3\mathcal{C}_2'$	$3\mathcal{C}_2''$
A_1	1	1	1	1	1	1
A_2	1	1	1	1	-1	-1
B_1	1	-1	1	-1	1	-1
B_2	1	-1	1	-1	-1	1
E_1	2	1	-1	-2	0	0
E_2	2	-1	-1	2	0	0

Table B.1: **Character table for the group D_6.**

D_{6h}	c	i·c
χ_g	$\chi(c)$	$\chi(c)$
χ_u	$\chi(c)$	$-\chi(c)$

Table B.2: **Character table for the group D_{6h} in terms of the character table of D_6.** Here, c are the conjugancy classes and χ the irreducible representations of D_6, respectively. $\chi(c)$ is the character of class c for the irreducible representation χ.

of the full crystal to D_{3h}. Fig. B.3 shows the group elements of D_{3h}. Similarly to D_{6h}, also D_{3h} is a direct sum of a smaller group with a group equivalent to C_2, since $D_{3h} = D_3 \bigoplus C_s$ with $C_s = \{E, \sigma_h\} \equiv C_2$. Again, the character table of D_{3h} in Table B.3 follows from the character table of the smaller group D_3 in Table B.4, which is the symmetry group of 1H-TMDs on a substrate that has rotational symmetry with regards to the z-axis.

D_{3h}	c	$\sigma_h \cdot c$
χ'	$\chi(c)$	$\chi(c)$
χ''	$\chi(c)$	$-\chi(c)$

Table B.3: **Character table for the group D_{3h} in terms of the character table of D_3.** Here c are the conjugancy classes and χ the irreducible representations of D_3, respectively. $\chi(c)$ is the character of class c for the irreducible representation χ.

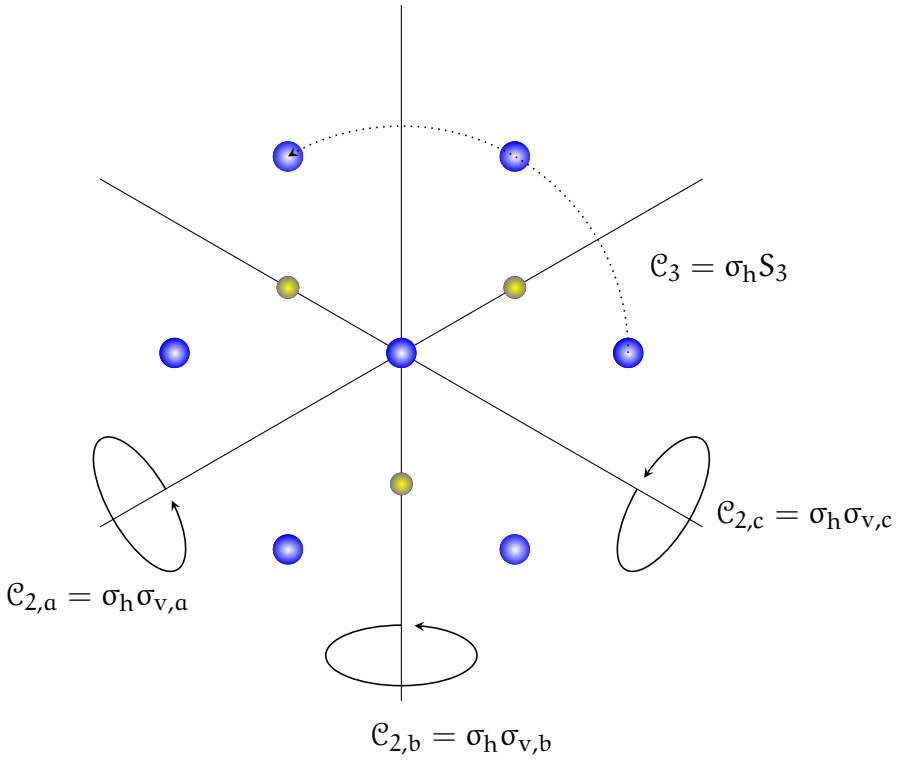

Figure B.3: **Group actions of D_{3h} on the crystal.**

D_3	E	$2C_3$	$3C_2$
A_1	1	1	1
A_2	1	1	-1
E	2	-1	0

Table B.4: **Character table for the group D_3.**

C

MODELS

This thesis employs multiple models for numerical and analytical calculations. This chapter aims to separate the details of their construction and related remarks from the results presented in the main parts of the thesis.

C.1 PARTICLE-CONSERVING BCS THEORY

Chapter 3 covers a particle-conserving formulation of the BCS theory of superconductivity [22, 38, 71–73, 117, 123, 143, 171]. This appendix provides some fundamental proofs complimenting the discussion in the PhD thesis of Picó-Cortés [71] and a version of the derivation of the zero-temperature BCS gap equation therein with some errors corrected.

Partitions of the ground state

When constructing excited states of the superconducting condensate with a fixed particle content, including the Bogoliubov quasiparticles, one faces the natural question to which degree a condensate of the remaining electrons is well-defined. The quasiparticles are not perfectly fermionic, since their creation operators do not fully anticommute. This is to be expected, since an excitation of a macroscopic fraction of the electrons contributing to the condensate into an excited state should reflect in a modified pairing strength [117]. The Cooper pairs that are broken during the excitation of quasiparticles modify the remaining quasiparticles by a change in the distribution funciton α_k. In other words, since the BCS-gap equation is a self-consistency equation, wherein the existence of the condensate provides its own pairing strength, the decrease of the number of Cooper pairs should decrease the modulus of the order parameter Δ. As such, it is clear that, in the following, one always relies on some notion of a "small" fraction of excited quasiparticles not significantly affecting the macroscopic number of electrons in the condensate.

The introduction of fermionic quasiparticles presupposes a decomposition of the condensate state $|M\rangle$ with fixed number of Cooper pairs into states where select momenta are excluded from the condensate as [71, 117]

$$|M, \mathbf{k}_1, .., \mathbf{k}_n\rangle = \mathcal{N}_{M,\mathbf{k}_1,..,\mathbf{k}_n} \left(\sum_{\mathbf{k}\neq\mathbf{k}_1,..,\mathbf{k}_n} \alpha_{\mathbf{k}} \hat{B}^\dagger_{\mathbf{k}} \right)^M |0\rangle \,, \tag{C.1}$$

with $n \ll M$ and $\forall_{i,j} \mathbf{k}_i \neq \mathbf{k}_j$. The definitions in Eq. (3.4) and Eq. (C.1) are consistent with the case where no momenta $\{\mathbf{k}_i\}$ are excluded from the sum. The decomposition can therefore proceed inductively for all n. Applying the binomial theorem to the bracket in Eq. (C.1), the nilpotence of the Kramers pair creation operator $\hat{B}^\dagger$ enables one to write

$$\begin{aligned}
&|M, \mathbf{k}_1, .., \mathbf{k}_n\rangle = \mathcal{N}_{M,\mathbf{k}_1,..,\mathbf{k}_n} \\
&\times \left[M\alpha_{\mathbf{k}_{n+1}} \hat{B}^\dagger_{\mathbf{k}_{n+1}} \left(\sum_{\mathbf{k}\neq\mathbf{k}_1,..,\mathbf{k}_{n+1}} \alpha_{\mathbf{k}} \hat{B}^\dagger_{\mathbf{k}} \right)^{M-1} + \left(\sum_{\mathbf{k}\neq\mathbf{k}_1,..,\mathbf{k}_{n+1}} \alpha_{\mathbf{k}} \hat{B}^\dagger_{\mathbf{k}} \right)^M \right] |0\rangle \\
&= \frac{\mathcal{N}_{M,\mathbf{k}_1,..,\mathbf{k}_n} M}{\mathcal{N}_{M-1,\mathbf{k}_1,..,\mathbf{k}_{n+1}}} \alpha_{\mathbf{k}_{n+1}} \hat{B}^\dagger_{\mathbf{k}_{n+1}} |M-1, \mathbf{k}_1, .., \mathbf{k}_{n+1}\rangle \\
&+ \frac{\mathcal{N}_{M,\mathbf{k}_1,..,\mathbf{k}_n}}{\mathcal{N}_{M,\mathbf{k}_1,..,\mathbf{k}_{n+1}}} |M, \mathbf{k}_1, .., \mathbf{k}_{n+1}\rangle \\
&\overset{*}{=} \frac{\mathcal{N}_{M,\mathbf{k}_1,..,\mathbf{k}_n}}{\mathcal{N}_{M,\mathbf{k}_1,..,\mathbf{k}_{n+1}}} \left(\alpha_{\mathbf{k}_{n+1}} \hat{B}^\dagger_{\mathbf{k}_{n+1}} |M-1, \mathbf{k}_1, .., \mathbf{k}_{n+1}\rangle + |M, \mathbf{k}_1, .., \mathbf{k}_{n+1}\rangle \right) \\
&= \frac{1}{\sqrt{1+|\alpha_{\mathbf{k}_{n+1}}|^2}} \left(\alpha_{\mathbf{k}_{n+1}} \hat{B}^\dagger_{\mathbf{k}_{n+1}} |M-1, \mathbf{k}_1, .., \mathbf{k}_{n+1}\rangle + |M, \mathbf{k}_1, .., \mathbf{k}_{n+1}\rangle \right) \,,
\end{aligned} \tag{C.2}$$

which is the starting point for the introduction of fermionic quasiparticles in the thesis of Picó-Cortés [71]. There, the possibility of this decomposition is proven to its lowest order $n = 0$. The general case for arbitrary n is more complicated to proof, as the $\overset{*}{=}$ denotes that this step is only valid if

$$\mathcal{N}_{M-1,\mathbf{k}_1,..,\mathbf{k}_{n+1}} \approx M\mathcal{N}_{M,\mathbf{k}_1,..,\mathbf{k}_{n+1}} \,, \tag{C.3}$$

holds for all $M \in [\bar{M} - \delta M, \bar{M} + \delta M]$ with $\bar{M}$ very large, $\delta M, n \ll \bar{M}$ and all $\mathbf{k}_1, .., \mathbf{k}_n$ with $\forall i \neq j : \mathbf{k}_i \neq \mathbf{k}_j$ simultaneously.

In the following, this property will be discussed and a proof that it indeed holds for "reasonable" distributions $\alpha_{\mathbf{k}}$ is provided. The constraints on the normalization can be split into two separate conditions. The first condition concerns the independence of the ratio between normalization factors on the removal of a limited number of momenta as

$$\text{I} \quad \frac{\mathcal{N}_{M,\mathbf{k}_1,..,\mathbf{k}_n}}{\mathcal{N}_{M-1,\mathbf{k}_1,..,\mathbf{k}_n}} = \frac{\mathcal{N}_{M,\mathbf{k}_1,..,\mathbf{k}_{n+1}}}{\mathcal{N}_{M-1,\mathbf{k}_1,..,\mathbf{k}_{n+1}}} (1 + \mathcal{O}(\epsilon)) \,, \tag{C.4}$$

where ϵ is a small number such that $n\epsilon, \delta M\epsilon \ll 1$ can be neglected for the relevant range of n. The second condition is the (approximate) independence of the ratio on M as

$$\textbf{II} \quad \forall M \in [\bar{M} - \delta M, \bar{M} + \delta M] : F(M, n) = F(\bar{M}, n)(1 + \mathcal{O}(\epsilon)), \tag{C.5}$$

$$F(M, n) := \frac{M\mathcal{N}_{M,k_1,..,k_n}}{\mathcal{N}_{M-1,k_1,..,k_n}}. \tag{C.6}$$

If both Eqs. (C.4) and (C.6) hold, the constraints upon $\alpha_{k_{n+1}}$ collapse, up to an error of $\mathcal{O}(\epsilon)$, into the condition that

$$\frac{\mathcal{N}_{M,k_1,\cdots,k_n}}{\mathcal{N}_{M,k_1,\cdots,k_n+1}} = \frac{1}{\sqrt{1 + |\alpha_{k_{n+1}}|^2}}, \tag{C.7}$$

which however is satisfied given that the states $|M, k_1, \cdots, k_n\rangle$ are normalized. Futhermore, it can even serve as the definition of $\mathcal{N}_{M,k_1,\cdots,k_{n'}}$, if one starts with $\mathcal{N}_M$ and recursively applies Eq. (C.7) for $n = 1, \cdots, n'$. The error in this procedure is negligible, provided $n, \delta M \ll \bar{M}$, which is assumed throughout.

First, one can show that the two conditions are not independent, since II $\Rightarrow$ I. To this end, one first notes that $(1 + \mathcal{O}(\epsilon))^{\delta M} = 1 + \mathcal{O}(\delta M\epsilon) \approx 1$. Condition **I** is equivalent to

$$(1 + \mathcal{O}(\epsilon))^{-2} = (1 + \mathcal{O}(\epsilon)) = \frac{\mathcal{N}^2_{M,k_1,..,k_{n+1}}}{\mathcal{N}^2_{M,k_1,..,k_n}} \frac{\mathcal{N}^2_{M-1,k_1,..,k_n}}{\mathcal{N}^2_{M-1,k_1,..,k_{n+1}}}. \tag{C.8}$$

For the remainder of this proof, both M and n are kept fixed, K is the large but finite number of considered momenta for applied periodic boundary conditions, and $\beta^{l,m}$ denotes $K - n - l$ multiindices with norm $|\beta^{l,m}| = M - m$. By inserting the definition of the normalization constants and the states $|M, k_1, \cdots, k_n\rangle$, one can use the multinomial theorem to write

$$\begin{aligned}
\frac{1}{\mathcal{N}^2_{M,k_1,..,k_n}} &= \frac{1}{\mathcal{N}^2_{M,k_1,..,k_n}} \langle M, k_1, .., k_n | M, k_1, .., k_n \rangle \\
&= \sum_{\beta_1^{0,0}, \beta_2^{0,0}} \binom{M}{\beta_1^{0,0}} \binom{M}{\beta_2^{0,0}} \langle 0 | \prod_{k,k' \neq k_1,..,k_n} \left(\alpha^*_{k'} \hat{B}_{k'}\right)^{\beta^{0,0}_{2,k}} \left(\alpha_k \hat{B}^\dagger_k\right)^{\beta^{0,0}_{1,k}} |0\rangle \\
&= (M!)^2 \sum_{\beta_1^{0,0}} \prod_{k \neq k_1,..,k_n} \left(|\alpha_k|^2\right)^{\beta^{0,0}_{1,k}}.
\end{aligned} \tag{C.9}$$

The nilpotence of the $\hat{B}$ restricts the multinomial coefficients to the range of $\{0, 1\}$. This allows for an easy evaluation of the brakets, since the product of the

operators either yields 1 for $\beta_1^{0,0} = \beta_2^{0,0}$ or vanishes otherwise. Since M and n were kept generic in Eq. (C.9), it follows by the same steps that

$$\frac{1}{\mathcal{N}^2_{M-1,k_1,..,k_{n+1}}} = ((M-1)!)^2 \sum_{\beta^{1,1}} \prod_{k \neq k_1,..,k_{n+1}} \left(|\alpha_k|^2\right)^{\beta_k^{1,1}}, \tag{C.10}$$

$$\frac{1}{\mathcal{N}^2_{M-1,k_1,..,k_n}} = ((M-1)!)^2 \sum_{\beta^{0,1}} \prod_{k \neq k_1,..,k_n} \left(|\alpha_k|^2\right)^{\beta_k^{0,1}}, \tag{C.11}$$

$$\frac{1}{\mathcal{N}^2_{M,k_1,..,k_{n+1}}} = ((M)!)^2 \sum_{\beta^{1,0}} \prod_{k \neq k_1,..,k_{n+1}} \left(|\alpha_k|^2\right)^{\beta_k^{1,0}}, \tag{C.12}$$

Splitting now the sum over $\beta^{0,0}$ in Eq. (C.9) into a part where $\beta_{k_{n+1}} = 1$ and one where it is 0, one finds

$$\begin{aligned}\frac{1}{\mathcal{N}^2_{M,k_1,..,k_n}} &= \frac{1}{\mathcal{N}^2_{M,k_1,..,k_{n+1}}} + |\alpha_{k_{n+1}}|^2 (M!)^2 \sum_{\beta^{1,1}} \prod_{k \neq k_1,..,k_{n+1}} \left(|\alpha_k|^2\right)^{\beta_k^{1,1}} \\ &= \frac{1}{\mathcal{N}^2_{M,k_1,..,k_{n+1}}} + |\alpha_{k_{n+1}}|^2 (M)^2 \frac{1}{\mathcal{N}^2_{M-1,k_1,..,k_{n+1}}},\end{aligned} \tag{C.13}$$

from which it follows that

$$\frac{\mathcal{N}^2_{M,k_1,..,k_{n+1}}}{\mathcal{N}^2_{M,k_1,..,k_n}} = 1 + \frac{|\alpha_{k_{n+1}}|^2 M^2 \mathcal{N}^2_{M,k_1,..,k_{n+1}}}{\mathcal{N}^2_{M-1,k_1,..,k_{n+1}}} = 1 + |\alpha_{k_{n+1}}|^2 F(M, n+1)^2. \tag{C.14}$$

Inserting Eq. (C.14) into the right-hand side of Eq. (C.8) yields

$$\frac{\mathcal{N}^2_{M-1,k_1,..,k_n}}{\mathcal{N}^2_{M,k_1,..,k_n}} \frac{\mathcal{N}^2_{M,k_1,..,k_{n+1}}}{\mathcal{N}^2_{M-1,k_1,..,k_{n+1}}} = \frac{1 + |\alpha_{k_{n+1}}|^2 F(M, n+1)^2}{1 + |\alpha_{k_{n+1}}|^2 F(M-1, n+1)^2} \tag{C.15}$$

Condition **II** implies $F(M, n+1)^2 = F(M-1, n+1)^2(1 + \mathcal{O}(\epsilon))$ and with $x = |\alpha_{k_{n+1}}|^2 F(M-1, n+1)^2 \in \mathbb{R}_0^+$, it follows for $x \neq 0$ that

$$\frac{1 + x(1 + \mathcal{O}(\epsilon))}{1 + x} = 1 + \frac{\mathcal{O}(\epsilon)}{1 + \frac{1}{x}} = 1 + \mathcal{O}(\epsilon), \tag{C.16}$$

while in the remaining edge case of $x = 0$ the equality between the left-hand side and the right-hand side of Eq. (C.16) follows trivially, without the intermediate step. This completes the proof that **II** implies **I**.

To proof **II**, it is sufficient to proof

$$F(M, n) = F(M-1, n)(1 + \mathcal{O}(\epsilon')), \tag{C.17}$$

where $\delta M^2 \epsilon', n\delta M \epsilon' \ll 1$, such that one can choose $\epsilon = \delta M \epsilon'$ later. Physically, this statement corresponds to the approximation that the change of normalization

upon lowering the condensates particle content by one Cooper pair only depends on the number of Cooper pairs M via the factor M arising from the combinatorics of all possible occupied momenta.

To gain some insight into how one might proof this, one can first consider a pathological case where this condition fails. A case of this type is provided by the zero-temperature Fermi sea, where $\alpha_{\mathbf{k}} = \Theta(k_F - |\mathbf{k}|)$ with k_F such that exactly M Kramers pairs lie inside the Fermi sphere. Obviously $\mathcal{N}_M = \frac{1}{M!}$, since there is exactly one β such that one generates a state with M Kramers pairs with $\mathbf{k} < k_F$. As expected, the "trivial" combinatoric factor M in the normalization appears for $\mathcal{N}_{M-1} = \frac{1}{(M-1)!} = M\mathcal{N}_M$. However, there is no way to include $M+1$ Kramers pairs without at least one $\mathbf{k}$ outside of the Fermi sphere, rendering $\mathcal{N}_{M+1}$ ill-defined.

Considering the cause of this failure, one can replace this zero-temperatur Fermi-Dirac distribution with the limit of $T \to 0^+$, where $\alpha_{\mathbf{k}}|_{|\mathbf{k}|=k_F+0^+} = 0^+$ and thus $\mathcal{N}_{M+1} \sim 1/0^+ = +\infty$. The normalization factor acquires a divergence as one approaches zero temperature from above. This reflects the fact that for the zero-temperature distribution, the maximum particle number is fixed and **II** therefore manifestly impossible to satisfy. Conversely, a similar argument shows that for this distribution **I** does not hold either, as removing a momentum $|\mathbf{k}| < k_F$ in $|M-1\rangle$ yields a finite $\mathcal{N}_{M-1,\mathbf{k}}$, while doing the same in $|M\rangle$ results in a divergence as $T \to 0^+$ for the same reason as before. While the right-hand side of **I** remains finite as $1/M = \mathcal{N}_M/\mathcal{N}_{M-1}$, the left-hand side diverges as $\mathcal{N}_{M,\mathbf{k}}/\mathcal{N}_{M-1,\mathbf{k}} \to +\infty$.

In the above pathological cases, the issue arose from the sharpness of the distribution function $\alpha_{\mathbf{k}}$ at some boundary. In general, the condition **II** can be understood as a requirement that the function $F(M,n)$ is for all n sufficiently "smooth" in M, that for very large $\bar{M}$ and in the narrow range δM, it does not noticeably change.

For the remaining part of the proof, it is helpful to change the normalization of $\alpha_{\mathbf{k}}$ to

$$\sum_{\mathbf{k}} |\alpha_{\mathbf{k}}|^2 = 1\,, \tag{C.18}$$

which does not change the above conditions **I** and **II**, since they depend only on ratios of the normalization constants. Taking the square of Eq. (C.17), bringing all Fs to the left, and inserting Eqs. (C.9) and (C.10) results in

$$\begin{aligned}\frac{F(M,n)^2}{F(M-1,n)^2} =& \frac{M^2\mathcal{N}^2_{M,\mathbf{k}_1,..,\mathbf{k}_n}\mathcal{N}^2_{M-2,\mathbf{k}_1,..,\mathbf{k}_n}}{(M-1)^2\mathcal{N}^2_{M-1,\mathbf{k}_1,..,\mathbf{k}_n}\mathcal{N}^2_{M-1,\mathbf{k}_1,..,\mathbf{k}_n}} \\ =& \frac{G(M,n)G(M-2,n)}{G(M-1,n)^2}\left(\frac{M}{M-1}\right)^2 = 1 + \mathcal{O}(\epsilon')\,,\end{aligned} \tag{C.19}$$

with the auxilliary function

$$G(M-m,n)=\sum_{\beta^{0,m}}\prod_{k\neq k_1,..,k_n}\left(|\alpha_k|^2\right)^{\beta_k^{0,m}}. \tag{C.20}$$

Bringing the fraction $[M/(M-1)]^2$ to the left and realizing that it amounts to a factor $(1-1/M)^2=1+\mathcal{O}(\epsilon')$, it follows that one just needs to proof

$$\frac{G(M,n)G(M-2,n)}{G(M-1,n)^2}=1+\mathcal{O}(\epsilon')\,. \tag{C.21}$$

The sum over all possible $K-n$ multiindices $\beta^{0,m}$ of range $\{0,1\}$ and norm $M-m$ in Eq. (C.20) can be related to the sum over all $K-n$ multiindices $\beta^{0,m+1}$, by

$$\sum_{\beta^{0,m}}X(\beta^{0,m})=\sum_{\beta^{0,m+1}}\sum_{k\neq k_1,\cdots,k_n}(1-\beta_k^{0,m+1})X(B(\beta^{0,m+1},k))\,, \tag{C.22}$$

$$B(\beta,k)_{k'}=\beta_{k'}||\delta_{k',k}\,, \tag{C.23}$$

where X is an arbitrary function of the multiindex $\beta^{0,m}$ and $||$ denotes the logical OR operation. By applying Eq. (C.22) to $G(M,n)$ and $G(M-1,n)$, one finds

$$\begin{aligned}G(M,n)=&\sum_{\beta^{0,2}}\prod_{k\neq k_1,..,k_n}\left(|\alpha_k|^2\right)^{\beta_k^{0,2}}\left(\sum_{k'\neq k_1,\cdots,k_n}(1-\beta_{k'}^{0,2})|\alpha_{k'}|^2\right.\\&\left.\times\sum_{k''\neq k_1,..,k_n}(1-\beta_{k''}^{0,2})(1-\delta_{k',k''})|\alpha_{k''}|^2\right)\\\overset{*}{=}&\sum_{\beta^{0,2}}\prod_{k\neq k_1,..,k_n}\left(|\alpha_k|^2\right)^{\beta_k^{0,2}}\left(\sum_{k'\neq k_1,..,k_n}(1-\beta_{k'}^{0,2})|\alpha_{k'}|^2\right)\\&\times\left(\sum_{k''\neq k_1,..,k_n}(1-\beta_{k''}^{0,2})|\alpha_{k''}|^2\right)(1+\mathcal{O}(\epsilon'))\,,\end{aligned} \tag{C.24}$$

$$G(M-1,n)=\sum_{\beta^{0,2}}\prod_{k\neq k_1,..,k_n}\left(|\alpha_k|^2\right)^{\beta_k^{0,2}}\left(\sum_{k'\neq k_1,..,k_n}(1-\beta_{k'}^{0,2})|\alpha_{k'}|^2\right), \tag{C.25}$$

while by definition

$$G(M-2,n)=\sum_{\beta^{0,2}}\prod_{k\neq k_1,..,k_n}\left(|\alpha_k|^2\right)^{\beta_k^{0,2}}. \tag{C.26}$$

The $\overset{*}{=}$ in Eq. (C.24) denotes that this property does not generally hold, but assumes "reasonable" distributions α_k, since the proof cannot be carried on for general distributions α_k. Rather, additional assumptions about the α_k for which

II will hold need to be made. Reasonable distributions α_k are close to the Fermi-Dirac distribution for energies deep below and high above the Fermi level. The modulus of the superconducting gap $|\Delta|$ self-consistenly provides the energy scale around the Fermi level where the distributions noticable differ. Furthermore, such distributions should be sufficiently "smooth" in the sense that for an enumeration $\pi(i)$ of all $K-n$ allowed momenta in ascending order of $|\alpha_{k=\pi(i)}|$ the resulting function $i \to |\alpha_{\pi(i)}|$ is "smooth", i.e., has no significant changes, on the scale of δM and n.

The statement of the $\stackrel{*}{=}$ in Eq. (C.24) is that the pathological case $k' = k''$ in Eq. (C.24) can be safely neglected. By the above assumption of "smoothness", there should exist many $k'' \neq k'$ such that $|\alpha_{k''}| \approx |\alpha_{k'}|$. In other words, having selected M-2 momenta contributing to a state, the exact choice of two further momenta, which in this case are allowed to agree, should be nearly independent. The pathological case of selecting the same momentum twice is a rare occurrence among many options with similar weight and neglecting it amounts to an error of order ϵ'.

Compare this to the case of the zero-temperature Fermi-Dirac distribution with M-1 momenta with non-zero $\alpha_k = 1$. This distribution fails to be smooth in the above sense, since $|\alpha_{\pi(M-1)}|$ is finite while $|\alpha_{\pi(M)}| = 0$. Having selected M-2 momenta according to π[1], the choice of the remaining two momenta cannot be independent, since the only non-vanishing choice for this distribution is $k' = k'' = \pi(M-1)$.

To complete the proof, one uses the property that the sums in the brakets are just partial sums of $|\alpha_k|^2$ over all "unoccupied" momenta not yet included in $\beta^{0,2}$. Due to the product over $|\alpha_k|$, the $\beta^{0,2}$ which carry most of the weigt in the sum over all multiindices are all similar in that they select M-2 momenta with large $|\alpha_k|$. Therefore, the sum of the modulus of the distribution function over the remaining momenta is for these $\beta^{0,2}$, and therefore for the sum overall, well approximated as the sum over the $K-n-M-2$ momenta with lowest $|\alpha_k|$. This approximation yields

$$G(M,n) = G(M-2,n)C(M)^2(1+\mathcal{O}(\epsilon'))\,, \tag{C.27}$$

$$G(M-1,n) = G(M-2,n)C(M)(1+\mathcal{O}(\epsilon'))\,, \tag{C.28}$$

$$C(M) = \sum_{i=1}^{K-n-M-2} |\alpha_{\pi(i)}|^2 \tag{C.29}$$

which immediately implies

$$\frac{G(M,n)G(M-2,n)}{G(M-1,n)^2} = \frac{G(M-2,n)^2C(M)^2}{G(M-2,n)^2C(M)^2}(1+\mathcal{O}(\epsilon') = (1+\mathcal{O}(\epsilon')\,, \tag{C.30}$$

completing the proof that **II** holds.

1 The choice of π is not unique since the modulus of the distribution is M-1 fold degenerate at the value 1. However, the discussion is independent of the arbitrary choice of π.

C.1.1 *Zero-temperature gap equation*

The (renormalized) ground state distribution function $\tilde{\alpha}_k$ can be obtained by varying the free energy F within a subspace of fixed particle content. The treatment of the entropic term for finite temperatures is the same as in the standard BCS-theory [22] and therefore not treated here. Instead, the following covers the derivation of the mean-field BCS gap equation of the particle-conserving theory for zero temperature, correcting and slightly extending a proof in the literature [71]. At zero temperature, the free energy reduces to the Hamiltonian

$$\hat{H} = \hat{H}_0 + \hat{V}\,. \tag{C.31}$$

Here, the single-particle term $\hat{H}_0$ is given by

$$\hat{H}_0 = \sum_{k,\sigma} (\xi_{k,\sigma} - \mu)\hat{c}^\dagger_{k,\sigma}\hat{c}_{k,\sigma}\,, \tag{C.32}$$

with ξ_k the single-particle energy of an electron with momentum k relative to the Fermi level μ, which is determined at the end in order to fix the particle content of the ground state. The single-particle energy for a free electron gas is $\xi_k = \frac{(\hbar k)^2}{2m}$, while for a lattice system, one should restrict the momenta k to the first Brillouin zone and introduce a band index. The interaction $\hat{V}$ is the Coulomb interaction modelled by[2].

$$\hat{V} = \frac{1}{2\mathcal{V}} \sum_{k,k',\sigma,\sigma',q} V_q \hat{c}^\dagger_{k+q,\sigma}\hat{c}^\dagger_{k'-q,\sigma'}\hat{c}_{k',\sigma'}\hat{c}_{k,\sigma}\,. \tag{C.33}$$

Obviously, this interaction is particle conservering, so that the relevant contribution of this interaction in the ground state of fixed particle content is described by the braket

$$\langle M|\,\hat{V}\,|M\rangle = \frac{1}{2\mathcal{V}} \sum_{k,k',\sigma,\sigma',q} V_q \,\langle M|\,\hat{c}^\dagger_{k+q,\sigma}\hat{c}^\dagger_{k'-q,\sigma'}\hat{c}_{k',\sigma'}\hat{c}_{k,\sigma}\,|M\rangle\,, \tag{C.34}$$

which contains three non-vanishing contributions. The first two are the Hartree- and the Fock term where $q = 0$ (Hartree) and $k' = k + q, \sigma = \sigma'$ (Fock), respectively. However, both of these contributions are weakly dependent on the distribution and can for most materials be approximated as constant [71]. They do therefore not contribute to the variation and can be dropped in the following.

The third contribution is the Cooper term. One obtains this term by assuming that the operators change the state $|M\rangle$ while requiring a finite overlap between the resulting state and $\langle M|$. Since $\langle M|$ is superposition of states composed solely

2 As discussed in Part III, this interaction will, in general, be more complicated and depend on k, k', and q. The form used here is the simple form as found for a free electron system, or as is proper for a simple metal within the jellium model.

of Kramers pairs, the overlap can only be finite for $\mathbf{k}' = -\mathbf{k}$ and $\sigma' = \bar{\sigma}$. Using the notation $\uparrow = +, \downarrow = -$ and the commutators

$$\begin{aligned}[\hat{B}_{\mathbf{k}'}, \hat{n}_{\mathbf{k},\sigma}] =& \hat{c}_{\bar{\mathbf{k}}',\downarrow}\hat{c}_{\mathbf{k}',\uparrow}\hat{c}^{\dagger}_{\mathbf{k},\sigma}\hat{c}_{\mathbf{k},\sigma} - \hat{c}^{\dagger}_{\mathbf{k},\sigma}\hat{c}_{\mathbf{k},\sigma}\hat{c}_{\bar{\mathbf{k}}',\downarrow}\hat{c}_{\mathbf{k}',\uparrow} \\ =& \delta_{\mathbf{k}',\mathbf{k}}\delta_{\sigma,\uparrow}\hat{B}_{\mathbf{k}'} + \delta_{\mathbf{k}',\bar{\mathbf{k}}}\delta_{\sigma,\downarrow}\hat{B}_{\mathbf{k}'} = \delta_{\mathbf{k}',\mathbf{k}\sigma}\hat{B}_{\mathbf{k}'}\,, \qquad \text{(C.35)} \\ [\hat{B}_{\mathbf{k}'}, \hat{B}_{\mathbf{k}}] =& \delta_{\mathbf{k},\mathbf{k}'}\left(1 - \hat{n}_{\mathbf{k},\uparrow} - \hat{n}_{\bar{\mathbf{k}},\downarrow}\right)\,, \qquad \text{(C.36)}\end{aligned}$$

one finds

$$\langle M|\,\hat{n}_{\mathbf{k},\sigma}\,|M\rangle = \frac{|\tilde{\alpha}_{\mathbf{k}\sigma}|^2}{1+|\tilde{\alpha}_{\mathbf{k}\sigma}|^2}\,\langle M-1,\mathbf{k}\sigma|\,\hat{B}_{\mathbf{k}\sigma}\hat{n}_{\mathbf{k},\sigma}\hat{B}^{\dagger}_{\mathbf{k}\sigma}\,|M-1,\mathbf{k}\sigma\rangle = \frac{|\tilde{\alpha}_{\mathbf{k}\sigma}|^2}{1+|\tilde{\alpha}_{\mathbf{k}\sigma}|^2}\,. \qquad \text{(C.37)}$$

Summing over all momenta and spin, this yields the condition

$$\sum_{\mathbf{k}} \frac{|\tilde{\alpha}_{\mathbf{k}}|^2}{1+|\tilde{\alpha}_{\mathbf{k}}|^2} = M\,. \qquad \text{(C.38)}$$

The expectation value of the single-particle Hamiltonian follows from Eq. (C.37) as

$$\langle M|\,\hat{H}_0\,|M\rangle = \sum_{\mathbf{k},\sigma}(\xi_{\mathbf{k},\sigma}-\mu)\,\langle M|\,\hat{n}_{\mathbf{k},\sigma}\,|M\rangle = \sum_{\mathbf{k},\sigma}(\xi_{\mathbf{k},\sigma}-\mu)\frac{|\tilde{\alpha}_{\mathbf{k}\sigma}|^2}{1+|\tilde{\alpha}_{\mathbf{k}\sigma}|^2}\,. \qquad \text{(C.39)}$$

In the presence of time-reversal symmetry, which is assumed in the following, one has $\xi_{\mathbf{k}} := \xi_{\mathbf{k},\uparrow} = \xi_{-\mathbf{k},\downarrow}$, such that in this case

$$\langle M|\,\hat{H}_0\,|M\rangle = 2\sum_{\mathbf{k}}(\xi_{\mathbf{k}}-\mu)\frac{|\tilde{\alpha}_{\mathbf{k}}|^2}{1+|\tilde{\alpha}_{\mathbf{k}}|^2}\,. \qquad \text{(C.40)}$$

Since derivatives of this type occur multiple times during the derivation, one can write for a general function X that

$$\frac{\delta}{\delta|\tilde{\alpha}_{\mathbf{k}}|}\frac{X(|\tilde{\alpha}_{\mathbf{k}}|)}{1+|\tilde{\alpha}_{\mathbf{k}}|^2} = \frac{X' + |\tilde{\alpha}_{\mathbf{k}}|^2X' - 2X|\tilde{\alpha}_{\mathbf{k}}|)}{(1+|\tilde{\alpha}_{\mathbf{k}}|^2)^2}, \qquad \text{(C.41)}$$

with X' the variational derivative of X. The variation of the single-particle energy in terms of the modulus $|\tilde{\alpha}_{\mathbf{k}}|$ then follows as

$$\frac{\delta}{\delta|\tilde{\alpha}_{\mathbf{k}}|}\,\langle M|\,\hat{H}_0\,|M\rangle = \frac{4(\xi_{\mathbf{k}}-\mu)|\tilde{\alpha}_{\mathbf{k}}|}{(1+|\tilde{\alpha}_{\mathbf{k}}|^2)^2}\,. \qquad \text{(C.42)}$$

Since the single-particle term is a function of the modulus only, the variation in terms of the phase $\arg(\tilde{\alpha}_{\mathbf{k}})$ vanishes.

For the Cooper term one finds the form [71]

$$\begin{aligned}
\langle M|\,\hat{V}_C\,|M\rangle &= \frac{1}{2\mathcal{V}}\sum_{k\neq k',\sigma} V_{k'-k}\,\langle M|\,\hat{c}^\dagger_{k',\sigma}\hat{c}^\dagger_{\bar{k}',\bar{\sigma}}\hat{c}_{\bar{k},\bar{\sigma}}\hat{c}_{k,\sigma}\,|M\rangle \\
&= \frac{1}{2\mathcal{V}}\sum_{k\neq k',\sigma} V_{k'-k}\,\langle M|\,\hat{B}^\dagger_{k'\sigma}\hat{B}_{k\sigma}\,|M\rangle = \frac{1}{\mathcal{V}}\sum_{k\neq k'} V_{k'-k}\,\langle M|\,\hat{B}^\dagger_{k'},\hat{B}_k\,|M\rangle \\
&= \frac{1}{\mathcal{V}}\sum_{k\neq k'} V_{k'-k}\frac{\tilde{\alpha}_k}{\sqrt{1+|\tilde{\alpha}_k|^2}}\frac{\tilde{\alpha}^*_{k'}}{\sqrt{1+|\tilde{\alpha}_{k'}|^2}}\,\langle M-1,k'|\,\hat{B}_{k'}\hat{B}^\dagger_{k'}\hat{B}_k\hat{B}^\dagger_k\,|M-1,k\rangle \\
&= \frac{1}{\mathcal{V}}\sum_{k\neq k'} V_{k'-k}\frac{\tilde{\alpha}_k}{\sqrt{1+|\tilde{\alpha}_k|^2}}\frac{\tilde{\alpha}^*_{k'}}{\sqrt{1+|\tilde{\alpha}_{k'}|^2}}\,\langle M-1,k'|\,|M-1,k\rangle \\
&= \frac{1}{\mathcal{V}}\sum_{k\neq k'} V_{k'-k}\frac{\tilde{\alpha}_k}{1+|\tilde{\alpha}_k|^2}\frac{\tilde{\alpha}^*_{k'}}{1+|\tilde{\alpha}_{k'}|^2}\,. \qquad \text{(C.43)}
\end{aligned}$$

The variation with respect to $\arg(\tilde{\alpha}_k)$ yields

$$\begin{aligned}
&\frac{\delta}{\delta\arg(\tilde{\alpha}_k)}\,\langle M|\,\hat{V}_C\,|M\rangle \\
&= \frac{i}{\mathcal{V}}\sum_{k\neq k'}\frac{1}{1+|\tilde{\alpha}_k|^2}\frac{1}{1+|\tilde{\alpha}_{k'}|^2}(V_{k'-k}\tilde{\alpha}_k\tilde{\alpha}^*_{k'}-\nu(k-k')\tilde{\alpha}_{k'}\tilde{\alpha}^*_k) \\
&= \frac{-2}{\mathcal{V}}\sum_{k\neq k'}\frac{1}{1+|\tilde{\alpha}_k|^2}\frac{1}{1+|\tilde{\alpha}_{k'}|^2}\mathfrak{Im}(V_{k'-k}\tilde{\alpha}_k\tilde{\alpha}^*_{k'})\,, \qquad \text{(C.44)}
\end{aligned}$$

which vanishes for all k and $|\tilde{\alpha}_k|$ simultaneously. This implies that the summands in the sum over k in Eq. (C.43) are real individually. Armed with this information, the variation with respect to the modulus $|\tilde{\alpha}_k|$ simplifies, since the variation of both quations via the product rule just yields twice the same term as

$$\begin{aligned}
&\frac{\delta}{\delta|\tilde{\alpha}_k|}\,\langle M|\,\hat{V}_C\,|M\rangle \\
&= \frac{2}{\mathcal{V}}\sum_{k\neq k'} V_{k'-k}\frac{e^{i\arg(\tilde{\alpha}_k)}}{(1+|\tilde{\alpha}_k|^2)^2}\frac{\tilde{\alpha}^*_{k'}}{1+|\tilde{\alpha}_{k'}|^2}(1-|\tilde{\alpha}_k|^2)\,, \qquad \text{(C.45)}
\end{aligned}$$

where Eq. (C.44) simplified the first and second quotient in Eq. (C.43). Since the variation of the Hamiltonian must vanish, the two contributions stemming from the Cooper term and the single-particle energy must be opposite, thereby yielding the gap equation

$$\begin{aligned}
4(\xi_k-\mu)|\tilde{\alpha}_k| &= -\frac{2}{\mathcal{V}}\sum_{k\neq k'} V_{k'-k}e^{i\arg(\tilde{\alpha}_k)}\frac{\tilde{\alpha}^*_{k'}}{1+|\tilde{\alpha}_{k'}|^2}(1-|\tilde{\alpha}_k|^2) \\
&= 2e^{i\arg(\tilde{\alpha}_k)}\Delta_k(1-|\tilde{\alpha}_k|^2)\,, \qquad \text{(C.46)}
\end{aligned}$$

where one introduces the gap function

$$\Delta_k = -\frac{1}{\mathcal{V}} \sum_{k' \neq k} V_{k'-k} \frac{\tilde{\alpha}^*_{k'}}{1 + |\tilde{\alpha}_{k'}|^2} \,. \tag{C.47}$$

The reality of the left-hand side of Eq. (C.46) ensures that $\Delta_k e^{i \arg(\tilde{\alpha}_k)}$ is real. As such, rewriting Eq. (C.46) as a quadratic equation for $|\tilde{\alpha}_k|$ of the form

$$0 = \Delta_k |\tilde{\alpha}_k|^2 + 2e^{-i \arg(\tilde{\alpha}_k)} (\xi_k - \mu) |\tilde{\alpha}_k| - \Delta_k \,, \tag{C.48}$$

one finds two possible solutions

$$\begin{aligned} |\tilde{\alpha}_k| =& \frac{-2e^{-i \arg(\tilde{\alpha}_k)} (\xi_k - \mu) \pm \sqrt{4e^{-i2 \arg(\tilde{\alpha}_k)} (\xi_k - \mu)^2 + 4\Delta_k^2}}{-2\Delta_k} \\ =& e^{-i \arg(\tilde{\alpha}_k)} \frac{-(\xi_k - \mu) \pm \sqrt{(\xi_k - \mu)^2 + |\Delta_k|^2}}{\Delta_k} \,. \end{aligned} \tag{C.49}$$

In terms of the quasiparticle excitation energy $E_k^2 = (\xi_k - \mu)^2 + \Delta_k^2$, one can write

$$\tilde{\alpha}_k = \frac{\pm E_k - (\xi_k - \mu)}{\Delta_k} \,. \tag{C.50}$$

As expected from variational calculus, not all extrema correspond to minima, and, as such, one should check which sign is the one corresponding to a stable superconducting phase. The choice of the sign dictates whether $|\tilde{\alpha}_k|$ approaches zero or grows large for energies ξ far below or above the chemical potential. The growth of $|\tilde{\alpha}_k|$ to infinity does not result in a divergence in the occoupany. Rather, growht present complete occupation of a state according to Eq. (C.37). For the plus sign, full occupancy is reached in the limit of small gaps for $\xi < \mu$, while the occupancy approaches zero for $\xi > \mu$. This choice of sign therefore allows the number of occupied states to be fixed by setting an appropriate μ and is connected to the Fermi-Dirac distribution at zero-temperature by the limit $\Delta \to 0^+$. Conversely, the choice of the minus sign results in growing occupancy of the levels for $\xi > \mu$. Since ξ for the free electron gas can grow arbitrarily large, this results in a divergence of the number of occupied states, irrespective of the choice of μ, which clearly represents an unphysical solution to the equation. Proceeding with the plus sign, one has

$$\tilde{\alpha}_k = \frac{E_k - \xi_k}{\Delta_k} \,, \tag{C.51}$$

such that

$$\frac{\tilde{\alpha}^*_k}{1 + |\tilde{\alpha}_k|^2} = \frac{E_k - \xi_k}{\Delta_k^*} \frac{\Delta_k \Delta_k^*}{2\Delta_k \Delta_k^* + 2\xi_k^2 - 2\xi_k E_k} = \frac{\Delta_k (E_k - \xi_k)}{2E_k^2 - 2E_k \xi_k} = \frac{\Delta_k}{2E_k} \,, \tag{C.52}$$

which, if inserted into Eq. (C.47), yields the usual BCS gap equation at zero temperature of the form

$$\Delta_k = -\frac{1}{\mathcal{V}} \sum_{q \neq 0} v(q) \frac{\Delta_{k+q}}{2E_{k+q}} \,. \tag{C.53}$$

The particle-conserving theory thus has the same well studied gap equation and quasiparticle excitations as the regular mean-field BCS theory [22, 71, 117].

C.2 HEISENBERG SPIN CHAINS

Heisenberg spin chains are a commonly used class of toy models for interacting one-dimensional quantum systems. In these models, a finite number of localized spins interact via exchange interaction in a direct analogue of the model of ferromagnetism proposed by Heisenberg [602].

The different models differ primarily in the type of exchange coupling and disorder they incorporate. The XXZ Heisenberg chain with disorder introduced by the presence of a random local field along the z-direction has the Hamiltonian

$$\hat{H}_{\text{XXZ,local-field}} = \sum_{i=1}^{N} J(\hat{S}_i^x \hat{S}_{i+1}^x + \hat{S}_i^y \hat{S}_{i+1}^y) + J_z \hat{S}_i^z \hat{S}_{i+1}^z + h_i \hat{S}_i^z \,. \tag{C.54}$$

In Eq. (C.54), i labels the sites, N is the length of the chain, periodic boundary conditions are applied such that $N+1 = 1$, $\hat{\mathbf{S}}$ are the spin operators with common spin length of either 0.5 or 1 and disorder is applied as a random field along the z-direction with random strength h_i drawn from some distribution. For uniform disorder in the range $[-h, h]$, this model exhibits signatures attributed to a quantum phase transition from an ergodic, thermalizing phase to a nonergodic many-body localized phase at a critical disorder strength h_c [267, 293, 296, 603–605].

Most investigations of the local-field-disordered model focus on the common spin length 0.5 [271, 279, 285, 297, 606–610], with comparatively fewer works also covering larger spin lengths starting with $S = 1$ [285, 611, 612]. When determining a value for the critical disorder strength of a transition to a many-body localized strength in the local-field-disordered (XXZ) Heisenberg chain, one needs to account for the fact that this value will, in general, not be a function only of h/J, but also of the ratio between J_z/J [81]. While there exist theoretical arguments in favor of the existence of a critical disorder strength for the transition to the many-body phase [279], the actual existence and the exact value of a critical disorder strength for such a quantum phase transition remains subject to an ongoing debate [248, 267, 287, 297, 613–617]. The range of values reported in the literature for a potential critical disorder strength varies based on the employed methodology, ranging from $h_c \approx 2.6\,J$ to $h_c \geqslant 4\,J$ for spin length 0.5 [285, 287, 296–298, 608, 613, 618]. Other investigations of a potential phase transition between

an ergodic and a many-body localized phase have pursued approaches based on matrix product states [287], Rényi entropies [619], considered thermalization via quantum avalanches [620–622], and Liouvillian relaxation due to residual coupling to an external bath [610]. The work by Schliemann et al. [285], which Chapter 5 refers to, treats the case $J_z = J$. This particular choice of J_z has the benefit that it has a direct connection to the exchange-disordered Heisenberg chain introduced below. In fact, at vanishing disorder h, respectively b, the two models agree as both merge into the isotropic $SU(2)$ symmetric Heisenberg chain.

Chapter 6 examines the effect of a global non-abelian symmetry, like the above global $SU(2)$ rotation of the spin orientation, on many-body localization. As such, the disorder needs to be compatible with this symmetry. A natural way to introduce such disorder into the model is to modify the exchange couplings with a random modulation as $J_i = J + b_i$, where $J \geqslant 0$, and b_i is a random variable. The resulting model is the exchange-disordered Heisenberg chain

$$\hat{H} = \sum_{i=1}^{N} J_i \hat{\mathbf{S}}_i \cdot \hat{\mathbf{S}}_{i+1}\,, \tag{C.55}$$

which is used in Siegl and Schliemann [227] for a uniform probability distribution with range of $[-b, b]$. In the limit of vanishing disorder, this model is analytically solvable via the Bethe ansatz [623]. Protopopov, W. W. Ho, and Abanin [242] investigated the same model with a more general probability distribution that reduces to the uniform case for fixed parameter $\alpha = 1.0$ and varying μ therein [242]. Saraidaris et al. [294] employed a normalized antiferromagnetic power-law distribution, which is also the subject of earlier works on this model [624–626], while Agarwal, Demler, and Martin investigated the noise spectrum of the model for signatures of many-body localization [627].

As pointed out by Theodorou and Cohen [624], there is a close relation between the Heisenberg spin chains and one-dimensional Hubbard models. This similarity extends even to the possibility of exactly mapping one model onto the other for specific limiting cases of their parameter spaces [628]. Moreover, the one-dimensional Hubbard models are also widely used in the study of many-body localization [81, 629–632], but are not covered in this thesis. Prelovšek, Barišić, and Žnidarič [629] discussed the absence of full many-body localization for a spin-ful Hubbard chain with global spin rotational invariance in a clear analogue to the imperfect many-body localized phase discussed in Part II, although they did not consider the resulting regime as a potential separate phase.

C.3 TIGHT-BINDING MODEL FOR TMD MONOLAYERS

Part III covers metallic 1H-transition metal dichalcogenides. Their chemical structure is MX_2, where M is a transition metal and X a chalcogen atom. For 1H-$NbSe_2$ the transition metal atom is niobium whose electronic configuration

is [Kr] $5s^1$ $4d^4$. With a proton number $Z = 41$, niobium is sufficiently heavy that significant spin-orbit interaction (SOI) is present due to the lack of inversion symmetry [466]. As an exception to the Madelung filling rules [633], niobium has an unfilled 5s shell with one electron transitioning to the nominally higher 4d shell [478, 634]. Thus, the frontier orbital in the single electron picture for niobium is the partially filled 4d shell. The chalcogen atom is selenium with orbital configuration [Ar]$3d^{10}4s^24p^4$ and a partially filled 4p shell as its frontier orbital [478, 634].

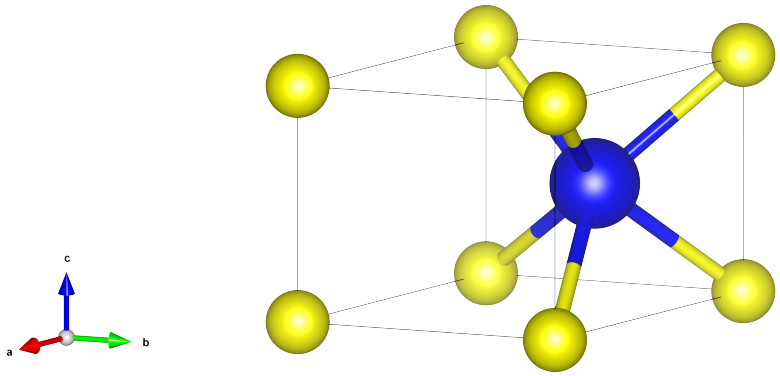

Figure C.1: **Prismatic trigonal unit cell of an 1H-TMD monolayer.** The crystal has space group P3m1. The basis has its highest symmetry of D_{3h} (Schönflies) or equiv. $\bar{6}$m2 (Hermann-Mauguin) at the transition metal site (blue).

Each monolayer consists of a two-dimensional hexagonal lattice endowed with a three-dimensional basis. One transition metal atom sits at the lattice site at the center of a trigonal prism oriented with its threefold axis (**c**-axis in Section C.3) perpendicular to the plane. X atoms are situated at the corners of the prism, resulting in two X atoms per unit cell as is shown in Section C.3. The X atoms generate two hexagonal, out-of-plane X sublattices, which are offset to the underlying hexagonal transition metal sublattice. The transition metal sublattice has higher symmetry D_{6h}, which includes inversion symmetry. The dominant contribution to the bands near the Fermi surface are from the transition metal frontier orbitals [329, 390, 450, 635] with some admixture of the chalcogen p orbitals. G.-B. Liu et al. constructed a tight-binding model starting from the three most relevant d orbitals of the transition model atoms; $|d_{z^2}\rangle$, $|d_{xy}\rangle$, and $|d_{x^2-y^2}\rangle$, using the symmetry of the basis to reduce the free parameters of the model by relating different hoppings with each other. An erratum [636] to the original derivation [329] fixed an issue with the symmetry of the next-nearest neighbors, and agrees with an independent derivation due to Möckli and Khodas [490]. This section recounts this symmetry based derivation, comments on some remaining

issues with both the erratum [636] and the derivation by Möckli and Khodas [490], and introduces the model numerically investigated in Part III. In the following, the origin of the coordinate system is at an transition metal site, the $\mathbf{c}$-axis of the crystal points along the positive z-axis, and the $\mathbf{a}$-axis points along the positive x-axis of the coordinate system, such that within the two-dimensional x-y-plane one has

$$\mathbf{R}_1 = a \begin{pmatrix} 1 \\ 0 \end{pmatrix} , \tag{C.56}$$

where the lattice vectors $\mathbf{R}_i, \mathbf{R}'_i, \mathbf{R}''_i$ label the nearest (NN), next-nearest (NNN) and third-nearest neighbors (TNN), respectively. These neareset-neighbor sites are shown in Fig. C.2.

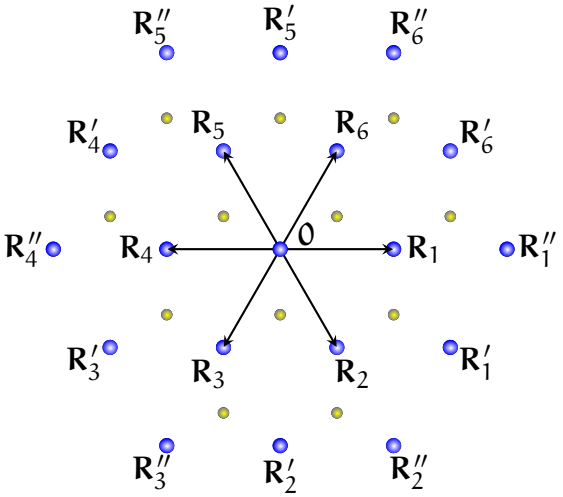

Figure C.2: **Topview along the c crystal axis of a 1H-monolayer TMD.** Vectors connecting the origint with the nearest neighbor ($\mathbf{R}_i$), next nearest neighbor ($\mathbf{R}'_i$) and third nearest neighbor ($\mathbf{R}''_i$) transition metal sites (blue) are shown. The X sites (yellow) form two mirror symmetric out-of-plane sublattices.

The transition metal sites are situated on the lattice and are thus invariant under C_s. Therefore, the symmetry operations generating the orbit (the codomain under the group action) of equivalent sites to $\mathbf{R}_1$ are the elements of D_3. Using these symmetry operations, the NN orbit of symmetry equivalent sites to $\mathbf{R}_1$ is given by

$$\begin{aligned} &\mathbf{R}_1 = E\mathbf{R}_1 , && \mathbf{R}_2 = \mathcal{C}_{2,c}\mathbf{R}_1 , && \mathbf{R}_3 = (\mathcal{C}_3)^2\mathbf{R}_1 , \\ &\mathbf{R}_4 = \mathcal{C}_{2,b}\mathbf{R}_1 , && \mathbf{R}_5 = \mathcal{C}_3\mathbf{R}_1 , && \mathbf{R}_6 = \mathcal{C}_{2,a}\mathbf{R}_1 . \end{aligned} \tag{C.57}$$

Both the NNN and the TNN sites can be given in terms of the NN sites as

$$\mathbf{R}'_i = \mathbf{R}_i + \mathbf{R}_{i+1} \qquad \mathbf{R}''_i = 2\mathbf{R}_i . \tag{C.58}$$

By construction, the TNN site's behavior under the group action of D_3 is the same as for the NN sites in Eq. (C.57). The NNN sites belong to two independent orbits under the symmetry group D_3 of the crystal, while the lattice itself has the higher symmetry D_6. As such, the two orbits are connected by inversion symmetry i as

$$\mathbf{R}'_{j+3} = i\mathbf{R}'_j\,, \tag{C.59}$$

where $\mathbf{R}'_7 = \mathbf{R}'_1$. Each orbit is generated by

$$\mathbf{R}'_{j+2} = \mathcal{C}_3\mathbf{R}'_j\,. \tag{C.60}$$

Since the considered orbital wavefunctions are real-valued, it implies that also the hopping integrals

$$E_{\nu,\nu'}(\mathbf{R}) = \langle \nu, \mathbf{R}+\mathbf{G}|\,\hat{H}\,|\nu', \mathbf{G}\rangle\ , \tag{C.61}$$

between orbitals $\nu, \nu' \in \{d_{z^2}, d_{xy}, d_{x^2-y^2}\}$ localized at transition metal sites $\mathbf{G}, \mathbf{R}+\mathbf{G}$, where $\mathbf{R}, \mathbf{G}$ are arbitrary lattice vectors, are real-valued. As the considered orbitals are also all invariant under C_s, it follows that one can consider the subgroup D_3 of D_{3h} for the following considerations. Since the X sublattices will influence the hopping matrix elements between transition metal sites, the Hamiltonian is invariant under D_3, but not under the higher symmetry D_6 of the transition metal sublattice. To study the symmetry constraints upon the hopping matrix, one can investigate the transformation behavior of the underlying orbitals. The orbital d_{z^2} belongs to the irreducible representation A_1, d_{xy} and $d_{x^2-y^2}$ to E. The respective matrices for the irreducible representations are listed in [601]. The labels of the orbitals correspond to the irreducible representation they belong to as

$$|\phi_1^1\rangle = d_{z^2}, \qquad |\phi_1^2\rangle = d_{xy}, \qquad |\phi_2^2\rangle = d_{x^2-y^2}\,. \tag{C.62}$$

$|\phi_1^1\rangle$ lies inside the one-dimensional irreducible representation A_1 for which all characters are equal to unity. Therefore, the matrix $D^1(g)$ representing the action of a group element g on this states is trivial as

$$D^1(g) = 1 \quad \forall g \in D_3\,. \tag{C.63}$$

$|\phi_1^2\rangle$ and $|\phi_2^2\rangle$ are part of the two-dimensional irreducible representation E. One only needs to construct the matrices of the group elements $\mathcal{C}_3$ and $\mathcal{C}_{2,a}$, as the remaining transformation matrices are fixed by the group property. The matrix representation of a rotation around the z-axis is easily constructed by expanding the real spherical harmonics in the angular-momentum basis $|L, L_z\rangle$ using $xy \propto \sin(2\phi), x^2-y^2 \propto \cos(2\phi)$, which yields

$$|\phi_1^2\rangle = \frac{1}{\sqrt{2}i}\left(|2,2\rangle - |2,-2\rangle\right), \qquad |\phi_2^2\rangle = \frac{1}{\sqrt{2}}\left(|2,2\rangle + |2,-2\rangle\right)\,. \tag{C.64}$$

The transformation behavior in the angular-momentum basis is well-known to be [601]

$$R(z,\phi)\,|L,L_z\rangle = e^{iL_z\phi}\,|L,L_z\rangle\ . \tag{C.65}$$

Using the transformation matrix

$$\begin{pmatrix}|\phi_1^2\rangle\\|\phi_2^2\rangle\end{pmatrix} = \frac{1}{\sqrt{2}}\begin{pmatrix}-i & i\\1 & 1\end{pmatrix}\begin{pmatrix}|2,2\rangle\\|2,-2\rangle\end{pmatrix}, \tag{C.66}$$

and the inverse transformation

$$\begin{pmatrix}|2,2\rangle\\|2,-2\rangle\end{pmatrix} = \frac{1}{\sqrt{2}}\begin{pmatrix}i & 1\\-i & 1\end{pmatrix}\begin{pmatrix}|\phi_1^2\rangle\\|\phi_2^2\rangle\end{pmatrix}, \tag{C.67}$$

the action of a rotation around the z-axis by an arbitrary rotation angle ϕ reads

$$\begin{aligned}
\hat{R}(z,\phi)\begin{pmatrix}|\phi_1^2\rangle\\|\phi_2^2\rangle\end{pmatrix} =& \hat{R}(z,\phi)\frac{1}{\sqrt{2}}\begin{pmatrix}-i & i\\1 & 1\end{pmatrix}\begin{pmatrix}|2,2\rangle\\|2,-2\rangle\end{pmatrix}\\
=& \frac{1}{\sqrt{2}}\begin{pmatrix}-i & i\\1 & 1\end{pmatrix}\hat{R}(z,\phi)\begin{pmatrix}|2,2\rangle\\|2,-2\rangle\end{pmatrix}\\
=& \frac{1}{\sqrt{2}}\begin{pmatrix}-i & i\\1 & 1\end{pmatrix}\begin{pmatrix}e^{2i\phi} & 0\\0 & e^{-2i\phi}\end{pmatrix}\begin{pmatrix}|2,2\rangle\\|2,-2\rangle\end{pmatrix}\\
=& \frac{1}{2}\begin{pmatrix}-i & i\\1 & 1\end{pmatrix}\begin{pmatrix}e^{2i\phi} & 0\\0 & e^{-2i\phi}\end{pmatrix}\begin{pmatrix}i & 1\\-i & 1\end{pmatrix}\begin{pmatrix}|\phi_1^2\rangle\\|\phi_2^2\rangle\end{pmatrix}\\
=& \begin{pmatrix}\cos(2\phi) & \sin(2\phi)\\-\sin(2\phi) & \cos(2\phi)\end{pmatrix}\begin{pmatrix}|\phi_1^2\rangle\\|\phi_1^2\rangle\end{pmatrix}.
\end{aligned} \tag{C.68}$$

For the choice of basis ordering used by G.-B. Liu et al., the rotation matrix here is equivalent to a rotation matrix of the coordinates x, y with $\phi \to -2\phi$. For $\mathcal{C}_3$, one has $\phi = \frac{2\pi}{3}$ and the resulting matrix representations are

$$D^2(\mathcal{C}_3) = \frac{1}{2}\begin{pmatrix}-1 & -\sqrt{3}\\\sqrt{3} & -1\end{pmatrix}, \qquad D^2((\mathcal{C}_3)^2) = \frac{1}{2}\begin{pmatrix}-1 & \sqrt{3}\\-\sqrt{3} & -1\end{pmatrix}. \tag{C.69}$$

For $\mathcal{C}_{2,a}$, its more convenient to start with $\mathcal{C}_{2,b}$, which flips the x-axis. There, the transformation behavior of the real spherical harmonics is

$$D^2(\mathcal{C}_{2,b}) = \begin{pmatrix}-1 & 0\\0 & 1\end{pmatrix}. \tag{C.70}$$

Using $\mathcal{C}_{2,a} = \mathcal{C}_3\mathcal{C}_{2,b}(\mathcal{C}_3)^2$ and $\mathcal{C}_{2,c} = (\mathcal{C}_3)^2\mathcal{C}_{2,b}\mathcal{C}_3$ yields

$$D^2(\mathcal{C}_{2,a}) = \frac{1}{2}\begin{pmatrix}1 & \sqrt{3}\\\sqrt{3} & -1\end{pmatrix}, \qquad D^2(\mathcal{C}_{2,c}) = \frac{1}{2}\begin{pmatrix}1 & -\sqrt{3}\\-\sqrt{3} & -1\end{pmatrix}. \tag{C.71}$$

The invariance of the crystal with respect to these operations implies for the hopping matrix E

$$E^{jj'}_{\mu\mu'}(\mathbf{R}) = \langle \phi^{j}_{\mu}(\mathbf{R}+\mathbf{G})|\,\hat{H}\,|\phi^{j'}_{\mu'}(\mathbf{G})\rangle\,, \tag{C.72}$$

the property [329]

$$E^{jj'}_{\mu\mu'}(\hat{g}\mathbf{R}) = \sum_{\nu\nu'} D^{j}_{\mu\nu}(\hat{g}) E^{jj'}_{\nu\nu'}(\mathbf{R}) \left[D^{j'}(\hat{g})\right]^{\dagger}_{\nu'\mu'}, \forall g \in D_3. \tag{C.73}$$

Eq. (C.73) itself only relates hopping matrices to sites in the same orbit under the group action of D_3. Symmetry under hermitian conjugation further implies the condition

$$E^{jj'}_{\mu\mu'}(\mathbf{R}) = (E^{j'j}_{\mu'\mu}(-\mathbf{R}))^{*} = E^{j'j}_{\mu'\mu}(-\mathbf{R}), \tag{C.74}$$

where one uses the translational invariance $\mathbf{G} \to \mathbf{G} - \mathbf{R}$ in the first step and the reality of the hopping matrix elements in the chosen basis in the second step. Combing these two conditions results in constraints on the elements of the hopping matrix whenever there is a group element $g \in D_3$ s.t. $g\mathbf{R} = -\mathbf{R}$. For the hopping matrix

$$E\,(\mathbf{R}) = \begin{pmatrix} E^{11}_{11}(\mathbf{R}) & E^{12}_{11}(\mathbf{R}) & E^{12}_{12}(\mathbf{R}) \\ E^{21}_{11}(\mathbf{R}) & E^{22}_{11}(\mathbf{R}) & E^{22}_{12}(\mathbf{R}) \\ E^{21}_{21}(\mathbf{R}) & E^{22}_{21}(\mathbf{R}) & E^{22}_{22}(\mathbf{R}) \end{pmatrix}, \tag{C.75}$$

one finds

$$E\,(g\mathbf{R}) = E^{\dagger}\,(\mathbf{R})\,\forall g \in D_3 : g\mathbf{R} = -\mathbf{R}. \tag{C.76}$$

For the NN and TNN orbits, such a constraint is given by $\mathcal{C}_{2,b}$ for the hopping along $\mathbf{R}_1$. Using the fact that the overlaps between the real orbitals are real, this results in the constraints

$$E^{22}_{21}(\mathbf{R}_1) = E^{22}_{12}(-\mathbf{R}_1) = -E^{22}_{12}(\mathbf{R}_1), \tag{C.77}$$
$$E^{21}_{11}(\mathbf{R}_1) = E^{12}_{11}(-\mathbf{R}_1) = -E^{12}_{11}(\mathbf{R}_1), \tag{C.78}$$
$$E^{21}_{21}(\mathbf{R}_1) = E^{12}_{12}(-\mathbf{R}_1) = E^{12}_{12}(\mathbf{R}_1). \tag{C.79}$$

The corresponding minimal set of real valued parameters is

$$E_{NN}(\mathbf{R}_1) = \begin{pmatrix} t_0 & t_1 & t_2 \\ -t_1 & t_{11} & t_{12} \\ t_2 & -t_{12} & t_{22} \end{pmatrix}, \quad E_{TNN}(\mathbf{R}''_1) = \begin{pmatrix} u_0 & u_1 & u_2 \\ -u_1 & u_{11} & u_{12} \\ u_2 & -u_{12} & u_{22} \end{pmatrix}. \tag{C.80}$$

The NN tight-binding Hamiltonian follows from the group properties as [329]

$$H_{tb,NN}(\mathbf{k}) = \sum_{g\in D_3} e^{i\mathbf{k}\cdot(g\mathbf{R}_1)} E_{NN}(g\mathbf{R}_1) = \begin{pmatrix} H^{11}_{11} & H^{12}_{11} & H^{12}_{12} \\ H^{12*}_{11} & H^{22}_{11} & H^{22}_{12} \\ H^{12*}_{12} & H^{22*}_{12} & H^{22}_{22} \end{pmatrix}, \tag{C.81}$$

where its elements in terms of $(a, b) = (k_x/2a, \sqrt{3}k_y/2a)$ read

$$
\begin{aligned}
H_{11}^{11} &= t_0(4\cos(a)\cos(b) + 2\cos(2a)) + \epsilon_1\,, && \text{(C.82)}\\
H_{11}^{12} &= -2\sqrt{3}t_2\sin(a)\sin(b) + 2it_1(\sin(a)\cos(b) + \sin(2a))\,,\\
H_{12}^{12} &= 2t_2(\cos(2a) - \cos(a)\cos(b)) + 2i\sqrt{3}t_1\cos(a)\sin(b)\,,\\
H_{11}^{22} &= (t_{11} + 3t_{22})\cos(a)\cos(b) + 2t_{11}\cos(2a) + \epsilon_2\,,\\
H_{12}^{22} &= -\sqrt{3}(t_{11} - t_{22})\sin(a)\sin(b) + 4it_{12}(\cos(a) - \cos(b)))\,,\\
H_{22}^{22} &= (3t_{11} + t_{22})\cos(a)\cos(b) + 2t_{22}\cos(2a) + \epsilon_2\,. && \text{(C.83)}
\end{aligned}
$$

For the NNN sites, Eq. (C.76) cannot be fulfilled as sites connected by inversion lie in different orbits. This was first mistakenly ignored in their original model [329], but later on justified as an approximation in an erratum [636] by G.-B. Liu et al. and adopted by Möckli and Khodas [490]. The model is still the most widely used tight-binding model for monolayer TMDs, warranting a brief discussion of the issue and a partial solution. The key approximation is that the symmetry breaking properties of the X sublattices on the hopping to the NNN sites are taken as sufficiently weak, that one can use the larger approximate symmetry group D_6 instead of the true symmetry group D_3. The $\mathcal{C}_2$ axes of D_3 are the $\mathcal{C}_2''$ axes of D_6, and are thus proper symmetries of the crystal for which the transformation matrices of the orbtials were already introduced above. However, both the $\mathcal{C}_2$ axis along z, and the axes $\mathcal{C}_2'$ along the NN directions, contribute new approximate symmetries which can fulfill Eq. (C.76). One can again label the three $\mathcal{C}_2'$ axes as a, b and c according to increasing mathematical angle of their rotational axes in plane with the x-axis. The orbitals considered here fall into the irreducible representations A_1 for $|d_z^2\rangle$ and E_2 for $|d_{xy}\rangle, |d_{x^2-y^2}\rangle$. The matrix representation for A_1 is trivial for all elements of D_6. For E_2 with basis functions xy and $x^2 - y^2$ the two fold rotation is equivalent to the identity as

$$
D^{E_2}(\mathcal{C}_2) = \begin{pmatrix} 1 & 0 \\ 0 & 1 \end{pmatrix}. \qquad \text{(C.84)}
$$

To construct the remaining matrix representations one can again start from a simpler two-fold rotation axis which in this case is provided by the $\mathcal{C}_{2,a}'$ axis that flips the y-direction and has matrix representation

$$
D^{E_2}(\mathcal{C}_{2,a}') = \begin{pmatrix} -1 & 0 \\ 0 & 1 \end{pmatrix}. \qquad \text{(C.85)}
$$

The matrix representations of the action of the other two $\mathcal{C}_2'$ axese can again be constructed by the group property and read

$$
D^{E_2}(\mathcal{C}_{2,b}') = \frac{1}{2}\begin{pmatrix} 1 & -\sqrt{3} \\ -\sqrt{3} & -1 \end{pmatrix}, \qquad D^{E_2}(\mathcal{C}_{2,c}') = \frac{1}{2}\begin{pmatrix} 1 & \sqrt{3} \\ \sqrt{3} & -1 \end{pmatrix}. \qquad \text{(C.86)}
$$

Again, the goal is to reduce the hopping matrices $E(\mathbf{R}_i')$ to all next-nearest neighbors to the hopping matrix $E(\mathbf{R}_1')$. Since the group action of D_6 on A_1 is trivial, no constraints arise for $E_{11}^{11}(\mathbf{R}_1')$. For the remaining matrix elements, one uses that $\mathbf{R}_4' = \mathcal{C}_2\mathbf{R}_1' = \mathcal{C}_{2,c}'\mathbf{R}_1'$ which implies a constraint on the elements of the hopping matrix $E(\mathbf{R}_1')$ as both of these transformations must yield equivalent results. Since the action of $\mathcal{C}_2$ is trivial both on A_1 and E_2, this equality imposes the conditions

$$E_{11}^{21}(\mathbf{R}_1') = \frac{1}{2}E_{11}^{21}(\mathbf{R}_1') - \frac{\sqrt{3}}{2}E_{21}^{21}(\mathbf{R}_1'), \quad E_{21}^{21}(\mathbf{R}_1') = -\frac{\sqrt{3}}{2}E_{11}^{21}(\mathbf{R}_1') - \frac{1}{2}E_{21}^{21}(\mathbf{R}_1'), \tag{C.87}$$

$$E_{11}^{12}(\mathbf{R}_1') = \frac{1}{2}E_{11}^{12}(\mathbf{R}_1') - \frac{\sqrt{3}}{2}E_{12}^{12}(\mathbf{R}_1'), \quad E_{12}^{12}(\mathbf{R}_1') = -\frac{\sqrt{3}}{2}E_{11}^{12}(\mathbf{R}_1') - \frac{1}{2}E_{12}^{12}(\mathbf{R}_1'), \tag{C.88}$$

which require $E_{21}^{21}(\mathbf{R}_1') = \frac{-1}{\sqrt{3}}E_{11}^{21}(\mathbf{R}_1')$ and $E_{12}^{12}(\mathbf{R}_1') = \frac{-1}{\sqrt{3}}E_{11}^{12}(\mathbf{R}_1')$. At this point G.-B. Liu et al. make the distinction that while they require equivalent symmetry operations to yield the same result, thereby giving the constraints above, they do not employ these approximate symmetries in Eq. (C.76) to fix $E_{11}^{12}(\mathbf{R}') = E_{11}^{21}$ as done above for t_1. Taking the difference between the two transformations yields for $E^{22}(\mathbf{R}')$ the conditions

$$0 = \frac{1}{4}(\sqrt{3}(E_{22}^{22} - E_{11}^{22}) - (E_{12}^{22} + E_{21}^{22})\begin{pmatrix}\sqrt{3} & 1\\ 1 & -\sqrt{3}\end{pmatrix} + (E_{12}^{22} - E_{21}^{22})\begin{pmatrix}0 & -1\\ 1 & 0\end{pmatrix}, \tag{C.89}$$

which has the solution $E_{12}^{22} = E_{21}^{22}$ and $E_{22}^{22} = E_{11}^{22} + \frac{2}{\sqrt{3}}E_{12}^{22}$.

Thus, the hopping matrix to the next nearest neighbor site $\mathbf{R}_1'$ is given by[3]

$$E(\mathbf{R}_1') = \begin{pmatrix} r_0 & r_1 & \frac{-1}{\sqrt{3}}r_1 \\ r_2 & r_{11} & r_{12} \\ \frac{-1}{\sqrt{3}}r_2 & r_{12} & r_{11} + \frac{2}{\sqrt{3}}r_{12} \end{pmatrix} \tag{C.90}$$

3 In the work by Möckli and Khodas [490] the convention on the order of next-nearest neighbors differs from the original work by G.-B. Liu et al. [329]. The nearest neighbor site S_6 of Möckli and Khodas is equivalent to $\tilde{\mathbf{R}}_1$ of G.-B. Liu et al. ($\mathbf{R}_1'$ here). Möckli and Khodas worked with $E_{11}^{12}(S_6) = -r_1$ instead of $E_{11}^{12}(\tilde{R}_1) = r_1$ is in the model by G.-B. Liu et al. [329, 636] indicating a possible sign mistake.

which yields a three-band model with hamiltonian $H_{tb,TNN}(\mathbf{k})$ with matrix elements

$$\begin{aligned}
H_{11}^{11} &= 4\cos(a)\cos(b)(-r_0 + t_0 + u_0) \\
&\quad + 2\cos(2a)(4r_0\cos(a)\cos(b) + t_0 + u_0) \\
&\quad + 2r_0\cos(2b) + \epsilon_1
\end{aligned} \tag{C.91}$$

$$\begin{aligned}
H_{11}^{12} &= 2\sin(a)\sin(b)\left(2\cos(2a)(r_1 + r_2) + r_1 + r_2 - \sqrt{3}(t_2 + u_2)\right) \\
&\quad + 2i\sin(a)\cos(b)(a + 2a\cos(2a) + t_1 + u_1) + 2i\sin(2a)(t_1 + u_1)\,,
\end{aligned} \tag{C.92}$$

$$\begin{aligned}
H_{12}^{12} &= \frac{1}{3}(-2\cos(a)\cos(b)\left(2\sqrt{3}\cos(2a)(r_1 + r_2) + 3(t_2 + u_2)\right) \\
&\quad + 2\sqrt{3}\cos(a)\cos(b)(r_1 + r_2) \\
&\quad + 2i\sqrt{3}\cos(a)\sin(b)(-a + 2a\cos(2a) + 3(t_1 + u_1)) \\
&\quad + 2i\sqrt{3}a\sin(2b) + 6\cos(2a)(t_2 + u_2) + 2\sqrt{3}\cos(2b)(r_1 + r_2))\,,
\end{aligned} \tag{C.93}$$

$$\begin{aligned}
H_{11}^{22} &= \cos(a)\cos(b)(-4r_{11} + t_{11} \\
&\quad + 3t_{22} + u_{11} + 3u_{22}) + 2\cos(2a)(4r_{11}\cos(a)\cos(b) + t_{11} + u_{11}) \\
&\quad + 2\cos(2b)\left(r_{11} + \sqrt{3}r_{12}\right) + \epsilon_2\,,
\end{aligned} \tag{C.94}$$

$$\begin{aligned}
H_{12}^{22} &= \sin(a)(\sin(b)\,(8r_{12}\cos(2a) + 4r_{12} \\
&\quad + \sqrt{3}\,(-t_{11} + t_{22} - u_{11} + u_{22})) + 4i(t_{12} + u_{12})(\cos(a) - \cos(b)))\,,
\end{aligned} \tag{C.95}$$

$$\begin{aligned}
H_{22}^{22} &= \frac{1}{3}(\cos(a)\cos(b)(8\cos(2a)\left(3r_{11} + 2\sqrt{3}r_{12}\right) \\
&\quad - 12r_{11} - 8\sqrt{3}r_{12} + 3(3t_{11} + t_{22} + 3u_{11} + u_{22})) \\
&\quad + 6\cos(2a)(t_{22} + u_{22}) + 2\cos(2b)\left(3r_{11} - \sqrt{3}r_{12}\right) + 3\epsilon_2)\,,
\end{aligned} \tag{C.96}$$

in agreement with the result of G.-B. Liu et al. [329]. The corresponding spinful three-band Hamiltonian with Ising SOI follows as

$$H_{tb,TNN,SOI}(\mathbf{k}) = \sigma_0 \otimes H_{tb,TNN}(\mathbf{k}) + \frac{\lambda}{2}\sigma_z \otimes L_z\,, \tag{C.97}$$

where $L_z = \mathrm{diag}(0, 2, -2)$ in the angular-momentum basis. Fig. C.3 depicts the resulting spin-split band structure for the parameter set of He et al. [383] in Table C.1.

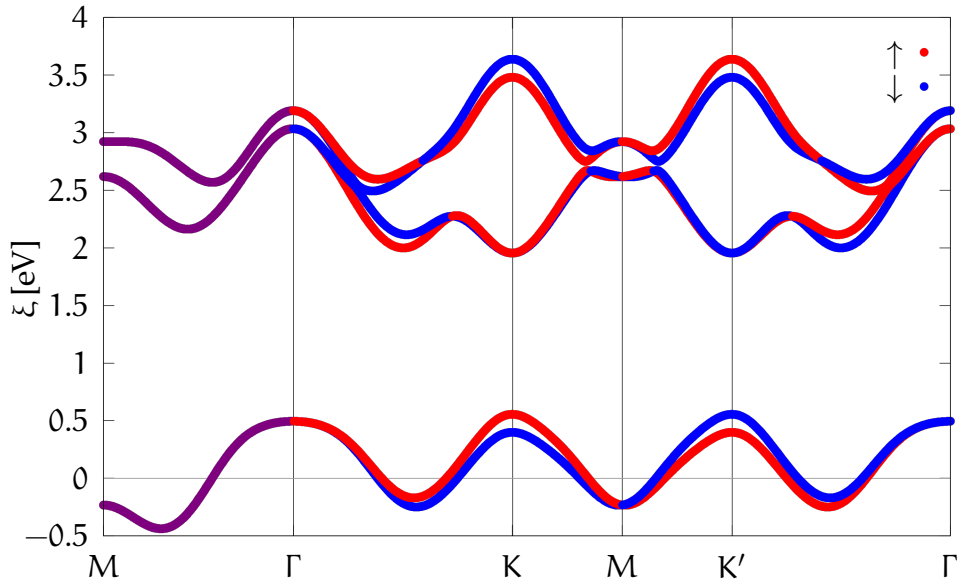

Figure C.3: **Ising-SOI-split band structure of 1H-$NbSe_2$ along high symmetry lines in the Brillouin zone.** The model is the same as in Fig. 7.2 and shows clearly the fully spin polarized nature of the bands throughout most of the Brillouin zone. The symmetry of the lattice forces the spin-orbit interaction to vanish along the $\Gamma - M$-direction.

Ref.	a	ϵ_1	ϵ_2	t_0	t_1	t_2	t_{11}	t_{12}	t_{22}	λ
[466]	3.445	1.408	2.048	-0.128	0.115	-0.466	0.115	0.122	0.036	0.075
r_0	r_1	r_2	r_{11}	r_{12}	u_0	u_1	u_2	u_{11}	u_{12}	u_{22}
0.025	0.194	-0.79	0.021	0.096	-0.031	-0.037	-0.002	0.258	-0.179	-0.167
Ref.	a	ϵ_1	ϵ_2	t_0	t_1	t_2	t_{11}	t_{12}	t_{22}	λ
[383]	3.445	1.447	1.850	-0.231	0.312	0.346	0.280	0.279	-0.054	0.078
r_0	r_1	r_2	r_{11}	r_{12}	u_0	u_1	u_2	u_{11}	u_{12}	u_{22}
0.004	-0.010	0.039	0.032	0.099	0.069	-0.038	0.054	0.060	-0.018	-0.043
Ref.	a	ϵ_1	ϵ_2	t_0	t_1	t_2	t_{11}	t_{12}	t_{22}	λ
[64]	3.474	1.347	2.120	-0.264	0.273	0.240	0.169	0.477	-0.054	0.075
r_0	r_1	r_2	r_{11}	r_{12}	u_0	u_1	u_2	u_{11}	u_{12}	u_{22}
0.204	-0.080	0.039	0.032	0.099	-0.070	-0.038	0.044	0.044	0.062	-0.167

Table C.1: **Tight-binding parameter sets.** All energies are in eV, and all distances in Å. The spin orbit coupling for Kim and Son [466] is not reported by the authors and thus taken from a digitized measurement of Figure 8 therein, while He et al. [383] do not report their lattice spacing a with the one from Kim and Son used instead.

D

DEVELOPED CODES

This chapter covers the different codes developed throughout the research for this thesis. For each code, a brief overview of the scope and functionalities is provided together with a link to the git repository of the university.

D.1 AC-DC-DRIVEN TRANSPORT CODE

This code generated the results presented in Part I and underpins the result published in Siegl, Picó-Cortés, and Grifoni [40]. The code implements the calculation within the Nakajima-Zwanzig formalism applied to the problem of an AC-DC-driven S-QD-S junction to sequential tunneling order. It calculates the steady-state current for a junction in which the superconducting leads are of the form discussed in Chapter 3, and where the quantum dot is represented by a single impurity Anderson model [125]. By making use of MATLAB's implementation of sparse matrices, the operators used for calculating both the propagation and current kernels are generalized to include a Floquet index in the driving frequency, which enables the treatment of periodic driving, as well as the calculation of harmonics of the current. The code allows for asymmetric tunneling coupling of the central system to an arbitrary number of leads. An implementation of selection rules and conserved quantities in terms of masks is provided to reduce the dimensionality of the final matrix problem to be solved. Different calculations are defined by configuration files, enabling a sequential processing of multiple jobs. So far, the only central system implemented is the single impurity Anderson model. However, the code is structured such as to enable a straightforward implementation of any other central system for which its Liovillian and the form of its annihilation operators $\hat{d}$ are known. The code is available on GitLab under https://git.uni-regensburg.de/sij35249/transportcodeac.git .

D.2 IMPERFECT MANY-BODY LOCALIZATION

This project covers the code that was used to generate the results shown in Part II and published in Siegl and Schliemann [227]. The code base is split into two separate logical steps. The first step is data production for the disorder average

mentioned in Chapter 5. As disorder averaging allows for trivial parallelization, this part of the code is split into two separate parts. A queuing script written in Python 3 allows for an easy sweep of parameters like the disorder strength. It further handles the distribution of individual jobs by sequentially submitting jobs to the torque queuing system currently used by the high-performance computing infrastructure of the University of Regensburg. The actual data production proceeds using a code implemented in the C standard C11 that sets up the Hamiltonian of an exchange-disordered Heisenberg chain as introduced in Section C.2, performs exact diagonalization using LAPACK's dsyevr routine to obtain the full spectrum, and saves the resulting eigenvalues for later use. The second step includes data processing and visualization using Python 3 with the Python packages NumPy [558] for data processing and Matplotlib [637] for visualization. Since the publication of Siegl and Schliemann [227], further additions to the code allow for the calculation of generalized inverse-participation ratios [304, 305]. The latter is implemented in the C++ standard C++17 using the linear algebra library Armadillo [638, 639]. The code is preserved on GitLab under https://git.uni-regensburg.de/sij35249/mb-loc.git, but is only partially publicly visible where required for publications (see Snippets).

D.3 INTERACTION IN TMD MONOLAYERS

This code calculates the polarizability tensor and the two-dimensional interaction tensor $W^{\mathrm{2D,RPA}}_{\mathbf{G},\mathbf{G}'}$ in random-phase approximation according to the approach discussed in Siegl et al. [64]. The language standard throughout most of the code is the C++ standard C++11, with most of the numerics utilizing the linear algebra library Armadillo [638, 639]. Some parts of the code further use Python 3, while plotting scripts use gnuplot 5.4, and overall scripting utilizes bash. Calculations in momentum-space work either with a k-space grid using the method of Monkhorst and Pack [640, 641] or an equivalent symmetry-adapted grid. The code contains routines for the back-Fourier transform to real space, as well as the calculation of the pairing kernel $\mathbb{U}_\sigma$, either directly on the Fermi surfaces of the tight-binding model in Section C.3, or projected on different sets of basis functions. The code is available on GitLab under https://git.uni-regensburg.de/sij35249/nbse2_sus.git.

D.4 SUPERCONDUCTIVITY IN TMD MONOLAYERS

This code calculates the solutions to both the linearized and the projected gap equations discussed in Siegl et al. [64] starting from the output of the code in Section D.3. The calculation of the eigensystem of the pairing kernel for the linearized gap equation utilizes the diagonalization of general complex square matrices as implemented by Numpy's "eig()" function [558]. The self-consistent gap equation is equivalent to a multidimensional root-finding problem. The code contains a solver for this type of problem and utilizes the components for such

a solver provided by the GNU Scientific Library [642]. The language standard for all codes written in C in this project is C17 with GNU-specific extensions as implemented in gcc 12.2 with the flag -std=gnu17. The plotting functions utilize gnuplot 5.4, while bash scripts are used for compilation and other miscellaneous tasks. The code uses some Python 3 scripts for small calculations. The calculation of the self-consistent solutions below the critical temperature is complemented with a suite of further programs calculating, among others, the free energy of the respective solutions as compared to the normal conducting state and the tunneling density of states. Finally, a fitting program making use of the Kubo formula for the differential conductance is also provided, which was used for the comparisons with the low-temperature scanning tunneling microscopy differential conductance measurements in Siegl et al. [64]. The code is available on GitLab under https://git.uni-regensburg.de/sij35249/nbse2_sc.git .

BIBLIOGRAPHY

[1] W. Heisenberg, "Über quantentheoretische Umdeutung kinematischer und mechanischer Beziehungen.", Z. Physik **33**, 879–893 (1925).

[2] F. Bloch, "Über die Quantenmechanik der Elektronen in Kristallgittern", Z. Physik **52**, 555–600 (1929).

[3] J. Bardeen and W. H. Brattain, "The Transistor, A Semi-Conductor Triode", Phys. Rev. **74**, 230–231 (1948).

[4] J. R. Biard and G. E. Pittman, "Semiconductor Radiant Diode", US3293513A (Dec. 1966).

[5] P. A. M. Dirac, "The Quantum Theory of the Electron", Proc. R. Soc. Lond. A **117**, 610–624 (1928).

[6] P. A. M. Dirac and N. H. D. Bohr, "The Quantum Theory of the Emission and Absorption of Radiation", Proc. R. Soc. Lond. A **114**, 243–265 (1927).

[7] M. E. Peskin, *An Introduction to Quantum Field Theory* (Avalon Publishing, Oct. 1995).

[8] M. K. Gaillard, P. D. Grannis, and F. J. Sciulli, "The Standard Model of Particle Physics", Rev. Mod. Phys. **71**, S96–S111 (1999).

[9] G. Isidori, F. Wilsch, and D. Wyler, "The Standard Model Effective Field Theory at Work", Rev. Mod. Phys. **96**, 015006 (2024).

[10] H. Goldstein, J. L. Safko, and C. P. Poole, *Classical Mechanics: Pearson New International Edition* (Pearson Education, Mar. 2014).

[11] H. Poincare, "Sur Le Problème Des Trois Corps et Les Équations de La Dynamique", Acta Math. **13**, 1–270 (1890).

[12] H. Bruus et al., *Many-Body Quantum Theory in Condensed Matter Physics: An Introduction*, Oxford Graduate Texts (Oxford University Press, Oxford, New York, Sept. 2004).

[13] L. D. Landau, "The Theory of a Fermi Liquid", JETP **3**, 920 (1956).

[14] L. D. Landau, "Oscillations in a Fermi Liquid", JETP **5**, 101 (1956).

[15] A. A. Abrikosov and I. M. Khalatnikov, "The Theory of a Fermi Liquid (the Properties of Liquid 3He at Low Temperatures)", Rep. Prog. Phys. **22**, 329 (1959).

[16] A. A. Abrikosov, *Fundamentals of the Theory of Metals* (Courier Dover Publications, Oct. 2017).

[17] P. W. Anderson, "More Is Different: Broken Symmetry and the Nature of the Hierarchical Structure of Science.", Science **177**, 393–396 (1972).

[18] R. B. Laughlin, "Anomalous Quantum Hall Effect: An Incompressible Quantum Fluid with Fractionally Charged Excitations", Phys. Rev. Lett. **50**, 1395–1398 (1983).

[19] A. Nardin and L. Mazza, "Laughlin's Quasielectron as a Nonlocal Composite Fermion", Phys. Rev. B **108**, L201106 (2023).
[20] H. K. Onnes, "Further Experiments with Liquid Helium. G. On the Electrical Resistance of Pure Metals, Etc. VI. On the Sudden Change in the Rate at Which the Resistance of Mercury Disappears.", in *Through Measurement to Knowledge*, Vol. 124 (Springer Netherlands, Dordrecht, 1991), pp. 267–272.
[21] L. N. Cooper, "Bound Electron Pairs in a Degenerate Fermi Gas", Phys. Rev. **104**, 1189–1190 (1956).
[22] J. Bardeen, L. N. Cooper, and J. R. Schrieffer, "Theory of Superconductivity", Phys. Rev. **108**, 1175–1204 (1957).
[23] L. P. Gorkov, "Microscopic Derivation of the Ginzburg-Landau Equations in the Theory of Superconductivity", JETP **9**, 1364 (1959).
[24] V. L. Ginzburg and L. D. Landau, "On the Theory of Superconductivity", in *On Superconductivity and Superfluidity: A Scientific Autobiography*, edited by V. L. Ginzburg (Springer, Berlin, Heidelberg, 2009), pp. 113–137.
[25] J. F. Cochran and D. E. Mapother, "Superconducting Transition in Aluminum", Phys. Rev. **111**, 132–142 (1958).
[26] S.-i. Tomonaga, "Remarks on Bloch's Method of Sound Waves Applied to Many-Fermion Problems", Prog Theor Phys **5**, 544–569 (1950).
[27] J. M. Luttinger, "An Exactly Soluble Model of a Many-Fermion System", J. Math. Phys. **4**, 1154–1162 (1963).
[28] D. C. Mattis and E. H. Lieb, "Exact Solution of a Many-Fermion System and Its Associated Boson Field", J. Math. Phys. **6**, 304–312 (1965).
[29] D. V. Averin, A. N. Korotkov, and K. K. Likharev, "Theory of Single-Electron Charging of Quantum Wells and Dots", Phys. Rev. B **44**, 6199–6211 (1991).
[30] C. W. J. Beenakker, "Theory of Coulomb-blockade Oscillations in the Conductance of a Quantum Dot", Phys. Rev. B **44**, 1646–1656 (1991).
[31] A. J. Leggett et al., "Dynamics of the Dissipative Two-State System", Rev. Mod. Phys. **59**, 1–85 (1987).
[32] Y. Makhlin, G. Schön, and A. Shnirman, "Quantum-State Engineering with Josephson-junction Devices", Rev. Mod. Phys. **73**, 357–400 (2001).
[33] T. D. Ladd et al., "Quantum Computers", Nature **464**, 45–53 (2010).
[34] G. Wendin, "Quantum Information Processing with Superconducting Circuits: A Review", Rep. Prog. Phys. **80**, 106001 (2017).
[35] R. Acharya et al., "Quantum Error Correction below the Surface Code Threshold", Nature **638**, 920–926 (2025).
[36] F. Arute et al., "Quantum Supremacy Using a Programmable Superconducting Processor", Nature **574**, 505–510 (2019).
[37] A. Blais et al., "Circuit Quantum Electrodynamics", Rev. Mod. Phys. **93**, 025005 (2021).
[38] B. D. Josephson, "Possible New Effects in Superconductive Tunnelling", Phys. Lett. **1**, 251–253 (1962).
[39] B. D. Josephson, "The Discovery of Tunnelling Supercurrents", Rev. Mod. Phys. **46**, 251–254 (1974).

[40]J. Siegl, J. Picó-Cortés, and M. Grifoni, "Particle Conserving Approach to Ac-Dc Driven Interacting Quantum Dots with Superconducting Leads", Phys. Rev. B **107**, 115405 (2023).
[41]K. N. Nesterov and I. V. Pechenezhskiy, "Measurement-Induced State Transitions in Dispersive Qubit-Readout Schemes", Phys. Rev. Appl. **22**, 064038 (2024).
[42]J. Picó-Cortés et al., "Nonequilibrium Cotunneling in Quantum Dot Josephson Junctions", Phys. Rev. B **110**, 125418 (2024).
[43]C. Padurariu and Y. V. Nazarov, "Theoretical Proposal for Superconducting Spin Qubits", Phys. Rev. B **81**, 144519 (2010).
[44]C. Janvier et al., "Coherent Manipulation of Andreev States in Superconducting Atomic Contacts", Science **349**, 1199–1202 (2015).
[45]S. Park and A. L. Yeyati, "Andreev Spin Qubits in Multichannel Rashba Nanowires", Phys. Rev. B **96**, 125416 (2017).
[46]L. Pavešić and R. Žitko, "Qubit Based on Spin-Singlet Yu-Shiba-Rusinov States", Phys. Rev. B **105**, 075129 (2022).
[47]M. Spethmann et al., "Coupled Superconducting Spin Qubits with Spin-Orbit Interaction", Phys. Rev. B **106**, 115411 (2022).
[48]Y. Bahri et al., "Localization and Topology Protected Quantum Coherence at the Edge of Hot Matter", Nat Commun **6**, 7341 (2015).
[49]A. Nico-Katz, A. Bayat, and S. Bose, "Information-Theoretic Memory Scaling in the Many-Body Localization Transition", Phys. Rev. B **105**, 205133 (2022).
[50]T. M. Gunawardana and B. Buča, "Dynamical L-Bits and Persistent Oscillations in Stark Many-Body Localization", Phys. Rev. B **106**, L161111 (2022).
[51]S. Sarkar and B. Buča, "Protecting Coherence from the Environment via Stark Many-Body Localization in a Quantum-Dot Simulator", Quantum **8**, 1392 (2024).
[52]M. Veldhorst et al., "A Two-Qubit Logic Gate in Silicon", Nature **526**, 410–414 (2015).
[53]D. Akinwande et al., "Graphene and Two-Dimensional Materials for Silicon Technology", Nature **573**, 507–518 (2019).
[54]W. Choi et al., "Recent Development of Two-Dimensional Transition Metal Dichalcogenides and Their Applications", Materials Today **20**, 116–130 (2017).
[55]G. Song et al., "NbSe2@PPy Nanosheets as Anode Materials for Flexible All-Solid-State Asymmetric Supercapacitors", J. Mater. Chem. A **11**, 11153–11160 (2023).
[56]A. K. Geim and I. V. Grigorieva, "Van Der Waals Heterostructures", Nature **499**, 419–425 (2013).
[57]K. S. Novoselov et al., "Electric Field Effect in Atomically Thin Carbon Films", Science **306**, 666–669 (2004).
[58]K. S. Novoselov et al., "Two-Dimensional Atomic Crystals", Proc. Natl. Acad. Sci. U.S.A. **102**, 10451–10453 (2005).
[59]X. Xi et al., "Strongly enhanced charge-density-wave order in monolayer NbSe2", Nat. Nanotech. **10**, 765–769 (2015).

[60]G. R. Bhimanapati et al., "Recent Advances in Two-Dimensional Materials beyond Graphene", ACS Nano **9**, 11509–11539 (2015).
[61]H. Wang et al., "High-Quality Monolayer Superconductor NbSe2 Grown by Chemical Vapour Deposition", Nat Commun **8**, 394 (2017).
[62]T. Hotta et al., "Molecular Beam Epitaxy Growth of Monolayer Niobium Diselenide Flakes", Appl. Phys. Lett. **109**, 133101 (2016).
[63]W. Wan et al., "Observation of Superconducting Collective Modes from Competing Pairing Instabilities in Single-Layer NbSe2", Adv. Mat. **34**, 2206078 (2022).
[64]J. Siegl et al., "Friedel Oscillations and Chiral Superconductivity in Monolayer NbSe2", Nat Commun **16**, 8228 (2025).
[65]X. Xi et al., "Ising pairing in superconducting NbSe2 atomic layers", Nat. Phys. **12**, 139–143 (2016).
[66]V. Vaňo et al., "Evidence of Nodal Superconductivity in Monolayer 1H-TaS_2 with Hidden Order Fluctuations", Adv. Mat. **35**, 2305409 (2023).
[67]A. Antony et al., "Making High-Quality Quantum Microwave Devices with van Der Waals Superconductors", J Phys Condens Matter **34**, 10.1088/1361-648X/ac3e9d (2021).
[68]W. Kohn and J. M. Luttinger, "New Mechanism for Superconductivity", Phys. Rev. Lett. **15**, 524–526 (1965).
[69]S. Das et al., "Electron-Phonon Coupling and Spin Fluctuations in the Ising Superconductor NbSe2", Npj Comput. Mater. **9**, 66 (2023).
[70]J. Siegl, "AC-driven Quasiparticle Tunneling in Superconducting Interacting Junctions", MA thesis (University of Regensburg, July 2021).
[71]J. Picó-Cortés, "AC Dynamics of Quantum Dots and Josephson Junctions for Quantum Technologies", PhD thesis (Sept. 2021).
[72]A. J. Leggett, "Number-Phase Fluctuations in Two-Band Superconductors", Prog. Theo. Phys. **36**, 901–930 (1966).
[73]A. Donarini and M. Grifoni, *Quantum Transport in Interacting Nanojunctions: A Density Matrix Approach*, Vol. 1024, Lecture Notes in Physics (Springer International Publishing, Cham, 2024).
[74]E. Schrödinger, "Quantisierung Als Eigenwertproblem", Ann. Phys. **384**, 361–376 (1926).
[75]E. Schrödinger, "Quantisierung Als Eigenwertproblem", Ann. Phys. **384**, 489–527 (1926).
[76]E. Schrödinger, "Quantisierung Als Eigenwertproblem", Ann. Phys. **385**, 437–490 (1926).
[77]E. Schrödinger, "Quantisierung Als Eigenwertproblem", Ann. Phys. **386**, 109–139 (1926).
[78]E. Schrödinger, "An Undulatory Theory of the Mechanics of Atoms and Molecules", Phys. Rev. **28**, 1049–1070 (1926).
[79]P. A. M. Dirac, "On the Theory of Quantum Mechanics", Proc. R. Soc. Lond. A **112**, 661–677 (1926).

[80]W. Pauli, "Zur Quantenmechanik des magnetischen Elektrons", Z. Physik **43**, 601–623 (1927).
[81]D. A. Abanin et al., "Colloquium: Many-body Localization, Thermalization, and Entanglement", Rev. Mod. Phys. **91**, 021001 (2019).
[82]U. Weiss, *Quantum Dissipative Systems*, 4th ed. (WORLD SCIENTIFIC, Mar. 2012).
[83]J. Schwinger, "Brownian Motion of a Quantum Oscillator", Journal of Mathematical Physics **2**, 407–432 (1961).
[84]L. V. Keldysh, "Diagram Technique for Nonequilibrium Processes", JETP **20**, 1018 (1965).
[85]Y. Meir and N. S. Wingreen, "Landauer Formula for the Current through an Interacting Electron Region", Phys. Rev. Lett. **68**, 2512–2515 (1992).
[86]R. P. Feynman and F. L. Vernon, "The Theory of a General Quantum System Interacting with a Linear Dissipative System", Annals of Physics **24**, 118–173 (1963).
[87]L. Magazzù and M. Grifoni, "Feynman-Vernon Influence Functional Approach to Quantum Transport in Interacting Nanojunctions: An Analytical Hierarchical Study", Phys. Rev. B **105**, 125417 (2022).
[88]J. Jin et al., "Non-Equilibrium Quantum Theory for Nanodevices Based on the Feynman–Vernon Influence Functional", New J. Phys. **12**, 083013 (2010).
[89]F. Bloch, "Generalized Theory of Relaxation", Phys. Rev. **105**, 1206–1222 (1957).
[90]A. Redfield, "The Theory of Relaxation Processes", in *Advances in Magnetic and Optical Resonance*, Vol. 1 (Elsevier, 1965).
[91]J. König et al., "Resonant Tunneling through Ultrasmall Quantum Dots: Zero-bias Anomalies, Magnetic-Field Dependence, and Boson-Assisted Transport", Phys. Rev. B **54**, 16820–16837 (1996).
[92]J. König, H. Schoeller, and G. Schön, "Zero-Bias Anomalies and Boson-Assisted Tunneling Through Quantum Dots", Phys. Rev. Lett. **76**, 1715–1718 (1996).
[93]J. König, H. Schoeller, and G. Schön, "Cotunneling at Resonance for the Single-Electron Transistor", Phys. Rev. Lett. **78**, 4482–4485 (1997).
[94]J. König, H. Schoeller, and G. Schön, "Cotunneling and Renormalization Effects for the Single-Electron Transistor", Phys. Rev. B **58**, 7882–7892 (1998).
[95]H. Schoeller and G. Schön, "Mesoscopic Quantum Transport: Resonant Tunneling in the Presence of a Strong Coulomb Interaction", Phys. Rev. B **50**, 18436–18452 (1994).
[96]H. Schoeller and G. Schön, "Resonant Tunneling and Charge Fluctuations in Mesoscopic Tunnel Junctions", Physica B: Condensed Matter **203**, 423–431 (1994).
[97]J. König, H. Schoeller, and G. Schön, "Resonant Tunneling and Coulomb Oscillations", EPL **31**, 31 (1995).
[98]J. N. Pedersen and A. Wacker, "Tunneling through Nanosystems: Combining Broadening with Many-Particle States", Phys. Rev. B **72**, 195330 (2005).
[99]C. Timm, "Tunneling through Molecules and Quantum Dots: Master-equation Approaches", Phys. Rev. B **77**, 195416 (2008).

[100]M. Leijnse and M. R. Wegewijs, "Kinetic Equations for Transport through Single-Molecule Transistors", Phys. Rev. B **78**, 235424 (2008).
[101]S. Koller et al., "Density-Operator Approaches to Transport through Interacting Quantum Dots: Simplifications in Fourth-Order Perturbation Theory", Phys. Rev. B **82**, 235307 (2010).
[102]O. Karlström et al., "A Diagrammatic Description of the Equations of Motion, Current and Noise within the Second-Order von Neumann Approach", J. Phys. A: Math. Theor. **46**, 065301 (2013).
[103]R. B. Saptsov and M. R. Wegewijs, "Fermionic Superoperators for Zero-Temperature Nonlinear Transport: Real-time Perturbation Theory and Renormalization Group for Anderson Quantum Dots", Phys. Rev. B **86**, 235432 (2012).
[104]J. Kern and M. Grifoni, "Transport across an Anderson Quantum Dot in the Intermediate Coupling Regime", Eur. Phys. J. B **86**, 384 (2013).
[105]S. Pfaller, A. Donarini, and M. Grifoni, "Subgap Features Due to Quasiparticle Tunneling in Quantum Dots Coupled to Superconducting Leads", Phys. Rev. B **87**, 155439 (2013).
[106]S. Ratz et al., "Thermally Induced Subgap Features in the Cotunneling Spectroscopy of a Carbon Nanotube", New J. Phys. **16**, 123040 (2014).
[107]R. B. Saptsov and M. R. Wegewijs, "Time-Dependent Quantum Transport: Causal Superfermions, Exact Fermion-Parity Protected Decay Modes, and Pauli Exclusion Principle for Mixed Quantum States", Phys. Rev. B **90**, 045407 (2014).
[108]C. Rohrmeier and A. Donarini, "Pseudospin Resonances Reveal Synthetic Spin-Orbit Interaction", Phys. Rev. B **103**, 205420 (2021).
[109]S. Nakajima, "On Quantum Theory of Transport Phenomena: Steady Diffusion", Prog. Theor. Phys. **20**, 948–959 (1958).
[110]R. Zwanzig, "Ensemble Method in the Theory of Irreversibility", J. Chem. Phys. **33**, 1338–1341 (1960).
[111]H.-P. Breuer and F. Petruccione, *The Theory of Open Quantum Systems* (Oxford University Press, Jan. 2007).
[112]M. Grifoni and P. Hänggi, "Driven Quantum Tunneling", Phys. Rep., 229–354 (1998).
[113]G. Platero and R. Aguado, "Photon-Assisted Transport in Semiconductor Nanostructures", Physics Reports **395**, 1–157 (2004).
[114]R. Peierls, "Spontaneously Broken Symmetries", J. Phys. A: Math. Gen. **24**, 5273–5281 (1991).
[115]M. Žonda et al., "Perturbation Theory for an Anderson Quantum Dot Asymmetrically Attached to Two Superconducting Leads", Phys. Rev. B **93**, 024523 (2016).
[116]J. Bardeen, "Tunneling Into Superconductors", Phys. Rev. Lett. **9**, 147–149 (1962).

[117] A. J. Leggett, *Quantum Liquids: Bose Condensation and Cooper Pairing in Condensed-Matter Systems*, Oxford Graduate Texts (Oxford University Press, Oxford ; New York, 2006).
[118] J. M. Blatt, "Electron Pairs in the Theory of Superconductivity:" Progress of Theoretical Physics **23**, 447–450 (1960).
[119] V. Irkhin and M. Katsnelson, "On the Ground-State Wavefunction of a Superconductor in the BCS Model", Physics Letters A **104**, 163–165 (1984).
[120] N. N. Bogoljubov, "On a New Method in the Theory of Superconductivity", Nuovo Cim. **7**, 794–805 (1958).
[121] N. N. Bogoljubov, "A New Method in the Theory of Superconductivity", JETP **34**, 58 (1958).
[122] J. G. Valatin, "Comments on the Theory of Superconductivity", Nuovo Cim **7**, 843–857 (1958).
[123] M. Governale, M. G. Pala, and J. König, "Real-Time Diagrammatic Approach to Transport through Interacting Quantum Dots with Normal and Superconducting Leads", Phys. Rev. B **77**, 134513 (2008).
[124] S. Shapiro, "Josephson Currents in Superconducting Tunneling: The Effect of Microwaves and Other Observations", Phys. Rev. Lett. **11**, 80–82 (1963).
[125] P. W. Anderson, "Localized Magnetic States in Metals", Phys. Rev. **124**, 41–53 (1961).
[126] J. Hubbard, "Electron Correlations in Narrow Energy Bands", Proc. R. Soc. Lond. A **276**, 238–257 (1963).
[127] M. Gaass et al., "Subgap Spectroscopy of Thermally Excited Quasiparticles in a Nb-contacted Carbon Nanotube Quantum Dot", Phys. Rev. B **89**, 241405 (2014).
[128] D. Futterer et al., "Nonlocal Andreev Transport through an Interacting Quantum Dot", Phys. Rev. B **79**, 054505 (2009).
[129] D. Futterer, M. Governale, and J. König, "Generation of Pure Spin Currents by Superconducting Proximity Effect in Quantum Dots", EPL **91**, 47004 (2010).
[130] B. Sothmann et al., "Probing the Exchange Field of a Quantum-Dot Spin Valve by a Superconducting Lead", Phys. Rev. B **82**, 094514 (2010).
[131] A. Braggio et al., "Superconducting Proximity Effect in Interacting Quantum Dots Revealed by Shot Noise", Solid State Communications **151**, 155–158 (2011).
[132] A. G. Moghaddam, M. Governale, and J. König, "Driven Superconducting Proximity Effect in Interacting Quantum Dots", Phys. Rev. B **85**, 094518 (2012).
[133] D. Futterer et al., "Renormalization Effects in Interacting Quantum Dots Coupled to Superconducting Leads", Phys. Rev. B **87**, 014509 (2013).
[134] B. Sothmann et al., "Unconventional Superconductivity in Double Quantum Dots", Phys. Rev. B **90**, 220501 (2014).
[135] S. Droste, J. Splettstoesser, and M. Governale, "Finite-Frequency Noise in a Quantum Dot with Normal and Superconducting Leads", Phys. Rev. B **91**, 125401 (2015).

[136]S. Droste and M. Governale, "Finite-Time Full Counting Statistics and Factorial Cumulants for Transport through a Quantum Dot with Normal and Superconducting Leads", J. Phys.: Condens. Matter **28**, 145302 (2016).
[137]M. Kamp and B. Sothmann, "Phase-Dependent Heat and Charge Transport through Superconductor–Quantum Dot Hybrids", Phys. Rev. B **99**, 045428 (2019).
[138]A. G. Bauer and B. Sothmann, "Phase-Dependent Transport in Thermally Driven Superconducting Single-Electron Transistors", Phys. Rev. B **104**, 195418 (2021).
[139]M. Kamp and B. Sothmann, "Higgs-like Pair Amplitude Dynamics in Superconductor–Quantum-Dot Hybrids", Phys. Rev. B **103**, 045414 (2021).
[140]M. Heckschen and B. Sothmann, "Pair-Amplitude Dynamics in Strongly Coupled Superconductor–Quantum Dot Hybrids", Phys. Rev. B **105**, 045420 (2022).
[141]C. B. Whan and T. P. Orlando, "Transport Properties of a Quantum Dot with Superconducting Leads", Phys. Rev. B **54**, R5255–R5258 (1996).
[142]C. Meyer, J. M. Elzerman, and L. P. Kouwenhoven, "Photon-Assisted Tunneling in a Carbon Nanotube Quantum Dot", Nano Lett. **7**, 295–299 (2007).
[143]B. Hiltscher, M. Governale, and J. König, "Ac Josephson Transport through Interacting Quantum Dots", Phys. Rev. B **86**, 235427 (2012).
[144]M.-S. Choi et al., "Kondo Effect and Josephson Current through a Quantum Dot between Two Superconductors", Phys. Rev. B **70**, 020502 (2004).
[145]C. Buizert et al., "Kondo Universal Scaling for a Quantum Dot Coupled to Superconducting Leads", Phys. Rev. Lett. **99**, 136806 (2007).
[146]R. S. Deacon et al., "Kondo-Enhanced Andreev Transport in Single Self-Assembled InAs Quantum Dots Contacted with Normal and Superconducting Leads", Phys. Rev. B **81**, 121308 (2010).
[147]Y. Avishai, A. Golub, and A. D. Zaikin, "Superconductor-Quantum Dot-Superconductor Junction in the Kondo Regime", Phys. Rev. B **67**, 041301 (2003).
[148]G. Sellier et al., "π junction behavior and Andreev bound states in Kondo quantum dots with superconducting leads", Phys. Rev. B **72**, 174502 (2005).
[149]R. López, M.-S. Choi, and R. Aguado, "Josephson Current through a Kondo Molecule", Phys. Rev. B **75**, 045132 (2007).
[150]R. S. Deacon et al., "Tunneling Spectroscopy of Andreev Energy Levels in a Quantum Dot Coupled to a Superconductor", Phys. Rev. Lett. **104**, 076805 (2010).
[151]A. Oguri and Y. Tanaka, "Transport through a Single Anderson Impurity Coupled to One Normal and Two Superconducting Leads", J. Phys.: Conf. Ser. **391**, 012146 (2012).
[152]A. Oguri, Y. Tanaka, and J. Bauer, "Interplay between Kondo and Andreev-Josephson Effects in a Quantum Dot Coupled to One Normal and Two Superconducting Leads", Phys. Rev. B **87**, 075432 (2013).

[153]E. Vecino, A. Martín-Rodero, and A. L. Yeyati, "Josephson current through a correlated quantum level: Andreev states and π junction behavior", Phys. Rev. B **68**, 035105 (2003).
[154]J. A. van Dam et al., "Supercurrent Reversal in Quantum Dots", Nature **442**, 667–670 (2006).
[155]K. Grove-Rasmussen et al., "Superconductivity-Enhanced Bias Spectroscopy in Carbon Nanotube Quantum Dots", Phys. Rev. B **79**, 134518 (2009).
[156]T. Dirks et al., "Superconducting Tunneling Spectroscopy of a Carbon Nanotube Quantum Dot", Appl. Phys. Lett. **95**, 192103 (2009).
[157]M. R. Buitelaar et al., "Multiple Andreev Reflections in a Carbon Nanotube Quantum Dot", Phys. Rev. Lett. **91**, 057005 (2003).
[158]E. Vecino et al., "Conductance Properties of Nanotubes Coupled to Superconducting Leads: Signatures of Andreev States Dynamics", Solid State Communications **131**, 625–630 (2004).
[159]J.-P. Cleuziou et al., "Carbon Nanotube Superconducting Quantum Interference Device", Nat Nanotechnol **1**, 53–59 (2006).
[160]A. Eichler et al., "Even-Odd Effect in Andreev Transport through a Carbon Nanotube Quantum Dot", Phys. Rev. Lett. **99**, 126602 (2007).
[161]J.-D. Pillet et al., "Andreev Bound States in Supercurrent-Carrying Carbon Nanotubes Revealed", Nature Phys **6**, 965–969 (2010).
[162]C. B. Winkelmann et al., "Superconductivity in a Single-C60 Transistor", Nature Phys **5**, 876–879 (2009).
[163]T. Dirks et al., "Transport through Andreev Bound States in a Graphene Quantum Dot", Nature Phys **7**, 386–390 (2011).
[164]A. Kadlecová, M. Žonda, and T. Novotný, "Quantum Dot Attached to Superconducting Leads: Relation between Symmetric and Asymmetric Coupling", Phys. Rev. B **95**, 195114 (2017).
[165]M. Abramowitz and I. A. Stegun, *Handbook of Mathematical Functions (Dover Books on Mathematics): With Formulas, Graphs, and Mathematical Tables*, 9th Revised ed (Dover Publications Inc., New York, NY, June 1965).
[166]M. Tinkham, *Introduction to Superconductivity*, 2nd ed., Doover Books on Physics (Dover Publications Inc., June 2004).
[167]R. C. Dynes, V. Narayanamurti, and J. P. Garno, "Direct Measurement of Quasiparticle-Lifetime Broadening in a Strong-Coupled Superconductor", Phys. Rev. Lett. **41**, 1509–1512 (1978).
[168]A. L. Yeyati et al., "Resonant Tunneling through a Small Quantum Dot Coupled to Superconducting Leads", Phys. Rev. B **55**, R6137–R6140 (1997).
[169]B. Siegert, A. Donarini, and M. Grifoni, "Effects of Spin–Orbit Coupling and Many-Body Correlations in STM Transport through Copper Phthalocyanine", Beilstein J. Nanotechnol. **6**, 2452–2462 (2015).
[170]M. G. Pala, M. Governale, and J. König, "Nonequilibrium Josephson and Andreev Current through Interacting Quantum Dots", New J. Phys. **9**, 278–278 (2007).

[171] B. Hiltscher et al., "Adiabatic Pumping in a Double-Dot Cooper-pair Beam Splitter", Phys. Rev. B **84**, 155403 (2011).
[172] V. Janiš and J. Yan, "Many-Body Perturbation Theory for the Superconducting Quantum Dot: Fundamental Role of the Magnetic Field", Phys. Rev. B **103**, 235163 (2021).
[173] J. Eldridge et al., "Superconducting Proximity Effect in Interacting Double-Dot Systems", Phys. Rev. B **82**, 184507 (2010).
[174] B. Sothmann and R. P. Tiwari, "Josephson Response of a Conventional and a Noncentrosymmetric Superconductor Coupled via a Double Quantum Dot", Phys. Rev. B **92**, 014504 (2015).
[175] A. V. Andreev, "The Thermal Conductivity of the Intermediate State in Superconductors", JETP **46**, 1823 (1964).
[176] G. E. Blonder, M. Tinkham, and T. M. Klapwijk, "Transition from Metallic to Tunneling Regimes in Superconducting Microconstrictions: Excess Current, Charge Imbalance, and Supercurrent Conversion", Phys. Rev. B **25**, 4515–4532 (1982).
[177] K. Flensberg, J. B. Hansen, and M. Octavio, "Subharmonic Energy-Gap Structure in Superconducting Weak Links", Phys. Rev. B **38**, 8707–8711 (1988).
[178] L. Bretheau et al., "Supercurrent Spectroscopy of Andreev States", Phys. Rev. X **3**, 041034 (2013).
[179] N. M. Chtchelkatchev and Y. V. Nazarov, "Andreev Quantum Dots for Spin Manipulation", Phys. Rev. Lett. **90**, 226806 (2003).
[180] M. Hays et al., "Coherent Manipulation of an Andreev Spin Qubit", Science **373**, 430–433 (2021).
[181] A. A. Clerk and V. Ambegaokar, "Loss of π-junction behavior in an interacting impurity Josephson junction", Phys. Rev. B **61**, 9109–9112 (2000).
[182] H. I. Jørgensen et al., "Critical Current 0-π Transition in Designed Josephson Quantum Dot Junctions", Nano Lett. **7**, 2441–2445 (2007).
[183] A. Martín-Rodero and A. Levy Yeyati, "Josephson and Andreev Transport through Quantum Dots", Adv. Phys. **60**, 899–958 (2011).
[184] L. I. Glazman and K. A. Matveec, "Resonant Josephson Current through Kondo Impurities in a Tunnel Barrier", JETP Lett. **49**, 570 (1989).
[185] A. Bespalov et al., "Theoretical Model to Explain Excess of Quasiparticles in Superconductors", Phys. Rev. Lett. **117**, 117002 (2016).
[186] D. Frombach and P. Recher, "Quasiparticle Poisoning Effects on the Dynamics of Topological Josephson Junctions", Phys. Rev. B **101**, 115304 (2020).
[187] J. Clarke, "Experimental Observation of Pair-Quasiparticle Potential Difference in Nonequilibrium Superconductors", Phys. Rev. Lett. **28**, 1363–1366 (1972).
[188] M. Tinkham, "Tunneling Generation, Relaxation, and Tunneling Detection of Hole-Electron Imbalance in Superconductors", Phys. Rev. B **6**, 1747–1756 (1972).
[189] I. Giaever, "Electron Tunneling Between Two Superconductors", Phys. Rev. Lett. **5**, 464–466 (1960).

[190]J. Gramich, A. Baumgartner, and C. Schönenberger, "Subgap Resonant Quasiparticle Transport in Normal-Superconductor Quantum Dot Devices", Appl. Phys. Lett. **108**, 172604 (2016).
[191]Y.-J. Doh et al., "Andreev Reflection versus Coulomb Blockade in Hybrid Semiconductor Nanowire Devices", Nano Lett. **8**, 4098–4102 (2008).
[192]K. Blum, *Density Matrix Theory and Applications*, Vol. 64, Springer Series on Atomic, Optical, and Plasma Physics (Springer Berlin Heidelberg, Berlin, Heidelberg, 2012).
[193]D. V. Averin and K. K. Likharev, "Coulomb Blockade of Single-Electron Tunneling, and Coherent Oscillations in Small Tunnel Junctions", J Low Temp Phys **62**, 345–373 (1986).
[194]S. Shapiro, A. R. Janus, and S. Holly, "Effect of Microwaves on Josephson Currents in Superconducting Tunneling", Rev. Mod. Phys. **36**, 223–225 (1964).
[195]P. W. Anderson and A. H. Dayem, "Radio-Frequency Effects in Superconducting Thin Film Bridges", Phys. Rev. Lett. **13**, 195–197 (1964).
[196]H.-J. Kwon, V. M. Yakovenko, and K. Sengupta, "Fractional Ac Josephson Effect in Unconventional Superconductors", Low Temperature Physics **30**, 613–619 (2004).
[197]L. P. Rokhinson, X. Liu, and J. K. Furdyna, "The Fractional a.c. Josephson Effect in a Semiconductor–Superconductor Nanowire as a Signature of Majorana Particles", Nature Phys **8**, 795–799 (2012).
[198]J. Wiedenmann et al., "4π-Periodic Josephson Supercurrent in HgTe-based Topological Josephson Junctions", Nat Commun **7**, 10303 (2016).
[199]J. Picó-Cortés, F. Domínguez, and G. Platero, "Signatures of a 4 π -Periodic Supercurrent in the Voltage Response of Capacitively Shunted Topological Josephson Junctions", Phys. Rev. B **96**, 125438 (2017).
[200]D. Laroche et al., "Observation of the 4π-Periodic Josephson Effect in Indium Arsenide Nanowires", Nat Commun **10**, 245 (2019).
[201]R. Fischer et al., "4π-periodic supercurrent tuned by an axial magnetic flux in topological insulator nanowires", Phys. Rev. Res. **4**, 013087 (2022).
[202]P. Dubos et al., "Coherent Low-Energy Charge Transport in a Diffusive S-N-S Junction", Phys. Rev. Lett. **87**, 206801 (2001).
[203]J. C. Cuevas et al., "Subharmonic Shapiro Steps and Assisted Tunneling in Superconducting Point Contacts", Phys. Rev. Lett. **88**, 157001 (2002).
[204]R. L. Kautz, "Noise, Chaos, and the Josephson Voltage Standard", Rep. Prog. Phys. **59**, 935–992 (1996).
[205]F. Domínguez et al., "Josephson Junction Dynamics in the Presence of 2 π - and 4 π -Periodic Supercurrents", Phys. Rev. B **95**, 195430 (2017).
[206]J. Park et al., "Characterization of Shapiro Steps in the Presence of a 4\ensuremath{\pi}-Periodic Josephson Current", Phys. Rev. B **103**, 235428 (2021).
[207]Y.-H. Li et al., "Doubled Shapiro Steps in a Topological Josephson Junction", Phys. Rev. B **97**, 045423 (2018).

[208] A. V. Galaktionov and A. D. Zaikin, "Fractional Shapiro Steps without Fractional Josephson Effect", Phys. Rev. B **104**, 054521 (2021).
[209] P. Virtanen and P. Recher, "Microwave Spectroscopy of Josephson Junctions in Topological Superconductors", Phys. Rev. B **88**, 144507 (2013).
[210] C. Metzger et al., "Circuit-QED with Phase-Biased Josephson Weak Links", Phys. Rev. Research **3**, 013036 (2021).
[211] A. Roychowdhury et al., "Microwave Photon-Assisted Incoherent Cooper-Pair Tunneling in a Josephson STM", Phys. Rev. Appl. **4**, 034011 (2015).
[212] O. Peters et al., "Resonant Andreev Reflections Probed by Photon-Assisted Tunnelling at the Atomic Scale", Nat. Phys. **16**, 1222–1226 (2020).
[213] P. Kot et al., "Microwave-Assisted Tunneling and Interference Effects in Superconducting Junctions under Fast Driving Signals", Phys. Rev. B **101**, 134507 (2020).
[214] J. H. Shirley, "Solution of the Schrödinger Equation with a Hamiltonian Periodic in Time", Phys. Rev. **138**, B979–B987 (1965).
[215] T. Oka and S. Kitamura, "Floquet Engineering of Quantum Materials", Ann. Rev. Condens. Matter Phys. **10**, 387–408 (2019).
[216] P. K. Tien and J. P. Gordon, "Multiphoton Process Observed in the Interaction of Microwave Fields with the Tunneling between Superconductor Films", Phys. Rev. **129**, 647–651 (1963).
[217] L. P. Kouwenhoven et al., "Photon-Assisted Tunneling through a Quantum Dot", Phys. Rev. B **50**, 2019–2022 (1994).
[218] L. P. Kouwenhoven et al., "Observation of Photon-Assisted Tunneling through a Quantum Dot", Phys. Rev. Lett. **73**, 3443–3446 (1994).
[219] T.-S. Ho, S.-I. Chu, and J. V. Tietz, "Semiclassical Many-Mode Floquet Theory", Chemical Physics Letters **96**, 464–471 (1983).
[220] Á. Gómez-León and G. Platero, "Designing Adiabatic Time Evolution from High-Frequency Bichromatic Sources", Phys. Rev. Res. **2**, 033412 (2020).
[221] M. Kostur et al., "Anomalous Transport in Biased Ac-Driven Josephson Junctions: Negative Conductances", Phys. Rev. B **77**, 104509 (2008).
[222] K. Kang, "Transport through an Interacting Quantum Dot Coupled to Two Superconducting Leads", Phys. Rev. B **57**, 11891–11894 (1998).
[223] C. Bruder and H. Schoeller, "Charging Effects in Ultrasmall Quantum Dots in the Presence of Time-Varing Fields", Phys. Rev. Lett. **72**, 1076–1079 (1994).
[224] M. H. Fischer, M. Sigrist, and D. F. Agterberg, "Superconductivity without Inversion and Time-Reversal Symmetries", Phys. Rev. Lett. **121**, 157003 (2018).
[225] R. Taranko, T. Kwapiński, and T. Domański, "Transient Dynamics of a Quantum Dot Embedded between Two Superconducting Leads and a Metallic Reservoir", Phys. Rev. B **99**, 165419 (2019).
[226] R. Seoane Souto et al., "Transient Dynamics of a Magnetic Impurity Coupled to Superconducting Electrodes: Exact Numerics versus Perturbation Theory", Phys. Rev. B **104**, 214506 (2021).
[227] J. Siegl and J. Schliemann, "Imperfect Many-Body Localization in Exchange-Disordered Isotropic Spin Chains", New J. Phys. **25**, 123002 (2023).

[228]I. Bloch, J. Dalibard, and W. Zwerger, "Many-Body Physics with Ultracold Gases", Rev. Mod. Phys. **80**, 885–964 (2008).
[229]R. Blatt and C. F. Roos, "Quantum Simulations with Trapped Ions", Nature Phys **8**, 277–284 (2012).
[230]M. Schreiber et al., "Observation of Many-Body Localization of Interacting Fermions in a Quasirandom Optical Lattice", Science **349**, 842–845 (2015).
[231]M. Ovadia et al., "Evidence for a Finite-Temperature Insulator", Sci Rep **5**, 13503 (2015).
[232]J. Smith et al., "Many-Body Localization in a Quantum Simulator with Programmable Random Disorder", Nature Phys **12**, 907–911 (2016).
[233]J.-y. Choi et al., "Exploring the Many-Body Localization Transition in Two Dimensions", Science **352**, 1547–1552 (2016).
[234]S. Choi et al., "Observation of Discrete Time-Crystalline Order in a Disordered Dipolar Many-Body System", Nature **543**, 221–225 (2017).
[235]P. Bordia et al., "Periodically Driving a Many-Body Localized Quantum System", Nature Phys **13**, 460–464 (2017).
[236]C.-Z. Xu et al., "Experimental and Theoretical Electronic Structure and Symmetry Effects in Ultrathin NbSe 2 Films", Phys. Rev. Mat. **2**, 064002 (2018).
[237]A. Lukin et al., "Probing Entanglement in a Many-Body–Localized System", Science **364**, 256–260 (2019).
[238]M. Rispoli et al., "Quantum Critical Behaviour at the Many-Body Localization Transition", Nature **573**, 385–389 (2019).
[239]L. F. Santos et al., "Strong Many-Particle Localization and Quantum Computing with Perpetually Coupled Qubits", Phys. Rev. A **71**, 012317 (2005).
[240]R. Vasseur, A. C. Potter, and S. A. Parameswaran, "Quantum Criticality of Hot Random Spin Chains", Phys. Rev. Lett. **114**, 217201 (2015).
[241]A. C. Potter and R. Vasseur, "Symmetry Constraints on Many-Body Localization", Phys. Rev. B **94**, 224206 (2016).
[242]I. V. Protopopov, W. W. Ho, and D. A. Abanin, "Effect of SU(2) Symmetry on Many-Body Localization and Thermalization", Phys. Rev. B **96**, 041122 (2017).
[243]A. Prakash et al., "Eigenstate Phases with Finite On-Site Non-Abelian Symmetry", Phys. Rev. B **96**, 165136 (2017).
[244]A. J. Friedman et al., "Localization-Protected Order in Spin Chains with Non-Abelian Discrete Symmetries", Phys. Rev. B **98**, 064203 (2018).
[245]I. V. Protopopov et al., "Non-Abelian Symmetries and Disorder: A Broad Nonergodic Regime and Anomalous Thermalization", Phys. Rev. X **10**, 011025 (2020).
[246]D. A. Abanin and Z. Papić, "Recent Progress in Many-Body Localization", Ann. Phys. **529**, 1700169 (2017).
[247]P. Sierant et al., "Many-Body Localization in the Age of Classical Computing*", Rep. Prog. Phys. **88**, 026502 (2025).
[248]F. Evers, I. Modak, and S. Bera, "Internal Clock of Many-Body Delocalization", Phys. Rev. B **108**, 134204 (2023).

[249]F. Bloch, "Bemerkung zur Elektronentheorie des Ferromagnetismus und der elektrischen Leitfähigkeit", Z. Physik **57**, 545–555 (1929).
[250]P. W. Anderson, "Absence of Diffusion in Certain Random Lattices", Phys. Rev. **109**, 1492–1505 (1958).
[251]F. M. Izrailev, A. A. Krokhin, and N. M. Makarov, "Anomalous Localization in Low-Dimensional Systems with Correlated Disorder", Physics Reports, Anomalous Localization in Low-Dimensional Systems with Correlated Disorder **512**, 125–254 (2012).
[252]E. Abrahams et al., "Scaling Theory of Localization: Absence of Quantum Diffusion in Two Dimensions", Phys. Rev. Lett. **42**, 673–676 (1979).
[253]N. Mott, "Electrons in Disordered Structures", Adv. Phys. **16**, 49–144 (1967).
[254]N. F. Mott and R. S. Allgaier, "Localized States in Disordered Lattices", Phys. Stat. Sol. B **21**, 343–356 (1967).
[255]N. F. Mott et al., "The Anderson Transition", Proc. R. Soc. Lond. A **345**, 169–205 (1975).
[256]C. J. Adkins, "Threshold Conduction in Inversion Layers", J. Phys. C: Solid State Phys. **11**, 851 (1978).
[257]F. Evers and A. D. Mirlin, "Anderson Transitions", Rev. Mod. Phys. **80**, 1355–1417 (2008).
[258]L. Fleishman, D. C. Licciardello, and P. W. Anderson, "Elementary Excitations in the Fermi Glass", Phys. Rev. Lett. **40**, 1340–1343 (1978).
[259]L. Fleishman and P. W. Anderson, "Interactions and the Anderson Transition", Phys. Rev. B **21**, 2366–2377 (1980).
[260]A. M. Finkelstein, "Influence of Coulomb Interaction on the Properties of Disordered Metals", JETP **57**, 97 (1983).
[261]T. Giamarchi and H. J. Schulz, "Anderson Localization and Interactions in One-Dimensional Metals", Phys. Rev. B **37**, 325–340 (1988).
[262]B. L. Altshuler et al., "Quasiparticle Lifetime in a Finite System: A Nonperturbative Approach", Phys. Rev. Lett. **78**, 2803–2806 (1997).
[263]I. V. Gornyi, A. D. Mirlin, and D. G. Polyakov, "Interacting Electrons in Disordered Wires: Anderson Localization and Low-T Transport", Phys. Rev. Lett. **95**, 206603 (2005).
[264]D. M. Basko, I. L. Aleiner, and B. L. Altshuler, "Metal-Insulator Transition in a Weakly Interacting Many-Electron System with Localized Single-Particle States", Ann. Phys. **321**, 1126–1205 (2006).
[265]D. M. Basko, I. L. Aleiner, and B. L. Altshuler, "Possible Experimental Manifestations of the Many-Body Localization", Phys. Rev. B **76**, 052203 (2007).
[266]F. Alet and N. Laflorencie, "Many-Body Localization: An Introduction and Selected Topics", C. R. Phys., Quantum Simulation / Simulation Quantique **19**, 498–525 (2018).
[267]V. Oganesyan and D. A. Huse, "Localization of Interacting Fermions at High Temperature", Phys. Rev. B **75**, 155111 (2007).
[268]J. M. Deutsch, "Quantum Statistical Mechanics in a Closed System", Phys. Rev. A **43**, 2046–2049 (1991).

[269]M. Srednicki, "Chaos and Quantum Thermalization", Phys. Rev. E **50**, 888–901 (1994).
[270]M. Srednicki, "The Approach to Thermal Equilibrium in Quantized Chaotic Systems", J. Phys. A: Math. Gen. **32**, 1163 (1999).
[271]R. Nandkishore and D. A. Huse, "Many-Body Localization and Thermalization in Quantum Statistical Mechanics", Ann. Rev. Condens. Matter Phys. **6**, 15–38 (2015).
[272]L. D'Alessio et al., "From Quantum Chaos and Eigenstate Thermalization to Statistical Mechanics and Thermodynamics", Adv. Phys. **65**, 239–362 (2016).
[273]M. Serbyn, Z. Papić, and D. A. Abanin, "Criterion for Many-Body Localization-Delocalization Phase Transition", Phys. Rev. X **5**, 041047 (2015).
[274]Y. Y. Atas et al., "Distribution of the Ratio of Consecutive Level Spacings in Random Matrix Ensembles", Phys. Rev. Lett. **110**, 084101 (2013).
[275]C. Gogolin, M. P. Müller, and J. Eisert, "Absence of Thermalization in Nonintegrable Systems", Phys. Rev. Lett. **106**, 040401 (2011).
[276]M. Serbyn, Z. Papić, and D. A. Abanin, "Local Conservation Laws and the Structure of the Many-Body Localized States", Phys. Rev. Lett. **111**, 127201 (2013).
[277]D. A. Huse, R. Nandkishore, and V. Oganesyan, "Phenomenology of Fully Many-Body-Localized Systems", Phys. Rev. B **90**, 174202 (2014).
[278]T. E. O'Brien et al., "Explicit Construction of Local Conserved Operators in Disordered Many-Body Systems", Phys. Rev. B **94**, 144208 (2016).
[279]J. Z. Imbrie, "On Many-Body Localization for Quantum Spin Chains", J. Stat. Phys. **163**, 998–1048 (2016).
[280]J. Z. Imbrie, V. Ros, and A. Scardicchio, "Local Integrals of Motion in Many-Body Localized Systems", Ann. Phys. **529**, 1600278 (2017).
[281]B. Bauer and C. Nayak, "Area Laws in a Many-Body Localized State and Its Implications for Topological Order", J. Stat. Mech. **2013**, P09005 (2013).
[282]M. Serbyn, Z. Papić, and D. A. Abanin, "Universal Slow Growth of Entanglement in Interacting Strongly Disordered Systems", Phys. Rev. Lett. **110**, 260601 (2013).
[283]P. Prelovšek et al., "Density Correlations and Transport in Models of Many-Body Localization", Ann. Phys. **529**, 1600362 (2017).
[284]A. D. Luca and A. Scardicchio, "Ergodicity Breaking in a Model Showing Many-Body Localization", EPL **101**, 37003 (2013).
[285]J. Schliemann et al., "Many-Body Localization: Transitions in Spin Models", Phys. Rev. B **103**, 174203 (2021).
[286]M. Serbyn and J. E. Moore, "Spectral Statistics across the Many-Body Localization Transition", Phys. Rev. B **93**, 041424 (2016).
[287]E. V. H. Doggen et al., "Many-Body Localization in Large Systems: Matrix-product-state Approach", Ann. Phys., Special Issue on Localisation 2020 **435**, 168437 (2021).
[288]J. Šuntajs et al., "Quantum Chaos Challenges Many-Body Localization", Phys. Rev. E **102**, 062144 (2020).

[289]F. Weiner, F. Evers, and S. Bera, "Slow Dynamics and Strong Finite-Size Effects in Many-Body Localization with Random and Quasiperiodic Potentials", Phys. Rev. B **100**, 104204 (2019).
[290]P. Sierant and J. Zakrzewski, "Challenges to Observation of Many-Body Localization", Phys. Rev. B **105**, 224203 (2022).
[291]C. Murthy et al., "Non-Abelian Eigenstate Thermalization Hypothesis", Phys. Rev. Lett. **130**, 140402 (2023).
[292]S. Majidy et al., "Non-Abelian Symmetry Can Increase Entanglement Entropy", Phys. Rev. B **107**, 045102 (2023).
[293]V. Oganesyan, A. Pal, and D. A. Huse, "Energy Transport in Disordered Classical Spin Chains", Phys. Rev. B **80**, 115104 (2009).
[294]D. Saraidaris et al., "Finite-size subthermal regime in disordered SU(N)-symmetric Heisenberg chains", Phys. Rev. B **109**, 094201 (2024).
[295]Y. Gao and R. A. Römer, "Spectral and Entanglement Properties of the Random-Exchange Heisenberg Chain", Phys. Rev. B **111**, 104202 (2025).
[296]A. Pal and D. A. Huse, "Many-Body Localization Phase Transition", Phys. Rev. B **82**, 174411 (2010).
[297]D. J. Luitz, N. Laflorencie, and F. Alet, "Many-Body Localization Edge in the Random-Field Heisenberg Chain", Phys. Rev. B **91**, 081103 (2015).
[298]E. V. H. Doggen et al., "Many-Body Localization and Delocalization in Large Quantum Chains", Phys. Rev. B **98**, 174202 (2018).
[299]F. D. M. Haldane, "Continuum Dynamics of the 1-D Heisenberg Antiferromagnet: Identification with the O(3) Nonlinear Sigma Model", Physics Letters A **93**, 464–468 (1983).
[300]F. D. M. Haldane, "Nonlinear Field Theory of Large-Spin Heisenberg Antiferromagnets: Semiclassically Quantized Solitons of the One-Dimensional Easy-Axis N\'eel State", Phys. Rev. Lett. **50**, 1153–1156 (1983).
[301]F. D. M. Haldane, ""Θ Physics" and Quantum Spin Chains (Abstract)", Journal of Applied Physics **57**, 3359 (1985).
[302]I. Affleck, "Quantum Spin Chains and the Haldane Gap", J. Phys.: Condens. Matter **1**, 3047 (1989).
[303]T. Jolicoeur and O. Golinelli, "Physics of Integer-Spin Antiferromagnetic Chains: Haldane Gaps and Edge States", Comptes Rendus Chimie **22**, 445–451 (2019).
[304]N. C. Murphy, R. Wortis, and W. A. Atkinson, "Generalized Inverse Participation Ratio as a Possible Measure of Localization for Interacting Systems", Phys. Rev. B **83**, 184206 (2011).
[305]D. Giri, J. Siegl, and J. Schliemann, *From Thermalization to Multifractality: Spin-Spin Correlation in Disordered* SU(2)*-Invariant 1D Heisenberg Spin Chains*, Aug. 2025.
[306]S. Bera et al., "Many-Body Localization Characterized from a One-Particle Perspective", Phys. Rev. Lett. **115**, 046603 (2015).
[307]D. S. Fisher, "Random Antiferromagnetic Quantum Spin Chains", Phys. Rev. B **50**, 3799–3821 (1994).

[308]K. Xu et al., "Emulating Many-Body Localization with a Superconducting Quantum Processor", Phys. Rev. Lett. **120**, 050507 (2018).
[309]T. Szołdra et al., "Detecting Ergodic Bubbles at the Crossover to Many-Body Localization Using Neural Networks", Phys. Rev. B **104**, L140202 (2021).
[310]T. Szołdra et al., "Unsupervised Detection of Decoupled Subspaces: Many-body Scars and Beyond", Phys. Rev. B **105**, 224205 (2022).
[311]T. Szołdra et al., "Catching Thermal Avalanches in the Disordered XXZ Model", Phys. Rev. B **109**, 134202 (2024).
[312]R. Vosk and E. Altman, "Many-Body Localization in One Dimension as a Dynamical Renormalization Group Fixed Point", Phys. Rev. Lett. **110**, 067204 (2013).
[313]R. Vosk, D. A. Huse, and E. Altman, "Theory of the Many-Body Localization Transition in One-Dimensional Systems", Phys. Rev. X **5**, 031032 (2015).
[314]A. Goremykina, R. Vasseur, and M. Serbyn, "Analytically Solvable Renormalization Group for the Many-Body Localization Transition", Phys. Rev. Lett. **122**, 040601 (2019).
[315]A. Morningstar and D. A. Huse, "Renormalization-Group Study of the Many-Body Localization Transition in One Dimension", Phys. Rev. B **99**, 224205 (2019).
[316]A. Morningstar, D. A. Huse, and J. Z. Imbrie, "Many-Body Localization near the Critical Point", Phys. Rev. B **102**, 125134 (2020).
[317]A. Guinier et al., "Nomenclature of Polytype Structures. Report of the International Union of Crystallography Ad Hoc Committee on the Nomenclature of Disordered, Modulated and Polytype Structures", Acta Cryst. A **40**, 399–404 (1984).
[318]K. Momma and F. Izumi, "VESTA 3 for Three-Dimensional Visualization of Crystal, Volumetric and Morphology Data", J Appl Cryst **44**, 1272–1276 (2011).
[319]X. Xi et al., "Gate Tuning of Electronic Phase Transitions in Two-Dimensional $NbSe_2$", Phys. Rev. Lett. **117**, 106801 (2016).
[320]O. Gunawan et al., "Valley Susceptibility of an Interacting Two-Dimensional Electron System", Phys. Rev. Lett. **97**, 186404 (2006).
[321]A. Rycerz, J. Tworzydło, and C. W. J. Beenakker, "Valley Filter and Valley Valve in Graphene", Nature Phys **3**, 172–175 (2007).
[322]W. Yao, D. Xiao, and Q. Niu, "Valley-Dependent Optoelectronics from Inversion Symmetry Breaking", Phys. Rev. B **77**, 235406 (2008).
[323]D. Xiao, W. Yao, and Q. Niu, "Valley-Contrasting Physics in Graphene: Magnetic Moment and Topological Transport", Phys. Rev. Lett. **99**, 236809 (2007).
[324]D. Xiao et al., "Coupled Spin and Valley Physics in Monolayers of MoS_2 and Other Group-VI Dichalcogenides", Phys. Rev. Lett. **108**, 196802 (2012).
[325]A. Altıntaş et al., "Spin-Valley Qubits in Gated Quantum Dots in a Single Layer of Transition Metal Dichalcogenides", Phys. Rev. B **104**, 195412 (2021).
[326]J. Boddison-Chouinard et al., "Anomalous Conductance Quantization of a One-Dimensional Channel in Monolayer WSe2", npj 2D Mater Appl **7**, 50 (2023).

[327]A. H. Castro Neto et al., "The Electronic Properties of Graphene", Rev. Mod. Phys. **81**, 109–162 (2009).
[328]S. Das Sarma et al., "Electronic Transport in Two-Dimensional Graphene", Rev. Mod. Phys. **83**, 407–470 (2011).
[329]G.-B. Liu et al., "Three-Band Tight-Binding Model for Monolayers of Group-VIB Transition Metal Dichalcogenides", Phys. Rev. B **88**, 085433 (2013).
[330]Z. Y. Zhu, Y. C. Cheng, and U. Schwingenschlögl, "Giant Spin-Orbit-Induced Spin Splitting in Two-Dimensional Transition-Metal Dichalcogenide Semiconductors", Phys. Rev. B **84**, 153402 (2011).
[331]S. Ilić, J. S. Meyer, and M. Houzet, "Enhancement of the Upper Critical Field in Disordered Transition Metal Dichalcogenide Monolayers", Phys. Rev. Lett. **119**, 117001 (2017).
[332]X. Xu et al., "Spin and Pseudospins in Layered Transition Metal Dichalcogenides", Nat. Phys. **10**, 343–350 (2014).
[333]I. Žutić, J. Fabian, and S. Das Sarma, "Spintronics: Fundamentals and Applications", Rev. Mod. Phys. **76**, 323–410 (2004).
[334]K. F. Mak et al., "Control of Valley Polarization in Monolayer MoS2 by Optical Helicity", Nat. Nanotech. **7**, 494–498 (2012).
[335]K. F. Mak et al., "The Valley Hall Effect in MoS ₂ Transistors", Science **344**, 1489–1492 (2014).
[336]H. Zeng et al., "Valley Polarization in MoS2 Monolayers by Optical Pumping", Nat. Nanotech. **7**, 490–493 (2012).
[337]T. Cao et al., "Valley-Selective Circular Dichroism of Monolayer Molybdenum Disulphide", Nat Commun **3**, 887 (2012).
[338]H. Zeng et al., "Optical Signature of Symmetry Variations and Spin-Valley Coupling in Atomically Thin Tungsten Dichalcogenides", Sci Rep **3**, 1608 (2013).
[339]E. Sosenko, J. Zhang, and V. Aji, "Unconventional Superconductivity and Anomalous Response in Hole-Doped Transition Metal Dichalcogenides", Phys. Rev. B **95**, 144508 (2017).
[340]M. Gmitra and J. Fabian, "Graphene on Transition-Metal Dichalcogenides: A Platform for Proximity Spin-Orbit Physics and Optospintronics", Phys. Rev. B **92**, 155403 (2015).
[341]V. Vescoli et al., "Dynamics of Correlated Two-Dimensional Materials: The 2H-$TaSe_2$ Case", Phys. Rev. Lett. **81**, 453–456 (1998).
[342]M. Calandra, I. I. Mazin, and F. Mauri, "Effect of dimensionality on the charge-density wave in few-layer 2H-$NbSe_2$", Phys. Rev. B **80**, 241108 (2009).
[343]W. L. McMillan, "Landau Theory of Charge-Density Waves in Transition-Metal Dichalcogenides", Phys. Rev. B **12**, 1187–1196 (1975).
[344]T. M. Rice and G. K. Scott, "New Mechanism for a Charge-Density-Wave Instability", Phys. Rev. Lett. **35**, 120–123 (1975).
[345]J. Wilson, F. Di Salvo, and S. Mahajan, "Charge-Density Waves and Superlattices in the Metallic Layered Transition Metal Dichalcogenides", Adv. Phys. **24**, 117–201 (1975).

[346]D. E. Moncton, J. D. Axe, and F. J. DiSalvo, "Neutron scattering study of the charge-density wave transitions in $2H-TaSe_2$ and $2H-NbSe_2$", Phys. Rev. B **16**, 801–819 (1977).
[347]N. V. Smith, S. D. Kevan, and F. J. DiSalvo, "Band Structures of the Layer Compounds 1T-TaS $_2$ and 2H-TaSe $_2$ in the Presence of Commensurate Charge-Density Waves", J. Phys. C: Solid State Phys. **18**, 3175–3189 (1985).
[348]A. H. Castro Neto, "Charge Density Wave, Superconductivity, and Anomalous Metallic Behavior in 2D Transition Metal Dichalcogenides", Phys. Rev. Lett. **86**, 4382–4385 (2001).
[349]K. Rossnagel et al., "Fermi surface of 2H-$NbSe_2$ and its implications on the charge-density-wave mechanism", Phys. Rev. B **64**, 235119 (2001).
[350]T. Valla et al., "Quasiparticle Spectra, Charge-Density Waves, Superconductivity, and Electron-Phonon Coupling in 2H-$NbSe_2$", Phys. Rev. Lett. **92**, 086401 (2004).
[351]K. Rossnagel et al., "Fermi surface, charge-density-wave gap, and kinks in 2H-$TaSe_2$", Phys. Rev. B **72**, 121103 (2005).
[352]D. S. Inosov et al., "Fermi Surface Nesting in Several Transition Metal Dichalcogenides", New J. Phys. **10**, 125027 (2008).
[353]S. V. Borisenko et al., "Two Energy Gaps and Fermi-Surface "Arcs" in $NbSe_2$", Phys. Rev. Lett. **102**, 166402 (2009).
[354]Y. Yang et al., "Enhanced superconductivity upon weakening of charge density wave transport in 2H-TaS_2 in the two-dimensional limit", Phys. Rev. B **98**, 035203 (2018).
[355]C.-S. Lian, C. Si, and W. Duan, "Unveiling Charge-Density Wave, Superconductivity, and Their Competitive Nature in Two-Dimensional NbSe2", Nano Lett. **18**, 2924–2929 (2018).
[356]F. Zheng et al., "First-principles study of charge and magnetic ordering in monolayer $NbSe_2$", Phys. Rev. B **97**, 081101 (2018).
[357]T. Kiss et al., "Charge-Order-Maximized Momentum-Dependent Superconductivity", Nat. Phys. **3**, 720–725 (2007).
[358]N. E. Staley et al., "Electric field effect on superconductivity in atomically thin flakes of $NbSe_2$", Phys. Rev. B **80**, 184505 (2009).
[359]D. Y. Qiu, F. H. da Jornada, and S. G. Louie, "Screening and many-body effects in two-dimensional crystals: Monolayer MoS_2", Phys. Rev. B **93**, 235435 (2016).
[360]J. M. Lu et al., "Evidence for Two-Dimensional Ising Superconductivity in Gated MoS2", Science **350**, 1353–1357 (2015).
[361]D. Costanzo et al., "Gate-Induced Superconductivity in Atomically Thin MoS2 Crystals", Nature Nanotech **11**, 339–344 (2016).
[362]Y. Fu et al., "Gated Tuned Superconductivity and Phonon Softening in Monolayer and Bilayer MoS2", npj Quantum Mater. **2**, 52 (2017).
[363]E. Sajadi et al., "Gate-Induced Superconductivity in a Monolayer Topological Insulator", Science **362**, 922–925 (2018).
[364]T. Brumme, M. Calandra, and F. Mauri, "First-Principles Theory of Field-Effect Doping in Transition-Metal Dichalcogenides: Structural Properties, Electronic

Structure, Hall Coefficient, and Electrical Conductivity", Phys. Rev. B **91**, 155436 (2015).
[365]J. T. Ye et al., "Superconducting Dome in a Gate-Tuned Band Insulator", Science **338**, 1193–1196 (2012).
[366]K. Taniguchi et al., "Electric-Field-Induced Superconductivity at 9.4 K in a Layered Transition Metal Disulphide MoS2", Appl. Phys. Lett. **101**, 042603 (2012).
[367]W. Shi et al., "Superconductivity Series in Transition Metal Dichalcogenides by Ionic Gating", Sci. Rep. **5**, 12534 (2015).
[368]Y. Saito et al., "Superconductivity Protected by Spin–Valley Locking in Ion-Gated MoS2", Nat. Phys. **12**, 144–149 (2016).
[369]E. Piatti et al., "Multi-Valley Superconductivity in Ion-Gated MoS $_2$ Layers", Nano Lett. **18**, 4821–4830 (2018).
[370]D. Wickramaratne and I. I. Mazin, "Effect of Alloying in Monolayer Niobium Dichalcogenide Superconductors", Nat. Commun. **13**, 2376 (2022).
[371]W. Wan et al., "Superconducting Dome by Tuning through a van Hove Singularity in a Two-Dimensional Metal", npj 2D Mater Appl **7**, 41 (2023).
[372]R. T. Leriche et al., "Misfit Layer Compounds: A Platform for Heavily Doped 2D Transition Metal Dichalcogenides", Adv. Funct. Mater. **31**, 2007706 (2021).
[373]P. A. Frigeri et al., "Superconductivity without Inversion Symmetry: MnSi versus $CePt_3Si$", Phys. Rev. Lett. **92**, 097001 (2004).
[374]A. P. Schnyder and S. Ryu, "Topological Phases and Surface Flat Bands in Superconductors without Inversion Symmetry", Phys. Rev. B **84**, 060504 (2011).
[375]M. Smidman et al., "Superconductivity and Spin–Orbit Coupling in Non-Centrosymmetric Materials: A Review", Rep. Prog. Phys. **80**, 036501 (2017).
[376]S. C. de la Barrera et al., "Tuning Ising Superconductivity with Layer and Spin–Orbit Coupling in Two-Dimensional Transition-Metal Dichalcogenides", Nat. Commun. **9**, 1427 (2018).
[377]J. N. Coleman et al., "Two-Dimensional Nanosheets Produced by Liquid Exfoliation of Layered Materials", Science **331**, 568–571 (2011).
[378]B. Radisavljevic et al., "Single-Layer MoS2 Transistors", Nat. Nanotech. **6**, 147–150 (2011).
[379]G.-B. Liu et al., "Electronic Structures and Theoretical Modelling of Two-Dimensional Group-VIB Transition Metal Dichalcogenides", Chem. Soc. Rev. **44**, 2643–2663 (2015).
[380]Y. Xing et al., "Ising Superconductivity and Quantum Phase Transition in Macro-Size Monolayer NbSe2", Nano Lett. **17**, 6802–6807 (2017).
[381]H. Jiang et al., "Two-Dimensional Materials: From Mechanical Properties to Flexible Mechanical Sensors", InfoMat **2**, 1077–1094 (2020).
[382]Y. Saito, T. Nojima, and Y. Iwasa, "Highly Crystalline 2D Superconductors", Nat Rev Mater **2**, 16094 (2016).
[383]W.-Y. He et al., "Magnetic Field Driven Nodal Topological Superconductivity in Monolayer Transition Metal Dichalcogenides", Commun Phys **1**, 40 (2018).

[384]Y. Bao et al., "Magnetic-Field Regulation of Nodal Topological Superconducting States in Monolayer Ising Superconductor NbSe $_2$", Physica Rap. Res. Let., 2300135 (2023).
[385]D. Qiu et al., "Recent Advances in 2D Superconductors", Adv. Mat. **33**, 2006124 (2021).
[386]L. Bauriedl et al., "Supercurrent Diode Effect and Magnetochiral Anisotropy in Few-Layer NbSe2", Nat. Commun. **13**, 4266 (2022).
[387]H. N. S. Lee et al., "The Low-Temperature Transport Properties of NbSe2", J. Appl. Phys. **40**, 602–604 (1969).
[388]H. N. S. Lee et al., "The Low-Temperature Electrical and Magnetic Properties of TaSe2 and NbSe2", Journal of Solid State Chemistry **1**, 190–194 (1970).
[389]F. Consadori and R. F. Frindt, "Anisotropy in the Optical Reflectivity of NbSe2", Solid State Communications **9**, 2151–2153 (1971).
[390]R. S. Title and M. W. Shafer, "Band Structure of the Layered Transition-Metal Dichalcogenides: An Experimental Study by Electron Paramagnetic Resonance on Nb-Doped MoS_2", Phys. Rev. Lett. **28**, 808–810 (1972).
[391]L. F. Mattheiss, "Band Structures of Transition-Metal-Dichalcogenide Layer Compounds", Phys. Rev. B **8**, 3719–3740 (1973).
[392]Y. Noat et al., "Quasiparticle Spectra of 2 H - NbSe 2 : Two-band Superconductivity and the Role of Tunneling Selectivity", Phys. Rev. B **92**, 134510 (2015).
[393]T. Dvir et al., "Spectroscopy of Bulk and Few-Layer Superconducting NbSe2 with van Der Waals Tunnel Junctions", Nat. Commun. **9**, 598 (2018).
[394]T. R. Devidas, I. Keren, and H. Steinberg, "Spectroscopy of NbSe2 Using Energy-Tunable Defect-Embedded Quantum Dots", Nano Lett. **21**, 6931–6937 (2021).
[395]J. Bardeen, "Wave Functions for Superconducting Electrons", Phys. Rev. **80**, 567–574 (1950).
[396]J. Bardeen and D. Pines, "Electron-Phonon Interaction in Metals", Phys. Rev. **99**, 1140–1150 (1955).
[397]H. Fröhlich, "Theory of the Superconducting State. I. The Ground State at the Absolute Zero of Temperature", Phys. Rev. **79**, 845–856 (1950).
[398]H. Fröhlich, "Superconductivity in Metals with Incomplete Inner Shells", J. Phys. C: Solid State Phys. **1**, 544 (1968).
[399]H. Fröhlich, "Interaction of Electrons with Lattice Vibrations", Proc. R. Soc. Lond. A **215**, 291–298 (1997).
[400]D. Shaffer et al., "Crystalline nodal topological superconductivity and Bogolyubov Fermi surfaces in monolayer $NbSe_2$", Phys. Rev. B **101**, 224503 (2020).
[401]D. Shaffer, F. J. Burnell, and R. M. Fernandes, "Weak-Coupling Theory of Pair Density Wave Instabilities in Transition Metal Dichalcogenides", Phys. Rev. B **107**, 224516 (2023).
[402]N. H. Aase, C. S. Johnsen, and A. Sudbø, "Constrained Weak-Coupling Superconductivity in Multiband Superconductors", Phys. Rev. B **108**, 024509 (2023).

[403]S. Hörhold et al., "Two-bands Ising superconductivity from Coulomb interactions in monolayer $NbSe_2$", 2D Mater. **10**, 025008 (2023).
[404]S. Roy et al., "Unconventional Pairing in Ising Superconductors: Application to Monolayer NbSe2", 2D Mater. **12**, 015004 (2024).
[405]D. Bohm and D. Pines, "A Collective Description of Electron Interactions. I. Magnetic Interactions", Phys. Rev. **82**, 625–634 (1951).
[406]D. Pines and D. Bohm, "A Collective Description of Electron Interactions: II. Collective vs Individual Particle Aspects of the Interactions", Phys. Rev. **85**, 338–353 (1952).
[407]D. Bohm and D. Pines, "A Collective Description of Electron Interactions: III. Coulomb Interactions in a Degenerate Electron Gas", Phys. Rev. **92**, 609–625 (1953).
[408]R. Brout, "Correlation Energy of a High-Density Gas: Plasma Coordinates", Phys. Rev. **108**, 515–517 (1957).
[409]M. Gell-Mann and K. A. Brueckner, "Correlation Energy of an Electron Gas at High Density", Phys. Rev. **106**, 364–368 (1957).
[410]K. Sawada, "Correlation Energy of an Electron Gas at High Density", Phys. Rev. **106**, 372–383 (1957).
[411]K. Sawada et al., "Correlation Energy of an Electron Gas at High Density: Plasma Oscillations", Phys. Rev. **108**, 507–514 (1957).
[412]P. Nozières and D. Pines, "Electron Interaction in Solids. The Nature of the Elementary Excitations", Phys. Rev. **109**, 1062–1074 (1958).
[413]P. Nozières and D. Pines, "Electron Interaction in Solids. Collective Approach to the Dielectric Constant", Phys. Rev. **109**, 762–777 (1958).
[414]P. Nozières and D. Pines, "Electron Interaction in Solids. General Formulation", Phys. Rev. **109**, 741–761 (1958).
[415]H. Ehrenreich and M. H. Cohen, "Self-Consistent Field Approach to the Many-Electron Problem", Phys. Rev. **115**, 786–790 (1959).
[416]T. R. Brown and C. C. Grimes, "Observation of Cyclotron Resonance in Surface-Bound Electrons on Liquid Helium", Phys. Rev. Lett. **29**, 1233–1236 (1972).
[417]A. L. Fetter, "Electrodynamics of a Layered Electron Gas. I. Single Layer", Ann. Phys. **81**, 367–393 (1973).
[418]E. D. Siggia and P. C. Kwok, "Properties of Electrons in Semiconductor Inversion Layers with Many Occupied Electric Subbands. I. Screening and Impurity Scattering", Phys. Rev. B **2**, 1024–1036 (1970).
[419]F. Stern, "Quantum Properties of Surface Space-Charge Layers", Crit. Rev. Solid. State Sci. **4**, 499–514 (1973).
[420]D. A. Dahl and L. J. Sham, "Electrodynamics of Quasi-Two-Dimensional Electrons", Phys. Rev. B **16**, 651–661 (1977).
[421]K. W. Chiu and J. J. Quinn, "Plasma Oscillations of a Two-Dimensional Electron Gas in a Strong Magnetic Field", Phys. Rev. B **9**, 4724–4732 (1974).
[422]L. V. Keldysh, "Coulomb Interaction in Thin Semiconductor and Semimetal Films", JETP Let. **29**, 716 (1979).

[423]T. Ando, A. B. Fowler, and F. Stern, "Electronic Properties of Two-Dimensional Systems", Rev. Mod. Phys. **54**, 437–672 (1982).
[424]P. Cudazzo, I. V. Tokatly, and A. Rubio, "Dielectric Screening in Two-Dimensional Insulators: Implications for Excitonic and Impurity States in Graphane", Phys. Rev. B **84**, 085406 (2011).
[425]T. Ando, "Screening Effect and Impurity Scattering in Monolayer Graphene", J. Phys. Soc. Jpn. **75**, 074716 (2006).
[426]B. Wunsch et al., "Dynamical Polarization of Graphene at Finite Doping", New J. Phys. **8**, 318 (2006).
[427]M. D. Johannes, I. I. Mazin, and C. A. Howells, "Fermi-surface nesting and the origin of the charge-density wave in $NbSe_2$", Phys. Rev. B **73**, 205102 (2006).
[428]E. H. Hwang and S. Das Sarma, "Dielectric Function, Screening, and Plasmons in Two-Dimensional Graphene", Phys. Rev. B **75**, 205418 (2007).
[429]F. Stern, "Polarizability of a Two-Dimensional Electron Gas", Phys. Rev. Lett. **18**, 546–548 (1967).
[430]M. S. Hybertsen and S. G. Louie, "Electron Correlation in Semiconductors and Insulators: Band Gaps and Quasiparticle Energies", Phys. Rev. B **34**, 5390–5413 (1986).
[431]M. S. Hybertsen and S. G. Louie, "Ab Initio Static Dielectric Matrices from the Density-Functional Approach. I. Formulation and Application to Semiconductors and Insulators", Phys. Rev. B **35**, 5585–5601 (1987).
[432]S. L. Adler, "Quantum Theory of the Dielectric Constant in Real Solids", Phys. Rev. **126**, 413–420 (1962).
[433]O. V. Dolgov, D. A. Kirzhnits, and E. G. Maksimov, "On an Admissible Sign of the Static Dielectric Function of Matter", Rev. Mod. Phys. **53**, 81–93 (1981).
[434]D. L. Price, S. K. Sinha, and R. P. Gupta, "Microscopic Theory of Dielectric Screening and Lattice Dynamics. II. Phonon Spectra and Effective Charges", Phys. Rev. B **9**, 2573–2589 (1974).
[435]S. K. Sinha, R. P. Gupta, and D. L. Price, "Microscopic Theory of Dielectric Screening and Lattice Dynamics. I. Local-field Corrections and Dielectric Constants", Phys. Rev. B **9**, 2564–2572 (1974).
[436]S. V. Kravchenko et al., "Possible Metal-Insulator Transition at B=0 in Two Dimensions", Phys. Rev. B **50**, 8039–8042 (1994).
[437]E. Abrahams, S. V. Kravchenko, and M. P. Sarachik, "Metallic Behavior and Related Phenomena in Two Dimensions", Rev. Mod. Phys. **73**, 251–266 (2001).
[438]S. V. Kravchenko and M. P. Sarachik, "Metal–Insulator Transition in Two-Dimensional Electron Systems", Rep. Prog. Phys. **67**, 1 (2003).
[439]S. D. Sarma and E. H. Hwang, "The So-Called Two Dimensional Metal–Insulator Transition", Solid State Commun., Fundamental Optical and Quantum Effects in Condensed Matter **135**, 579–590 (2005).
[440]B. Spivak et al., "Colloquium: Transport in Strongly Correlated Two Dimensional Electron Fluids", Rev. Mod. Phys. **82**, 1743–1766 (2010).
[441]S. Das Sarma and E. H. Hwang, "Screening and Transport in 2D Semiconductor Systems at Low Temperatures", Sci. Rep. **5**, 16655 (2015).

[442]P. A. Lee and T. V. Ramakrishnan, "Disordered Electronic Systems", Rev. Mod. Phys. **57**, 287–337 (1985).
[443]D. Belitz and T. R. Kirkpatrick, "The Anderson-Mott Transition", Rev. Mod. Phys. **66**, 261–380 (1994).
[444]A. Punnoose and A. M. Finkel'stein, "Metal-Insulator Transition in Disordered Two-Dimensional Electron Systems", Science **310**, 289–291 (2005).
[445]A. W. Tsen et al., "Nature of the Quantum Metal in a Two-Dimensional Crystalline Superconductor", Nat. Phys. **12**, 208–212 (2016).
[446]A. Kapitulnik, S. A. Kivelson, and B. Spivak, "Colloquium: Anomalous Metals: Failed Superconductors", Rev. Mod. Phys. **91**, 011002 (2019).
[447]E. Wigner, "Effects of the Electron Interaction on the Energy Levels of Electrons in Metals", Trans. Faraday Soc. **34**, 678–685 (1938).
[448]H. J. Monkhorst and J. Oddershede, "Random-Phase-Approximation Correlation Energy in Metallic Hydrogen Using Hartree-Fock Bloch Functions", Phys. Rev. Lett. **30**, 797–800 (1973).
[449]S. Lebègue and O. Eriksson, "Electronic Structure of Two-Dimensional Crystals from Ab Initio Theory", Phys. Rev. B **79**, 115409 (2009).
[450]C. Ataca, H. Şahin, and S. Ciraci, "Stable, Single-Layer MX2 Transition-Metal Oxides and Dichalcogenides in a Honeycomb-Like Structure", J. Phys. Chem. C **116**, 8983–8999 (2012).
[451]J. B. Mann, *Atomic Structure Calculations. II. Hartree-Fock Wavefunctions and Radial Expectation Values: Hydrogen to Lawrencium*, tech. rep. LA-3691 (Los Alamos National Lab. (LANL), Los Alamos, NM (United States), Jan. 1968).
[452]J. F. Cooke, H. L. Davis, and M. Mostoller, "Electronic Susceptibility of Niobium", Phys. Rev. B **9**, 2485–2489 (1974).
[453]J. Rath and A. J. Freeman, "Generalized Magnetic Susceptibilities in Metals: Application of the Analytic Tetrahedron Linear Energy Method to Sc", Phys. Rev. B **11**, 2109–2117 (1975).
[454]R. P. Gupta and A. J. Freeman, "Role of Matrix Elements in the Theoretical Determination of Generalized Susceptibilities in Metals", Phys. Rev. B **13**, 4376–4386 (1976).
[455]M. Fabrizio, *A Course in Quantum Many-Body Theory: From Conventional Fermi Liquids to Strongly Correlated Systems*, Graduate Texts in Physics (Springer International Publishing, Cham, 2022).
[456]G. Czycholl, *Theoretische Festkörperphysik Band 2: Anwendungen: Nichtgleichgewicht, Verhalten in äußeren Feldern, kollektive Phänomene* (Springer, Berlin, Heidelberg, 2017).
[457]G. D. Mahan, *Many-Particle Physics* (Springer US, Boston, MA, 2000).
[458]A. Madhukar, "Coupled Electron-Phonon System in Two Dimensions and Its Implications for Inversion Layers", Solid State Communications **24**, 11–14 (1977).
[459]T. Cea and F. Guinea, "Coulomb Interaction, Phonons, and Superconductivity in Twisted Bilayer Graphene", Proc. Natl. Acad. Sci. U.S.A. **118**, e2107874118 (2021).

[460]P. J. Hirschfeld, M. M. Korshunov, and I. I. Mazin, "Gap Symmetry and Structure of Fe-based Superconductors", Rep. Prog. Phys. **74**, 124508 (2011).
[461]Y. Zhumagulov, D. Kochan, and J. Fabian, "Emergent Correlated Phases in Rhombohedral Trilayer Graphene Induced by Proximity Spin-Orbit and Exchange Coupling", Phys. Rev. Lett. **132**, 186401 (2024).
[462]Y. Zhumagulov, D. Kochan, and J. Fabian, "Swapping Exchange and Spin-Orbit Induced Correlated Phases in Proximitized Bernal Bilayer Graphene", Phys. Rev. B **110**, 045427 (2024).
[463]A. Davydov et al., "Ab Initio Theory of Plasmonic Superconductivity within the Eliashberg and Density-Functional Formalisms", Phys. Rev. B **102**, 214508 (2020).
[464]C. Pellegrini, C. Kukkonen, and A. Sanna, "Ab Initio Calculations of Superconducting Transition Temperatures: When Going beyond RPA Is Essential", Phys. Rev. B **108**, 064511 (2023).
[465]S. Brodersen, D. Lukas, and W. Schattke, "Calculation of the Dielectric Function in a Local Representation", Phys. Rev. B **66**, 085111 (2002).
[466]S. Kim and Y.-W. Son, "Quasiparticle energy bands and Fermi surfaces of monolayer $NbSe_2$", Phys. Rev. B **96**, 155439 (2017).
[467]D. Wickramaratne et al., "Ising Superconductivity and Magnetism in $NbSe_2$", Phys. Rev. X **10**, 041003 (2020).
[468]P. Blaha et al., "WIEN2k: An APW+lo Program for Calculating the Properties of Solids", J. Chem. Phys. **152**, 074101 (2020).
[469]L. N. Oliveira, E. K. U. Gross, and W. Kohn, "Density-Functional Theory for Superconductors", Phys. Rev. Lett. **60**, 2430–2433 (1988).
[470]J. P. Carbotte, "Properties of Boson-Exchange Superconductors", Rev. Mod. Phys. **62**, 1027–1157 (1990).
[471]E. Pavarini et al., eds., *Emergent Phenomena in Correlated Matter: Lecture Notes of the Autumn School Correlated Electrons 2013: At Forschungszentrum Jülich, 23-27 September 2013*, Schriften Des Forschungszentrums Jülich. Reihe Modeling and Simulation Band 3 (Forschungszentrum, Zentralbibliothek, Jülich, 2013).
[472]E. Pavarini et al., eds., *The Physics of Correlated Insulators, Metals, and Superconductors: Lecture Notes of the Autumn School on Correlated Electrons 2017: At Forschungszentrum Jülich, 25-29 September 2017*, Schriften Des Forschungszentrums Jülich. Reihe Modeling and Simulation Band 7 (Forschungszentrum, Zentralbibliothek, Jülich, 2017).
[473]T. Wang et al., "Origin of the Coulomb Pseudopotential", Phys. Rev. B **107**, L140507 (2023).
[474]F. Essenberger et al., "Superconducting Pairing Mediated by Spin Fluctuations from First Principles", Phys. Rev. B **90**, 214504 (2014).
[475]A. Linscheid et al., "Ab Initio Theory of Superconductivity in a Magnetic Field. I. Spin Density Functional Theory for Superconductors and Eliashberg Equations", Phys. Rev. B **92**, 024505 (2015).
[476]F. Essenberger et al., "Ab Initio Theory of Iron-Based Superconductors", Phys. Rev. B **94**, 014503 (2016).

[477]A. Linscheid, A. Sanna, and E. K. U. Gross, "Ab Initio Theory of Superconductivity in a Magnetic Field. II. Numerical Solution", Phys. Rev. B **92**, 024506 (2015).
[478]E. Clementi, D. L. Raimondi, and W. P. Reinhardt, "Atomic Screening Constants from SCF Functions. II. Atoms with 37 to 86 Electrons", J. Chem. Phys. **47**, 1300–1307 (1967).
[479]J. C. Slater, "Atomic Shielding Constants", Phys. Rev. **36**, 57–64 (1930).
[480]G. E. Simion and G. F. Giuliani, "Friedel Oscillations in a Fermi Liquid", Phys. Rev. B **72**, 045127 (2005).
[481]A. V. Chubukov, "Kohn-Luttinger Effect and the Instability of a Two-Dimensional Repulsive Fermi Liquid at T=0", Phys. Rev. B **48**, 1097–1104 (1993).
[482]M. J. Lighthill, *An Introduction to Fourier Analysis and Generalised Functions*, Cambridge Monographs on Mechanics (Cambridge University Press, Cambridge, 1958).
[483]J. Friedel, "XIV. The Distribution of Electrons Round Impurities in Monovalent Metals", London Edinburgh Philos. Mag. & J. Sci. **43**, 153–189 (1952).
[484]S. M. Badalyan et al., "Beating of Friedel Oscillations Induced by Spin-Orbit Interaction", Phys. Rev. B **81**, 205314 (2010).
[485]S. Ahn and S. Das Sarma, "Screening, Friedel Oscillations, RKKY Interaction, and Drude Transport in Anisotropic Two-Dimensional Systems", Phys. Rev. B **103**, 165303 (2021).
[486]S. Graser et al., "Near-Degeneracy of Several Pairing Channels in Multiorbital Models for the Fe Pnictides", New J. Phys. **11**, 025016 (2009).
[487]N. F. Q. Yuan, K. F. Mak, and K. T. Law, "Possible Topological Superconducting Phases of MoS_2", Phys. Rev. Lett. **113**, 097001 (2014).
[488]P. J. Hirschfeld, "Using gap symmetry and structure to reveal the pairing mechanism in Fe-based superconductors", C. R. Phys. **17**, 197–231 (2016).
[489]Y.-T. Hsu et al., "Topological Superconductivity in Monolayer Transition Metal Dichalcogenides", Nat. Commun. **8**, 14985 (2017).
[490]D. Möckli and M. Khodas, "Robust Parity-Mixed Superconductivity in Disordered Monolayer Transition Metal Dichalcogenides", Phys. Rev. B **98**, 144518 (2018).
[491]R. Oiwa, Y. Yanagi, and H. Kusunose, "Theory of superconductivity in hole-doped monolayer MoS_2", Phys. Rev. B **98**, 064509 (2018).
[492]R. Oiwa, Y. Yanagi, and H. Kusunose, "Time-Reversal Symmetry Breaking Superconductivity in Hole-doped Monolayer MoS2", J. Phys. Soc. Jpn. **88**, 063703 (2019).
[493]J. Hutchinson and F. Marsiglio, "Mixed Temperature-Dependent Order Parameters in the Extended Hubbard Model", J. Phys.: Condens. Matter **33**, 065603 (2021).
[494]G. Margalit, E. Berg, and Y. Oreg, "Theory of Multi-Orbital Topological Superconductivity in Transition Metal Dichalcogenides", Ann. Phys., Special Issue on Philip W. Anderson **435**, 168561 (2021).

[495]L. Gibelli et al., *A universal route to chiral Ising superconductivity in monolayer TaS_2 and $NbSe_2$*, Sept. 2025.
[496]F. London, H. London, and F. A. Lindemann, "The Electromagnetic Equations of the Supraconductor", Proc. R. Soc. Lond. A **149**, 71–88 (1997).
[497]W. Meissner and R. Ochsenfeld, "Ein neuer Effekt bei Eintritt der Supraleitfähigkeit", Naturwissenschaften **21**, 787–788 (1933).
[498]A. A. Abrikosov, "On the Magnetic Properties of Superconductors of the Second Group", JETP **5**, 1174 (1957).
[499]S. Reinhardt et al., "Link between Supercurrent Diode and Anomalous Josephson Effect Revealed by Gate-Controlled Interferometry", Nat Commun **15**, 4413 (2024).
[500]R. Kishore and S. Lamba, "Specific Heat Jump in BCS Superconductors", Eur. Phys. J. B **8**, 161–164 (1999).
[501]P.-G. de Gennes, *Superconductivity of Metals and Alloys*, Advanced Book Classics (Advanced Book Program, Perseus Books, Reading, Mass, 1999).
[502]C. Baumgartner et al., "Supercurrent Rectification and Magnetochiral Effects in Symmetric Josephson Junctions", Nat. Nanotechnol. **17**, 39–44 (2022).
[503]A. Costa, J. Fabian, and D. Kochan, "Microscopic Study of the Josephson Supercurrent Diode Effect in Josephson Junctions Based on Two-Dimensional Electron Gas", Phys. Rev. B **108**, 054522 (2023).
[504]F. Marsiglio, "Eliashberg Theory: A Short Review", Ann. Phys., Eliashberg Theory at 60: Strong-coupling Superconductivity and Beyond **417**, 168102 (2020).
[505]A. Bardasis and J. R. Schrieffer, "Excitons and Plasmons in Superconductors", Phys. Rev. **121**, 1050–1062 (1961).
[506]Y. in't Veld et al., "Screening Induced Crossover between Phonon- and Plasmon-Mediated Pairing in Layered Superconductors", 2D Mater. **10**, 045031 (2023).
[507]D. Allender, J. Bray, and J. Bardeen, "Model for an Exciton Mechanism of Superconductivity", Phys. Rev. B **7**, 1020–1029 (1973).
[508]F. Viñas Boström and E. Viñas Boström, "Magnon-Mediated Topological Superconductivity in a Quantum Wire", Phys. Rev. Res. **6**, L022042 (2024).
[509]A. V. Chubukov and M. Y. Kagan, "On the Superfluid Transition in Dense Electron Systems", J. Phys.: Condens. Matter **1**, 3135 (1989).
[510]N. F. Berk and J. R. Schrieffer, "Effect of Ferromagnetic Spin Correlations on Superconductivity", Phys. Rev. Lett. **17**, 433–435 (1966).
[511]C. M. Varma et al., "Phenomenology of the Normal State of Cu-O High-Temperature Superconductors", Phys. Rev. Lett. **63**, 1996–1999 (1989).
[512]I. I. Mazin et al., "Unconventional Superconductivity with a Sign Reversal in the Order Parameter of $LaFeAsO_{1-x}F_x$", Phys. Rev. Lett. **101**, 057003 (2008).
[513]L. Fanfarillo et al., "Theory of Fluctuation Conductivity from Interband Pairing in Pnictide Superconductors", Phys. Rev. B **79**, 172508 (2009).
[514]I. I. Mazin, "Superconductivity Gets an Iron Boost", Nature **464**, 183–186 (2010).
[515]A. Chubukov, "Pairing Mechanism in Fe-Based Superconductors", Ann. Rev. Cond. Matter Phys. **3**, 57–92 (2012).

[516] A. Kreisel et al., "Orbital Selective Pairing and Gap Structures of Iron-Based Superconductors", Phys. Rev. B **95**, 174504 (2017).
[517] L. Benfatto, B. Valenzuela, and L. Fanfarillo, "Nematic Pairing from Orbital-Selective Spin Fluctuations in FeSe", npj Quantum Mater. **3**, 56 (2018).
[518] A. Kreisel, P. J. Hirschfeld, and B. M. Andersen, "On the Remarkable Superconductivity of FeSe and Its Close Cousins", Symmetry **12**, 1402 (2020).
[519] D. J. Scalapino, "A Common Thread: The Pairing Interaction for Unconventional Superconductors", Rev. Mod. Phys. **84**, 1383–1417 (2012).
[520] A. P. Mackenzie et al., "Even Odder after Twenty-Three Years: The Superconducting Order Parameter Puzzle of Sr2RuO4", npj Quantum Mater. **2**, 40 (2017).
[521] A. T. Rømer et al., "Knight Shift and Leading Superconducting Instability from Spin Fluctuations in Sr_2RuO_4", Phys. Rev. Lett. **123**, 247001 (2019).
[522] T. Han et al., "Signatures of Chiral Superconductivity in Rhombohedral Graphene", Nature **654–661**, 654–661 (2025).
[523] Y. Cao et al., "Unconventional Superconductivity in Magic-Angle Graphene Superlattices", Nature **556**, 43–50 (2018).
[524] T. Sohier et al., "Enhanced Electron-Phonon Interaction in Multivalley Materials", Phys. Rev. X **9**, 031019 (2019).
[525] C. Chen et al., "Strong Electron–Phonon Coupling in Magic-Angle Twisted Bilayer Graphene", Nature **636**, 342–347 (2024).
[526] A. Perali et al., "Two-Gap Model for Underdoped Cuprate Superconductors", Phys. Rev. B **62**, R9295–R9298 (2000).
[527] S. Divilov et al., "Magnetic correlations in single-layer $NbSe_2$", J. Phys.: Condens. Matter **33**, 295804 (2021).
[528] S. Das and I. I. Mazin, "Quantitative Assessment of the Role of Spin Fluctuations in 2D Ising Superconductor NbSe2", Computational Materials Science **200**, 110758 (2021).
[529] A. T. Costa, M. Costa, and J. Fernández-Rossier, "Ising and XY paramagnons in two-dimensional 2H−$NbSe_2$", Phys. Rev. B **105**, 224412 (2022).
[530] C. Heil et al., "Origin of Superconductivity and Latent Charge Density Wave in NbS 2", Phys. Rev. Lett. **119**, 087003 (2017).
[531] A. Sanna et al., "Real-Space Anisotropy of the Superconducting Gap in the Charge-Density Wave Material 2H-NbSe2", npj Quantum Mater. **7**, 6 (2022).
[532] F. Zheng and J. Feng, "Electron-phonon coupling and the coexistence of superconductivity and charge-density wave in monolayer $NbSe_2$", Phys. Rev. B **99**, 161119 (2019).
[533] Z. Yang et al., "Superconductivity in Unconventional Metals", Npj Comput. Mater. **10**, 25 (2024).
[534] A. A. Taleb et al., *Electron-phonon coupling and phonon dynamics in single-layer $NbSe_2$ on graphene: the role of moiré phonons*, Jan. 2025.
[535] R. Roldán, E. Cappelluti, and F. Guinea, "Interactions and superconductivity in heavily doped MoS_2", Phys. Rev. B **88**, 054515 (2013).

[536]E. Dagotto, "Correlated Electrons in High-Temperature Superconductors", Rev. Mod. Phys. **66**, 763–840 (1994).
[537]H. Mukuda et al., "High-Tc Superconductivity and Antiferromagnetism in Multilayered Copper Oxides –A New Paradigm of Superconducting Mechanism–", J. Phys. Soc. Jpn. **81**, 011008 (2012).
[538]P. Fulde and R. A. Ferrell, "Superconductivity in a Strong Spin-Exchange Field", Phys. Rev. **135**, A550–A563 (1964).
[539]A. I. Larkin and Y. N. Ovchinnikov, "Nonuniform state of superconductors", JETP **Vol: 47** (1964).
[540]A. P. Mackenzie and Y. Maeno, "The superconductivity of Sr_2RuO_4 and the physics of spin-triplet pairing", Rev. Mod. Phys. **75**, 657–712 (2003).
[541]D. Möckli and M. Khodas, "Magnetic-field induced $s + if$ pairing in Ising superconductors", Phys. Rev. B **99**, 180505 (2019).
[542]P. Wan et al., "Orbital Fulde–Ferrell–Larkin–Ovchinnikov State in an Ising Superconductor", Nature, 10.1038/s41586-023-05967-z (2023).
[543]M. Haim, D. Möckli, and M. Khodas, "Signatures of Triplet Correlations in Density of States of Ising Superconductors", Phys. Rev. B **102**, 214513 (2020).
[544]M. Kuzmanović et al., "Tunneling spectroscopy of few-monolayer $NbSe_2$ in high magnetic fields: Triplet superconductivity and Ising protection", Phys. Rev. B **106**, 184514 (2022).
[545]M. Haim, A. Levchenko, and M. Khodas, "Mechanisms of in-plane magnetic anisotropy in superconducting $NbSe_2$", Phys. Rev. B **105**, 024515 (2022).
[546]D. Ding et al., "Multivalley Superconductivity in Monolayer Transition Metal Dichalcogenides", Nano Lett. **22**, 7919–7926 (2022).
[547]L. Benfatto et al., "Multiple Gaps and Superfluid Density from Interband Pairing in a Four-Band Model of the Iron Oxypnictides", Phys. Rev. B **78**, 140502 (2008).
[548]W.-M. Huang and H.-H. Lin, "Pairing Mechanism in Multiband Superconductors", Sci. Rep. **10**, 7439 (2020).
[549]A. Guidini and A. Perali, "Band-Edge BCS–BEC Crossover in a Two-Band Superconductor: Physical Properties and Detection Parameters", Supercond. Sci. Technol. **27**, 124002 (2014).
[550]Q. Chen et al., "When Superconductivity Crosses over: From BCS to BEC", Rev. Mod. Phys. **96**, 025002 (2024).
[551]M. Lüders et al., "Ab Initio Theory of Superconductivity. I. Density Functional Formalism and Approximate Functionals", Phys. Rev. B **72**, 024545 (2005).
[552]M. A. L. Marques et al., "Ab Initio Theory of Superconductivity. II. Application to Elemental Metals", Phys. Rev. B **72**, 024546 (2005).
[553]A. Altland and B. D. Simons, *Condensed Matter Field Theory*, 2nd ed. (Cambridge University Press, Cambridge, 2010).
[554]G. M. Eliashberg, "Interactions between Electrons and Lattice Vibrations in a Superconductor", JETP **11**, 696 (1959).
[555]G. M. Eliashberg, "Temperature Green's Function for Electrons in a Superconductor", JETP **12**, 1000 (1960).

[556] A. Weiße et al., "The Kernel Polynomial Method", Rev. Mod. Phys. **78**, 275–306 (2006).
[557] L. Covaci, F. M. Peeters, and M. Berciu, "Efficient Numerical Approach to Inhomogeneous Superconductivity: The Chebyshev-Bogoliubov–de Gennes Method", Phys. Rev. Lett. **105**, 167006 (2010).
[558] C. R. Harris et al., "Array Programming with NumPy", Nature **585**, 357–362 (2020).
[559] P. Debye, "Zur Theorie der spezifischen Wärmen", Ann. Phys. **344**, 789–839 (1912).
[560] Y. Cao et al., "Quality Heterostructures from Two-Dimensional Crystals Unstable in Air by Their Assembly in Inert Atmosphere", Nano Lett. **15**, 4914–4921 (2015).
[561] D. Phan and A. V. Chubukov, "Kohn-Luttinger correction to T_c in a phonon superconductor", Phys. Rev. B **101**, 024503 (2020).
[562] S. Biswas et al., "Hybrid *s*-wave superconductivity in CrB_2", Phys. Rev. B **108**, L020501 (2023).
[563] A. M. Black-Schaffer and C. Honerkamp, "Chiral D-Wave Superconductivity in Doped Graphene", J. Phys.: Condens. Matter **26**, 423201 (2014).
[564] C. Kallin and J. Berlinsky, "Chiral Superconductors", Rep. Prog. Phys. **79**, 054502 (2016).
[565] M. I. Bannikov et al., "Breaking of Ginzburg-Landau Description in the Temperature Dependence of the Anisotropy in a Nematic Superconductor", Phys. Rev. B **104**, L220502 (2021).
[566] A. Hamill et al., "Two-Fold Symmetric Superconductivity in Few-Layer NbSe2", Nat. Phys. **17**, 949–954 (2021).
[567] C.-w. Cho et al., "Nodal and Nematic Superconducting Phases in $NbSe_2$ Monolayers from Competing Superconducting Channels", Phys. Rev. Lett. **129**, 087002 (2022).
[568] J. Bardeen, "Tunnelling from a Many-Particle Point of View", Phys. Rev. Lett. **6**, 57–59 (1961).
[569] J. Tersoff, "Theory and Application for the Scanning Tunneling Microscope", Phys. Rev. Lett. **50**, 1998–2001 (1983).
[570] J. Tersoff and D. R. Hamann, "Theory of the Scanning Tunneling Microscope", Phys. Rev. B **31**, 805–813 (1985).
[571] M. M. Ugeda et al., "Characterization of Collective Ground States in Single-Layer NbSe2", Nat. Phys. **12**, 92–97 (2016).
[572] J.-F. Ge, M. Ovadia, and J. E. Hoffman, "Achieving Low Noise in Scanning Tunneling Spectroscopy", Rev. Sci. Instrum. **90**, 101401 (2019).
[573] S. Onishi et al., "Selenium Capped Monolayer NbSe2 for Two-Dimensional Superconductivity Studies", Phys. Stat. Sol. B **253**, 2396–2399 (2016).
[574] P. Virtanen et al., "SciPy 1.0: Fundamental Algorithms for Scientific Computing in Python", Nat Methods **17**, 261–272 (2020).

[575]C. J. Arguello et al., "Quasiparticle Interference, Quasiparticle Interactions, and the Origin of the Charge Density Wave in 2H−$NbSe_2$", Phys. Rev. Lett. **114**, 037001 (2015).
[576]L. Chen, P. Cheng, and K. Wu, "Quasiparticle Interference in Unconventional 2D Systems", J. Phys.: Condens. Matter **29**, 103001 (2017).
[577]R. Sharma et al., "Momentum-Resolved Superconducting Energy Gaps of Sr2RuO4 from Quasiparticle Interference Imaging", Proc. Natl. Acad. Sci. U.S.A. **117**, 5222–5227 (2020).
[578]J. Haniš, M. Milivojević, and M. Gmitra, "Distinguishing nodal and nonunitary superconductivity in quasiparticle interference of an Ising superconductor with Rashba spin-orbit coupling: The example of $NbSe_2$", Phys. Rev. B **110**, 104502 (2024).
[579]M. M. Ugeda et al., "Giant Bandgap Renormalization and Excitonic Effects in a Monolayer Transition Metal Dichalcogenide Semiconductor", Nature Mater **13**, 1091–1095 (2014).
[580]D. S. Inosov et al., "Crossover from Weak to Strong Pairing in Unconventional Superconductors", Phys. Rev. B **83**, 214520 (2011).
[581]E. Boaknin et al., "Heat Conduction in the Vortex State of $NbSe_2$: Evidence for Multiband Superconductivity", Phys. Rev. Lett. **90**, 117003 (2003).
[582]M. Zehetmayer and H. W. Weber, "Experimental evidence for a two-band superconducting state of $NbSe_2$ single crystals", Phys. Rev. B **82**, 014524 (2010).
[583]T. Yokoya et al., "Fermi Surface Sheet-Dependent Superconductivity in 2H-NbSe2", Science **294**, 2518–2520 (2001).
[584]J. D. Fletcher et al., "Penetration Depth Study of Superconducting Gap Structure of 2H-$NbSe_2$", Phys. Rev. Lett. **98**, 057003 (2007).
[585]C. L. Huang et al., "Experimental evidence for a two-gap structure of superconducting $NbSe_2$: A specific-heat study in external magnetic fields", Phys. Rev. B **76**, 212504 (2007).
[586]I. Guillamon et al., "Intrinsic atomic-scale modulations of the superconducting gap of 2H-$NbSe_2$", Phys. Rev. B **77**, 134505 (2008).
[587]W. Bao et al., "High Mobility Ambipolar MoS2 Field-Effect Transistors: Substrate and Dielectric Effects", Appl. Phys. Lett. **102**, 042104 (2013).
[588]K. Noori et al., "Dielectric Screening by 2D Substrates", 2D Mater. **6**, 035036 (2019).
[589]P. Dreher et al., "Proximity Effects on the Charge Density Wave Order and Superconductivity in Single-Layer NbSe2", ACS Nano **15**, 19430–19438 (2021).
[590]T. Yang et al., "Interaction between a gold substrate and monolayer MoS_2: An azimuthal-dependent sum frequency generation study", Phys. Rev. B **107**, 155433 (2023).
[591]N. Read and D. Green, "Paired States of Fermions in Two Dimensions with Breaking of Parity and Time-Reversal Symmetries and the Fractional Quantum Hall Effect", Phys. Rev. B **61**, 10267–10297 (2000).

[592] A. M. Black-Schaffer, "Edge Properties and Majorana Fermions in the Proposed Chiral d -Wave Superconducting State of Doped Graphene", Phys. Rev. Lett. **109**, 197001 (2012).
[593] A. Jimeno-Pozo et al., "Superconductivity from Electronic Interactions and Spin-Orbit Enhancement in Bilayer and Trilayer Graphene", Phys. Rev. B **107**, L161106 (2023).
[594] S. Kezilebieke et al., "Topological Superconductivity in a van Der Waals Heterostructure", Nature **588**, 424–428 (2020).
[595] X. Hu and Y. Ran, "Engineering Chiral Topological Superconductivity in Twisted Ising Superconductors", Phys. Rev. B **106**, 125136 (2022).
[596] E. Cappelluti et al., "Tight-binding model and direct-gap/indirect-gap transition in single-layer and multi-layer MoS_2", Phys. Rev. B **88**, 075409 (2013).
[597] M. Kreidel et al., "Measuring Kinetic Inductance and Superfluid Stiffness of Two-Dimensional Superconductors Using High-Quality Transmission-Line Resonators", Phys. Rev. Res. **6**, 043245 (2024).
[598] T. Cea and F. Guinea, "Band Structure and Insulating States Driven by Coulomb Interaction in Twisted Bilayer Graphene", Phys. Rev. B **102**, 045107 (2020).
[599] D. Wickramaratne and I. I. Mazin, "Ising superconductivity: A first-principles perspective", Appl. Phys. Lett. **122**, 240503 (2023).
[600] S. Droste, S. Andergassen, and J. Splettstoesser, "Josephson Current through Interacting Double Quantum Dots with Spin–Orbit Coupling", J. Phys.: Condens. Matter **24**, 415301 (2012).
[601] J. F. Cornwell, *Group Theory in Physics: An Introduction* (Academic Press, San Diego, Calif, 1997).
[602] W. Heisenberg, "Zur Theorie des Ferromagnetismus", Z. Physik **49**, 619–636 (1928).
[603] M. Žnidarič, T. Prosen, and P. Prelovšek, "Many-Body Localization in the Heisenberg XXZ Magnet in a Random Field", Phys. Rev. B **77**, 064426 (2008).
[604] T. C. Berkelbach and D. R. Reichman, "Conductivity of Disordered Quantum Lattice Models at Infinite Temperature: Many-body Localization", Phys. Rev. B **81**, 224429 (2010).
[605] J. H. Bardarson, F. Pollmann, and J. E. Moore, "Unbounded Growth of Entanglement in Models of Many-Body Localization", Phys. Rev. Lett. **109**, 017202 (2012).
[606] E. Altman and R. Vosk, "Universal Dynamics and Renormalization in Many-Body-Localized Systems", Ann. Rev. Condens. Matter Phys. **6**, 383–409 (2015).
[607] K. Agarwal et al., "Rare-Region Effects and Dynamics near the Many-Body Localization Transition", Ann. Phys. **529**, 1600326 (2017).
[608] D. J. Luitz and Y. B. Lev, "The Ergodic Side of the Many-Body Localization Transition", Ann. Phys. **529**, 1600350 (2017).
[609] A. Haldar and A. Das, "Dynamical Many-Body Localization and Delocalization in Periodically Driven Closed Quantum Systems", Ann. Phys. **529**, 1600333 (2017).

[610]D. Sels, "Bath-Induced Delocalization in Interacting Disordered Spin Chains", Phys. Rev. B **106**, L020202 (2022).
[611]J. Gu et al., "Many-Body Localization from Random Magnetic Anisotropy", Phys. Rev. Res. **1**, 033183 (2019).
[612]J. Richter and A. Pal, "Many-Body Localization and Delocalization Dynamics in the Thermodynamic Limit", Phys. Rev. B **105**, L220405 (2022).
[613]T. Devakul and R. R. P. Singh, "Early Breakdown of Area-Law Entanglement at the Many-Body Delocalization Transition", Phys. Rev. Lett. **115**, 187201 (2015).
[614]F. Pietracaprina et al., "Shift-Invert Diagonalization of Large Many-Body Localizing Spin Chains", SciPost Phys. **5**, 45 (2018).
[615]N. Macé, F. Alet, and N. Laflorencie, "Multifractal Scalings Across the Many-Body Localization Transition", Phys. Rev. Lett. **123**, 180601 (2019).
[616]P. Sierant, M. Lewenstein, and J. Zakrzewski, "Polynomially Filtered Exact Diagonalization Approach to Many-Body Localization", Phys. Rev. Lett. **125**, 156601 (2020).
[617]D. Sels and A. Polkovnikov, "Thermalization of Dilute Impurities in One-Dimensional Spin Chains", Phys. Rev. X **13**, 011041 (2023).
[618]T. Chanda, P. Sierant, and J. Zakrzewski, "Time Dynamics with Matrix Product States: Many-body Localization Transition of Large Systems Revisited", Phys. Rev. B **101**, 035148 (2020).
[619]M. Kiefer-Emmanouilidis et al., "Slow Delocalization of Particles in Many-Body Localized Phases", Phys. Rev. B **103**, 024203 (2021).
[620]G. Biroli, C. Kollath, and A. M. Läuchli, "Effect of Rare Fluctuations on the Thermalization of Isolated Quantum Systems", Phys. Rev. Lett. **105**, 250401 (2010).
[621]T. Thiery et al., "Many-Body Delocalization as a Quantum Avalanche", Phys. Rev. Lett. **121**, 140601 (2018).
[622]A. Morningstar et al., "Avalanches and Many-Body Resonances in Many-Body Localized Systems", Phys. Rev. B **105**, 174205 (2022).
[623]H. Bethe, "Zur Theorie der Metalle", Z. Physik **71**, 205–226 (1931).
[624]G. Theodorou and M. H. Cohen, "Paramagnetic Susceptibility of Disordered N-Methyl-Phenazinium Tetracyanoquinodimethanide", Phys. Rev. Lett. **37**, 1014–1017 (1976).
[625]S.-k. Ma, C. Dasgupta, and C.-k. Hu, "Random Antiferromagnetic Chain", Phys. Rev. Lett. **43**, 1434–1437 (1979).
[626]C. Dasgupta and S.-k. Ma, "Low-Temperature Properties of the Random Heisenberg Antiferromagnetic Chain", Phys. Rev. B **22**, 1305–1319 (1980).
[627]K. Agarwal, E. Demler, and I. Martin, "$1/f^{\alpha}$ noise and generalized diffusion in random Heisenberg spin systems", Phys. Rev. B **92**, 184203 (2015).
[628]F. H. L. Essler et al., *The One-Dimensional Hubbard Model* (Cambridge University Press, Cambridge, 2005).
[629]P. Prelovšek, O. S. Barišić, and M. Žnidarič, "Absence of Full Many-Body Localization in the Disordered Hubbard Chain", Phys. Rev. B **94**, 241104 (2016).

[630]M. Kozarzewski, P. Prelovšek, and M. Mierzejewski, "Spin Subdiffusion in the Disordered Hubbard Chain", Phys. Rev. Lett. **120**, 246602 (2018).
[631]S. J. Thomson and M. Schiró, "Time Evolution of Many-Body Localized Systems with the Flow Equation Approach", Phys. Rev. B **97**, 060201 (2018).
[632]S.-H. Lin et al., "Many-Body Localization of Spinless Fermions with Attractive Interactions in One Dimension", SciPost Phys. **4**, 002 (2018).
[633]E. Madelung, "Eine anschauliche Deutung der Gleichung von Schrödinger", Naturwissenschaften **14**, 1004–1004 (1926).
[634]E. Clementi and D. L. Raimondi, "Atomic Screening Constants from SCF Functions", J. Chem. Phys. **38**, 2686–2689 (1963).
[635]J. B. Goodenough, "Band Model for Transition-Metal Chalcogenides Having Layer Structures with Occupied Trigonal-Bipyramidal Sites", Mat. Res. Bull. **3**, 409–415 (1968).
[636]G.-B. Liu et al., "Erratum: Three-band Tight-Binding Model for Monolayers of Group-VIB Transition Metal Dichalcogenides [Phys. Rev. B 88, 085433 (2013)]", Phys. Rev. B **89**, 039901 (2014).
[637]J. D. Hunter, "Matplotlib: A 2D Graphics Environment", Comput. Sci. Eng. **9**, 90–95 (2007).
[638]C. Sanderson and R. Curtin, "Practical Sparse Matrices in C++ with Hybrid Storage and Template-Based Expression Optimisation", Math. Comput. Appl. **24**, 70 (2019).
[639]C. Sanderson and R. Curtin, "Armadillo: An Efficient Framework for Numerical Linear Algebra", in 2025 17th Int. Conf. Comput. Autom. Eng. ICCAE (Mar. 2025), pp. 303–307.
[640]H. J. Monkhorst and J. D. Pack, "Special Points for Brillouin-zone Integrations", Phys. Rev. B **13**, 5188–5192 (1976).
[641]J. D. Pack and H. J. Monkhorst, "Special Points for Brillouin-zone Integrations - a Reply", Phys. Rev. B **16**, 1748–1749 (1977).
[642]M. Galassi and et. al., *GNU Scientific Library Reference Manual*, 2009.

ACKNOWLEDGEMENTS

I would like to use this opportunity to thank the people who supported me during my PhD.

Starting with my family, I thank my wife Daniela for supporting me during these trying times and affording me the necessary time and space to work on my scientific career. I thank my parents, Sabine and Karlheinz, for their support, without which I could not have pursued my studies. I thank my brother Tobias, especially for supporting me during the hardest time of my PhD. I thank my parents in law, Gerlinde and Herbert, for their plentiful support, including, but not limited to, the opportunity to live in their house and leave the daycare of our dogs to them, freeing myself to work on this project. I further thank my uncle Hans-Jürgen for his good advice in life, especially in financial matters, and for his fostering of my early interest in science. I thank my other uncle Roland, my grandparents Laura and Karlheinz, and my remaining family for supporting me throughout my PhD. I remember kindly my late great-grandmother Laura and grandmother Elisabeth, both of whom raised me.

With great gratitude, I thank Maria, Jordi, Johannes, and Magda for their proof-reading of parts of this thesis. Turning to my further friends, I want to thank Torsten, Christina, Isabella, Ludwig, Hannah, Daniel, and Josy for many game nights and plenty of cherished memories I share with them. I thank Nithin for the opportunity to visit Kerala. I thank Tobias, Moritz, Thomas, and Adrian for their open ear in times of need, and the music we played together.

At the chair, I thank John, Milena, and Magda for the opportunity to engage in this scientific endeavor. I thank Andrea for bringing me to the chair, plenty of discussions, and even more good coffee. I thank Max, Patrick, and Paul for the brilliant discussions on all things IT. I especially thank Maria for putting up with me handing over my knowledge as WGM. I apologize to Lucia for every buggy line of code she inherited, but thank her for the incredible enthusiasm she showed when working together. I thank Alessandro, Juliane, Anton, and Simon, all of whom had to endure my supervision at some point. I thank Jan for discussions about good music, Luca for guitars, and Christoph for all things finance. I further thank Moritz, Debasmita, Alex, Bashab, Masseim, Atiye, and Adrian for plenty of pleasant discussions over lunch or coffee. I thank the local IT-superheros, Fritz and Peter, for plenty of WGM-related shenanigans, the secretaries Sylvia, Petra, Berna, Alex for their great support and pleasant discussions. I especially thank Bettina for plenty of good laughs. Finally, I thank my coauthors Miguel and Marcin for their scientific cooperation and sound advice.

Eidesstattliche Erklärung

(1) Ich erkläre hiermit an Eides statt, dass ich die vorliegende Arbeit ohne unzulässige Hilfe Dritter und ohne Benutzung anderer als der angegebenen Hilfsmittel angefertigt habe; die aus anderen Quellen direkt oder indirekt übernommenen Daten und Konzepte sind unter Angabe des Literaturzitats gekennzeichnet.

(2) Bei der Auswahl und Auswertung folgenden Materials haben mir die nachstehend aufgeführten Personen in der jeweils beschriebenen Weise entgeltlich/unentgeltlich geholfen:

(3) Weitere Personen waren an der inhaltlich-materiellen Herstellung der vorliegenden Arbeit nicht beteiligt. Insbesondere habe ich hierfür nicht die entgeltliche Hilfe eines Promotionsberaters oder anderer Personen in Anspruch genommen. Niemand hat von mir weder unmittelbar noch mittelbar geldwerte Leistungen für Arbeiten erhalten, die im Zusammenhang mit dem Inhalt der vorgelegten Dissertation stehen.

(4) Die Arbeit wurde bisher weder im In- noch im Ausland in gleicher oder ähnlicher Form einer anderen Prüfungsbehörde vorgelegt.